



**MATERIALS CHARACTERIZATION AND MICROELECTRONIC
IMPLEMENTATION OF METAL-INSULATOR TRANSITION MATERIALS
AND PHASE CHANGE MATERIALS**

THESIS

Alexander H. Gwin, 1st Lt, USAF

AFIT-ENG-MS-15-M-016

**DEPARTMENT OF THE AIR FORCE
AIR UNIVERSITY**

AIR FORCE INSTITUTE OF TECHNOLOGY

Wright-Patterson Air Force Base, Ohio

DISTRIBUTION STATEMENT A.
APPROVED FOR PUBLIC RELEASE; DISTRIBUTION UNLIMITED.

The views expressed in this thesis are those of the author and do not reflect the official policy or position of the United States Air Force, Department of Defense, or the United States Government. This material is declared a work of the U.S. Government and is not subject to copyright protection in the United States.

AFIT-ENG-MS-15-M-016

MATERIALS CHARACTERIZATION AND MICROELECTRONIC
IMPLEMENTATION OF METAL-INSULATOR TRANSITION MATERIALS AND
PHASE CHANGE MATERIALS

THESIS

Presented to the Faculty

Department of Electrical and Computer Engineering

Graduate School of Engineering and Management

Air Force Institute of Technology

Air University

Air Education and Training Command

In Partial Fulfillment of the Requirements for the
Degree of Master of Science in Electrical Engineering

Alexander H. Gwin, BS

First Lieutenant, USAF

March 2015

DISTRIBUTION STATEMENT A.
APPROVED FOR PUBLIC RELEASE; DISTRIBUTION UNLIMITED

AFIT-ENG-MS-15-M-016

MATERIALS CHARACTERIZATION AND MICROELECTRONIC
IMPLEMENTATION OF METAL-INSULATOR TRANSITION MATERIALS AND
PHASE CHANGE MATERIALS

Alexander H. Gwin, BS

First Lieutenant, USAF

Committee Membership:

Dr. Ronald A. Coutu, Jr.
Chair

Maj Derrick Langley, PhD
Member

Dr. Alex Li
Member

Abstract

Vanadium dioxide (VO_2) is a metal-insulator transition (MIT) material, and germanium telluride (GeTe) is a phase change material (PCM), both of which undergo several orders of magnitude increase in electrical conductivity from room temperature to their transition temperatures. They are candidates for many important technologies, including ultra-fast electronic memory, optical switches and filters, and active layers in terahertz metamaterials, among others. The physical mechanisms causing the phase transitions in these materials are explained and investigated experimentally. These materials were incorporated into six types of microelectronic devices, which were designed, fabricated, and tested at the Air Force Institute of Technology (AFIT). Additionally, these materials were investigated by materials characterization methods spanning the majority of the electromagnetic spectrum. The results show a most suitable applicability to electronic radio frequency (RF) switches, terahertz (THz) modulators, and phase change random access memory (PCRAM). Simple RF switches had 2-dB insertion losses and 30 dB of isolation, THz transmittance modulation of up to 99.5%, and PCRAM cells with threshold electric fields of approximately 1 V/ μm .

Keywords: Germanium telluride, phase change random access memory, radio frequency switch, terahertz modulator, vanadium dioxide

Acknowledgments

There are many people I would like to thank for their contributions to this research. First, I am indebted to my research advisor, Dr. Ron Coutu, for his valuable feedback and mentoring. My committee members, Dr. Derrick Langley and Dr. Alex Li, were always helpful in answering questions and discussing experimental results. I am appreciative of many people who helped me due to their kindness and pure enthusiasm for learning and researching. These people are Seth Brittle (Wright State University), Dr. Mike Jespersen (AFRL/RXA), Rob Lake (AFIT/ENG), Tod Laurvick (AFIT/ENG), Doug McFarland (AFRL/RXD), Greg Smith (AFIT/ENP), and Steve Tetlak (AFRL/RXD). Next, I would like to thank the AFIT cleanroom technicians, Rich Johnston and Tom Stephenson, for their consistent support. Lastly, I would like to thank my student colleagues, Tom Donigan, Joe Haefner, Rob LaFleur, Jim Sattler, and John P. K. Walton, for keeping the mood light and for providing feedback and encouragement.

Table of Contents

	<u>Page</u>
Abstract	iv
Acknowledgments	v
Table of Contents	vi
List of Figures	ix
List of Tables	xvii
List of Acronyms	xviii
1. Introduction	1
2. Literature Review	4
2.1. Introduction	4
2.2. Crystallography	4
2.3. Transition Metal Oxides	8
2.4. Metal-Insulator Transition	23
2.5. Applications for MIT Devices	40
2.6. Phase Change Materials	45
2.6.1. History	45
2.6.2. Optical Memory	46
2.7. Germanium Telluride	51
2.8. Phase Change Electronic Memory	53
2.9. Applications for Phase Change Materials	63
2.10. Materials Characterization Methods	65
2.11. Fabrication Methods	80
2.12. Summary	81
3. Methodology	82
3.1. Introduction	82
3.2. Design	82
3.3. Fabrication	87
3.4. Measurements of Devices	89
3.5. Materials Characterization	96
3.6. Considerations when using a Probe Station	100
3.7. Sputtering Experiments	101
3.8. Testing Methodology	103
3.9. Summary	104

4. Results.....	105
4.1. Introduction.....	105
4.2. Vanadium Oxide	106
4.2.1. Resistance Measurements	106
4.2.2. EDS	108
4.2.3. XPS.....	110
4.2.4. Micro-Raman	113
4.3. Germanium Telluride.....	115
4.3.1. Resistance Measurements	115
4.3.2. Application of Voltage Pulses.....	116
4.3.3. I-V Curves	117
4.3.4. Capacitance Measurements	124
4.3.5. S Parameters	124
4.3.6. Determination of T_c for various thicknesses	140
4.3.7. Terahertz Transmittance and Absorbance.....	142
4.3.8. Spectroscopic Ellipsometry.....	146
4.3.9. Spectral Reflectance	149
4.3.10. Spectrophotometry and FTIR.....	154
4.4. Summary	156
5. Analysis.....	158
5.1. Introduction.....	158
5.2. Vanadium Oxide	158
5.2.1. Sputtering Experiments	158
5.2.2. Resistance Measurements	158
5.2.3. EDS	159
5.2.4. XPS.....	159
5.2.5. Micro-Raman	160
5.3. Germanium Telluride.....	163
5.3.1. Resistance Measurements	163
5.3.2. Application of Voltage Pulses.....	166
5.3.3. I-V Curves	166
5.3.4. Capacitance Measurements	170
5.3.5. S Parameters	170
5.3.6. Determination of T_c for various thicknesses	172
5.3.7. Terahertz Transmittance and Absorbance.....	173
5.3.8. Spectroscopic Ellipsometry.....	175
5.3.9. Spectral Reflectance	176
5.3.10. Spectrophotometry and FTIR.....	178
5.4. Summary	179
5.4.1. Vanadium Oxide	179
5.4.2. Germanium Telluride	180

6. Conclusions.....	182
6.1. Conclusions of Research.....	182
6.2. Contributions.....	183
6.3. Recommendations for Future Research	185
Appendix A. Process Follower for GeTe on 3” Silicon Wafers	187
Appendix B. Process Follower for GeTe on 2” Sapphire Wafers	190
Bibliography	193

List of Figures

<u>Figure</u>	<u>Page</u>
Figure 1. Venn diagram of materials discussed in this thesis. Solids span an area which extends much farther than what is shown. The areas of sets are intentionally relative (i.e., chalcogenides comprise a greater percentage of PCMs than MIT materials do TMOs). TMOs are transition metal oxides, MIT materials are metal-insulator transition materials, VO ₂ is vanadium dioxide, PCMs are phase change materials, and GeTe is germanium telluride.	2
Figure 2. Vectors (red) and angles in a crystal unit cell. Angle α is the angle in the plane formed by vectors b and c , angle β is formed between a and c , and angle γ is formed between a and b	5
Figure 3. Bravais Lattices [1].....	7
Figure 4. NaCl and CsCl crystal structures [1].....	7
Figure 5. The transition metals in the Periodic Table [4].	8
Figure 6. Coordination geometries where M is the metal and O is oxygen: (a) tetrahedral, (b) square planar, (c) octahedral, (d) distorted octahedral for Mo in MoO ₃ , and (e) distorted octahedral for Cu in La _{1.85} Sr _{0.15} CuO ₄ . Interatomic distances are in pm (i.e., 100 pm = 1 Å) [5]......	10
Figure 7. Three-dimensional shorthand notation for several binary octahedra; oxygen atoms occupy vertices and metal atoms are located in the centers of each octahedron. (a) Rhenium trioxide which is uncommon but forms the basis for important perovskite ternary structures, (b) rutile (body-centered tetragonal) which is common in dioxides, and (c) corundum (trigonal) which is common for M ₂ O ₃ trioxide compounds [5].	11
Figure 8. (a) The <i>d</i> orbitals of a metal ion, organized by e _g and t _{2g} symmetry sets, and (b) associated orbital energies with crystal field splitting Δ [5]......	12
Figure 9. Qualitative molecular orbital (MO) diagram for an octahedral transition <i>d</i> metal ion and 2 <i>p</i> oxygen ions [5]. Particular attention should be paid to the 3 <i>d</i> -2 <i>p</i> MO energies.	13
Figure 10. Oxygen 2 <i>p</i> orbitals in an octahedron bonding (or not bonding) with the centered metal orbital [5]......	14
Figure 11. Representative one-dimensional band diagram for a 3 <i>d</i> metal oxide over the interval $0 < k < \pi a$. In compounds which are mostly ionic (e.g., transition metal oxides), oxygen predominantly contributes to bonding orbitals, and the metal to antibonding orbitals [5]......	15
Figure 12. Fermi surface for RuO ₂ , where occupied energy states lie within the locus of the surface and unoccupied states lie outside the surface [5].	16

Figure 13. (a) Relationship between superlattice periodicity, a' , and lattice distortions; (b) Formation of a new bandgap at $k = \pi a'$ [5].	17
Figure 14. Process of determining ionic band model of NiO; Madelung potential is an electrostatic charge due to placing the ions in the lattice; and CFSE is the Crystal Field stabilization energy equivalent to $-(2/5)\Delta$ for t_{2g} orbitals and $+(3/5)\Delta$ for e_g orbitals. The bandgap is E_g , and the bandwidths are the energy thicknesses (heights) of each band represented by rectangles. Occupied bands are dashed [5].	19
Figure 15. Upper and lower Hubbard sub-bands which overlap at bandwidth $W \sim U$ to yield a metallic state [5].	20
Figure 16. (a) Localized atomic orbital energies due to numerous defects in the lattice; (b) Density of states with mobility edges represented by the boundaries between the center extended states and (dashed) localized states [5].	21
Figure 17. Metal-insulator transition (MIT) mechanism due to Anderson localization, where impurity concentration increases from (a) to (e). (a) Dilute impurities below the conduction band, (b) Impurity band formed by an increased concentration which is half-filled with one electron per defect site, (c) Formation of Lower and Upper Hubbard Sub-bands, where the UHSB overlaps the conduction band, (d) The impurity band broadens and the sub-bands converge and Anderson localization occurs, (e) Fermi level extends through the material which contributes to metallic conductivity [5].	22
Figure 18. Measured electrical conductivity (F. J. Morin, 1959) of several vanadium and titanium oxides; note the inverse-temperature scale of the x-axis [8].	23
Figure 19. Selected oxides sorted by transition temperature, T_{MIT} [11]. VO_2 has the closest T_{MIT} above room temperature. The error bar for Ti_2O_3 is indicative of a gradual transition.	24
Figure 20. Band diagram of VO_2 by J. Goodenough [12, p. 1232].	27
Figure 21. Lattice structure in (a) Monoclinic/insulating phase and (b) Tetragonal/metallic phase [14].	27
Figure 22. Simplified representation of the thinning of $3d$ wavefunction oxide bandwidth, from left to right, in row 4 [7].	28
Figure 23. Energy levels for Ti_2O_3 : (a) Trigonal $3d$ splitting of t_{2g} and e_g orbitals, (b) Formation of bonding and antibonding levels, (c)-(d) Converging of energy bands due to increased temperature [5].	29
Figure 24. Experiment combining electric field and heat in VO_2 . (a) I-V curves at stepped temperatures, (b) Observed linear relationship between V^2 and applied temperature [19].	33
Figure 25. Three-terminal field-effect device with VO_2 as the semiconductor channel material; (a) Cross-sectional view, (b) Top view [14].	35

Figure 26. Phase diagram of vanadium oxide (VO_x), temperature plotted vs. oxygen-to-vanadium ratio. At the far left is vanadium monoxide (VO), and vanadium pentoxide (V_2O_5) is on the far right. Deposition temperatures when sputtering do not typically exceed 600°C [11].	36
Figure 27. Thornton's three-zone surface morphology model. T_M is the melting temperature and T is the substrate temperature during deposition [35].	37
Figure 28. Typical hysteresis of VO_2 ($5 - 10^\circ\text{C}$) [17].	40
Figure 29. Simulated and measured tip displacement of VO_2/SiO_2 MEMS bimorph cantilever beams. Large displacements are due to VO_2 's coefficient of thermal expansion which increases at T_{MT} [57].	41
Figure 30. Measured transmission in OFF (blue) and ON (red) in a VO_2 RF switch [58].	42
Figure 31. VO_2 terahertz transmission modulation vs. temperature. The decrease in transmission directly correlates to the change of the material's resistivity [60].	43
Figure 32. Infrared reflectance of VO_2 on Sapphire. (a) Reflectance vs. sweeping of photon energy while stepping temperature; (b) Reflectance vs. sweeping of temperature while stepping photon energy [48].	44
Figure 33. Portion of the Periodic Table; the chalcogens are in Group 16 [4].	48
Figure 34. Typical cross-sectional structure of phase change optical memory (after ref. [76]). The dielectric layer is typically ZnS-SiO_2 with total thickness on the order of 50 nm.	49
Figure 35. Ge-Sb-Te ternary system with highlighted stoichiometries along the $\text{GeTe-Sb}_2\text{Te}_3$ tie line. (GeTe has 50% Te, and Sb_2Te_3 has 40% Sb.) Listed optical contrasts $\Delta n + i\Delta k$ are for 405-nm Blu-ray systems [78].	50
Figure 36. (a) Rhombohedral GeTe lattice without defects, (b) Illustration of the effect of a Ge vacancy on the GeTe lattice. Red atoms are Ge, gold atoms are Te, and blue atoms are Te nearest neighbor atoms to the Ge vacancy [88].	52
Figure 37. Vertically oriented PCRAM cell [74].	54
Figure 38. Horizontally oriented PCRAM cell fabricated by electron-beam lithography; image captured with a scanning electron microscope [95].	54
Figure 39. Typical I-V curve of a PCRAM cell which exhibits a highly resistive amorphous OFF state, threshold switching, a more conductive amorphous ON state, memory switching, and a low resistance crystalline ON state [78].	56
Figure 40. Barrier between two trap states I and II; the electric field F increases from (a) to (c) and the barrier height is reduced by ΔU [93].	57
Figure 41. Simple I-V curve of a PCRAM cell showing the characteristic snap of threshold voltage. In this experiment a resistor was placed in series with the cell to prevent large voltage drops across the cell; the resistor's voltage IR_{series} is subtracted	

out of the values in the horizontal axis [95]. The linearly increasing current in the a-ON region is likely due to the large resistive bottom heater in Figure 37.....	59
Figure 42. Energy bands (conduction band, E_C , Fermi energy, E_F , and valence band, E_V) and traps in chalcogenides for (a) low to moderate electric fields and (b) high electric fields. The electrons jump to unoccupied trap states via thermionic emission or direct tunneling. [93].	59
Figure 43. OFF and ON regions in amorphous chalcogenides due to high electric fields for (a) low currents and an equilibrium distribution of electrons and (b) high currents and electrons occupying shallow trap states. The cathode is the grey region on the left, and the anode is the grey region on the right [93]......	60
Figure 44. Conductivity drift in amorphous chalcogenides from time t_1 to t_2 explained by shift of the Fermi energy and increase in activation energy, E_A [98]......	61
Figure 45. Possible electron transitions for K, L, and M shells [114]	66
Figure 46. Reflection and transmission of light in air, thin film, and substrate [118]. The complex index of refraction for layer i is \tilde{N}_i	69
Figure 47. Layout of nine identical reticles (each reticle is shown in Figure 48) on a 3-inch-diameter wafer. The reticles are spaced evenly across the wafer. These spaces between reticles provide adequate room for dicing the wafer before testing.	83
Figure 48. Mask design of one reticle using Tanner L-Edit CAD software. Black horizontal lines were used for alignment and were deleted before creating fabrication files. Light blue, red, and brown correspond to bottom gold layer, active layer (VO_2 or GeTe), and top gold layer, respectively. Each row contains a category of devices with dimensions decreasing from left to right.	84
Figure 49. Six categories of devices designed to test the electrical and thermal characteristics of the active layer (VO_2 or GeTe). Each of these devices has seven variations in dimensions. Orange layers are metal (gold) contact pads and blue layers are the active layer. The categories are the following: (a) Simple resistor, (b) Resistor with gaps between contact pads, (c) Resistor with bottom heater, (d) RF switch, (e) Resistor with top heater, and (f) Capacitor.	87
Figure 50. Measurement setup for resistance vs. temperature. The red platform represents the heating stage, through which heat is conducted by a ceramic plate. One reticle (multiple devices) is heated per measurement.	90
Figure 51. Instrumentation for two-terminal device, including a voltmeter (V), ammeter (A), and power source (\leftarrow). The voltmeter is switched off prior to measuring current. Depending on the resistance of the active layer, the power source is switched between constant voltage (CV) mode and constant current (CC) mode. ...	92
Figure 52. Implementation of a series resistor to reduce the voltage drop across the device under test.	93
Figure 53. Instrumentation for measuring I-V curves on a three-terminal device. (a) Setup includes an amplifier and (b) Setup for when V_1 is large enough and an	

amplifier is unnecessary. The voltmeter (V) is open-circuited before measuring current.	94
Figure 54. Electromagnetic Spectrum. Blue regions indicate portions of the spectrum used in this research for characterization of materials. The characterization methods are listed at the bottom of the figure. Those methods which do not correspond to a specific portion of the spectrum (XPS, EDS, and Micro-Raman) are listed at the very bottom, roughly correlated to their characteristic energies.	97
Figure 55. Wide-angle SEM capture of fabricated devices; each category of devices is listed on the left-hand side of the figure.	106
Figure 56. Change in resistance for several VO ₂ thin films. The current through the VO ₂ thin film and voltage across it are measured, and resistance is calculated from these values. The probe spacing is held constant within each trial.	107
Figure 57. EDS measurement of sample 5a from 0 to approximately 7 eV.	109
Figure 58. EDS measurement of sample 5a; closer view of the 0 to 1.4 eV range.	110
Figure 59. XPS plot of sample 5a.	111
Figure 60. XPS plot of sample 11a.	112
Figure 61. XPS plot of sample 12a; suboxide is V _x O _y with y:x ratio of less than 3:2... ..	112
Figure 62. Several Raman spectra of sample 1 excited by a 532-nm laser.	113
Figure 63. Raman spectra of sample 5a excited by a 633-nm laser.	114
Figure 64. Raman spectra of sample 11a (633-nm laser). The blue and black spectra are the same data set with different magnifications. Because the silicon peak (524 cm ⁻¹) is so strong in the black spectra, the other peak intensities are very small by comparison. The intensity range from 0 to 1,000 is magnified for the blue spectra. This aids in identifying the peaks.	114
Figure 65. Raman spectra of sample 12a (633-nm laser).	115
Figure 66. Log plots of resistance vs. temperature with linearly scaled inset plots: (a) GeTe on SiO ₂ /c-Si substrate, (b) GeTe on Si ₃ N ₄ /c-Si substrate, (c) GeTe on c-Si substrate, and (d) GeTe on (0001) Al ₂ O ₃ substrate. The top plots show a nonvolatile change in resistance indicative of permanent crystallization, while the bottom plots show a volatile transition.	116
Figure 67. Measured I-V curves for amorphous GeTe thin films in simple resistors (second smallest) on various substrates: (a) Log plot of all four I-V curves for comparison, (b) Memory curve of GeTe on c-Si substrate showing amorphous ON and crystallization, (c) GeTe on Si ₃ N ₄ /c-Si substrate, and (d) SiO ₂ /c-Si and Al ₂ O ₃ plots which do not reach an amorphous ON state. The PCM cell on Al ₂ O ₃ is shown in Figure 1(b) whereas all others are 1(a); no current could be measured on Al ₂ O ₃ in the larger cell structure 1(a).	118

Figure 68. Measured I-V curves for amorphous GeTe thin films in simple resistors (smallest) on various substrates: (a) Log plot of all four I-V curves for comparison, (b) Two curves of GeTe on c-Si substrate from two different devices in the middle right (MR) and top left (TL) reticles, (c) GeTe on $\text{Si}_3\text{N}_4/\text{c-Si}$ substrate, and (d) $\text{SiO}_2/\text{c-Si}$ plot. The PCM cell on sapphire is shown in Figure 67.	120
Figure 69. I-V curves of the simple resistor of Figure 67(b) of four subsequent trials, all of which show a voltage snap-back at their threshold voltage: (a) All four trials for comparison where Trial 1 is the same as Figure 67(b), (b) Trials 2, 3, and 4, (c) Closer view of the threshold voltages for trials 2-4, (d) Resistance of the cells vs. applied voltage, where the curves cycle to the right and downward.	121
Figure 70. Resistor with melted GeTe and probes removed; 50 \times magnification.	121
Figure 71. I-V curves of the top heater (smallest) on $\text{Si}_3\text{N}_4/\text{c-Si}$ substrate; V_d is the applied voltage as in the previous figures (“drain” voltage), and V_g is the stepped voltage (“gate” voltage) from the top heater to the “drain” voltage pad. Reference Figure 53 for the experimental setup.	123
Figure 72. Resistor tested in Figure 71, showing placement of probes and melted GeTe; 10 \times magnification.	123
Figure 73. Placement of probes for a capacitance measurement	124
Figure 74. S parameters of RF switches on c-Si substrate, 300kHz to 3 GHz; (a) RF1, (b) RF2, (c) RF3, (d) RF4, (e) RF5, (f) RF6, (g) RF7.	127
Figure 75. S parameters of RF switches on c-Si substrate, 10 MHz to 20 GHz; (a) RF1, (b) RF2, (c) RF3, (d) RF4, (e) RF5, (f) RF6, (g) RF7.	128
Figure 76. S parameters of RF switches on $\text{Si}_3\text{N}_4/\text{c-Si}$ substrate, 300 kHz to 3 GHz; (a) RF1, (b) RF2, (c) RF3, (d) RF4, (e) RF5, (f) RF6, (g) RF7.	129
Figure 77. S parameters of RF switches on $\text{Si}_3\text{N}_4/\text{c-Si}$ substrate, 10 MHz to 20 GHz; (a) RF1, (b) RF2, (c) RF3, (d) RF4, (e) RF5, (f) RF6, (g) RF7.	130
Figure 78. S parameters of RF switches on $\text{SiO}_2/\text{c-Si}$ substrate, 300 kHz to 3 GHz; (a) RF1, (b) RF2, (c) RF3, (d) RF4, (e) RF5, (f) RF6, (g) RF7.	131
Figure 79. S parameters of RF switches on $\text{SiO}_2/\text{c-Si}$ substrate, 10 MHz to 20 GHz; (a) RF1, (b) RF2, (c) RF3, (d) RF4, (e) RF5, (f) RF6, (g) RF7.	132
Figure 80. Insertion loss and Isolation of RF switches on c-Si substrate, 300kHz to 3 GHz; (a) RF1, (b) RF2, (c) RF3, (d) RF4, (e) RF5, (f) RF6, (g) RF7.	134
Figure 81. Insertion loss and Isolation of RF switches on c-Si substrate, 10 MHz to 20 GHz; (a) RF1, (b) RF2, (c) RF3, (d) RF4, (e) RF5, (f) RF6, (g) RF7.	135
Figure 82. Insertion loss and Isolation of RF switches on $\text{Si}_3\text{N}_4/\text{c-Si}$ substrate, 300kHz to 3 GHz; (a) RF1, (b) RF2, (c) RF3, (d) RF4, (e) RF5, (f) RF6, (g) RF7.	136
Figure 83. Insertion loss and Isolation of RF switches on $\text{Si}_3\text{N}_4/\text{c-Si}$ substrate, 10MHz to 20 GHz; (a) RF1, (b) RF2, (c) RF3, (d) RF4, (e) RF5, (f) RF6, (g) RF7.	137

Figure 84. Insertion loss and Isolation of RF switches on SiO ₂ /c-Si substrate, 300kHz to 3 GHz; (a) RF1, (b) RF2, (c) RF3, (d) RF4, (e) RF5, (f) RF6, (g) RF7.	138
Figure 85. Insertion loss and Isolation of RF switches on SiO ₂ /c-Si substrate, 10 MHz to 20 GHz; (a) RF1, (b) RF2, (c) RF3, (d) RF4, (e) RF5, (f) RF6, (g) RF7.	139
Figure 86. Terahertz time-domain signal showing the peak intensities and scanner position. The decrease in peak intensity corresponds to increased absorbance. A shift of scanner position to the right corresponds to a thicker sample.....	143
Figure 87. (a) Terahertz transmittance as the sample is heated from R. T. to 250°C, (b) Closer view of 10 – 60 cm ⁻¹ and the relative transmittance of the Relaxed sample to the other waveforms.	144
Figure 88. (a) Terahertz absorbance as the sample is heated from R. T. to 250°C, (b) Closer view of 10 – 60 cm ⁻¹ and the relative absorbance of the Relaxed sample to the other waveforms.	144
Figure 89. GeTe terahertz transmittance modulation; state-of-the-art systems have modulation depths of 50%, and VO ₂ on sapphire (heated) has a modulation depth of approximately 80%.	146
Figure 90. SE models of amorphous and crystalline GeTe from 1.5 eV to 6.5 eV. (a) – (b) Index of refraction, n , and extinction coefficient, k ; (c) – (d) Real and imaginary components of the complex dielectric function, ϵ_r and ϵ_i , respectively. Plots on the left are of an amorphous sample, and plots on the right are of a crystalline sample heated by conduction beyond its crystallization temperature. Both samples were prepared by RF sputtering on single-sided-polished c-Si in the same processing batch. There was no discernible difference between the measured data and ellipsometry models (measured data not plotted).	148
Figure 91. Measured absorption coefficient, α , of GeTe in crystalline and amorphous phases: (a) 1.5 eV – 6.5 eV and (b) 191 nm – 827 nm.	149
Figure 92. Spectral reflectance of GeTe on various substrates, where each curve corresponds to a sample. Within each plot, the upper set of curves are crystalline and the lower set are amorphous. (a) All sample measurements, (b) Averages within each type of substrate, (c) c-Si, (d) Si ₃ N ₄ /c-Si, (e) Al ₂ O ₃ , (f) SiO ₂ /c-Si.	151
Figure 93. Contrast in spectral reflectance for GeTe by each substrate type. The average of the crystalline and amorphous data are subtracted to determine the contrast, in percent reflection.	152
Figure 94. Spectral reflectance of (a) Sets 2 – 5 on c-Si, (b) The average reflection of both phases of Set 1, (c) Measurements of Set 2, (d) Measurements of Set 3, (e) Measurements of Set 4. Sets 5 and 6 were not crystallized and are not shown in this figure.	153
Figure 95. Spectral reflectance of (a) Set 5 and (b) Set 6.	154

Figure 96. Optical transmission of GeTe on double-sided-polished (DSP) c-Si; (a) Spectrophotometry, (b) FTIR. FTIR is plotted vs. wavenumber, so the upper x-axis is converted to wavelength in microns. There is some overlap between the two plots, from 1.33 to 2.5 μm	155
Figure 97. Optical transmission by spectrophotometry of GeTe on sapphire; (a) showing amorphous and crystalline data relative to the sapphire data, (b) closer view of GeTe transmission, (c) GeTe thin film transmission relative to the sapphire transmission at each wavelength. The small jumps apparent in the sapphire and a-GeTe data are due to the mechanical switching of optical sources.	156
Figure 98. Measured spectral reflectance of GeTe on $\text{SiO}_2/\text{c-Si}$ substrate.....	177

List of Tables

<u>Table</u>	<u>Page</u>
Table 1. Seven Crystal Systems and Associated Bravais Lattices [1]	6
Table 2. Vanadium oxides and their metal-insulator transition temperatures (compiled from numerous references).	26
Table 3. Review of Sputtering Parameters for VO ₂	39
Table 4. Characteristic x-ray energies of selected elements [114]	67
Table 5. Calculated relationship between decibels (dB) and magnitude in increments of 10 dB. The scientific notation in the right column helps to clarify the logarithmic periodicity of decibels.....	78
Table 6. Parallel resistance R_p for various resistances of voltmeter R_m and device resistance R_d . For less than ten percent error between R_d and R_p , R_d must be less than 1 M Ω	92
Table 7. Materials characterization systems used.....	98
Table 8. VO ₂ sputtering experiments.....	102
Table 9. Resistance values for RF switches, organized by substrate type	126
Table 10. Correlation of GeTe crystallization temperature, T _c , and sputtering parameters	141
Table 11. Raman spectra of various vanadium oxides; listed values are Raman shifts in units of cm ⁻¹	162
Table 12. Heat conduction parameters (blank values are N/A).	165

List of Acronyms

a. u.	Arbitrary Units
AC	Alternating Current
AFIT	Air Force Institute of Technology
AO	Atomic Orbital
CAD	Computer Aided Design
CC	Constant Current
CCD	Charge Coupled Device
CD	Compact Disc
CF	Crystal Field
CFSE	Crystal Field Stabilization Energy
CMOS	Complementary Metal-Oxide-Semiconductor
CV	Constant Voltage
CVD	Chemical Vapor Deposition
DC	Direct Current
DI	De-ionized
DRAM	Dynamic Random Access Memory
DRIE	Deep Reactive Ion Etching
DSP	Double-sided Polished
DVD	Digital Versatile Disc
EDS	Energy Dispersive Spectroscopy
EHF	Extremely High Frequency
FeRAM	Ferroelectric Random Access Memory
FET	Field-effect Transistor
FIR	Far-Infrared
FTIR	Fourier Transform Infrared
FWHM	Full Width at Half Maximum
HARMST	High Aspect Ratio Microsystems Technology
LCAO	Linear Combination of Atomic Orbital
LHSB	Lower Hubbard Sub-band
LIGA	Lithographie, Galvanoformung, Abformung (German)
LPCVD	Low Pressure Chemical Vapor Deposition
MEMS	Microelectromechanical Systems
M	Metal Atom
MIR	Mid-Infrared
MIT	Metal-Insulator Transition
MM	Metamaterial
MO	Molecular Orbital
MRAM	Magnetic Random Access Memory
MTFET	Mott Transition Field-effect Transistor
NA	Numerical Aperture
NDR	Negative Differential Resistance
NIR	Near-Infrared

NW	Nanowire
O	Oxygen Atom
OUM	Ovonic Universal Memory
PCM	Phase Change Material
PCRAM	Phase Change Random Access Memory
PECVD	Plasma Enhanced Chemical Vapor Deposition
PMMA	Polymethyl Methacrylate
PNA	Programmable Network Analyzer
R	Rutile
R. T.	Room Temperature
RAM	Random Access Memory
RENS	Resolution Near-Field Structure
RF	Radio Frequency
RIE	Reactive Ion Etching
RRAM	Resistive Random Access Memory
SE	Spectroscopic Ellipsometry
SEM	Scanning Electron Microscope
SIL	Solid Immersion Lens
SOA	State-of-the-art
SRAM	Static Random Access Memory
SRR	Split Ring Resonator
SSP	Single-sided Polished
TAGS	Tellurium-Antimony-Germanium-Silver
TDS	Time-Domain Spectroscopy
TE	Thermoelectric
TEM	Transmission Electron Microscope
T_c	Crystallization Temperature
T_g	Glass Temperature
THz	Terahertz
T_m	Melting Temperature
T_{MIT}	Metal-Insulator Transition Temperature
TMO	Transition Metal Oxide
T_s	Substrate Temperature
UHSB	Upper Hubbard Sub-band
UHV	Ultra High Vacuum
UV	Ultraviolet
Vis	Visible
WDS	Wavelength Dispersive Spectroscopy
XPS	X-ray Photoelectron Spectroscopy

MATERIALS CHARACTERIZATION AND MICROELECTRONIC IMPLEMENTATION OF METAL-INSULATOR TRANSITION MATERIALS AND PHASE CHANGE MATERIALS

1. Introduction

Materials with various types of stimulus-dependent properties are an elegant solution to many scientific challenges. These various properties are typically manifested as changes in electrical, thermal, and optical properties such as electrical conductivity, thermal conductivity, and optical transmittance, respectively. The modulation of these properties offers broad applicability in many emerging technologies. As with many revolutionary materials like crystalline semiconductors, graphene, and composites, the materials discussed here could have a significant impact.

This thesis investigates two classes of materials, metal-insulator transition (MIT) materials and phase change materials (PCMs), shown in Figure 1. The former is a subset of transition metal oxides (TMOs) like MnO, NiO, and Ti_2O_3 , among many others. Specifically, vanadium dioxide (VO_2) and germanium telluride (GeTe) are studied here as representatives of MIT materials and PCMs. While providing a detailed physics background for both types of materials is truly a formidable task for one thesis, and considering many books have been written on only a portion of their properties, a best effort is accomplished by providing the salient and pertinent information for today's applications. These materials are discussed with undertones of chemistry, solid state physics, and materials science with applications in electrical engineering. Enough information from several disciplines is used to informatively discuss their properties and to adequately predict their behavior when experiments are conducted.

Solids

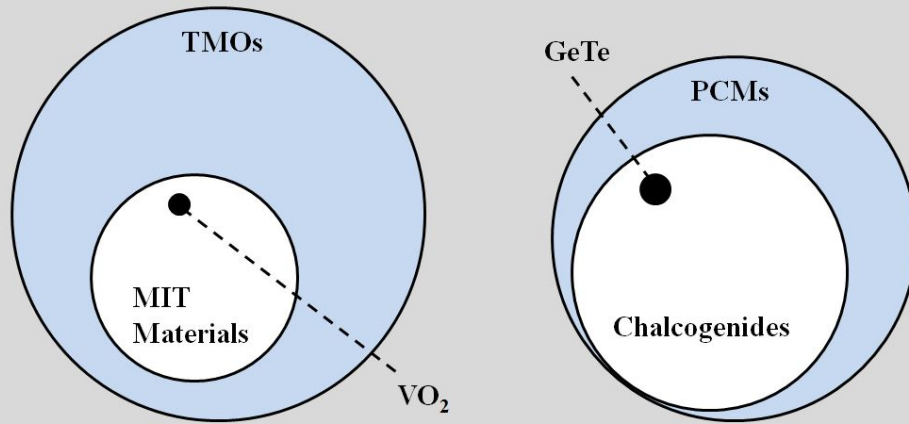


Figure 1. Venn diagram of materials discussed in this thesis. Solids span an area which extends much farther than what is shown. The areas of sets are intentionally relative (i.e., chalcogenides comprise a greater percentage of PCMs than MIT materials do TMOs). TMOs are transition metal oxides, MIT materials are metal-insulator transition materials, VO₂ is vanadium dioxide, PCMs are phase change materials, and GeTe is germanium telluride.

There are many applications in which these materials are already being integrated and many more which present exciting opportunities. PCMs have been vital to the multi-billion-dollar industry of optical memory (CDs, DVDs, and Blu-ray discs) since the 1970s and continue to be a contender for a faster and more capable next generation of Flash memory. Other applications include invisibility cloaks in the infrared and terahertz spectra, “smart” auto-tinting windows and windshields, and solid state solutions to thermo-mechanical technologies like heat turbines, refrigerators, and heat pumps. Additionally, these materials are being researched for ultra-fast transistors, more capable thermal and chemical sensors, ultra-fast random access memory, terahertz transmittance modulators, radio frequency (RF) electrical switches, tunable layers on terahertz

metamaterials, and high performance bimorph layers for microelectromechanical systems (MEMS) actuators.

The specific military applications for these materials are also numerous. Energy harvesting is an advancing field which attempts to mine waste energy for charging electronics; GeTe is being investigated for its role in thermoelectric (Seebeck) devices and VO₂ for non-thermoelectric (MEMS) devices for that application. Additionally, research of VO₂ and GeTe as terahertz modulators has direct applications to electromagnetic waves in the microwave and RF regimes for radar applications, where the energy transmitted through and reflected from the material can be electrically controlled. Infrared cloaking is an application that could yield great success for covert operations. The optimization of more capable electronic memory and RF switches is broadly applicable to commercial and military technologies alike.

The goal of this work was to deposit stoichiometric thin films of these materials and contribute to the body of knowledge about possible applications. Completed experiments include optical transmission and reflection, spectroscopic ellipsometry, terahertz spectroscopy, RF electrical characterization, and I-V curves. Various geometries of six types of fabricated devices are used in addition to four types of substrates to experiment with these materials. The majority of the electromagnetic spectrum is used for characterization.

After the literature review in Chapter 2, the methodology of design, fabrication, and testing is addressed in Chapter 3. The results are presented in Chapter 4, and a detailed analysis is presented in Chapter 5. Finally, conclusions and recommendations are presented in Chapter 6.

2. Literature Review

2.1. Introduction

This chapter addresses two classes of materials, metal-insulator transition (MIT) materials and phase change materials (PCMs). MIT materials are discussed first. To address TMOs broadly is insufficient because many TMOs do not have a metal-insulator transition. Note that with respect to MIT materials, special attention is given to vanadium dioxide, and to PCMs, germanium telluride. An overview of the physics on the molecular level is given in addition to related concepts such as past and future applications. The discourse on these materials is bookended by a brief review of crystallography and materials characterization methods, respectively.

2.2. Crystallography

Describing materials, specifically solids, by their three-dimensional configurations helps to determine many material properties. The field of crystallography is the study of three-dimensional crystal geometry [1]. All materials' crystal structures are either amorphous or crystalline, and the latter can be classified further as monocrystalline or polycrystalline. Amorphous structures are randomly oriented and typically have many lattice imperfections (e.g., vacancies and dangling bonds). They can be considered "supercooled liquids of enormous viscosity" [1]. Typical window glass (soda-lime-silica glass) is an example of an amorphous material. Monocrystals are considered perfectly arranged, where each atom occupies equilibrium positions on the lattice. Spacings between atoms may be as small as one angstrom (\AA), where $10 \text{ \AA} = 1 \text{ nm}$ [1]. Because they are simpler, it is easier to model a polycrystalline material as

monocrystalline. These structures are said to have long-range order. An example of a monocrystalline structure is crystalline silicon which is used in wafers for microelectronics fabrication. Polycrystalline materials are formed by regions of monocrystalline structure with thin boundary regions, called grain boundaries, between crystalline areas. Most metals are naturally polycrystalline [1].

Figure 2 shows a unit cell which is defined by its lattice parameters a , b , and c . By choosing an arbitrary origin, these lattice parameters are created by drawing vectors \mathbf{a} , \mathbf{b} , and \mathbf{c} (shown in red) between adjacent atoms. These vectors may not be orthogonal as shown in the figure. In fact, the angles between the vectors are defined by α , β , and γ .

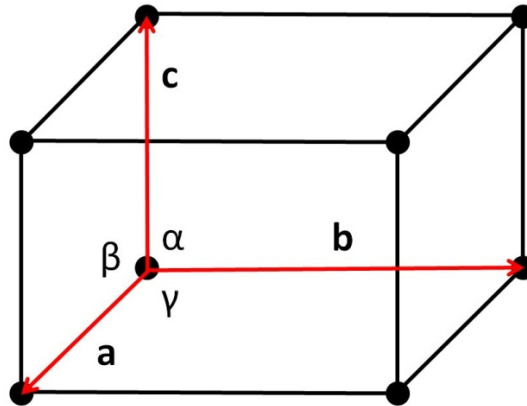


Figure 2. Vectors (red) and angles in a crystal unit cell. Angle α is the angle in the plane formed by vectors \mathbf{b} and \mathbf{c} , angle β is formed between \mathbf{a} and \mathbf{c} , and angle γ is formed between \mathbf{a} and \mathbf{b} .

All crystals can be categorized by seven crystal systems: Cubic, tetragonal, orthorhombic, monoclinic, triclinic, trigonal, and hexagonal. Furthermore, there are 14 Bravais lattices which are unique forms of unit cells [1].

The crystal systems along with their associated Bravais lattices are listed in Table 1 and are graphically depicted in Figure 3. The angles and interatomic spacings listed in the last column of Table 1 comprise the quantitative dimensions of the crystals.

Table 1. Seven Crystal Systems and Associated Bravais Lattices [1]

System	Unique Symmetry Element	Bravais Lattice	Unit Cell
Cubic	Four 3-fold rotation axes (cube diagonals)	Simple Body-centered Face-centered	$a = b = c$ $\alpha = \beta = \gamma = 90^\circ$
Tetragonal	One 4-fold rotation axis	Simple Body-centered	$a = b \neq c$ $\alpha = \beta = \gamma = 90^\circ$
Orthorhombic	Three mutually orthogonal 2-fold rotation axes	Simple Base-centered Body-centered Face-centered	$a \neq b \neq c$ $\alpha = \beta = \gamma = 90^\circ$
Monoclinic	One 2-fold rotation axis	Simple Base-centered	$a \neq b \neq c$ $\alpha = \beta = 90^\circ \neq \gamma$
Triclinic	None	Simple	$a \neq b \neq c$ $\alpha \neq \beta \neq \gamma \neq 90^\circ$
Trigonal	One 3-fold rotation axis	Simple	$a = b = c$ $\alpha = \beta = \gamma \neq 90^\circ$
Hexagonal	One 6-fold rotation axis	Simple	$a = b \neq c$ $\alpha = \beta = 90^\circ$ $\gamma = 120^\circ$

Additionally, many compounds, especially ionic crystals, bond in NaCl (sodium chloride) and CsCl (cesium chloride) arrangements. NaCl is two interpenetrating face-centered cubic lattices, where each lattice is composed of only one type of element. The CsCl structure can be considered two interpenetrating simple cubic lattices. These are shown in Figure 4.

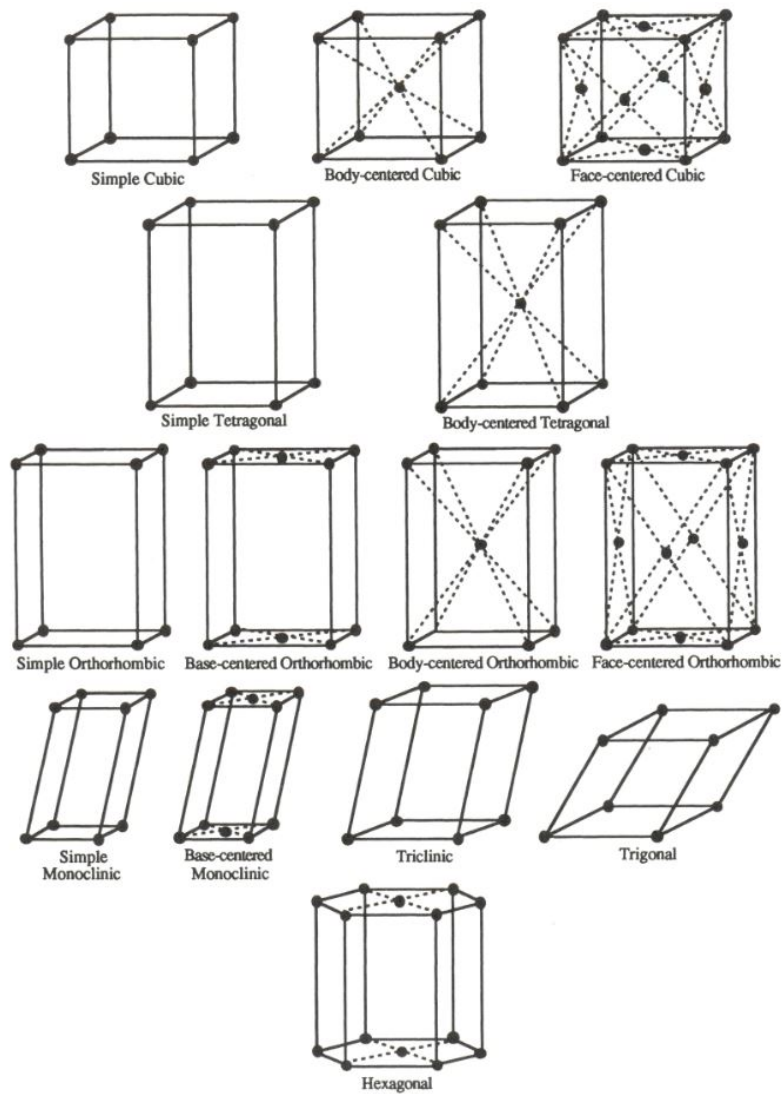


Figure 3. Bravais Lattices [1]

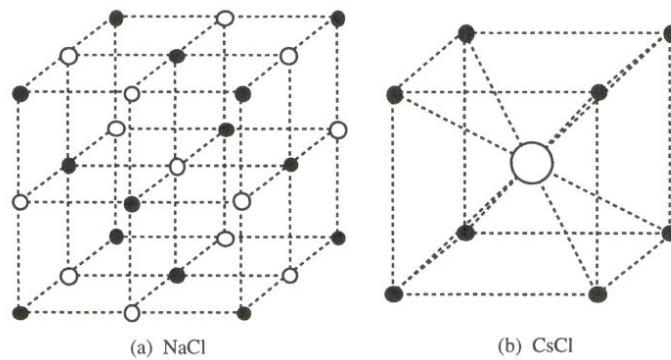


Figure 4. NaCl and CsCl crystal structures [1]

2.3. Transition Metal Oxides

This section provides an overview of the significant details of transition metal oxides as they pertain to the metal-insulator transition. By the end of this section, the goal is to reasonably explain competing theories for the cause of the observed metal-insulator transition in VO_2 , namely metal-metal bonding, Peierls theorem, Mott-Hubbard model, and Anderson localization.

The transition metals are found in groups three through 12 of the Periodic Table, as shown in Figure 5. These elements are the d group, meaning they have partially filled d shells. (Recall that shells s , p , d , and f refer to the total angular momentum of the atom, $l = 0, 1, 2$, and 3 , respectively) [1]. Group 12 (zinc, cadmium, mercury, and copernicium) are usually excluded from the transition metals because they have completely filled d shells [2, 3].

3	4	5	6	7	8	9	10	11	12
21 Sc Scandium 44.956	22 Ti Titanium 47.88	23 V Vanadium 50.942	24 Cr Chromium 51.996	25 Mn Manganese 54.938	26 Fe Iron 55.933	27 Co Cobalt 58.933	28 Ni Nickel 58.693	29 Cu Copper 63.546	30 Zn Zinc 65.39
39 Y Yttrium 88.906	40 Zr Zirconium 91.224	41 Nb Niobium 92.906	42 Mo Molibdenum 95.94	43 Tc Technetium 98.907	44 Ru Ruthenium 101.07	45 Rh Rhodium 102.906	46 Pd Palladium 106.42	47 Ag Silver 107.868	48 Cd Cadmium 112.411
57-71 Lanthanides	72 Hf Hafnium 178.49	73 Ta Tantalum 180.948	74 W Tungsten 183.85	75 Re Rhenium 186.207	76 Os Osmium 190.23	77 Ir Iridium 192.22	78 Pt Platinum 195.08	79 Au Gold 196.967	80 Hg Mercury 200.59
89-103 Actinides	104 Rf Rutherfordium [261]	105 Db Dubnium [262]	106 Sg Seaborgium [266]	107 Bh Bohrium [264]	108 Hs Hassium [269]	109 Mt Meitnerium [268]	110 Ds Darmstadtium [269]	111 Rg Roentgenium [272]	112 Cn Copernicium [277]

Figure 5. The transition metals in the Periodic Table [4].

TMOs are predominantly ionic, where the smallest interatomic distances occur in metal-oxygen bonds. The manner in which the metal atom (M) is surrounded by arrangements of oxygen atoms (O) is important. The coordination number is the number of nearest neighbor oxygen atoms, where 12 is the highest possible. Figure 6 shows the common coordination geometries; octahedral (six-fold coordination) is the most common in transition metal oxides, especially binary ones which have only one species of cation [1, 5]. In the octahedral arrangement, individual octahedra have various ways of arranging themselves within the material based on the unit cell structure of the compound. Another way to describe Figure 3 with emphasis on the connections is shown in Figure 7. The octahedra are capable of sharing corners, edges, and faces. From left to right in Figure 7, ReO_3 has corner-sharing connections, rutile has corner and edge-sharing along the c-axis, and corundum has face sharing. Stronger interactions between the metal atoms in the rutile structure are a result of their close proximity [5].

There are several ways to describe the electronic properties of transition metal oxides. No single theory is available which is all-encompassing and accounts for all observed characteristics; therefore several models exist which are excellent at describing one set of phenomena. Such models are the ionic model, cluster models, and band theory [5].

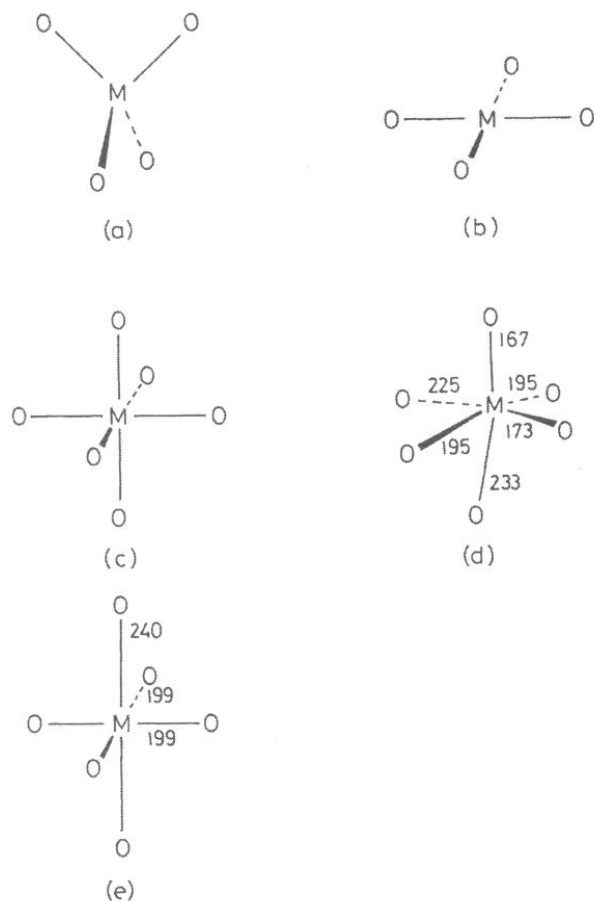


Figure 6. Coordination geometries where M is the metal and O is oxygen: (a) tetrahedral, (b) square planar, (c) octahedral, (d) distorted octahedral for Mo in MoO_3 , and (e) distorted octahedral for Cu in $\text{La}_{1.85}\text{Sr}_{0.15}\text{CuO}_4$. Interatomic distances are in pm (i.e., 100 pm = 1 Å) [5].

Crystal field (CF) theory is an ionic model which provides a qualitative view of “how transition metal ions with d^n configurations are perturbed by their chemical environment” [5]. For a metal with d^n configuration in an octahedral coordination, the five d orbitals are split into two sets of lobes. The first set has its lobes directed toward the nearest neighbor oxygen atoms (d_{z^2} and $d_{x^2-y^2}$), and the second has nodal planes in those same directions (d_{xy} , d_{yz} , and d_{zx}). The first set of orbitals are referred to as e_g and the second t_{2g} . These are also referred to as σ -type orbitals and π -type orbitals,

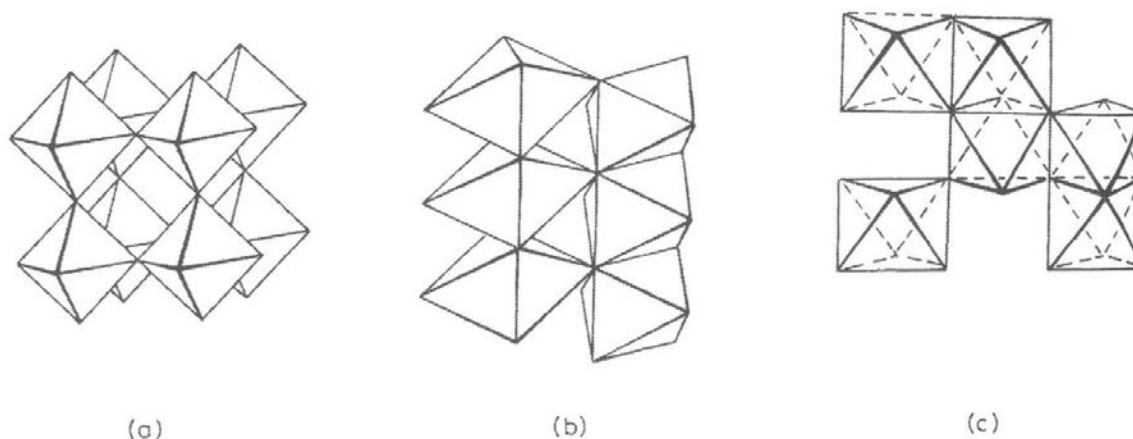


Figure 7. Three-dimensional shorthand notation for several binary octahedra; oxygen atoms occupy vertices and metal atoms are located in the centers of each octahedron. (a) Rhenium trioxide which is uncommon but forms the basis for important perovskite ternary structures, (b) rutile (body-centered tetragonal) which is common in dioxides, and (c) corundum (trigonal) which is common for M_2O_3 trioxide compounds [5].

respectively. These are shown in Figure 8. The splitting of energies between the two sets is a result of orbital overlap between the metal and surrounding oxygen atoms and covalent interactions [5]. There is much more involved with this model, but introducing it here helps to become familiarized with probability lobes and bonding energies.

A useful cluster model is the molecular orbital (MO) method. It provides a localized view, like CF theory, but involves one metal ion's interactions with several oxygen ions. Complex cluster models treat several octahedra within the same model. The movement of electrons in an electric field is approximated by an average inter-electron repulsion between their negative charges. The linear combination of atomic orbital (LCAO) approximation is the most common approach to modeling MO energies; it is similar to the tight-bonding model of solid-state physics [1].

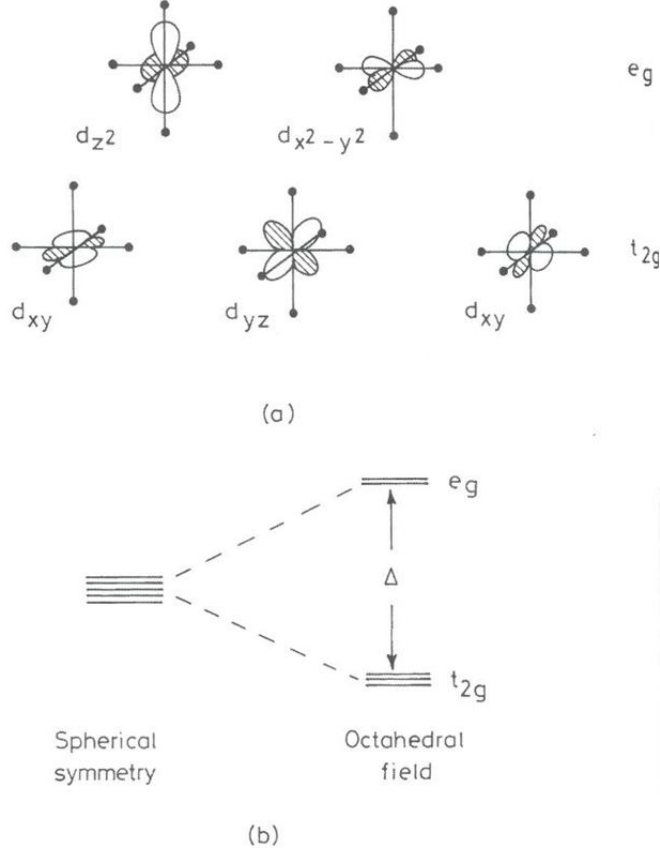


Figure 8. (a) The d orbitals of a metal ion, organized by e_g and t_{2g} symmetry sets, and (b) associated orbital energies with crystal field splitting Δ [5].

In this approximation, each MO is represented by

$$\Psi = \sum_i^N c_i \phi_i \quad (1)$$

where $\{\phi\}$ is the basis for N atomic orbitals, and $\{c\}$ coefficients are determined by the following equation. The eigenfunction of $\{c\}$ coefficients is given by

$$\mathcal{H}c = \epsilon \mathcal{S}c \quad (2)$$

where \mathcal{H} is the Hamiltonian matrix, \mathcal{S} is the overlap matrix, and ϵ is the orbital energy. The solutions to these equations have N solutions of MOs, determined by the number of atomic orbitals (AOs) [5]. This can be pictured qualitatively in Figure 9 below.

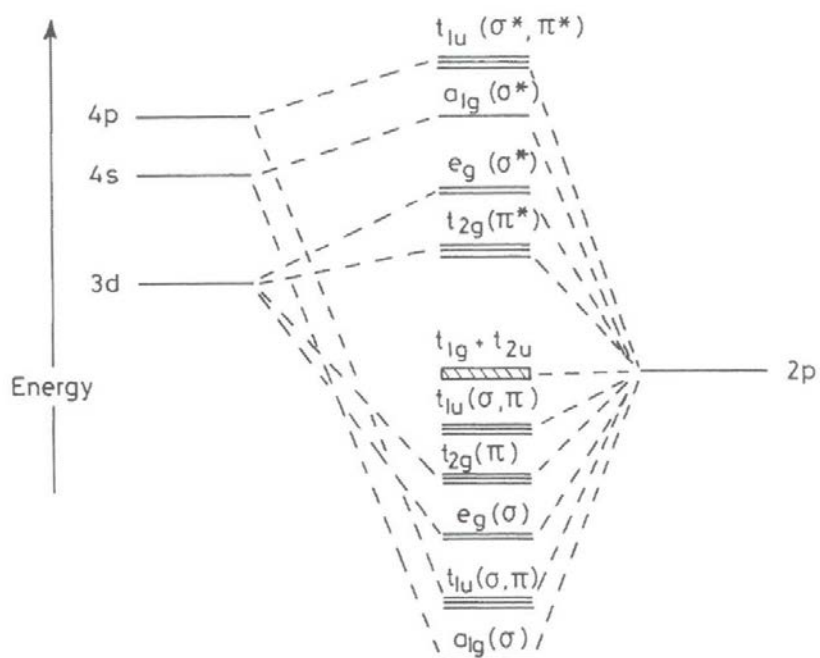


Figure 9. Qualitative molecular orbital (MO) diagram for an octahedral transition d metal ion and $2p$ oxygen ions [5]. Particular attention should be paid to the $3d$ - $2p$ MO energies.

The σ and π bonds are indicated in this figure as well. With reference to CF theory, the orbital mixing results in a larger perturbation for e_g compared to t_{2g} . This can be seen from Figure 10 in terms of the shapes of the σ and π orbitals: σ orbitals have their lobes in the direction of the metal-oxygen bond whereas π orbitals are perpendicular. Therefore, e_g orbitals produce MOs which are bonding in nature, and t_{2g} orbitals are predominantly antibonding.

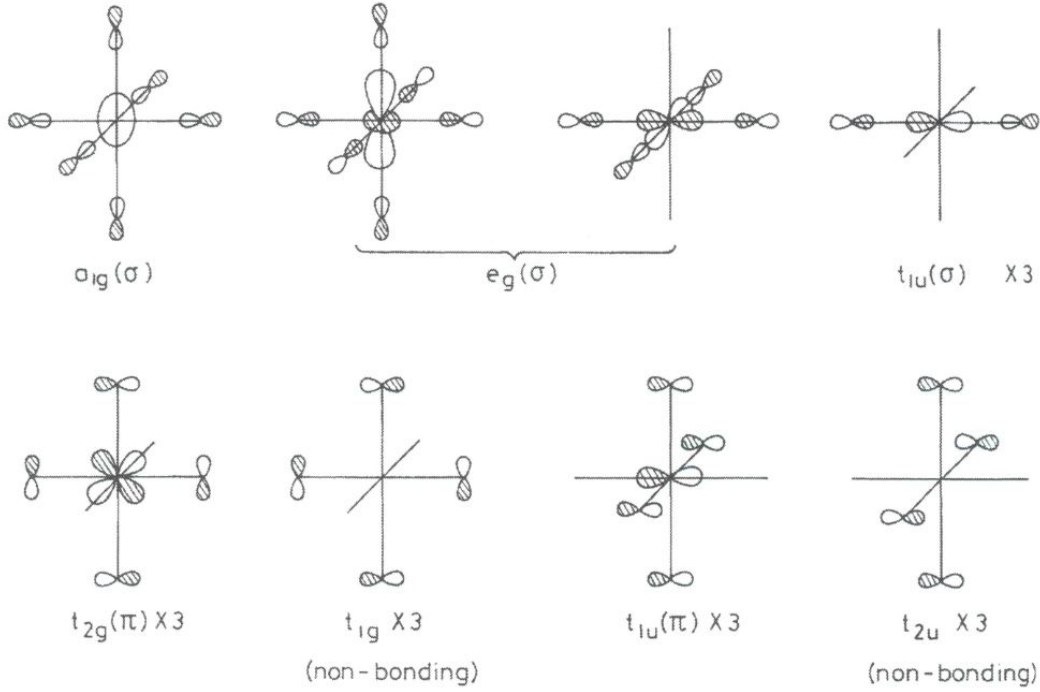


Figure 10. Oxygen 2p orbitals in an octahedron bonding (or not bonding) with the centered metal orbital [5].

The third type of model, which is the most common due to its wide applicability in solid-state physics, is band theory. Unlike the two previous models described, it provides a delocalized view of energies within the lattice. Given a free electron, the perturbations due to the periodic crystal lattice are modeled as a function of wavevector k , where orbitals are modeled to have a wave-like form. This relationship is given by

$$\lambda = \frac{2\pi}{k} \quad (3)$$

where λ is the wavelength of these orbital waves. For k -values $\frac{-\pi}{a} < k \leq \frac{\pi}{a}$, all linear combinations of states are possible; this range of k -values is called the first Brillouin zone. The constant a is the distance between unit cells, which is also called the lattice constant. Note that the approximation of matter behaving as waves, while somewhat

peculiar, is standard in quantum mechanics and was first developed by Louis de Broglie. His theories were refined by Erwin Schrödinger who developed quantum mechanics in 1926 [1].

This model does not apply well to transition metals because their electrons are not represented well by free electrons; however, the LCAO method discussed previously can be used as an approximation to the solid-state physics tight-binding method. The result of this model is a band diagram, as shown in Figure 11.

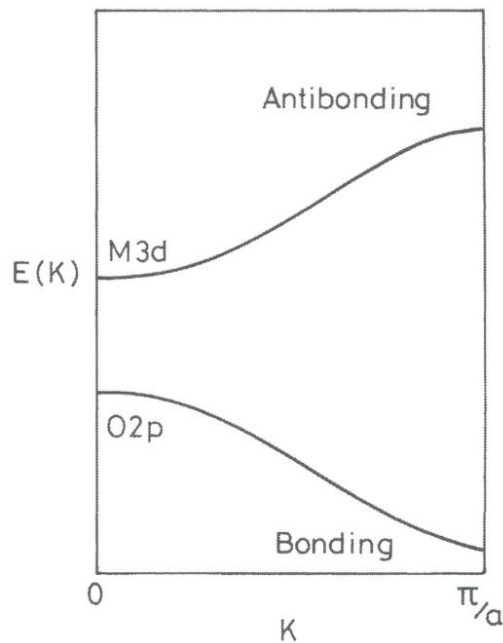


Figure 11. Representative one-dimensional band diagram for a 3d metal oxide over the interval $0 < k < \pi/a$. In compounds which are mostly ionic (e.g., transition metal oxides), oxygen predominantly contributes to bonding orbitals, and the metal to antibonding orbitals [5].

Again, bonding and antibonding characteristics are observed albeit not on a molecular level. With reference to Figure 11, energy states between the two bands are forbidden, and the interband distance is called the bandgap energy. Because the bonding

character depends on k , the energy/wavevector relationship is dispersive. The upper band is the conduction band, and the lower band is the valence band. The location of the Fermi level (not pictured) in addition to the bandgap energy, dictates the electrical conductivity of the material. The Fermi level is the statistical energy level for the highest occupied electron energy state in the system. In semiconductors, if the Fermi level is closer to the conduction band, the material is n-type; if it is closer to the valence band, it is p-type [1].

Because the lattice is three-dimensional, the energy-wavevector relationship is also three-dimensional, as shown in Figure 12. Typically band diagrams are presented in one dimension for simplicity. One method of drawing conclusions on the three-dimensional energy structure is with Fermi surfaces. The three-dimensional k -space is

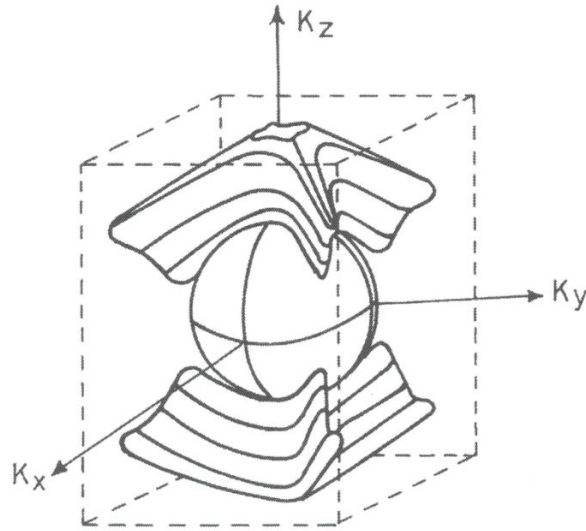


Figure 12. Fermi surface for RuO_2 , where occupied energy states lie within the locus of the surface and unoccupied states lie outside the surface [5].

called the reciprocal lattice, which can be considered a Fourier three-dimensional space, analogous to the frequency/time relationship [6].

Peierls instabilities are periodic lattice distortions in a one-dimensional lattice (the instabilities do not apply for two and three dimensions). Due to these distortions, the lattice periodicity is modified over integral multiples of π/a' , where a' is the superlattice periodicity (Figure 13). As a result, new Brillouin zones and Fermi surfaces appear based on the new periodicity, and the band gap and electrical conductivity in the material also change.

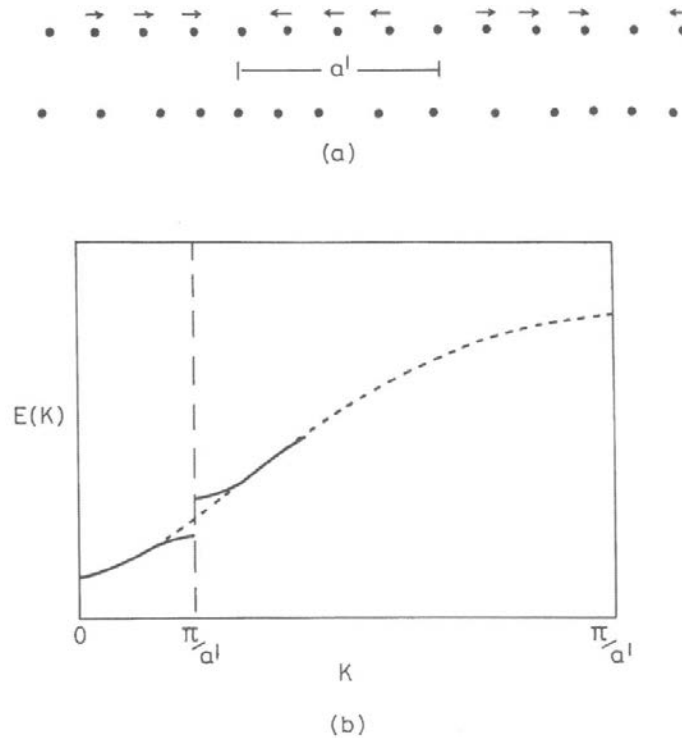


Figure 13. (a) Relationship between superlattice periodicity, a' , and lattice distortions; (b) Formation of a new bandgap at $k = \pi/a'$ [5].

Simply put, the Peierls theorem states that one-dimensional metals do not exist because there will always be distortions which are energetically favorable. There are some compounds for which this theorem provides an accurate model of one-dimensional

conductivity, such as blue bronzes $A_{0.3}\text{MoO}_3$, where A is potassium (K), rubidium (Rb), or thallium (Tl) [5].

Two categories of models of electronic properties were previously discussed: Localized (ionic and cluster models) and delocalized (band theory). Between localized and delocalized models are intermediate models, which attempt to take into consideration three main forces: “Repulsion between electrons, the interaction of band electrons with lattice vibrations, and the influence of defects and disorder in the solid” [5]. Two intermediate models which will be discussed next are the Hubbard model and Anderson model.

In metals, an effective average repulsion between electrons works well due to the high concentration of electrons. When the concentration is lower, however, such as in narrow bandgap metal oxides, electron correlation is significant. Electron correlation is when an electron will change its path in order to avoid other electrons, unlike the independent free electron assumption in quantum mechanics. The Hubbard model (or Mott-Hubbard model) is concerned with neglecting these interatomic electron repulsions and only considering charges within the same atom. The repulsion of electrons in partially filled d shells yields a bandgap indicative of the system’s energy states, as shown in Figure 14. The bandwidths are indicative of interatomic overlap and are represented in the figure as the heights of the bands.

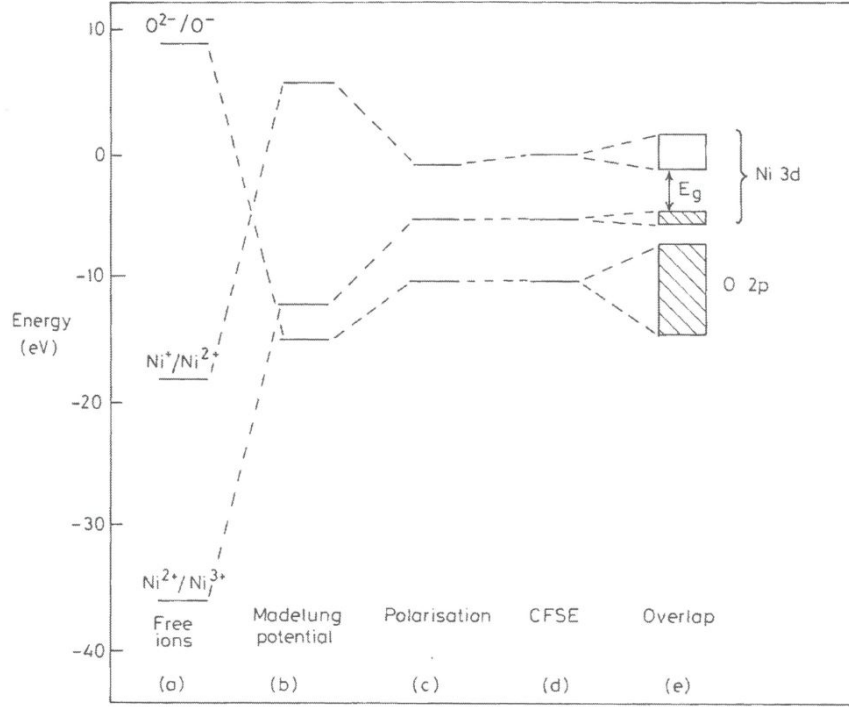


Figure 14. Process of determining ionic band model of NiO; Madelung potential is an electrostatic charge due to placing the ions in the lattice; and CFSE is the Crystal Field stabilization energy equivalent to $-(2/5)\Delta$ for t_{2g} orbitals and $+(3/5)\Delta$ for e_g orbitals. The bandgap is E_g , and the bandwidths are the energy thicknesses (heights) of each band represented by rectangles. Occupied bands are dashed [5].

The ionization process $Ni^{2+} = Ni^{3+} + e^-$ corresponds to the top-filled level (narrow, filled band in Figure 14) and $Ni^{2+} + e^- = Ni^+$ corresponds to the lowest empty level. The bandgap excitation is



In terms of d shells,

$$d^8 + d^8 = d^9 + d^7 \quad (5)$$

The input energy required for the excitation is equal to the repulsion from the more negative d^9 term. This input energy is called the Hubbard U . The Hubbard model states that at a bandwidth equivalent to U , the upper and lower Hubbard bands will

converge to create a metallic state (Figure 15). Thus, for an applied stimulus energy U , the system transitions from insulating to metallic. The lower Hubbard band corresponds to the binding energies of electrons in the occupied levels, and the upper band corresponds to empty levels. Many researchers have attempted to quantitatively determine the Hubbard U for various compounds, but none have been successful. The Hubbard model is not one that can be comprehensively applied to model metal-insulator transitions—at least not yet [5].

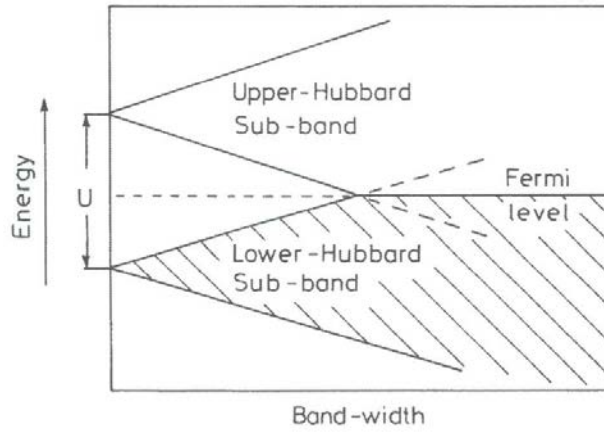


Figure 15. Upper and lower Hubbard sub-bands which overlap at bandwidth $W \sim U$ to yield a metallic state [5].

The Mott MIT is dependent on the transition from insulating to metallic at bandwidth $W \sim U$, which can be estimated in terms of an increase in carrier concentration, n_c . This is the Mott criterion for metallic conduction

$$n_c^{1/3} a_0 \sim 0.25 \quad (6)$$

where a_0 is the hydrogenic Bohr radius of $53 \text{ pm} = 0.53 \text{ \AA}$. (Although the dielectric constant ϵ_r must be very high for the model to apply, this criterion has worked well for a

variety of compounds, including those with low ϵ_r .) For a given n_c which is dependent on the material, an electric field can be applied to reach this criterion.

Anderson localization is an intermediate model which is concerned with solids with numerous defects. If the defect concentration is so high that they cannot be considered isolated, they can be organized into their own energy band of defects (see Figure 16). In this case, the atomic orbital energies can no longer be organized into an energy band; rather, they are *localized* energy levels.

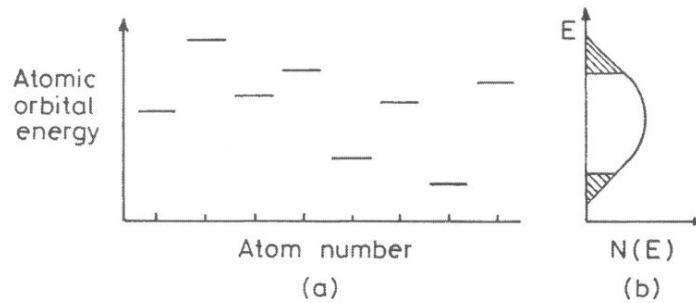


Figure 16. (a) Localized atomic orbital energies due to numerous defects in the lattice; (b) Density of states with mobility edges represented by the boundaries between the center extended states and (dashed) localized states [5].

The density of band states resembles the center region of Figure 16(b) because most of the atoms are likely to have energies near the average value. Conversely, some atoms will exist with energy states unlike the majority of the band states which are represented by the dashed portion of the density of states. Orbitals with energies in the tails will therefore be localized to individual atoms. The edges between the bulk energy states and the disordered states are called mobility edges. If the Fermi level lies within the localized energy levels, the carrier mobility is zero. Electrons in localized states are capable of transport via a phenomenon known as variable-range hopping [5]. Thus Anderson

localization can account for insulating behavior in a material that is otherwise metallic, due to defects such as dopants. This process is detailed in Figure 17.

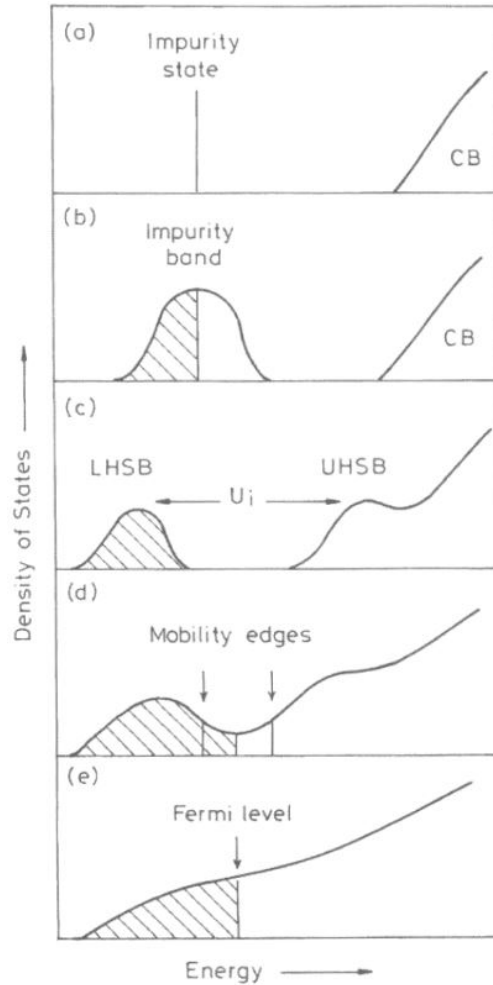


Figure 17. Metal-insulator transition (MIT) mechanism due to Anderson localization, where impurity concentration increases from (a) to (e). (a) Dilute impurities below the conduction band, (b) Impurity band formed by an increased concentration which is half-filled with one electron per defect site, (c) Formation of Lower and Upper Hubbard Sub-bands, where the UHSB overlaps the conduction band, (d) The impurity band broadens and the sub-bands converge and Anderson localization occurs, (e) Fermi level extends through the material which contributes to metallic conductivity [5].

2.4. Metal-Insulator Transition

F. J. Morin of Bell Telephone Laboratories was the first to investigate the physics of metal-insulator transitions. He published a review in 1958 [7], and his succinct paper in 1959 [8] is regarded as the seminal paper in the field. This paper motivated many physicists' work for the next 25 or so years. He presented data on electrical conductivity for several oxides of titanium and vanadium (Figure 18), which show a large, abrupt change in conductivity with increased temperature. Another major contributor to the

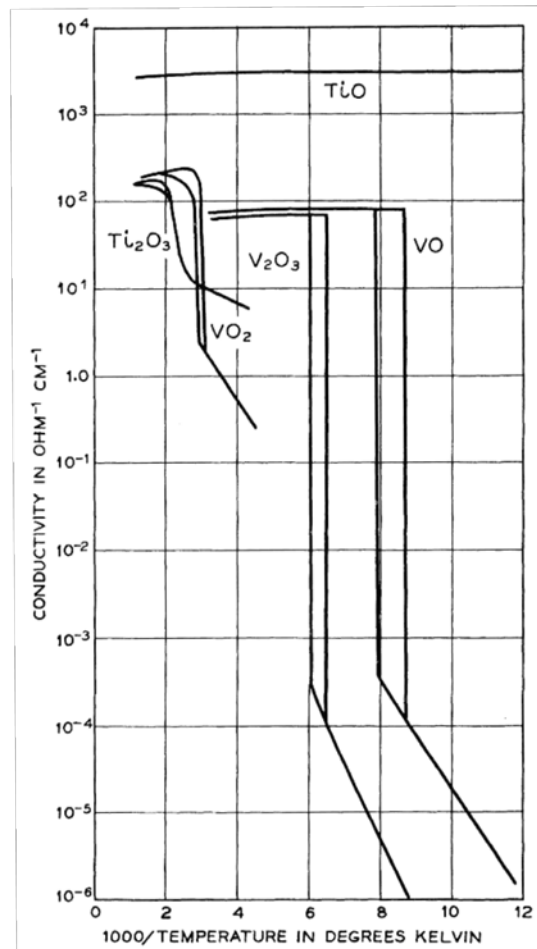


Figure 18. Measured electrical conductivity (F. J. Morin, 1959) of several vanadium and titanium oxides; note the inverse-temperature scale of the x-axis [8].

field was N. F. Mott, who won the Nobel Prize for Physics for his work with magnetic and amorphous semiconductors. He postulated much of the correlated electron theory of MIT physics, where MIT occurs in some materials due to the correlated electron theory discussed previously [9, 10].

There are many materials which show changes of several orders of magnitude between insulating and metallic phases; these can be grouped into their own set of materials known as MIT materials. These include oxides of vanadium, iron, nickel, and titanium, among others [11, 12]. Most of these compounds are displayed in Figure 19 according to their transition temperatures, T_{MIT} . The reader is referred to the review by Imada, Fujimori, and Tokura [12] for an exhaustive review of MIT materials.

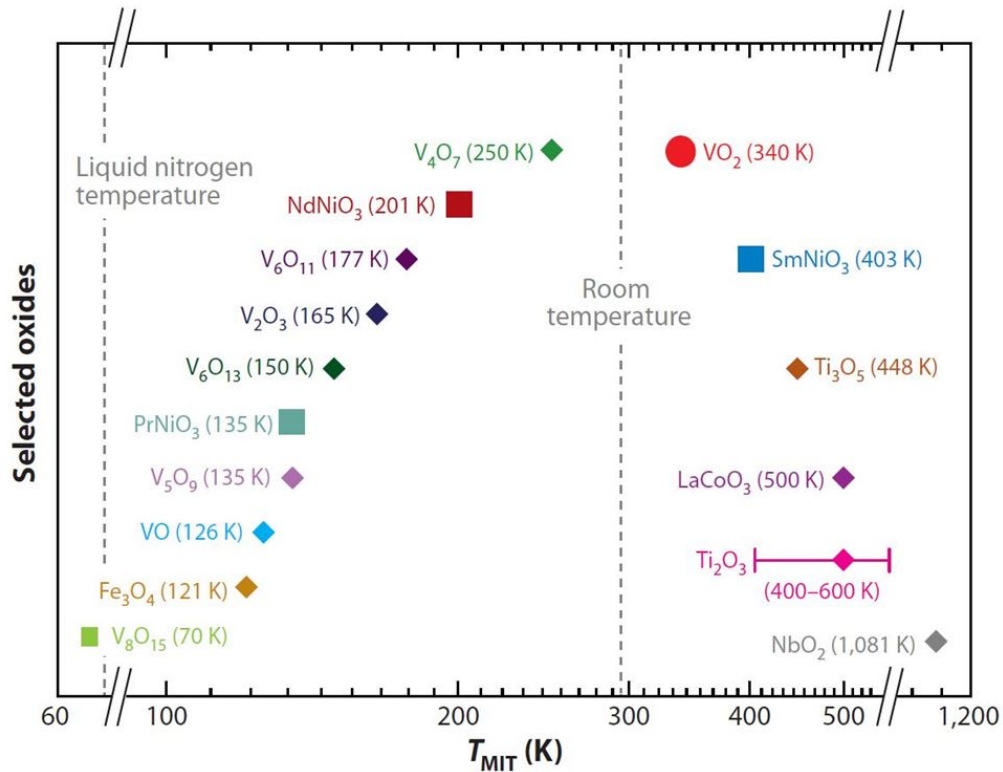


Figure 19. Selected oxides sorted by transition temperature, T_{MIT} [11]. VO_2 has the closest T_{MIT} above room temperature. The error bar for Ti_2O_3 is indicative of a gradual transition.

As seen in Figure 19, VO₂ has the closest T_{MIT} above room temperature. Note that room temperature is approximated as 295 K, equivalent to 22°C or 71°F. The least amount of applied energy is required to cause a transition in VO₂ compared to any other MIT material. It is for this reason that most of MIT material research has been primarily focused on VO₂.

Vanadium (symbol V) is element 23, is located in the fourth row and group five, and has electron configuration $1s^2 2s^2 2p^6 3s^2 3p^6 4s^2 3d^3$ [13]. Its core configuration is argon (Ar) which has an electron configuration of $1s^2 2s^2 2p^6 3s^2 3p^6$. Because vanadium is in group five, it is a $3d$ metal with three electrons in its valence shell ($3d^3$). Oxygen has the configuration $1s^2 2s^2 2p^4$ which has two electrons less than neon (Ne) noble gas. Therefore, oxygen forms the anion O²⁻ and metal cations (positive ions) balance the charges when bonding with oxygen [5]. Vanadium has many oxidation (cation) states. These numerous oxides are listed in Table 2 according to increasing T_{MIT}.

Table 2. Vanadium oxides and their metal-insulator transition temperatures (compiled from numerous references).

Formula	Name	MIT Temp (K)	MIT Temp (°C)
V ₈ O ₁₅	Octavanadium Quindeciaoxide	70	-203
VO	Vanadium Monoxide Vanadium (II) Oxide	126	-147
V ₅ O ₉	Pentavanadium Nonaoxide	135	-138
V ₆ O ₁₃	Hexavanadium Tredecaoxide	150	-123
V ₂ O ₃	Vandium Trioxide Vanadium (III) Oxide	165	-108
V ₆ O ₁₁	Hexavanadium Undecaoxide	177	-96
V ₄ O ₇	Vandium Heptaoxide	250	-23
VO ₂	Vanadium Dioxide Vanadium (IV) Oxide	340	67
V ₂ O ₅	Divanadium Pentoxide Vanadium (V) Oxide	None	None
V ₃ O ₅	Trivanadium Pentoxide	None	None
V ₃ O ₇	Trivanadium Heptaoxide	None	None

In vanadium trioxide (V₂O₃) and vanadium dioxide (VO₂), J. Goodenough modeled their *3d* band being split into two sub-bands that lie on either side of the Fermi level at room temperature with a band gap of about 0.65 eV [12, p. 1232]. In VO₂, as temperature is elevated past 340 K (67°C, 152°F), the two sub-bands collapse into one *3d'* band that straddles the Fermi level (Figure 20). This band is partially filled with electrons which contribute to electron flow and metallic conductivity.

VO₂'s lattice structure changes from monoclinic to body-centered tetragonal (rutile) when transitioned from insulator to metal. As shown in Figure 21, in the monoclinic (M1) phase, its lattice constants are 4.54, 5.75, and 5.38 Å. In its metallic/

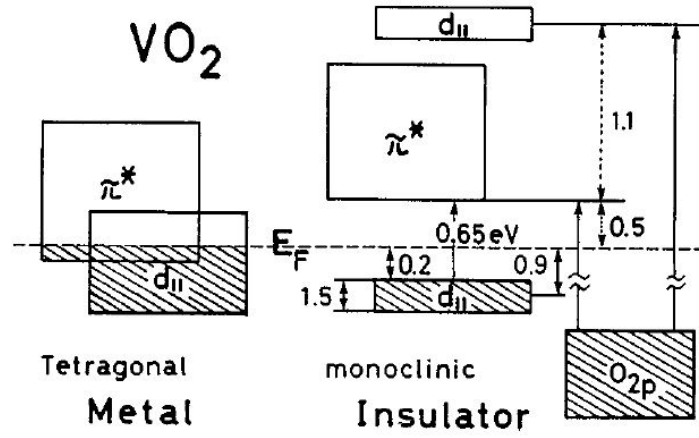


Figure 20. Band diagram of VO₂ by J. Goodenough [12, p. 1232].

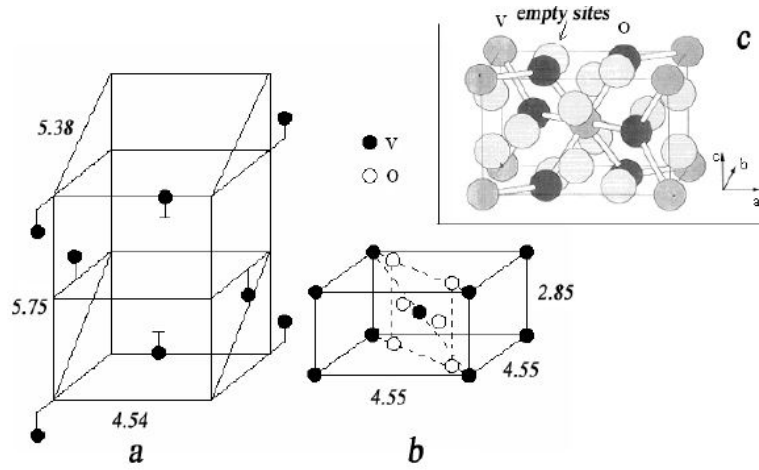


Figure 21. Lattice structure in (a) Monoclinic/insulating phase and (b) Tetragonal/metallic phase [14].

rutile (R) phase, its base is square with lattice constant 4.55 Å, and its height is 2.85 Å [14]. Additionally, the following relationships exist between unit vectors: $\mathbf{a}_{\text{mono}} = 2\mathbf{c}_{\text{tetra}}$, $\mathbf{b}_{\text{mono}} = \mathbf{a}_{\text{tetra}}$, and $\mathbf{c}_{\text{mono}} = \mathbf{a}_{\text{tetra}} - \mathbf{c}_{\text{tetra}}$ [11].

The intrinsic carrier mobility of VO_2 has been shown with Hall Effect measurements to remain relatively constant throughout the MIT at a low value of $0.05 - 0.1 \text{ cm}^2\text{V}^{-1}\text{s}^{-1}$ [15]. Additionally, the dominant carriers in VO_2 are electrons, making it n-type, and the concentrations typically vary from about 4×10^{18} to $1.4 \times 10^{23} \text{ cm}^{-3}$ from insulator to metal, respectfully [15]. This increase corresponds to five orders of magnitude increase in electrical conductivity.

In the later transition elements, metal-metal bonds are not as common due to a contraction of the d orbitals and therefore less overlap between neighboring atoms. Metal-metal bonding is observed in d^1 configurations for $3d$ elements and d^2 and d^3 configurations for $4d$ elements [5]. This phenomenon was postulated by Morin (Figure 22) when he did not observe similar MIT behavior in chromium as with titanium and vanadium [7]. Most of the interesting MIT phenomena do indeed occur with titanium and vanadium oxides.

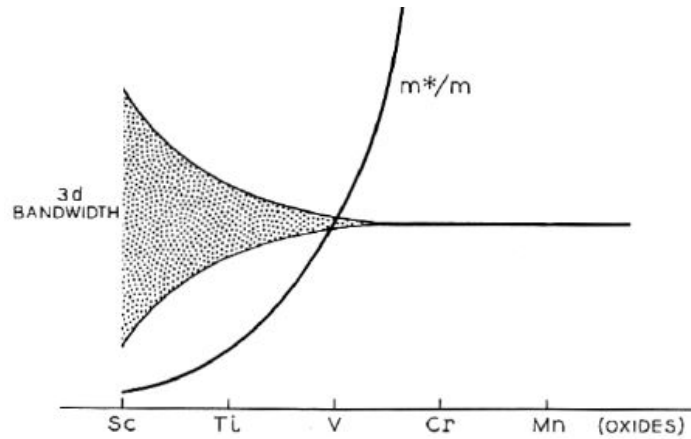


Figure 22. Simplified representation of the thinning of $3d$ wavefunction oxide bandwidth, from left to right, in row 4 [7].

The increase in electrical conductivity as observed by Morin may be accounted for by metal-metal bonding, in which d electrons are directly involved. At lower temperatures, these electrons occupy an energy band that is split from the rest of the electrons which prevents electrical conduction. As temperature increases, phonon vibrations occur and the lattice expands, which weakens the metal-metal bonds. Such is the case with many transition metal oxides, including vanadium and titanium oxides. Structural distortion is involved with this metal-metal bonding which is specifically determined by the cation species (i.e., Ti_2O_3 maintains a corundum (trigonal) structure throughout its MIT). VO_2 is a very interesting d^1 compound, like Ti_2O_3 , which is regarded as somewhat more complicated than the latter compound. Its transition is first order instead of gradual as would be expected and is the case with Ti_2O_3 (shown in Figure 23). Although it is diamagnetic (repelled by magnetic fields), some interesting magnetic properties are observed when doped with magnetic impurities, which implies it is almost a magnetic insulator [5].

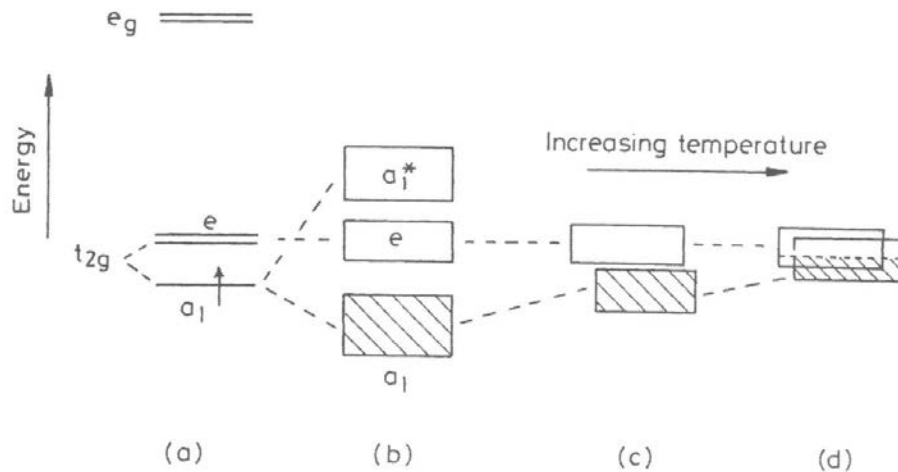


Figure 23. Energy levels for Ti_2O_3 : (a) Trigonal 3d splitting of t_{2g} and e_g orbitals, (b) Formation of bonding and antibonding levels, (c)-(d) Converging of energy bands due to increased temperature [5].

There are several other competing theories for MIT observed in VO₂, which were discussed previously—Peierls, Mott-Hubbard, and Anderson. It is generally regarded that the actual MIT mechanism is still unknown because many experiments which have claimed to be conclusive have contradicted each other. Most claim Mott-Hubbard (correlated electron theory) or Peierls (electron-lattice interactions) or a combination of the two theories.

Experiments have been conducted to prove the dominant MIT mechanism. Mott MIT seems to be dominant while transitioning VO₂ with a laser while cooling the crystal to maintain it at room temperature. On the other hand, transitioning with mechanical strain seems to prove Peierls MIT [11]. Due to these conflicting conclusions, there is still dispute among experts in the field as to the dominant MIT mechanism [16].

As described by Mott-Hubbard theory, MIT materials can be transitioned electronically by applying an electric field across the crystal, where the electric field intensity is the voltage divided by the distance between the terminals of the applied potential. That is,

$$E = \frac{V}{d} \quad (7)$$

When the carrier concentration exceeds the Mott criterion for MIT, approximately $n_c \approx 3 \times 10^{18} \text{ cm}^{-3}$ for VO₂, the transition occurs [14, 17]. This is defined by Mott as

$$n_c = \left(\frac{0.25}{a_0} \right)^3 \approx 3 \times 10^{18} \text{ cm}^{-3} \quad (8)$$

where a_0 is Bohr's radius [17]. Using Bohr's radius (hydrogenic model) is a simplification for molecules because Bohr originally used it as a simple model for atoms [1]. The Bohr's radius of VO_2 —and compounds in general—is written as

$$a_0 = \frac{\epsilon_r \epsilon_0 \hbar^2}{m^* q^2} \quad (9)$$

where ϵ_r is the relative dielectric constant on the insulating side of the transition (about 100), ϵ_0 is the dielectric permittivity of free space, \hbar is Planck's constant divided by the multiple 2π , m^* is the effective mass of VO_2 (about two times that of a resting electron), and q is the charge of an electron [14]. The Poole-Frenkel effect at a given temperature T and electric field E is written in terms of the carrier concentration n as

$$n = N_0 \exp\left(-\frac{W - \beta_{PF} \sqrt{E}}{kT}\right) \quad (10)$$

where N_0 is a fabrication-dependent constant, W is the ionization energy (0.2 eV), $\beta_{PF} = 2\sqrt{q^3/\epsilon_r \epsilon_0}$ is the Poole-Frenkel constant, and k is Boltzmann's constant [17]. The Poole-Frenkel effect can be considered a “field-assisted thermal ionization” in insulators where the barriers of positively charged traps are reduced by the electric field thus requiring less thermal energy for conduction [18]. Using n_c identified by the Mott criterion in the Poole-Frenkel relationship at room temperature and solving for E in equation 10 yields $E_c \approx 5 \times 10^7 \text{ V/m} = 50 \text{ V}/\mu\text{m}$, which is rather high [17]. In many experiments, VO_2 crystals have been transitioned with electric fields one-tenth of the calculated value [19, 20]. An explanation for this drastic reduction within the construct of the model has not been identified, but it is possible that it is dependent on the quality

of deposition. Well deposited, monocrystalline films will promote current flow more than polycrystalline films [1].

Peierls MIT is a competing theory for the MIT caused by electron-phonon interactions. This theory suggests that MIT is due to a lattice structural change and not an electron-electron interaction. As the lattice is modified, the periodic ionic potential changes as a result which changes the band structure of the compound. As expected, this model is used to explain MIT caused by mechanical stressors and heating.

The final theory is Anderson MIT, which accounts for insulating states with randomly distributed defects. Anderson MIT has been proven to be found in strongly disordered materials and materials with strong impurity scattering (i.e. heavily doped semiconductors) [11]. While it does account for MIT in some compounds, this is unlikely for VO₂ [5].

It has also been predicted that only a portion of the material will become metallic while the rest remains insulating (i.e., the top layer of the crystal transitions and the bulk does not). In many oxides, a charged accumulated layer forms on the surface which acts to shield the bulk from the applied electric field [17]. In VO₂, the charge accumulation layer's thickness, λ , is estimated to be 0.4 nm by the following Thomas-Fermi approximation,

$$\lambda_{TF} = \sqrt{\frac{\epsilon_r \epsilon_0 \pi^2 \hbar^2}{m^* q^2 k_f}} \quad (11)$$

where k_f is the Fermi wave-vector [17]. This is a crude approximation due to the simplifications in the model; however, it elucidates the two-dimensional metallic nature of VO₂ near an applied electric field.

Mun et al. conducted an experiment that tested the MIT behavior of VO₂ when combining electric field and heat stimuli [19]. Their data show that the transition temperature can be reduced from its nominal value of 340 K (66°C) by applying an electric field across the crystal. Even more interestingly, they proved the existence of a linear relationship in MIT between voltage squared applied across the crystal and applied temperature (see Figure 24). Where there is no voltage applied, the transition temperature is 66°C; otherwise the transition temperature is reduced, down to 40°C with 22.3 V applied.

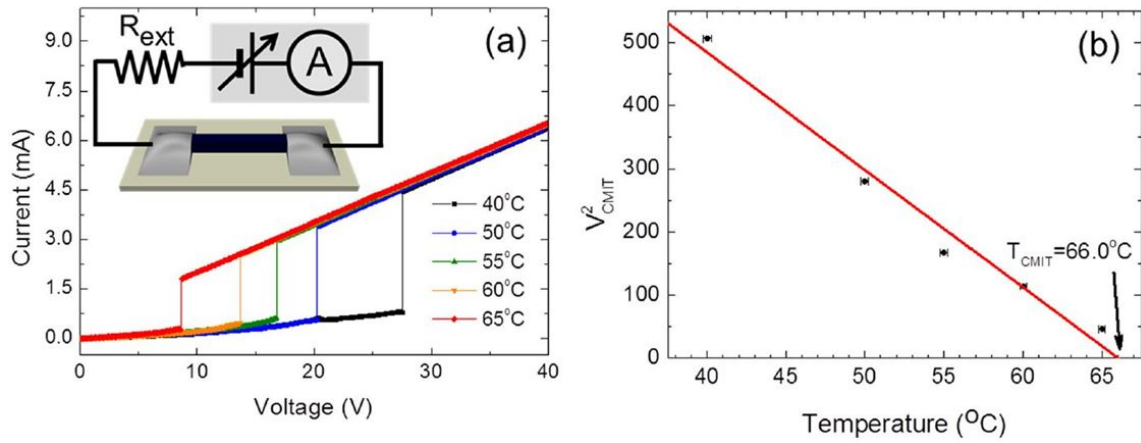


Figure 24. Experiment combining electric field and heat in VO₂. (a) I-V curves at stepped temperatures, (b) Observed linear relationship between V^2 and applied temperature [19].

They developed the following relationship between temperature and voltage:

$$V_{C,MIT}^2 = (kR_{C,MIT})(T_{C,MIT} - T_A) \quad (12)$$

In this equation, C stands for critical, MIT is the quantity at the point of transition, the negative sign indicates approaching the transition from the left (insulator) side, k is the

effective thermal conductance which is approximately $7 \times 10^{-4} \text{ WK}^{-1}$, and T_A is the applied temperature [19].

Three-terminal field-effect devices using MIT materials are usually called MottFETs or MTFETs (Mott Transition Field-effect Transistors). The implementation of VO_2 in these devices utilizing the field effect (see Figure 25) has not ended with very good results [21]. The large voltage needed to reach the Mott criterion in some cases has caused dielectric breakdown before MIT [14]. The very thin charge accumulation layer is detrimental to reducing resistance of the majority of the VO_2 layer. However, research is being completed on using a VO_2 channel layer thickness of $\sim 5 \text{ nm}$, using double-gated structures, and doping to reduce the required voltage needed for MIT [14]. MTFETs using other MIT materials have been more successful. Newns et al. [22] achieved good results from an MTFET with doped SrTiO_3 as the gate electrode, undoped SrTiO_3 as the gate oxide, and YBPCO ($\text{Y}_{1-x}\text{Pr}_x\text{Ba}_2\text{Cu}_3\text{O}_{7-\delta}$) as the channel material. There are many fabrication concerns that arise with MIT materials instead of silicon [23], but results look promising.

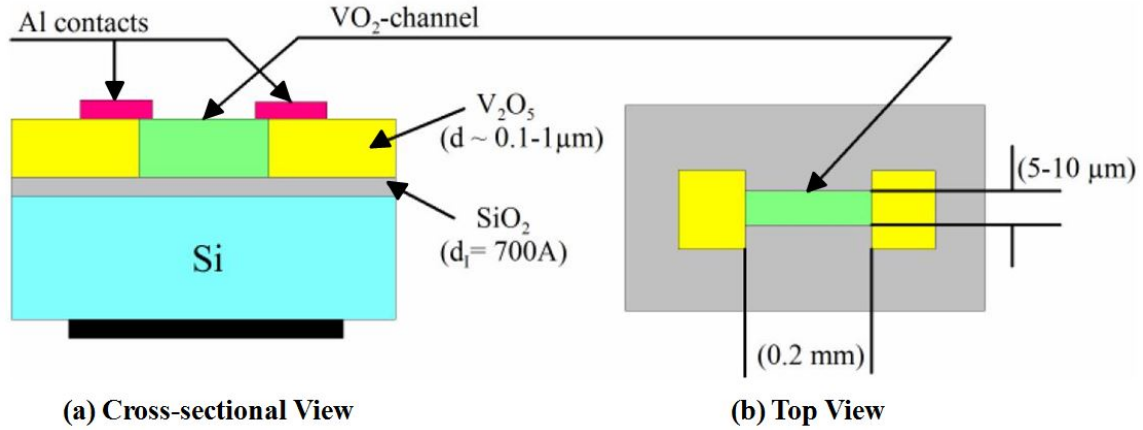


Figure 25. Three-terminal field-effect device with VO_2 as the semiconductor channel material; (a) Cross-sectional view, (b) Top view [14].

The deposition of stoichiometric VO_2 is somewhat complex. Because of vanadium's multiple oxidation states, there are 11 distinct vanadium oxides, three of which show no change in conductivity when heated (see Table 2). Of all the oxides, VO_2 has the highest transition temperature at 340 K; V_8O_{15} has the lowest transition at 70 K. The balancing of O:V ratio must be carefully controlled. By inspecting VO_x 's phase diagram (Figure 26), one can see how easily a small fluctuation in deposition conditions can change the characteristics of the compound.

VO_2 can be deposited using a variety of fabrication methods, including electron-beam evaporation [24], DC sputtering [25], RF sputtering [26], inductively-coupled plasma-assisted sputtering [27], sol-gel coating [28], atmospheric pressure chemical vapor deposition (CVD) [29], metalorganic CVD [30], pulsed laser deposition [31], and ion beam deposition [32]. DC and RF sputtering are the most widely used methods for depositing thin films. Additionally, procedures for sputtering have been well documented by many researchers.

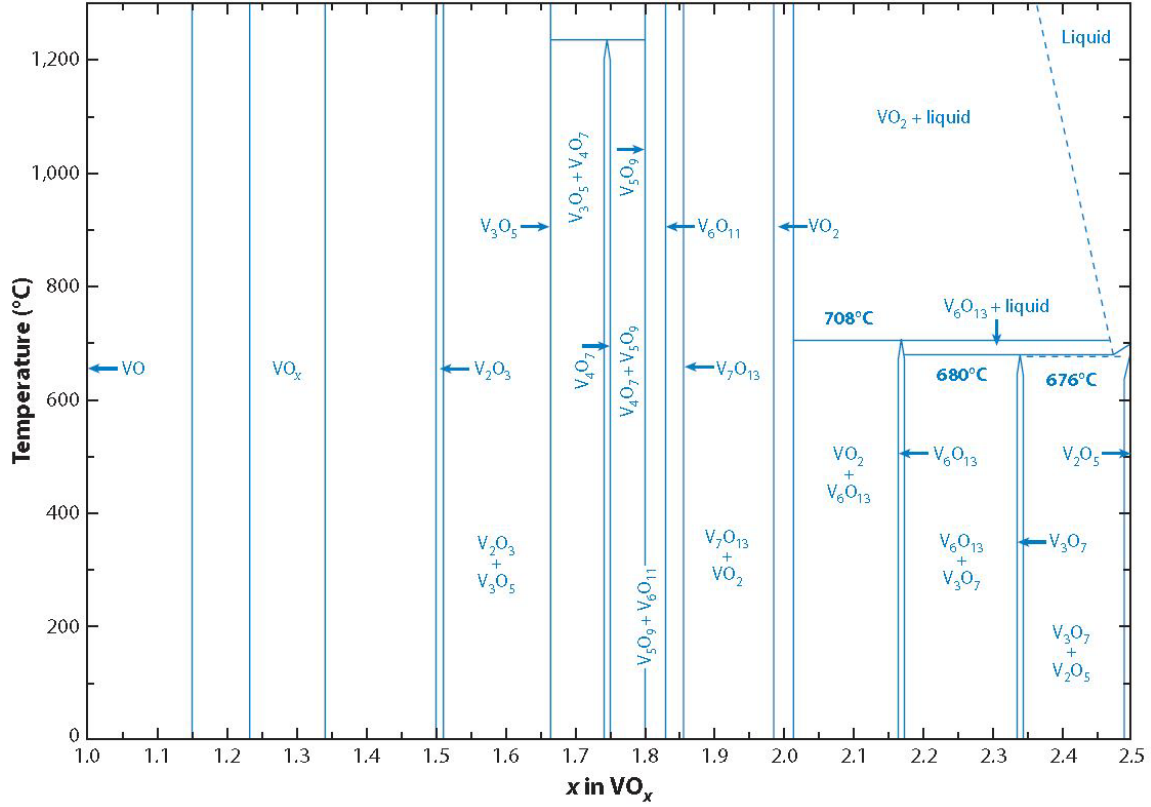


Figure 26. Phase diagram of vanadium oxide (VO_x), temperature plotted vs. oxygen-to-vanadium ratio. At the far left is vanadium monoxide (VO), and vanadium pentoxide (V_2O_5) is on the far right. Deposition temperatures when sputtering do not typically exceed 600°C [11].

When sputtering, oxygen flow and substrate temperature are the two most critical parameters in the growth of stoichiometric VO_2 thin films. The highest order of magnitude of conductivity change occurs between 7.8 and 8.8 percent O_2 (the remainder is Ar) when using a V target [11]. E. Chain conducted a deposition experiment varying substrate temperature, T_s [33]. He found limited evidence of MIT behavior for $350 < T_s < 435^\circ\text{C}$, one to two orders of magnitude change for $505 < T_s < 570^\circ\text{C}$, and about three orders of magnitude for $585 < T_s < 620^\circ\text{C}$. Other studies typically do not exceed $T_s = 550^\circ\text{C}$ (Table 3), perhaps due to heater limitations. Heating the substrate encourages oxidation of the vanadium ions [34, 33]; higher substrate temperatures of at least 450°C

correspond to the formation of a VO_x compound and a higher magnitude of MIT. Heating the substrate also increases the rate of deposition [33] and changes the grain size and surface morphology [35]. Thornton's model of surface morphology [36], shown in Figure 27, describes the grain structure as a function of substrate temperature when sputtering. Note that the melting temperature, T_m , for VO_2 is approximately 2,240 K (1,967°C) [33].

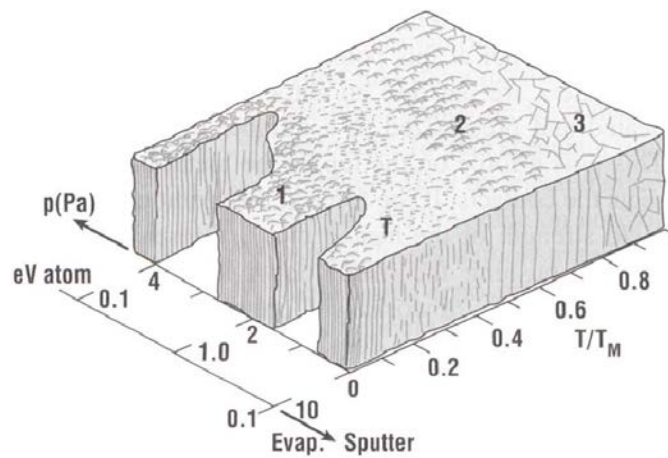


Figure 27. Thornton's three-zone surface morphology model. T_M is the melting temperature and T is the substrate temperature during deposition [35].

Oxygen partial pressure of 7.8 to 8.8 percent gives a good stoichiometry of two oxygen atoms per vanadium atom, based on experimental results completed by many others in the field [11, 37]. Less oxygen slides the compound composition to the left in Figure 26; conversely, more oxygen moves the number of oxygen atoms per vanadium to the right [11, 38].

Additionally, the quality of MIT can be controlled intentionally by extrinsic factors. T_{MIT} can be varied with substrate growth temperature [39], oxygen flow composition [37], and doping. T_{MIT} can be lowered by doping with tungsten (W),

niobium (Nb), hydrogen (H), [14] or molybdenum (Mo) ions, or raised by doping with aluminum (Al) or chromium (Cr) [16]. By doping with Cr, other M2 and M3 insulating phases are introduced between the M1 insulating phase and R metallic phase [40]; these additional phases likely exist for the other dopants also. The magnitude of the transition can be controlled by oxygen flow [11], grain size [41], substrate growth temperature [11], film thickness [41, 42], substrate type [38, 42], and annealing in cold gaseous environments [43]. In addition, doping with fluorine (F) significantly increases the resistance of the metallic phase while causing no change to the resistance of the insulating phase [44].

An in-depth research of sputtering methods and configurations was conducted to understand the variables which produce the best VO₂ thin films [references listed in Table 3]. Researchers tend to vary parameters due to scientific curiosity and also due to resource limitations. The reactive sputtering variables are type (DC or RF), substrate, target, substrate growth temperature, chamber vacuum pressure, total gas flow rate, percentage of oxygen flow relative to argon, power, time, and thickness of deposition (a function of time and power) [35, 34, 45]. Generally, lower growth rates form less disordered thin films because the surface mobility of the atoms on the substrate is greater [36].

Table 3. Review of Sputtering Parameters for VO₂.

Ref	Type	Target	O ₂ Flow	Ar Flow	Substrate (°C)	P (mTorr)	Pwr (W)	Substrate	Other/Notes
[11]	DC	No Info	7.8 – 8.8%	92.2 – 91.2%	550	No Info	No Info	No Info	3 good sputtering figures
[46]	DC	V	8.8%	91.2%	550	10	Variable	(001) n-Si	Base pressure, 2×10^{-8} Torr
[37]	DC	V	6.8%	93.2%	550	10	Variable	SiO ₂ on Si	No change (flat)
[37]	DC	V	7.8%	92.2%	550	10	Variable	SiO ₂ on Si	2nd best change (about 3x)
[37]	DC	V	8.8%	91.2%	550	10	Variable	SiO ₂ on Si	Best change (about 4x)
[37]	DC	V	9.8%	90.2%	550	10	Variable	SiO ₂ on Si	Poor change (1x)
[37]	DC	V	10.8%	89.2%	550	10	Variable	SiO ₂ on Si	No abrupt change (linear)
[47]	DC	V	8.8%	91.2%	550	10	Variable	c-Sapphire	Base Pressure, 2×10^{-8} Torr
[48]	DC	V	8.8%	91.2%	550	10	Variable	SiO ₂ on (001) Si	Base Pressure, 2×10^{-8} Torr; 100-nm thick; rapidly cooled in N ₂ (improved transition)
[15]	DC	V	8.8%	91.2%	550	10	Variable	Sapphire	100-nm thick; 4x change at 70°C
[49]	DC	V	9%	91%	550	10	250	Sapphire	5x abrupt change; pre-annealed at 550°C for 30 min; 50-nm thick
[25]	Pulsed DC	V	6.7%	92.3%	Not heated	5	300	SiO ₂	20 kHz pulsed DC mode; O ₂ rate varied for 6 different VO _x
[26]	RF	V	6%	94%	450	5	300	c-Sapphire	Post-annealing has no effect at 450°C; only at lower deposition temps
[41]	RF	V	10%	90%	500	2	Variable	LPCVD Si ₃ N ₄ on Si	Base Pressure, 2×10^{-8} Torr; 350 nm thickness needed for abrupt change
[50]	RF	VO ₂	No Info	No Info	550	10	270	n-Si	Large hysteresis
[20]	RF	V ₂ O ₃	2.5%	97.5%	600	4	100	r-Sapphire	O ₂ partial pressure 0.1 mTorr
[47]	RF	V ₂ O ₅	0.75%	99.25%	550	10	Variable	(001) n-Si	Base Pressure, 2×10^{-8} Torr
[51]	RF	V ₂ O ₅	0.75%	99.25%	550	10	80	HfO ₂ on Si	N/A
[42]	RF	V ₂ O ₅	0.75%	99.25%	550	10	120	SiO ₂ on (100) Si	> 200 nm needed for appreciable change
[42]	RF	V ₂ O ₅	0.75%	99.25%	550	10	120	(0001) Sapphire	100x more abrupt change than SiO ₂

2.5. Applications for MIT Devices

There are myriad applications for MIT devices, including but not limited to 3-D circuitry, spintronics, quantum actuation, hysteretic memory, nonlinear neural elements, solid-oxide fuel cells, MEMS devices, circuit protection, energy dissipation, and thermal computing [11].

The opportunity exists for VO_2 to greatly increase CMOS processing speeds. VO_2 's MIT switching has been detected to be as fast as 75 femtoseconds [11]. This is about 3 orders of magnitude faster than the present day CMOS capability of 16 picoseconds [52]. These figures are based on single devices and do not account for propagation delay. VO_2 has been shown to perform well under reliability testing. It has consistent resistivity and hysteresis (see Figure 28) for at least several hundred switching cycles [49, 53]. Also, Gurvitch et al. found negligible change in reflectance of VO_2 after storing in normal, open air conditions for 11.5 months [53].

The hysteretic nature of VO_2 is an attribute that opens its applicability to volatile

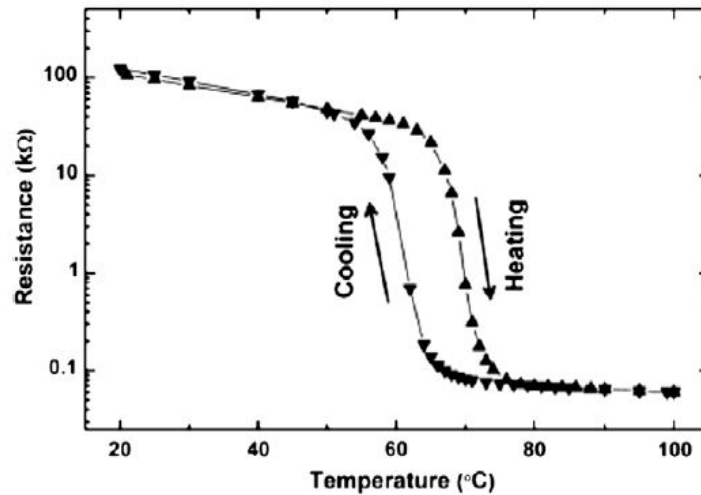


Figure 28. Typical hysteresis of VO_2 (5 – 10°C) [17].

solid state memory. Resistivity is hysteric in nature when heated and cooled; hysteresis is typically five to ten degrees. Present day resistive random access memory (RRAM) is being researched as a faster alternative to volatile memory like SRAM and DRAM [54]. Proven RRAM technology uses materials such as TiO_2 , Ta_2O_5 , ZrO_2 , and HfO_2 , whose formation of conducting filaments is limited by the diffusion of oxygen atoms [54]. The coalescing of conducting filaments in MIT materials such as VO_2 is not limited by oxygen diffusion [55] and it therefore switches faster than existing RRAM materials [54]. When cooled, resistance follows a path several degrees to the left; therefore the state of ON with applied voltage and OFF with a reduction in voltage provides VO_2 built-in memory. Since the transition in VO_2 is volatile, a small bias must be applied on the memory cell to maintain the current memory state [56].

Another application is the actuation of microelectromechanical systems (MEMS) bimorph cantilever beams which deflect downward when they are heated past T_{MIT} (see Figure 29). The thermal expansion coefficient of VO_2 increases abruptly across the phase

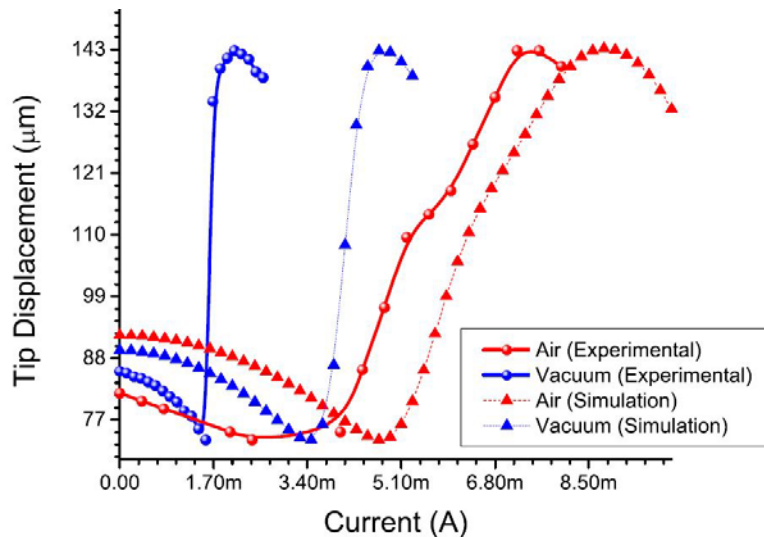


Figure 29. Simulated and measured tip displacement of VO_2/SiO_2 MEMS bimorph cantilever beams. Large displacements are due to VO_2 's coefficient of thermal expansion which increases at T_{MIT} [57].

transition. In a relaxed state, the induced strain between it and the underlying layer tends to bend the beam upward. Cabrera et al. achieved extremely large vertical throws of 28.5 μm for 200- μm -long beams and 68.7 μm for 300- μm -long beams [57].

VO_2 has been incorporated into electronic filters in the microwave regime for both band-stop [58] and band-pass filtering [59] with very good results. The band-stop filter developed by Givernaud et al. switches in hundreds of nanoseconds, which is faster than MEMS devices but slower than semiconductor switching [58]. The results of their experiment are shown in Figure 30; VO_2 is deposited in the signal line of the RF switch shown in the inset. Both lines are transmitted signals; the blue line is no stimulus applied to the VO_2 , and the red line is with a stimulus applied. As this technology matures, it could prove to be a very robust filtering method.

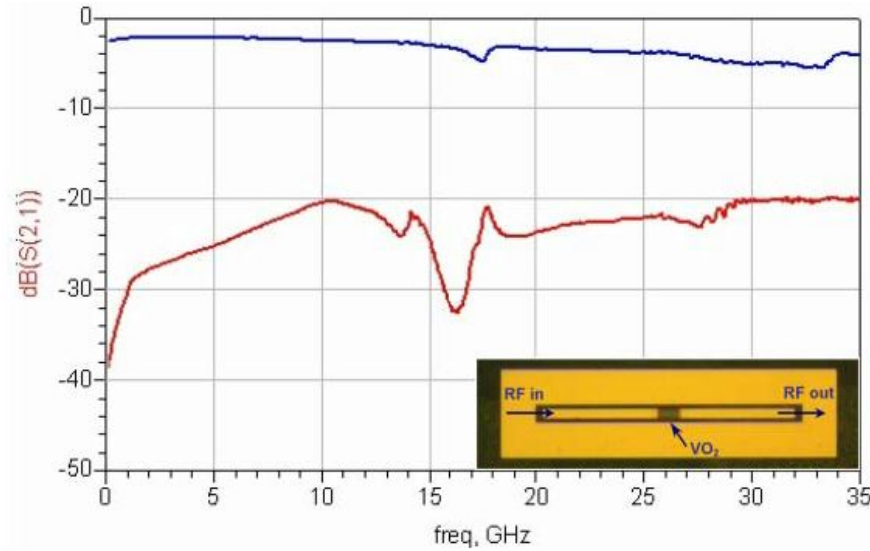


Figure 30. Measured transmission in OFF (blue) and ON (red) in a VO_2 RF switch [58].

As terahertz (THz) technology progresses, requirements have developed for switches and modulators with large transmission modulation depths. The benchmark for

transmission modulation is 50%, which has been set by many state-of-the-art (SOA) THz devices [60]. Modulation depths of 80% have been reported for VO₂ on sapphire [60], as shown in Figure 31, mostly due to the high carrier concentration in its metallic phase.

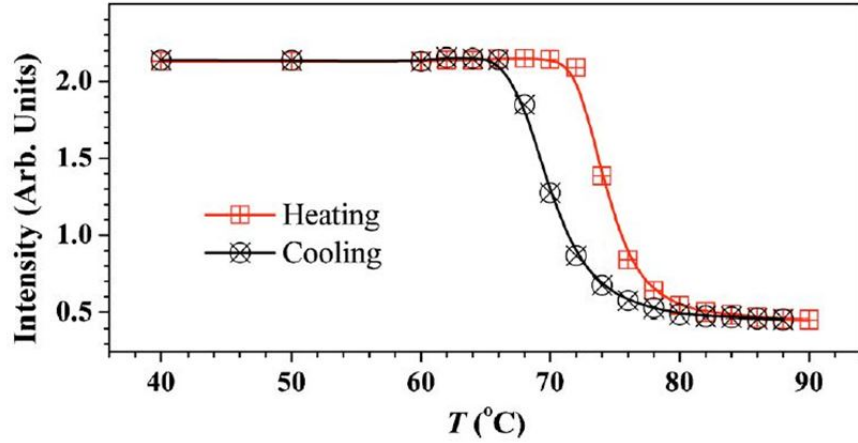


Figure 31. VO₂ terahertz transmission modulation vs. temperature. The decrease in transmission directly correlates to the change of the material's resistivity [60].

For comparison, a unit cell metamaterial has been presented which has 70% absorbance at 1.3 THz [61]. It should be noted that these metamaterial absorbance results are narrowband (full width at half maximum, FWHM, of 0.25 THz) whereas the results of VO₂ modulation are broadband, meaning the attenuation occurs across the entire spectrum. Nevertheless, incorporating VO₂ in metamaterial devices for tunable absorbance looks promising.

VO₂'s varying reflectance of infrared wavelengths (thermochromism, see Figure 32) presents an opportunity for optical filtering and energy efficient windows [62, 48]. As seen in Figure 32, the infrared wavelengths are reflected primarily at higher temperatures. Energy efficient windows (also called “intelligent window coatings” or “smart windows”) could reduce air conditioning costs by adaptively and passively

reducing transmitted heat in the near-infrared. To be useful, these coatings need a lower transition temperature which can be accomplished by doping with tungsten, as previously discussed [63]. Research for the last 15 years has been aimed at increasing transmittance in the optical and decreasing transmittance in the infrared [64]. Additionally, using anti-reflective coatings has been shown to increase the reflectance modulation [65].

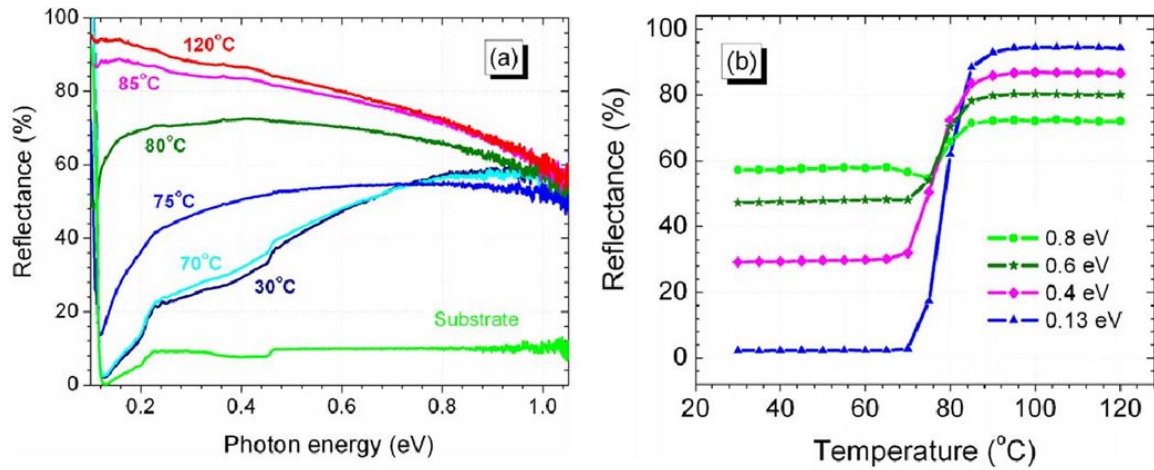


Figure 32. Infrared reflectance of VO₂ on Sapphire. (a) Reflectance vs. sweeping of photon energy while stepping temperature; (b) Reflectance vs. sweeping of temperature while stepping photon energy [48].

Another application of thermochromism is infrared cloaking. Kats et al. have observed negative differential thermal resistance corresponding to the metal-insulator transition. The metallic “nanoscale inclusions” within the narrow transition window are much smaller than infrared wavelengths; therefore VO₂ behaves as an infrared metamaterial. As the material is heated from 60 to 85°C, the material appears warmer, but once it transitions to a metal, it appears cooler. Therefore, if a VO₂ thin film were in front of something warmer than its transition temperature, a thermal camera would only see the cooler temperature of the VO₂. This interesting behavior could be applied to

infrared cloaking/camouflage or an infrared blackboard. The “blackboard” would consist of the VO₂ maintained at its MIT temperature. By using a hot/cold probe or laser, messages could be written on the VO₂ surface which would only be seen with an infrared camera [66].

2.6. Phase Change Materials

2.6.1. History

The first person to publish results of negative differential resistance in phase change materials was Alan Tower Waterman of Yale University. While studying thermionic emission of molybdenite (MoS₂) in 1917, he observed conductivity changes which violated Ohm’s Law and a breakdown at which point the material became permanently ohmic. He called the high resistance phase α and the low resistance phase β [67].

While extremely interesting, Waterman’s observations were not immediately integrated into any technology, as there was no need for materials of varying electrical conductivity. Not until Alan Turing’s 1947 lecture, which called for a solid-state alternative to punch cards, did scientists begin developing magnetic core memory. The transistor was invented in 1948, the integrated circuit in 1958, and in the 1960s random access memory (RAM) replaced magnetic core memory. The major drawback of static and dynamic RAM was—and still is—an erasure of the memory when not powered. At this point, a search for nonvolatile memory began. Two groups of materials were chiefly investigated for integration into a new memory construct: Transition metal oxides and chalcogenides [68].

Starting in 1960, much of the innovative work in chalcogenide research was completed by Stanford R. Ovshinsky, a self-educated man who founded Energy Conversion Devices [68]. His seminal paper in 1968 demonstrated electrical switching in amorphous chalcogenides [69], and his 1970 paper demonstrated the crystallization of amorphous chalcogenides with short laser pulses [70].

This 1970 paper opened the door to an extremely lucrative field of nonvolatile optical memory. This has been manifested as compact discs (CDs), digital versatile discs (DVDs), and Blu-ray discs. Improvements in laser diodes in the 1970s and 1980s (small and high power) were just as crucial as phase change materials engineering [71]. CDs were first demonstrated by Sony in 1977 [72] albeit with limited storage capabilities. Storage density was increased as time progressed.

2.6.2. Optical Memory

Phase change materials, as the name suggests, include compounds which have a reversible, nonvolatile phase change. Chalcogenides are a subset of PCMs (Figure 1); there are also other subsets, such as antimony (Sb) compounds like GaSb. Additionally, many PCMs are doped with indium (In), silver (Ag), tin (Sn), among others, in concentrations of 2 – 10% [73]. Chalcogenides, in general, are poor glass formers, meaning they are able to change phases extremely quickly. The transition from amorphous to polycrystalline phase occurs on the order of tens of nanoseconds [74].

The phase transition is said to be *reversible* because it can be reset to a metastable amorphous (glass) phase. Glasses are the most common form of amorphous structure. They do not possess the long-range order and periodicity of crystalline materials, but they

do have a form of short-range order in the “immediate vicinity of any selected atom” [75]. Amorphization of the material is completed by raising the material’s temperature above its melting temperature, T_m , and quickly cooling below its glass temperature, T_g . This causes a drastic reduction in carrier mobility once it is melted, essentially locking the material into a metastable amorphous (glassy) state. This amorphization process is referred to as heat quenching [76]. When in the amorphous state, crystallization is completed by heating and cooling more slowly, which allows the material to reach its stable, crystalline structure. Because the material will naturally tend to reach a crystalline state when given enough energy, slowly cooling it permits this phase change. Many scientists refer to the glass temperature and crystallization temperature (T_g and T_c , respectively) as synonymous terms; however, when referring to the temperature required to crystallize the material, T_c is more appropriate.

Group 16 (VI) contains the following elements: Oxygen (O), sulfur (S), selenium (Se), tellurium (Te), and polonium (Po). They are shown below in Figure 33. S, Se, and Te are referred to as chalcogens, and their compounds are chalcogenides [68]. Polonium is excluded from the chalcogen group because it has no stable isotope, no common compounds, and only occurs in the radioactive decay of uranium (U) and thorium (Th). Additionally, oxygen is excluded from the chalcogens because of the major differences of oxygen compared to the others (e.g., higher electronegativity, limited coordination number of 4 and valence of 2, and lack of tendency to catenate, which is forming bonds with atoms of the same element) [77]. Oxides do not exhibit nonvolatile phase changes like chalcogenides.

						18			
						2 He Helium 4.003			
13		14		15		16		17	
5 B Boron 10.811	6 C Carbon 12.011	7 N Nitrogen 14.007	8 O Oxygen 15.999	9 F Fluorine 18.998	10 Ne Neon 20.180				
13 Al Aluminum 26.982		14 Si Silicon 28.086		15 P Phosphorus 30.974		16 S Sulfur 32.066		17 Cl Chlorine 35.453	
18 Ar Argon 39.948									
12									
30 Zn Zinc 65.39	31 Ga Gallium 69.732	32 Ge Germanium 72.61	33 As Arsenic 74.922	34 Se Selenium 78.09	35 Br Bromine 79.904	36 Kr Krypton 84.80			
48 Cd Cadmium 112.411	49 In Indium 114.818	50 Sn Tin 118.71	51 Sb Antimony 121.760	52 Te Tellurium 127.6	53 I Iodine 126.904	54 Xe Xenon 131.29			
80 Hg Mercury 200.59	81 Tl Thallium 204.383	82 Pb Lead 207.2	83 Bi Bismuth 208.980	84 Po Polonium [208.982]	85 At Astatine 209.987	86 Rn Radon 222.018			

Figure 33. Portion of the Periodic Table; the chalcogens are in Group 16 [4].

Associated with the crystallization of PCMs is an increase in optical reflectivity which has been exploited for optical data storage [78]. This increase in reflectivity is due to a structural change, increase in density, or both [74]. The recording layer in optical media is typically deposited between two layers of dielectrics atop a metallic layer (Figure 34), which serve to maximize the contrast of reflectivity between ON and OFF states and also to rapidly cool the PCM when heated [76]. The deposition of complex chalcogenide materials to optimize read/write times by laser pulses and data retention has largely been an empirical process spanning the last 30 years. PCMs researched for the purpose of optical memory are various stoichiometries of GeSbTe, InSbTe, AgSbTe, GaSbTe, and GaSb, among others [73].

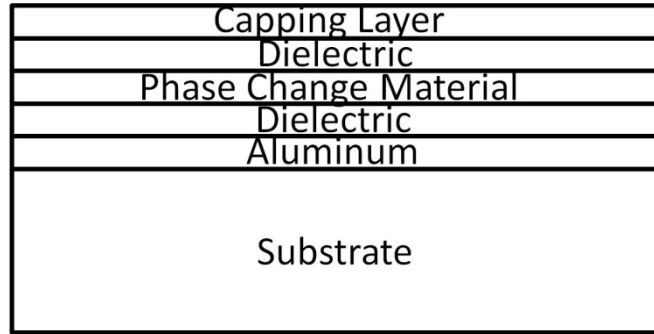


Figure 34. Typical cross-sectional structure of phase change optical memory (after ref. [76]). The dielectric layer is typically ZnS-SiO₂ with total thickness on the order of 50 nm.

Crystallization of PCM cells is characterized by nucleation of crystallites followed by growth of these sites. In growth-dominated materials, the crystallites grow from the interfaces of the material, whereas in nucleation-dominated materials, crystallization begins primarily in the inner bulk of the material [76]. Typically the nucleation rate is much shorter than the growth rate [73], but by decreasing the interfacial area of the cell the growth rate is reduced.

The major design considerations for phase change media are the following: Amorphous phase stability, crystallization/amorphization rate, nucleation time, data retention, optical constants, and media noise (the last two only apply to optical media) [73]. Additionally, the parameters of the thin film PCM vary with thickness, since the values deviate from bulk values [79]. There are essentially no structural changes when in the crystalline phase; however, the amorphous phase tends to reach a lower energy state which can affect its properties such as optical constants and electrical conductivity [80]. Two other important design considerations are the laser's numerical aperture (NA) and the maximum disc spinning velocity for low media noise [81, 73].

In 1991, Yamada et al. discovered a correlation of strong optical contrast for chalcogenides along the GeTe-Sb₂Te₃ tie line in the Ge-Sb-Te ternary system (Figure 35) [82]. To this day, compositions along this tie line are being used for Blu-rays [83]. CDs use 780-nm laser diodes, DVDs 650-nm, and Blu-rays 405-nm; the phase change compositions are Ge₂Sb₂Te₅ for CDs and DVDs and Ge₈Sb₂Te₁₁ for Blu-ray [74]. The motivation behind decreasing the light's wavelength is to facilitate the decrease of bit sizes on the optical disc and consequently increase the memory storage for each disc. For instance with Blu-ray movies, much higher definition can be obtained due to the large amount of available data. Additionally, by engineering two layers of phase change media on one disc, Blu-ray capacity doubles from 25 GB to 50 GB [81].

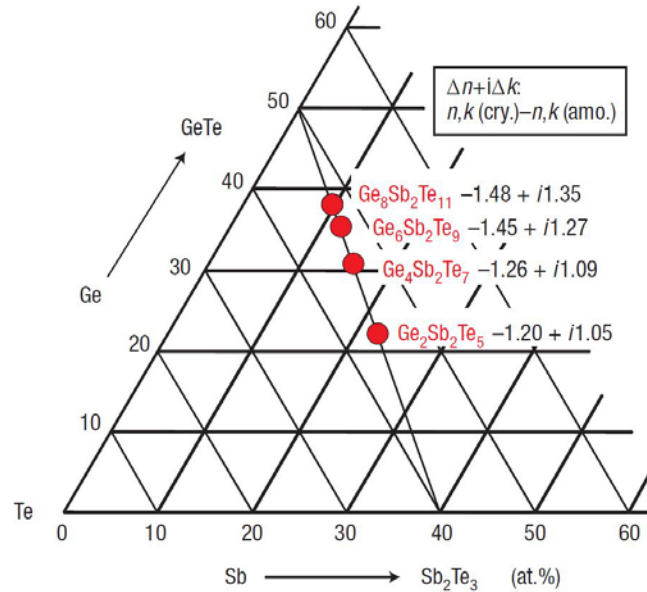


Figure 35. Ge-Sb-Te ternary system with highlighted stoichiometries along the GeTe-Sb₂Te₃ tie line. (GeTe has 50% Te, and Sb₂Te₃ has 40% Sb.) Listed optical contrasts $\Delta n + i\Delta k$ are for 405-nm Blu-ray systems [78].

2.7. Germanium Telluride

Germanium telluride (GeTe) is a chalcogenide glass and phase change material which, like other chalcogenides, exhibits a negative differential resistance as it is heated from its amorphous phase due to a reversible crystallization. The resistivity of GeTe may decrease by as much as six orders of magnitude between room temperature and its crystallization temperature [84]. The applied stimuli have worked well as laser pulses [70] but research of transitions via conductive heating and Joule heating [85] are not as common.

The study of GeTe films for data storage was pioneered by Chen et al. [86] in 1986. Two commonly used elements in PCMs, Te and Sb, are unstable in their amorphous phase but cross-linking with other elements such as Ge, As, and Se increases their stability [86, 87].

Crystalline GeTe (c-GeTe) is relatively well understood. It is known to be p-type exhibiting a degenerate degree of conduction [88]. Density functional theory calculations have shown the discrepancy between calculated bandgaps of 0.4 – 0.7 eV and actual metallic conductivity is due to Ge vacancies which contribute two holes to the valence band. These vacancies are the most common defect and are formed with low formation energies [88]. Hence, it has been proposed that vacancies in chalcogenides cause p-type conductivity and may additionally play a role in nanosecond-order switching and accommodate the volume change in reversible phase switching [89]. The vacancies are estimated to comprise ten percent of the Ge sublattice [90]. Figure 36 shows the effect of one Ge vacancy on the c-GeTe lattice. X-ray diffraction measurements indicate the crystalline cell structure is rhombohedral which is a slightly distorted NaCl-type

configuration [91]. In this structure, angles $\alpha = \beta = \gamma = 88.37^\circ$, and lattice parameters $a = b = c = 5.98 \text{ \AA}$, at room temperature [92]. Large electronic conduction in c-GeTe is reliant on a high hole concentration of $8 \times 10^{20} \text{ cm}^{-3}$; as expected, GeTe has a rather low carrier mobility of $55 \text{ cm}^2\text{V}^{-1}\text{s}^{-1}$ at room temperature which decreases with increasing temperature [92].

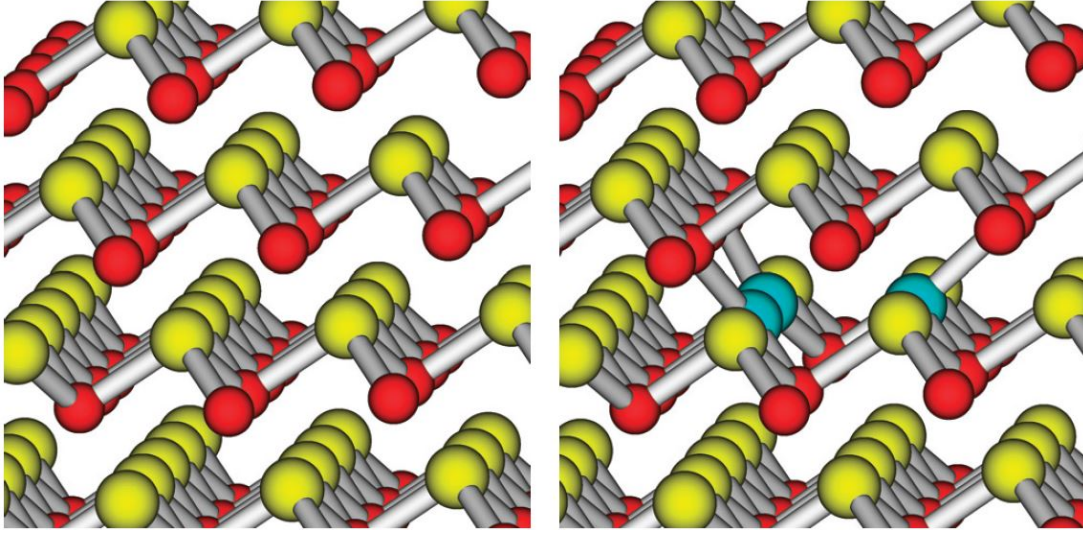


Figure 36. (a) Rhombohedral GeTe lattice without defects, (b) Illustration of the effect of a Ge vacancy on the GeTe lattice. Red atoms are Ge, gold atoms are Te, and blue atoms are Te nearest neighbor atoms to the Ge vacancy [88].

The amorphous phase of chalcogenides is regarded as more complex than the crystalline phase. Ge atoms have octahedral coordination in the crystalline state and tetragonal coordination in the amorphous state (see Figure 6) [74]. While c-GeTe is ohmic, amorphous GeTe (a-GeTe) displays several types of conductivity. From its initially very resistive state, conductivity increases exponentially until a threshold point is reached, and then conductivity increases even more drastically [93]. This threshold switching is critical for amorphous (highly resistive) PCMs because it reduces the current required to heat the PCM cell to its crystalline state. Low power consumption is a major

concern for battery-powered RAM in the future. The threshold criterion is actually dependent on the electric field (voltage and cell length) [93]. This phenomenon is elaborated upon in the next section.

2.8. Phase Change Electronic Memory

PCMs have recently (in the past ten years or so) been integrated into prototype electronic memory called Phase Change Random Access Memory (PCRAM) or Ovonic Universal Memory (OUM). Flash memory has been a commercial success due to its nonvolatility, durability, low power consumption, and low cost [94]; however, programming voltages become too high when scaled to nanometer sizes, and it has rather long write times of approximately 10 μ s [95]. There are currently three major contenders for succeeding Flash as the next generation of nonvolatile memory: Ferroelectric RAM (FeRAM), Magnetic RAM (MRAM), and PCRAM [95].

PCRAM has several traits which make it a worthwhile successor to Flash memory. It can be written in tens of nanoseconds, requires threshold voltages of approximately 0.8 – 1.5 V, and cells can be downscaled to tens of nanometers [78, 95]. There are still many improvements that can be made as the understanding of the physical processes in PCMs is improved upon in the future.

PCRAM cells are typically vertically oriented as shown in Figure 37. The PCM layer is heated by a resistor through which heat is conducted and spreads into the PCM

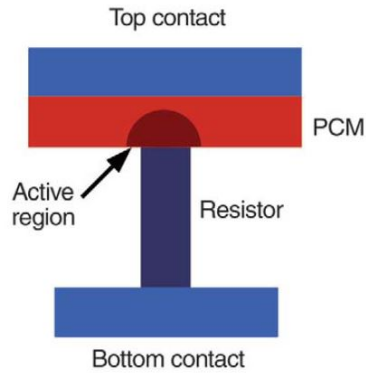


Figure 37. Vertically oriented PCRAM cell [74]

layer. The resistance between the top and bottom contacts is reduced by several orders of magnitude when crystallized [74]. In addition to the vertical cells, recently horizontal cells (Figure 38) have been proposed by Lankhorst et al. They are simpler than the

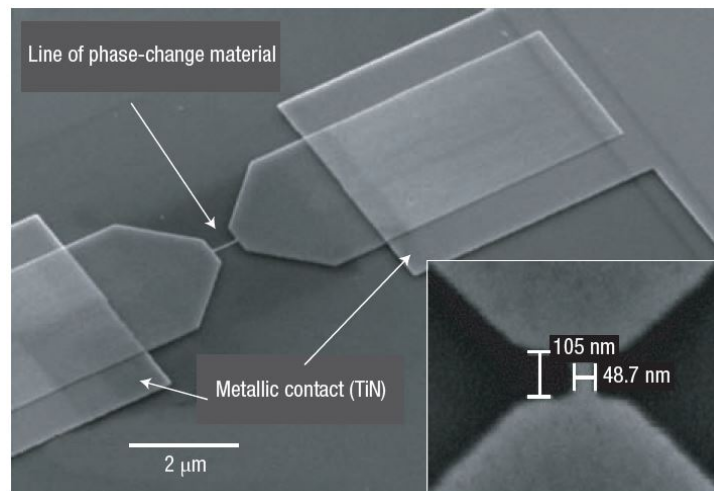


Figure 38. Horizontally oriented PCRAM cell fabricated by electron-beam lithography; image captured with a scanning electron microscope [95].

vertical cells and eliminate three to four fabrication steps. They should also be easier to integrate into silicon CMOS processing. The drawback of this method is that nanometer

size cell lengths must be patterned with electron-beam lithography which is more time and resource intensive than UV or Deep UV lithography.

The following discussion of amorphous conduction is made with reference to Figure 39. With the PCM cell initially in its amorphous state, it has a very high resistance and therefore very little current flows through the cell; however, the current increases exponentially. As the voltage across the cell is increased to a critical point, the current abruptly rises, with usually a negative voltage drop. This threshold switching mechanism is crucial for the operation of PCMs for memory because it reduces the required power for crystallization. As current is increased more, an amorphous ON state is reached which exhibits negative differential resistance; the cell begins to crystallize in this state as the high current generates enough heating. Once another critical point is reached where the cell is sufficiently crystallized, the voltage across the cell can be reduced. This bend toward a crystalline state is called memory switching. The subsequent I-V curve is linear due to the ohmic, low resistance state of the cell [78].

For practical memory applications, a power pulse is applied to the PCM cell which quickly transitions the cell to the opposite phase to write the bit (1 or 0). As in the crystallization of amorphous PCMs shown in Figure 39, crystallization can occur with DC power. As a general rule, the amorphization must be sufficiently short to heat quench the material as discussed previously. Set (crystallization) pulses must be no shorter than 85 – 100 ns, and reset (amorphization) pulses must be no longer than 10 – 50 ns; rising and falling edges of the waveforms are typically 5 ns for both [96, 95]. With these short pulses, the time to write gigabytes of data is relatively short. Reading of bits is done with

low applied power, and the output power is proportional to the resistance of the programmed bit.

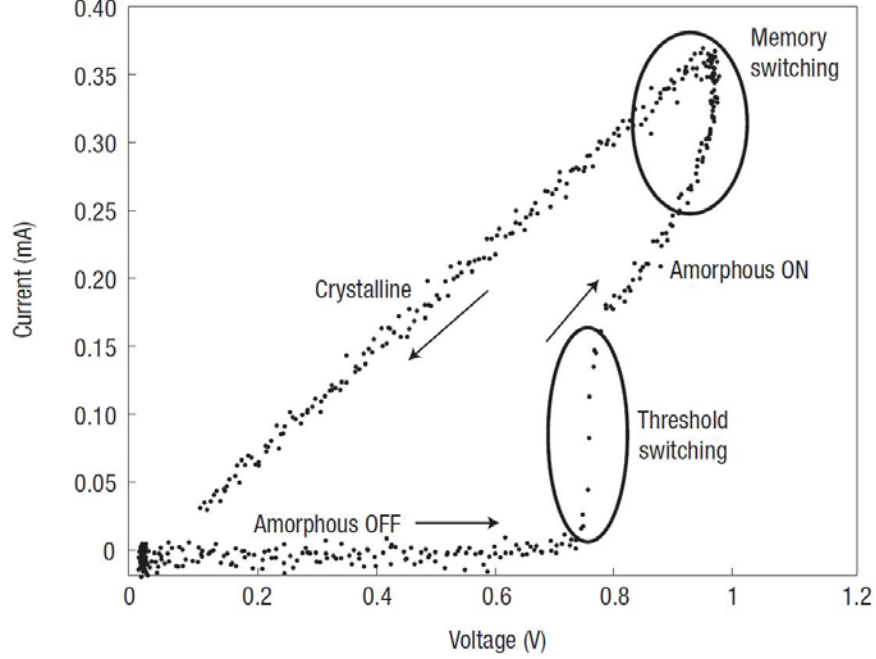


Figure 39. Typical I-V curve of a PCRAM cell which exhibits a highly resistive amorphous OFF state, threshold switching, a more conductive amorphous ON state, memory switching, and a low resistance crystalline ON state [78].

The varying electrical conductivity of the amorphous phase is extremely interesting, and until recently, no theory existed for this uncanny behavior. The physics behind the subthreshold conduction and threshold switching mechanism in PCMs has been postulated by Ielmini and Zhang [93]. Subthreshold conduction occurs by trap-limited transport, and the current is expressed as

$$I = 2qAN_{T,tot} \frac{\Delta z}{\tau_0} \exp\left(\frac{-(E_C - E_F)}{kT}\right) \sinh\left(\frac{qV_A}{kT} \frac{\Delta z}{2u_a}\right) \quad (13)$$

where q is the electron charge, A is the cross-sectional area of the PCM cell, $N_{T,tot}$ is the integration of the trap distribution above the Fermi level, Δz is the intertrap distance, τ_0 is

the characteristic attempt-to-escape time for a trapped electron, E_C is the conduction band energy, E_F is the Fermi level, kT is the thermal energy, V_A is the applied voltage, and u_a is the thickness of the PCM cell from one electrode to the other. The \sinh term comes from a balancing of forward and reverse current which is important for small V_A (recall that $2 \sinh x = e^x - e^{-x}$). They reason the barrier height $E_C - E_T$ between two donor-like traps is reduced by an increment ΔU by an applied electric field F . As the field increases, the barrier is reduced (Figure 40) and electrons flow into the conduction band

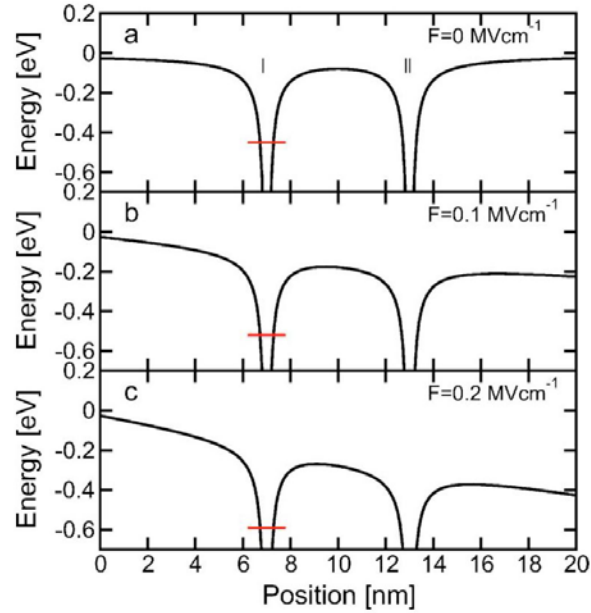


Figure 40. Barrier between two trap states I and II; the electric field F increases from (a) to (c) and the barrier height is reduced by ΔU [93].

via thermal emission over the barriers or by direct tunneling through the barriers. This barrier height reduction is equivalent to

$$\Delta U \approx -qF \frac{\Delta z}{2} = -q \frac{V_A}{u_a} \frac{\Delta z}{2} = -qV_A \frac{\Delta z}{2u_a} \quad (14)$$

One important observation is that their model is valid for vertically integrated PCM cells where the electrodes are above and below the PCM layer. Therefore u_a is both the thickness of the thin film *and* the distance between electrodes (~30 nm). Their model can be used for horizontal structures by modifying u_a . As u_a increases in their model, resistance increases, subthreshold slope of current decreases, and threshold voltage increases [93]. Therefore, there is a trade-off between saving fabrication processing steps and higher threshold voltages; this trade-off can be lessened by using electron-beam lithography to reduce the length of the PCM cell.

The act of threshold switching reduces the power required to program the cell. It is marked by a snap backward to lower voltages. Once the voltage drops, the current and voltage increase within the amorphous ON region, as shown in Figure 41. An explanation of the sudden voltage drop has been debated for many years; Ielmini and Zhang propose an explanation that is consistent with data provided in chalcogenide research. The lowest occupied state is the valence band energy, E_V , the highest occupied trap state is the Fermi level, E_F , and the highest unoccupied trap state is the conduction band energy, E_C . (Note that because chalcogenides are p-type, the conduction process can be interpreted in terms of holes occupying traps from E_C to E_F rather than electrons occupying trap states from E_V to E_F at equilibrium.) As the magnitude of the electric fields increases, the bands become distorted as shown in Figure 42. This facilitates the transfer of energy to the carriers as well as electron heating within trap states. As energy is transferred to one electron, the energy becomes shared among many electrons as the electric field is increased.

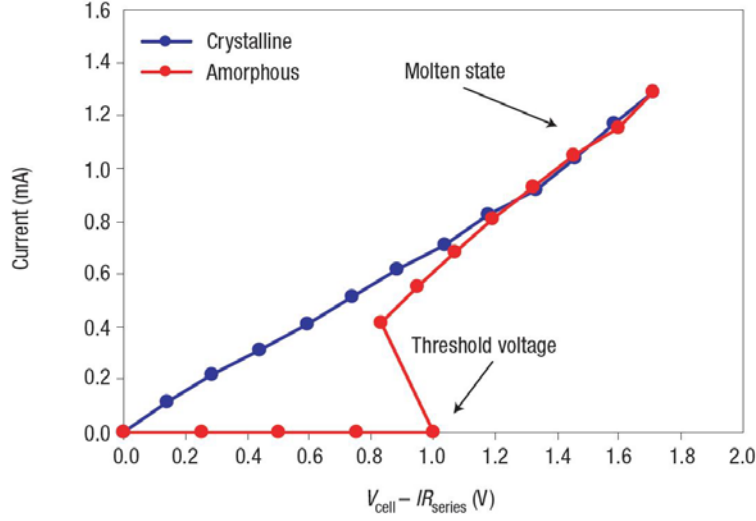


Figure 41. Simple I-V curve of a PCRAM cell showing the characteristic snap of threshold voltage. In this experiment a resistor was placed in series with the cell to prevent large voltage drops across the cell; the resistor's voltage IR_{series} is subtracted out of the values in the horizontal axis [95]. The linearly increasing current in the a-ON region is likely due to the large resistive bottom heater in Figure 37.

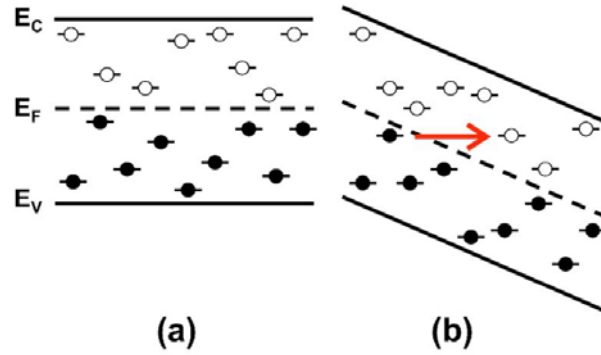


Figure 42. Energy bands (conduction band, E_C , Fermi energy, E_F , and valence band, E_V) and traps in chalcogenides for (a) low to moderate electric fields and (b) high electric fields. The electrons jump to unoccupied trap states via thermionic emission or direct tunneling. [93].

The distance an electron jumps is $\Delta E/(qF)$ where F is the electric field magnitude and ΔE is the energy difference between traps. Therefore, the minimum distance to reach the conduction band E_C is

$$u_{a.OFF} = \frac{E_C - E_F}{qF} \quad (15)$$

Electrons can only occupy nonequilibrium traps within the ON region $u_{a,ON}$. Because the currents in the ON and OFF regions flowing from one electrode to the other must be equal, and the conductivities of the ON and OFF regions are dissimilar, there will be a resulting nonuniformity in the electric field, as seen in Figure 43. Within the OFF region, electrical conductivity and electric field are uniform. There are two resultant electric fields, F_{OFF} and F_{ON} . Therefore the applied voltage V_A between the electrodes is represented by

$$V_A = F_{OFF}u_{a,OFF} + F_{ON}u_{a,ON} \quad (16)$$

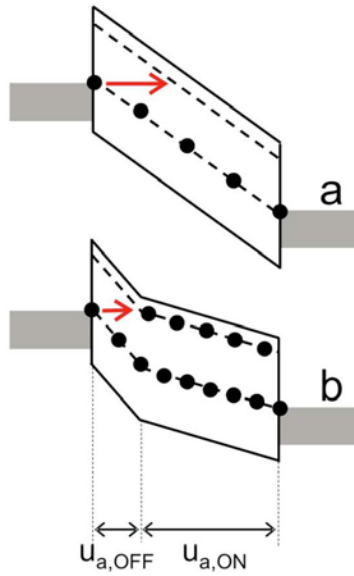


Figure 43. OFF and ON regions in amorphous chalcogenides due to high electric fields for (a) low currents and an equilibrium distribution of electrons and (b) high currents and electrons occupying shallow trap states. The cathode is the grey region on the left, and the anode is the grey region on the right [93].

As F_{ON} decreases due to the increase in conductivity (carrier distribution and velocity), V_A decreases, which accounts for voltage snap back at threshold switching. F_{OFF} remains high which permits a large current to flow [93].

As mentioned previously with reference to optical memory, the stability of the amorphous phase is very crucial. The crystallization (increase in conductivity) of the amorphous phase is unwanted due to bit read errors. In all memory applications, at least 10 years of data retention is required [94] and commercial testing is completed at elevated temperatures (e.g., 50 – 85°C) and elevated humidity [76]. Additionally, in automotive environments, 10 years at 125°C is required [97]. Therefore amorphous bits cannot crystallize for ten years in temperatures lower than 85°C (185°F). On the other hand, the upward creep of resistance (conductivity drift) of the amorphous phase is due to structural relaxation (see Figure 44). This phenomenon is observed in numerous

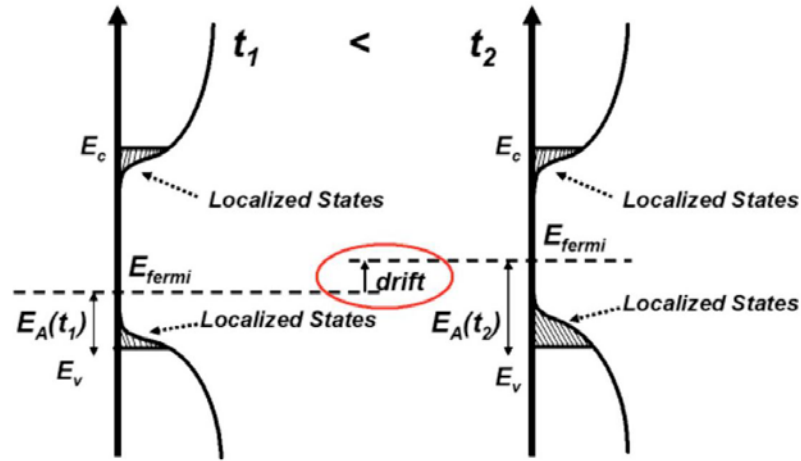


Figure 44. Conductivity drift in amorphous chalcogenides from time t_1 to t_2 explained by shift of the Fermi energy and increase in activation energy, E_A [98].

amorphous semiconductors, including silicon and germanium. Structural relaxation is due to defect annihilation which occurs as the amorphous material tends to reach a minimum energy state and decrease of disorder [99]. These point defects, which occur as vacancies, dangling bonds, distorted bonds, etc., are critical to electronic conduction in

amorphous materials. As these recombine, the conductivity decreases [100]. Consequently, the threshold voltage, V_T , tends to increase due to an increase in energy barriers between traps [101]. This is problematic because this increase in V_T means more power is required to program a PCM cell. Additional materials engineering in this area is required for implementation of commercial PCRAM technology. However, some progress has been made by Mitra et al. who have designed phase change nanowires (NWs) with low conductivity drift [80]. These NW structures have variable surface-to-volume ratios—and stresses in their amorphous phase—depending on their dimensions.

Due to stringent data retention requirements at elevated temperatures, some PCMs with higher crystallization temperatures may be favorable to those with lower crystallization temperatures. $\text{Ge}_2\text{Sb}_2\text{Te}_5$ (GST-225) has a crystallization temperature of approximately 145°C, and GeTe has a crystallization temperature of approximately 185°C [97]. It is GST-225, however, that is chiefly being investigated as the chalcogenide material in PCRAM due to its familiarity and extensive use in optical memory (CDs and DVDs). Perniola et al. [102] have shown, however, that GeTe may be better suited to commercial PCRAM applications due to the higher crystallization temperature and larger contrast between amorphous and crystalline resistances for 30-ns-duration electrical pulses. It has been observed [103] that the *optical* pulse width requirement for GST-225 and GeTe is 20 ns and 100 ns, respectively. Therefore GeTe seems to be better suited to electronic memory applications, and GST-225 and GST-8211 (along the tie line in Figure 35) are better for optical memory. Additionally, 2% nitrogen-doped [104] and 10% carbon-doped [105] GeTe further improve data retention.

As with many amorphous semiconductors, including Si and Ge, many properties change as the film thicknesses decrease. Because PCM thicknesses continue to decrease in PCRAM applications in order to decrease the threshold voltage, the correlation of crystallization temperature, T_c , and PCM thickness is important. For instance, if the crystallization temperature is increased for thinner films, a higher current than estimated will be required for crystallization. In Si and Ge, substantial changes are observed for thicknesses below 20 nm. Along with changes in the crystallization temperature, other material properties change, such as crystallization rate, optical constants, and electrical conduction [106, 107, 79]. The change in crystallization temperature is a very strong function of any adjacent materials. For instance, sandwiching a PCM between dielectrics increases the crystallization temperature, and between metals, decreases it [106].

2.9. Applications for Phase Change Materials

Engineers are currently developing the fourth generation of optical memory. Ultra-high definition television ($7,680 \times 4,320$ pixels) first demonstrated by NHK is the main driver for more capable optical memory [81]. This successor to Blu-ray will likely be either SIL (Solid Immersion Lens) or Super-RENS (Super-Resolution Near-Field Structure). In SIL, the lens is 30 nm above the disc which increases the NA of Blu-ray from 0.85 to 1.9. Due to this increase in resolution, smaller bits can be written and read by the laser [74]. Super-RENS uses another non-linear layer stacked on top of the phase change layer. This additional layer acts as a mask which permits bits to be written shorter than the wavelength of the laser [108, 109].

As discussed with reference to VO₂ terahertz modulation, phase change materials may also be well suited for terahertz modulation. By extrapolating the optical contrast between amorphous and crystalline thin films, the absorption across the terahertz spectrum should also increase as the film crystallizes. However, this crystallization is nonvolatile, unlike VO₂. This would open the material to nonvolatile memory applications and memory metamaterials [110, 61]. Additionally, because of their relatively high crystallization temperatures, their data retention for terahertz applications (relatively low temperature) should be practically infinite. Little research has been completed in applying phase change materials to terahertz spectroscopy.

Phase change materials are being investigated for the novel use as thermoelectric (TE) materials. These materials could one day replace mechanical systems such as air conditioners, refrigerators, heat pumps, heat exchangers, and turbine engines [111]. They are in fact already being used for DNA synthesizers, heating and cooling of car seats, heat engines for space applications, and cooling for heat-seeking missiles and night vision systems [111]. The figure of merit for TE materials is ZT ,

$$ZT = \frac{S^2 \sigma T}{k} \quad (17)$$

where S is the Seebeck coefficient (thermopower), σ is the electrical conductivity, T is the absolute temperature, and k is the thermal conductivity [112]. Thus by increasing the Seebeck coefficient and reducing the thermal conductivity, materials with optimized ZT may be designed. GeTe has been investigated as a thermoelectric base since the 1970s, manifested in TAGS (Tellurium-Antimony-Germanium-Silver) in various stoichiometries, used by NASA for space applications [92]. Bi₂Te₃ has traditionally been

considered the best TE material with $ZT = 0.75$ [113]. However, by creating heterojunctions of Bi_2Te_3 and Sb_2Te_3 [113] or by doping GeTe with heavy dopants such as Ga and In to reduce its thermal conductivity [112], ZT values are approaching 2.5. TE materials comprise a technology that could be disruptive to many traditional thermo-mechanical systems. Additionally, the small size, elimination of CO_2 waste, and ability to improve efficiency by harvesting waste heat in a variety of applications (e.g., electric vehicles) [111] could be a great application for solid state electronics.

2.10. Materials Characterization Methods

Because there are so many materials characterization methods, only the methods used in this research are addressed. An overview of each method is provided in this section, and the methodology of using them is explained later in Chapter 3.

Energy dispersive spectroscopy (EDS) and wavelength dispersive spectroscopy (WDS) are two types of x-ray spectroscopy typically packaged in a scanning electron microscope (SEM) system. Both methods consist of an x-ray source, detection system, and data collection and processing. While somewhat similar, they differ in their detection systems: EDS detects x-ray photon energies with a photon detector, and WDS detects x-ray photon wavelengths using single crystal diffraction. Additionally, EDS is faster and costs less than WDS. As x-rays strike an atom, inner electrons are displaced, and outer electrons fill their vacancies. Characteristic x-rays are emitted that are indicative of the atom's energy state and atomic structure. Based on this emitted energy, the elements in the thin film can be identified. This type of study is useful in determining the oxidation states of thin films (i.e., the ratio of oxygen to the cation). Each atom has

an associated energy or multiple energies, depending on the atomic number (Z) of the atom. The possible emitted energies are dependent on outer electrons filling the inner electrons' vacancies, all of which are shown in Figure 45. Greek letters α , β , and γ correspond to the x-ray intensities. K and L energies for selected elements are provided in Table 4. The output plot in EDS is detected photon counts vs. energy [114].

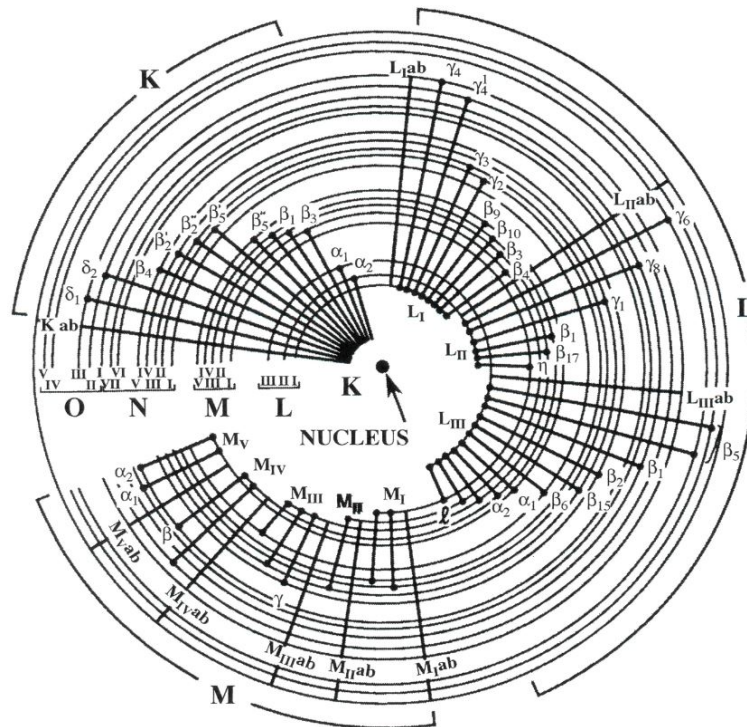


Figure 45. Possible electron transitions for K, L, and M shells [114]

By comparing the intensity of the detected peaks, a fairly accurate quantitative elemental analysis may be obtained. If the peak for the substrate is detected, then confidence in the measurement is increased since it is certain the X-rays penetrated the thin film.

Table 4. Characteristic x-ray energies of selected elements [114]

Atomic No.	Element	K α E (keV)	L α E (keV)
4	Be	0.109	--
5	B	0.183	--
6	C	0.277	--
7	N	0.392	--
8	O	0.525	--
9	F	0.677	--
10	Ne	0.849	--
11	Na	1.041	--
12	Mg	1.254	--
13	Al	1.487	--
14	Si	1.740	--
15	P	2.014	--
16	S	2.308	--
17	Cl	2.622	--
...
19	K	3.314	--
20	Ca	3.692	0.341
21	Sc	4.091	0.395
22	Ti	4.511	0.452
23	V	4.952	0.511
24	Cr	5.415	0.573
25	Mn	5.899	0.637
26	Fe	6.404	0.705
27	Co	6.930	0.776
28	Ni	7.478	0.852
29	Cu	8.048	0.930
30	Zn	8.639	1.012
...
45	Rh	20.13	2.697
46	Pd	21.18	2.839
47	Ag	22.16	2.984

X-ray photoelectron spectroscopy (XPS) is concerned with the emitted electrons when x-rays displace them. These electrons are called photoelectrons, and each has a binding energy which must be exceeded in order to displace it. The binding energy, E_B , is calculated by

$$E_B = h\nu - E_K - \Phi \quad (18)$$

where $h\nu$ is the energy of the incident x-ray, E_K is the measured kinetic energy of the photoelectron, and Φ is the energy required for the photoelectron to escape from the material's surface (known value) [114]. Binding energies are also known for electrons and are used to identify the elements in the material. XPS data is plotted as counts (a. u.) vs. binding energy (eV). Each peak is identified with an element and its atomic subshell (e.g., s , p , d , and f). Associated with each subshell is the quantum number of total angular momentum; p has $\frac{1}{2}$ and $\frac{3}{2}$; d has $\frac{3}{2}$ and $\frac{5}{2}$; and f has $\frac{5}{2}$ and $\frac{7}{2}$ [115, 114]. Additionally, XPS systems must have ultra-high vacuums. This prevents the scattering of lower-energy electrons by gas molecules and also rids the surface of gas contamination [114].

Raman microspectroscopy (Micro-Raman) has many applications such as the measurement of elemental composition, internal strain, crystallographic orientation, and phase identification [114]. Micro-Raman systems are equipped with one or several continuous-wave, monochromatic lasers. Micro-Raman utilizes the Raman Effect which is a change in frequency of light when scattered by molecules. As light strikes the material, it is scattered elastically and inelastically. Elastic scattering (without change in energy) is called Rayleigh scattering [116]. Inelastic scattering is Raman scattering; the change in frequency is directly related to the molecular composition of the material [114]. That is, if molecules are in a low energy state, incident energy is transferred to the molecule and a negative Raman shift is observed (anti-Stokes scattering); if the molecules are in a higher energy state than the incident energy $E = h\nu$, then a positive

shift is observed (Stokes scattering) [117]. The output data is plotted in arbitrary units (a. u.) vs. Raman shift in units of cm^{-1} . The location of the peaks can be used with other published data to determine the composition of the sample, provided both samples are in the same physical state (i.e., crystalline). The fingerprint region, approximately $200 - 550 \text{ cm}^{-1}$, is the most useful portion of the spectrum for materials characterization [114].

Spectroscopic ellipsometry (SE) is used to optically analyze thin films. The measured values of Δ and Ψ are related to the total reflection coefficients \mathcal{R} by the fundamental equation of ellipsometry,

$$\rho \equiv \tan \Psi e^{j\Delta} = \frac{\mathcal{R}^p}{\mathcal{R}^s} \quad (19)$$

Where p signifies light polarized in the plane of incidence and s is polarized orthogonal to this plane. The phase shift between incident and reflected light is Δ , and the ratio of reflected to incident amplitudes is $\tan \Psi = \left| \mathcal{R}^p \right| / \left| \mathcal{R}^s \right|$. From these values of \mathcal{R}^p and \mathcal{R}^s , the extracted values of index of refraction n , extinction coefficient k , and film

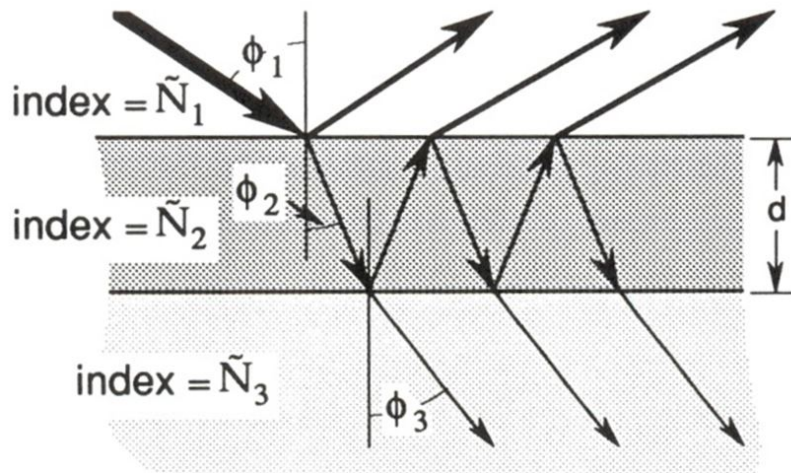


Figure 46. Reflection and transmission of light in air, thin film, and substrate [118]. The complex index of refraction for layer i is \tilde{N}_i .

thickness d are determined. These three output parameters are linked by the expression for the thin film, $\beta = 2\pi (d/\lambda) (n - jk) \cos \phi_2$, where ϕ_2 is the angle in the thin film between incident light and the top surface of the thin film, as shown in Figure 46. An exponential relationship exists between β and \Re^p and \Re^s such that

$$\Re^p = \frac{r_{12}^p + r_{23}^p e^{-j2\beta}}{1 + r_{12}^p r_{23}^p e^{-j2\beta}} \quad (20)$$

$$\Re^s = \frac{r_{12}^s + r_{23}^s e^{-j2\beta}}{1 + r_{12}^s r_{23}^s e^{-j2\beta}} \quad (21)$$

The r_{ij}^p and r_{ij}^s terms are the Fresnel reflection coefficients for the interface between layers i and j which are in turn calculated by

$$r_{ij}^p = \frac{\tilde{N}_j \cos \phi_i - \tilde{N}_i \cos \phi_j}{\tilde{N}_j \cos \phi_i + \tilde{N}_i \cos \phi_j} \quad (22)$$

$$r_{ij}^s = \frac{\tilde{N}_i \cos \phi_i - \tilde{N}_j \cos \phi_j}{\tilde{N}_i \cos \phi_i + \tilde{N}_j \cos \phi_j} \quad (23)$$

where for a given material, \tilde{N} is the complex index of refraction, $\tilde{N} = n - jk$ [118].

The Tauc-Lorentz dispersion model is excellent at modeling amorphous semiconductors. It was developed by Jellison and Modine [119] and combines the Tauc joint density of states with the Lorentz oscillator. The components of the complex dielectric function, $\varepsilon = \varepsilon_r + j\varepsilon_i$, are expressed as

$$\varepsilon_i(E) = \begin{cases} \frac{1}{E} \frac{AE_0 C (E - E_g)^2}{(E^2 - E_0^2)^2 + C^2 E^2} & E > E_g \\ 0 & E \leq E_g \end{cases} \quad (24)$$

$$\varepsilon_r(E) = \varepsilon_\infty + \frac{2}{\pi} P \int_{E_g}^{\infty} \frac{\xi \varepsilon_i(\xi)}{\xi^2 - E^2} d\xi \quad (25)$$

where in the ε_i equation, A is the peak strength, C is the broadening term, E_g is the bandgap energy, and E_0 is the position of the peak. ε_r is obtained by Kramers-Kronig integration; ε_∞ is the high frequency dielectric constant equivalent to $\varepsilon_r(E \rightarrow \infty)$ and P is the Cauchy principal part of the integral [119]. Additionally, the Classical dispersion model is suitable for modeling some crystalline semiconductors and metals. It is expressed as the sum of four terms as

$$\varepsilon(\omega) = \varepsilon_\infty + \frac{(\varepsilon_s - \varepsilon_\infty)\omega_t^2}{\omega_t^2 - \omega^2 + i\Gamma_0\omega} + \frac{\omega_p^2}{-\omega^2 + i\Gamma_D\omega} + \sum_{j=1}^2 \frac{f_j\omega_{0j}^2}{\omega_{0j}^2 - \omega^2 + i\gamma_j\omega} \quad (26)$$

where the first term is the high frequency dielectric constant, the second is the Lorentz oscillator, the third is the Drude oscillator, and the fourth term is for two additional oscillators, if needed [120]. ε_s is the static dielectric constant at zero frequency equivalent to $\varepsilon_r(\omega = 0)$, ω_t is the resonant frequency of the Lorentz oscillator, Γ_0 is the broadening (damping) of the Lorentz oscillator, ω_p is the plasma frequency where $\varepsilon_r(\omega_p = 0)$, Γ_D is the collision frequency where $\varepsilon_r = \varepsilon_i$, f_j is the oscillator peak strength, ω_{0j} is the resonant frequency of each oscillator peak, and γ_j is the broadening of each oscillator peak [120].

Spectral reflectance can be considered a simplified version of ellipsometry. The unpolarized light is emitted along the normal vector of the sample (i.e., with $\phi_I = 0$ in Figure 46). In the case of one thin film on a substrate, light is reflected at the air/film and film/substrate interfaces. This reflected light is measured at the same angle as the emitted

light and can be used to model refractive index, extinction coefficient, and thickness.

The measured reflection, R , for an absorptive and dispersive material is expressed as

$$R = \frac{(n-1)^2 + k^2}{(n+1)^2 + k^2} \quad (27)$$

and for a non-absorptive dielectric, the reflection becomes

$$R = \left(\frac{n-1}{n+1} \right)^2 \quad (28)$$

Depending on the thickness of the films, the light adds constructively when it is an integral multiple of the light's wavelength. Destructive interference occurs when the thickness is an integral multiple of one-half of the light's wavelength. Thicker films will naturally have more oscillations in the reflectance [117, 121].

Additionally, the absorption coefficient α can be calculated from results of both ellipsometry and spectral reflectance; is related to the extinction coefficient, k , by the following two equations:

$$k = \frac{\lambda}{4\pi} \alpha \quad (29)$$

$$I(z) = I_0 e^{-\alpha z} \quad (30)$$

where z is the penetration depth of the light and I is the light's intensity.

Optical transmission experiments such as spectrophotometry and FTIR measure the transmission of light through a material. These measurements are valid from ultraviolet (UV) wavelengths to far infrared (FIR). When measuring the transmission through a thin film, care must be taken to choose a substrate that does not have a bandgap within the range of study. For instance, the bandgap of silicon is approximately 1.1 eV

and therefore all energies above (wavelengths shorter than) the bandgap will be blocked. This is a crucial consideration in analyzing thin films that are transmissive to optical and ultraviolet energies, for applications such as solar cell coatings. Another substrate must be chosen to analyze these wavelengths, such as Quartz, MgF_2 , or CaF_2 . Additionally, substrates with crystal orientations different than (001) Si will introduce stresses in the thin films not present in the Si-thin film interface. For instance, c- Al_2O_3 (sapphire) has a hexagonal lattice, so the stresses and bonding in this interface will be different. For very thin films ($\sim \text{nm}$), the substrate-thin film interface will affect the transmission more so than with bulk materials.

The terahertz (THz) portion of the spectrum is commonly referred to as the “Terahertz Gap.” To the right of the gap (smaller frequencies), the elementary particle is the electron, and to the left (greater frequencies), the photon. Traditionally, the terahertz gap was inaccessible until terahertz spectroscopy and cascade laser systems were developed approximately 20 years ago [122]. Materials characterization in the THz spectrum is still considered in its infancy and is benefitting from fairly basic research such as characterization of perfectly transmissive and perfectly absorptive materials. Terahertz time-domain spectroscopy (THz-TDS) is being used for a wide variety of applications including studying DNA [123], cancer diagnosis [124], crystallinity of pharmaceutical materials [125], materials diagnosis for restoration of paintings [126], and materials research [127], among others. There is also some exciting research ongoing such as invisibility cloaks [128, 129] using metamaterials. Metamaterials (MMs) are synthetic, man-made structures that output desired electromagnetic responses. The product of the complex electrical permittivity $\tilde{\epsilon} = \epsilon_r + j\epsilon_i$ and complex magnetic

permeability $\tilde{\mu} = \mu_r + j\mu_i$ is equal to the complex index of refraction squared [61]; that is,

$$\tilde{N}(\omega) = \sqrt{\tilde{\epsilon}(\omega)\tilde{\mu}(\omega)} = n + jk \quad (31)$$

Materials with $\epsilon_r < 0$ are found in nature, like metals and degenerate semiconductors. There are no naturally occurring materials with $\mu_r < 0$, however; this is only possible with metamaterials such as split ring resonators (SRRs) [122]. The feature sizes of MMs are much smaller than the wavelength of the terahertz laser (100 GHz to 10 THz, corresponding to wavelengths of 3 mm to 30 μm , respectively). Some previous research has determined materials and MM structures that absorb certain wavelengths (narrowband) or all wavelengths (broadband) depending on an input stimulus (i.e., heat, electrical biasing, optical laser, or mechanical stressors). VO_2 is such a material that exhibits broadband absorption when transitioned to its metallic phase and is very transmissive in its insulating phase [60]. Within a THz-TDS system, the crystallinity can be changed by using a heating module. This affords the experimenter *in-situ* measurements of transmission and absorption vs. temperature.

Several researchers have conducted experiments with VO_2 in the MIR, FIR, and THz regimes, including incorporating VO_2 into metamaterials for greater transmittance modulation [130, 131, 132]. On the other hand, very little (if any) research has been completed with chalcogenides in terahertz [133]. This could be because of the relatively high crystallization temperatures; however, they should not be discounted for this reason. Many terahertz technologies are reliant on voltage biasing, such as semiconductor modulators [134, 135]. Therefore, if chalcogenides can be characterized by *in-situ* heating methods and determined to be suitable for terahertz modulation, then work can be

done to apply them in devices which are designed to be conducive to Joule heating via voltage pulsing.

The terahertz transmittance, T , is equivalent to

$$T = \frac{E_s}{E_r} \quad (32)$$

where E_s is the magnitude of the electric field detected through the sample and E_r for the reference. Absorbance, A , is expressed as

$$A = -\log_{10} \frac{E_s}{E_r} = -\log_{10} T \quad (33)$$

Because the absorbance is the logarithm of the transmittance, it is decadic in nature. Additionally, the terahertz modulation M between two transmittances T_1 and T_2 , where T_1 is the reference, is

$$M = \frac{T_1 - T_2}{T_1} \quad (34)$$

For frequencies lower than the terahertz gap, electrons are the elementary particles rather than photons. One method of determining a material's response to this part of the spectrum is to measure its network parameters when incorporated into a network. The network can be thought of as a “black box” [136] and experiments are conducted to determine how it responds to various electrical stimuli.

Electrical switches are one case of a two-port network, where there is one input port and one output port. Two technologies currently used for RF switches are *p-i-n* diodes and MESFETs. These have limitations such as high forward bias resistance and performance degradation at high frequencies [137]. PCMs such as GeTe have been

explored as possible RF switching materials due to their high contrast of resistance between crystalline ON and amorphous OFF states [138].

Networks can be characterized by different sets of parameters (e.g., y, h, g, z, and S parameters) [139, 140]. S (scattering) parameters apply particularly to microwave, radio frequencies (RF), and even longer wavelengths (smaller frequencies), and are defined by the expression

$$\begin{bmatrix} V_1^- \\ V_2^- \end{bmatrix} = \begin{bmatrix} S_{11} & S_{12} \\ S_{21} & S_{22} \end{bmatrix} \begin{bmatrix} V_1^+ \\ V_2^+ \end{bmatrix} \quad (35)$$

where V_i^- terms are wave components traveling away from the i^{th} port, and V_i^+ terms are wave components traveling toward the i^{th} port. It follows that

$$\begin{cases} V_1^- = S_{11}V_1^+ + S_{12}V_2^+ \\ V_2^- = S_{21}V_1^+ + S_{22}V_2^+ \end{cases} \quad (36)$$

Therefore the four S parameters are the following:

$$S_{11} = \left. \frac{V_1^-}{V_1^+} \right|_{V_2^+=0} \quad (37a)$$

$$S_{12} = \left. \frac{V_1^-}{V_2^+} \right|_{V_1^+=0} \quad (37b)$$

$$S_{21} = \left. \frac{V_2^-}{V_1^+} \right|_{V_2^+=0} \quad (37c)$$

$$S_{22} = \left. \frac{V_2^-}{V_2^+} \right|_{V_1^+=0} \quad (37d)$$

By analyzing these ratios of incident and outgoing wave components, it can be determined that S_{11} is the reflection coefficient for port 1, S_{12} is the insertion loss from

port 2 to port 1, S_{21} is the insertion loss from port 1 to port 2, and S_{22} is the reflection coefficient for port 2. $V_1^+ = 0$ and $V_2^+ = 0$ are achieved by impedance matching the ports and the virtual transmission lines to the characteristic impedance Z_0 , which is usually 50 Ω [140].

Programmable network analyzers (PNAs) are used to measure S parameters which are output in real and imaginary components, where $\vec{S} = S_r + jS_i$. Recall its magnitude $\|S\|$ and phase $\angle S$ are

$$\|S\| = \sqrt{S_r^2 + S_i^2} \quad (38)$$

$$\angle S = \tan^{-1} \frac{S_i}{S_r} \quad (39)$$

Furthermore, the magnitude is converted to units of dB by

$$S_{dB} = 20 \log_{10} \|S\| \quad (40)$$

Therefore, for a given S parameter in dB, the magnitude of S is [136]

$$\|S\| = 10^{S_{dB}/20} \quad (41)$$

The relationship between dB and magnitude is presented below in Table 5.

Table 5. Calculated relationship between decibels (dB) and magnitude in increments of 10 dB. The scientific notation in the right column helps to clarify the logarithmic periodicity of decibels.

dB	Magnitude	Magnitude
0	1	1.00×10^0
-10	0.316	3.16×10^{-1}
-20	0.1	1.00×10^{-1}
-30	0.0316	3.16×10^{-2}
-40	0.01	1.00×10^{-2}
-50	0.00316	3.16×10^{-3}
-60	0.001	1.00×10^{-3}
-70	0.000316	3.16×10^{-4}
-80	0.0001	1.00×10^{-4}

The performance of RF switches can be taken one step further and be measured in terms of insertion loss and isolation. These are two common measures of the performance of RF switches. Insertion loss is the ratio of power delivered to the load in the ON state to the actual power delivered to the switch. Therefore this can be easily measured in terms of S parameters as $-S_{21,ON}$. Insertion loss is ideally zero in order to deliver the maximum amount of power to the load. On the other hand, isolation is the primary measure of the OFF state of the switch. It is the ratio of power delivered to the load in the ON state to the power delivered to the load in the OFF state [137]. This can be measured as $|S_{21,OFF}| - |S_{21,ON}|$. Because the S parameters are expressed as losses and are negative, this is equivalent to $S_{21,ON} - S_{21,OFF}$. If $S_{21,OFF}$ is lower (higher in magnitude) than $S_{21,ON}$, then isolation is positive. If $S_{21,ON}$ is higher in magnitude, then isolation is negative. Isolation is ideally infinite so that the switch is infinitely attenuating in its OFF state.

For frequencies greater than or equal to terahertz frequencies, it is important to know the relationship between energy, frequency, wavelength, and wavenumber. Recall for an electromagnetic wave, the relationship between its energy E and frequency ν is

$$E = h\nu \quad (42)$$

where h is Planck's constant (6.626×10^{-34} J·s or 4.136×10^{-15} eV·s). Photon energy in units of electron-volts (eV) is calculated using Planck's constant in units of eV·s. Note that frequency is in units of hertz (Hz) which is equivalent to s^{-1} . Additionally, wavelength λ and frequency ν are related to the speed of light by

$$c = \lambda \nu \quad (43)$$

where $c = 2.998 \times 10^8$ m·s⁻¹. Therefore a wave's energy can be correlated to its wavelength by

$$E = h\nu = \frac{hc}{\lambda} \quad (44)$$

Wavenumber $\tilde{\nu}$ is a unit of measure used in many spectroscopic and optical methods. It is calculated by

$$\tilde{\nu} = \frac{10,000}{\lambda_{\mu\text{m}}} \quad (45)$$

where $\lambda_{\mu\text{m}}$ is the wavelength in units of microns (μm). Wavenumbers are in units of cm^{-1} [117].

2.11. Fabrication Methods

In the field of MEMS, there are three fabrication methods: Bulk, surface, and LIGA [35]. It is possible to fabricate devices by combining several of these methods, which are described below.

Relative to a blank crystal-silicon wafer, bulk micromachining is the fabrication of devices beneath the surface—within the *bulk* of the wafer. Masking of the wafer is typically accomplished with photoresist which is easily patterned by exposing it with ultraviolet light. These patterns in the masking layer are the basis for the etched cavities underneath [45]. Etching of the silicon wafer is accomplished with wet or dry etching of the windows formed by the masking layer. Wet etching can be done with isotropic or anisotropic etchants. Isotropic etchants like hydrofluoric acid (HF) etch in all directions at the same rate. The etch rate of anisotropic etchants like potassium hydroxide (KOH) depends on the exposed crystal plane. The (111) silicon plane etches more slowly than the (100) plane, which can be used to create pyramidal shaped cavities in the bulk [141]. On the other hand, dry etching, as with deep reactive ion etching (DRIE), gives the designer more precision of the etched cavity with vertical sidewalls. The energetic ions excited with RF power bombard and etch the material. There are other considerations in selecting an etchant method such as material selectivity, cost, etch rate, undercutting, and etch precision [142].

The second type of fabrication is surface micromachining which is the deposition of materials above the surface of the wafer [35]. The deposition of thin films falls under this category. Masking is also typically accomplished with photoresist. After the deposition is completed, the photoresist and all layers above it are easily stripped with

acetone or another chemical stripper. Fabrication of devices composed of thin films is discussed in detail in this research.

The third type of fabrication is LIGA, also known as HARMST (High Aspect Ratio Microsystems Technology). This fabrication technique is used to create high-aspect-ratio devices as great as 100:1 with heights on the order of hundreds of microns [35]. These devices are typically patterned with PMMA (and exposed with x-rays) or SU-8 (and exposed with UV light). This technique is most widely used in the field of microfluidics, where casting molds of MEMS structures consisting of polymers is used [35].

In this research, low aspect ratio devices are fabricated above the surface of the substrate and therefore fall under the second type of fabrication, surface micromachining. Thin films of metal are deposited using electron-beam evaporation, and the active layers of VO₂ or GeTe are deposited using sputtering.

2.12. Summary

The details of the physical phenomena of phase transitions in transition metal oxides and phase change materials were discussed. While there is still more to be determined, it is certain these materials are well suited to many applications. Based on the differences between the volatility of MIT materials and PCMs, the former are more suitable for switching and the latter for nonvolatile memory. Additionally, some materials characterization methods were presented, which are used in this research to characterize these materials. Finally, MEMS fabrication methods were discussed.

3. Methodology

3.1. Introduction

Within the constructs of TMOs and PCMs (e.g., MIT materials and chalcogenides) reviewed in Chapter 2, VO₂ and GeTe are used here as representing those materials which are incorporated into microelectronic devices. This chapter presents the methodology of design, fabrication, and testing of these devices. Additionally, materials characterization of thin films deposited uniformly on substrates are reviewed.

3.2. Design

The mask design was created for three-inch-diameter crystal-silicon wafers; this equates to 76.2 mm from point A to C in Figure 47. By the Pythagorean Theorem, the length of the secant line between the corner points A and B is 53.88 mm. Each reticle is 12.0 mm × 12.0 mm. This leaves approximately 8.5 mm of gap between adjacent reticles. The advantage of this grid pattern of identical reticles is the mitigation of flaws that may be limited to one area of the wafer (e.g., contaminants, flaws in the photoresist, and misalignment). Therefore the probability of creating successful devices increases. The disadvantage of this design is the close proximity of the corners of the reticles to the outside of the wafer: During evaporation, the wafers are held in place with metal jigs that cover about 2 mm within the edge of the wafer. However, using nine identical copies of the reticles more than compensates for this disadvantage.

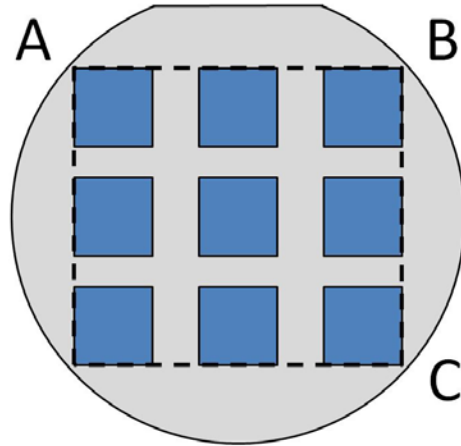


Figure 47. Layout of nine identical reticles (each reticle is shown in Figure 48) on a 3-inch-diameter wafer. The reticles are spaced evenly across the wafer. These spaces between reticles provide adequate room for dicing the wafer before testing.

Design of the devices started with the creation of three masks in Tanner L-Edit software. This is computer aided design (CAD) software and is an industry standard for designing masks. Figure 48 shows the design of one reticle in L-Edit. Nine identical reticles were fabricated on each wafer. Located within each reticle are two sets of isolated rectangles of each layer (see the upper right and lower right corners of Figure 48). These are used for post-fabrication characterization such as thickness measurements.

Within each reticle, there are six categories of devices, each in its own row. By aligning their centers vertically, testing on a probe station is simplified because the sample stage is easily moved from one device to the next. Each category has the largest device on the left based on the area of the active layer; the size decreases toward the right. This design of reducing the spacing between the contact pads (interelectrode distance) facilitates the analysis of the dimensions on the phase change process. The phase change for both VO_2 and GeTe is dependent on the applied electric field $E = V/d$,

where V is the applied voltage and d is the interelectrode distance. Additionally, imperfect alignment between the wafer and the mask may prevent the smallest devices from being resolved (i.e., the gold pad does not touch the active layer when it should because the alignment is too far in one direction).

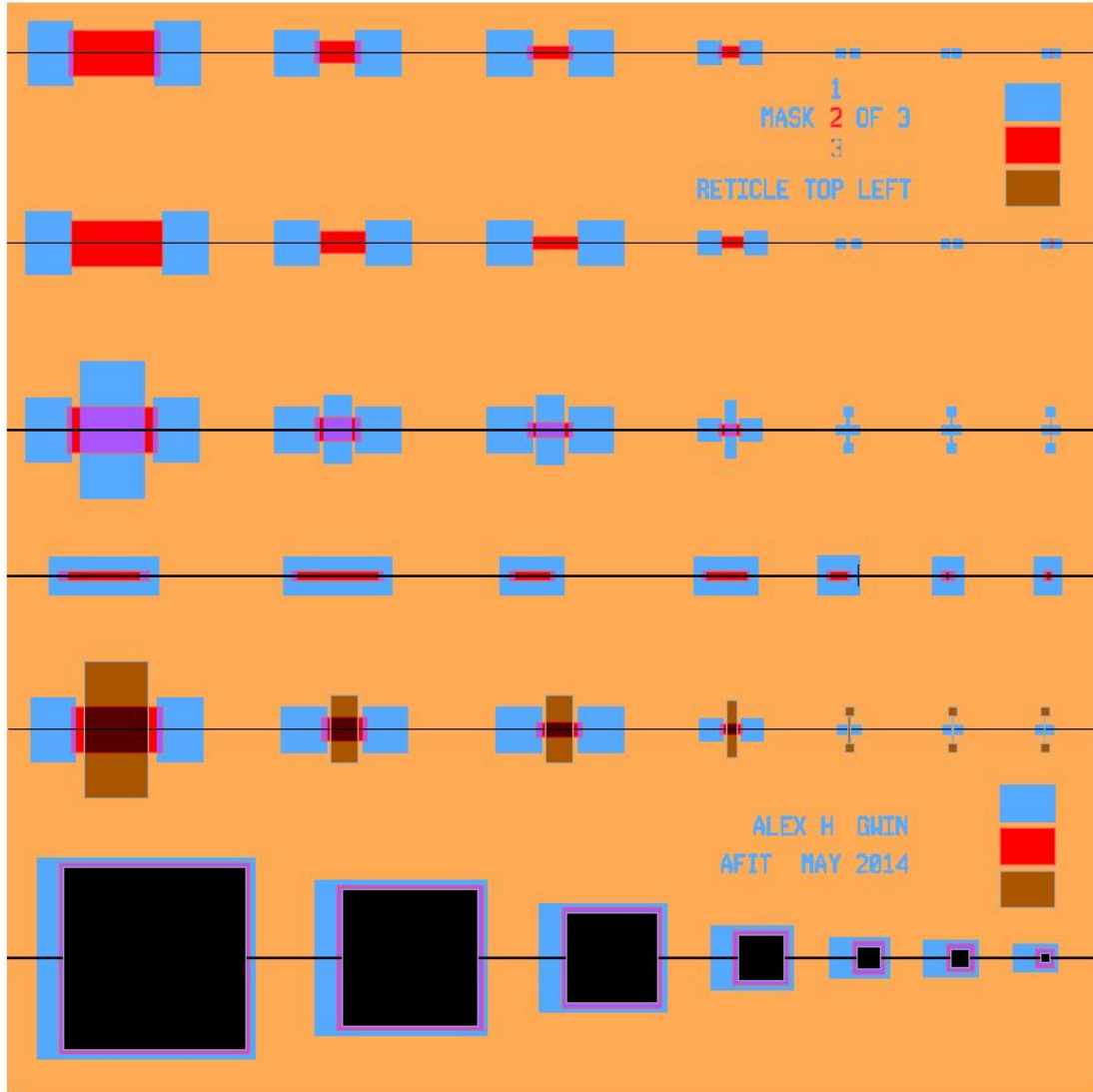


Figure 48. Mask design of one reticle using Tanner L-Edit CAD software. Black horizontal lines were used for alignment and were deleted before creating fabrication files. Light blue, red, and brown correspond to bottom gold layer, active layer (VO_2 or GeTe), and top gold layer, respectively. Each row contains a category of devices with dimensions decreasing from left to right.

In order to adequately test the electrical and thermal responses of VO₂ and GeTe, six categories of devices were designed. They were designed to be $\sim\text{M}\Omega$ in their insulating phase in order to provide enough room for the several orders of magnitude decrease in resistivity. Published values of resistivity were used with the overall equation for resistance R ,

$$R = \rho \frac{l}{A} \quad (46)$$

where ρ is the electrical resistivity, l is the interelectrode distance, and A is the cross-sectional area. A material thickness of 350 nm was used for calculations. Conservatively speaking, the resistivity of VO₂ varies from approximately 0.05 $\Omega\cdot\text{cm}$ in its metallic phase to 20 $\Omega\cdot\text{cm}$ in its insulating phase [19, 41]. GeTe has up to six orders of magnitude decrease. The third largest device was targeted as being switched with moderate electric fields of approximately 20 V. From there, smaller and larger devices were designed to allow for fluctuations in resistivity values, the threshold electric field, and round-off errors in the design.

Schematics of the fabricated devices are shown in Figure 49. These are referred to as simple resistors, gapped resistors, bottom heaters, RF switches, top heaters, and capacitors. Note that while the term “resistor” is used, a more accurate term is “nonlinear resistor,” or “cell” when applied to memory applications. Simple resistors contain a rectangular area of the active layer connecting two metal contact pads on either end; these pads make an ohmic contact with the active layer. The second type of resistor has gaps between the contact pads and the active layer. This design is intended to possibly analyze the electric field effects by neglecting Joule heating. The bottom resistor is similar to the

simple resistor with an added resistive element below the active layer and between the two contact pads. This extra resistor has contact pads of its own away from the other two pads. This extra resistor enhances the Joule heating in the active layer when applied with a voltage. The fourth type of device is an RF switch. It is a simple resistor with three coplanar waveguides. The middle waveguide is the signal line and the outside waveguides are the ground lines. There is a pitch of 138 μm between the centers of adjacent pads (the ground line height is 150 μm , there is a 13 μm gap between the ground and signal lines, and the signal line height is 100 μm .) The active layer connects the input and output terminals of the signal line. The ground lines extend from one side to the other but are cut short for demonstration purposes. The fifth device is a top resistor. Its layout is the same as the bottom resistor but with the resistive element above the active layer instead of below it. Finally, the sixth device is a capacitor. The active layer is sandwiched between two metal layers. The bottom layer has a platform extended to one side for probe contact.

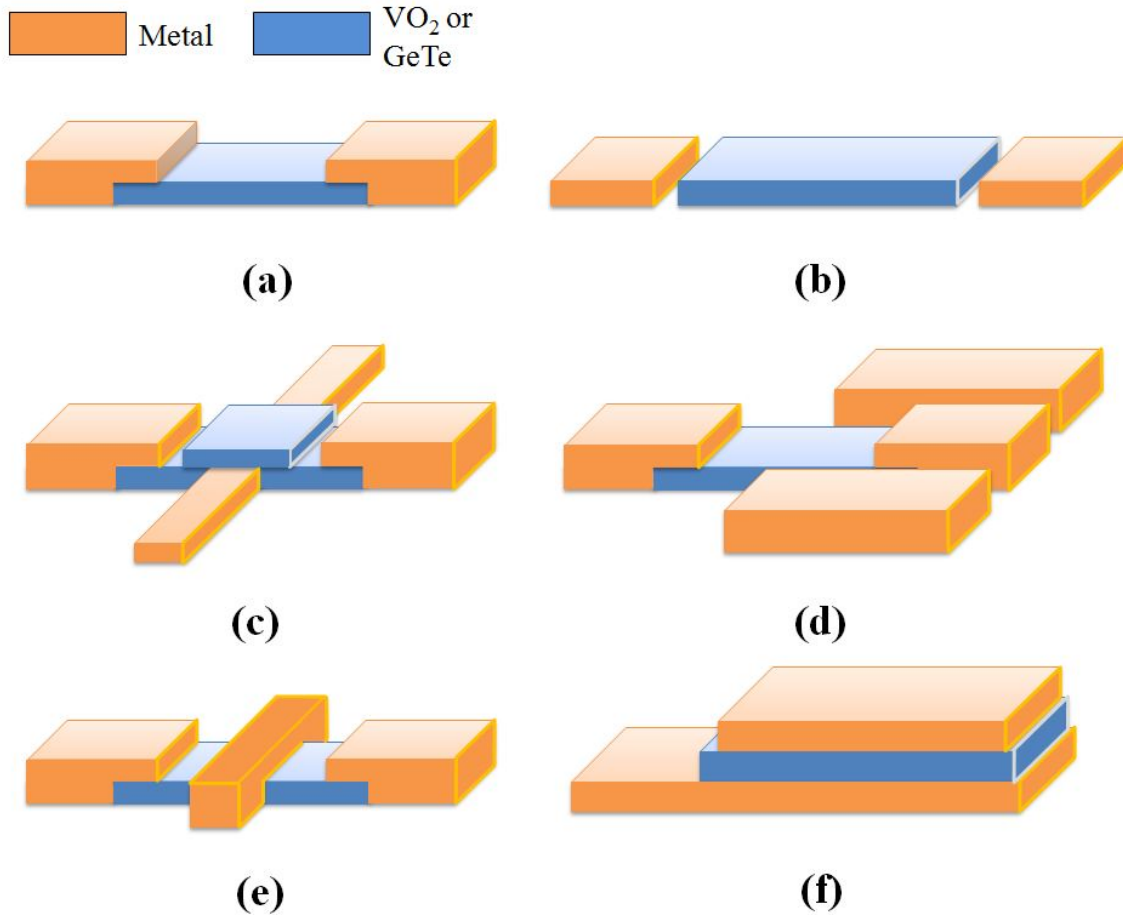


Figure 49. Six categories of devices designed to test the electrical and thermal characteristics of the active layer (VO_2 or GeTe). Each of these devices has seven variations in dimensions. Orange layers are metal (gold) contact pads and blue layers are the active layer. The categories are the following: (a) Simple resistor, (b) Resistor with gaps between contact pads, (c) Resistor with bottom heater, (d) RF switch, (e) Resistor with top heater, and (f) Capacitor.

3.3. Fabrication

All devices for this research were created from the same mask set. While the masks were designed for three-inch-diameter wafers, they were also used with two-inch-diameter sapphire (Al_2O_3) wafers. Three-inch substrate variations are crystal silicon (c-Si), silicon nitride (Si_3N_4) on c-Si, and silicon dioxide (SiO_2) on c-Si. For two-inch-diameter sapphire wafers, the alignment was done for the four reticles in the upper right corner of the nine reticles in Figure 47. Fabrication steps are detailed in the process

followers in the appendix. Standard lithographic procedures and thin film deposition were used. When starting with a blank wafer, the native oxide is removed by dipping in a buffered oxide etch (HF and H₂O); cleaning is done with rinsing of acetone, methanol, and water for 30 seconds each while spinning the wafer at 500 rpm; and drying is done with nitrogen. The masking material used for each of the three layers is Microposit S1818 photoresist whose nominal thickness was 1.8 μm when spun at 4,000 rpm for 30 seconds. This is a sufficient thickness for lift-off since the thin films deposited are no thicker than 0.2 μm . Lift-off is traditionally associated with metal evaporation because the sidewalls of the photoresist are deposited with a fairly small amount of metal (nonconformal step coverage). Lift-off can, however, be effectively used for sputtering when used in combination with sonification. Sputtered films conformally coat the sidewalls of the photoresist, so cracks in the film can be created by placing the sample in an ultrasonic bath. After applying and removing the tape for lift-off to remove metal on the surface, putting the wafer in the ultrasonic bath will create cracks in the sputtered film which permit the flow of acetone toward the photoresist. Ten minutes of sonification is sufficient for GeTe sputter deposition. The disadvantage of using this method is the presence of metal “wings” which form as a result of the coating of the sidewalls. These wings are small extensions of the metal at the edges of the three-dimensional metal volume. They are typically very small, but it is possible for them to touch other materials nearby.

The most complex fabrication consideration is the lithographic patterning of VO₂. 1818 positive photoresist is used as the masking layer for the devices, but because VO₂ must be deposited at temperatures well in excess of 1818’s boiling point of 145°C [143],

etch-back must be used instead of lift-off. Etch-back is the process of etching a film (patterning it) after it has been depositing on the wafer. This is completed in the following steps: Sputter VO_2 on the entire wafer, coat the wafer with 1818 photoresist, align and expose using an inverse of the mask used for lift-off, develop the photoresist, wet etch with diluted HNO_3 (nitric acid), and strip the photoresist. The bottom and top layers of metal can be deposited using normal lift-off procedure, as found in the process followers. It is evident that the procedure for VO_2 deposition is more complicated than standard lift-off; it also requires an etch study to be completed prior to fabrication. Gurvitch et al. [53, pp. 11-12] determined diluted nitric acid selectively etched VO_2 over aluminum (Al); to etch VO_2 and Al, they used a mixture of phosphoric, nitric, and acetic acids diluted in water (ratio of 16:1:1:2, respectively). In their paper, they do not include the etch rates. This etch study of VO_2 selective over Au was not performed in this research because stoichiometric VO_2 was never successfully deposited. Because the deposition of amorphous GeTe does not require substrate heating, those devices may be fabricated using lift-off.

3.4. Measurements of Devices

The measurement of resistance vs. temperature is fairly straightforward. The terminals of an ohmmeter are placed on either metal contact pad (Figure 50). Care must be taken to prevent oxidation of the probe tips at high temperatures; therefore, the probe tips are lifted from the devices immediately after each measurement. Temperatures are indicated on the open-loop temperature controller. Because the readings can be

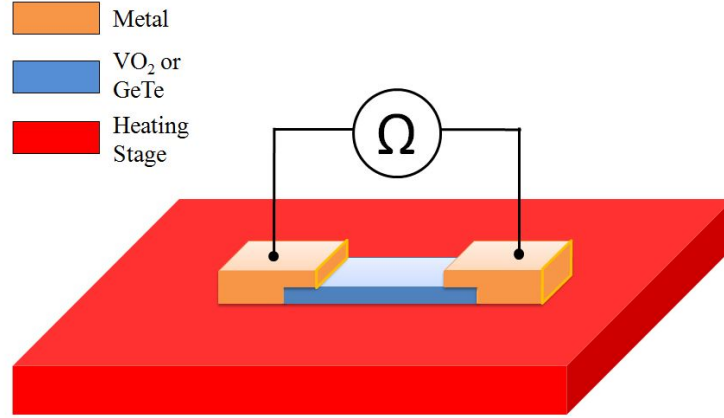


Figure 50. Measurement setup for resistance vs. temperature. The red platform represents the heating stage, through which heat is conducted by a ceramic plate. One reticle (multiple devices) is heated per measurement.

inaccurate, they were also recorded by an Agilent U1602B digital oscilloscope with a thermocouple attachment. Differences in temperatures of more than 30°C were observed between the controller and meter. The measurement of resistance, R , is related to the device's resistivity, ρ , as shown in equation 46. An additional R_c term can be added to include all contact resistances, such that

$$R = \rho \frac{l}{A} + R_c \quad (47)$$

Because the device dimensions are constant and reconfigurations in the volume due to a phase shift are negligible, resistivity can effectively be measured using a multimeter. Thickness can be measured with about 50 nm of accuracy with a profilometer and verified with an ellipsometer to approximately 1 Å. Resistivity is directly correlated to the atomic structure of the material (e.g., crystallinity), so these simple measurements are very valuable.

DC electrical measurements were also made on the probe station. The reticle is placed on the stage but not heated. Figure 51 shows the measurement scheme. The

resistance of the voltmeter in typical cases is considered to be extremely high and to have a negligible effect on current flow [144]. This was determined to be false for this research, however, because MIT materials and PCMs in their insulating state can have resistances as high as several $\text{G}\Omega$ (recall $1 \text{ G}\Omega = 1,000 \text{ M}\Omega$). Based on the slope of measured I-V curves (where the slope $R^{-1} = I/V$), the resistance of the voltmeter was determined to be approximately $10 \text{ M}\Omega$. Therefore, for devices with large resistances, the voltmeter was switched off before recording current data. In the case of two parallel resistances, the parallel resistance is calculated as the product of the resistances divided by their sum [136],

$$R_p = R_m \parallel R_d = \frac{R_m R_d}{R_m + R_d} \quad (48)$$

where R_m is the resistance of the meter and R_d is the resistance of the device under test. Table 6 shows the effect of the voltmeter on the parallel resistance. When VO_2 is in its monoclinic insulating phase or GeTe is in its amorphous phase, large ($\sim \text{M}\Omega - \text{G}\Omega$) values are expected. To switch off the voltmeter, one of the wires leading from the voltmeter to the device terminal is disconnected. This creates an open circuit in the upper branch of Figure 51, and all of the current flows through the lower branch.

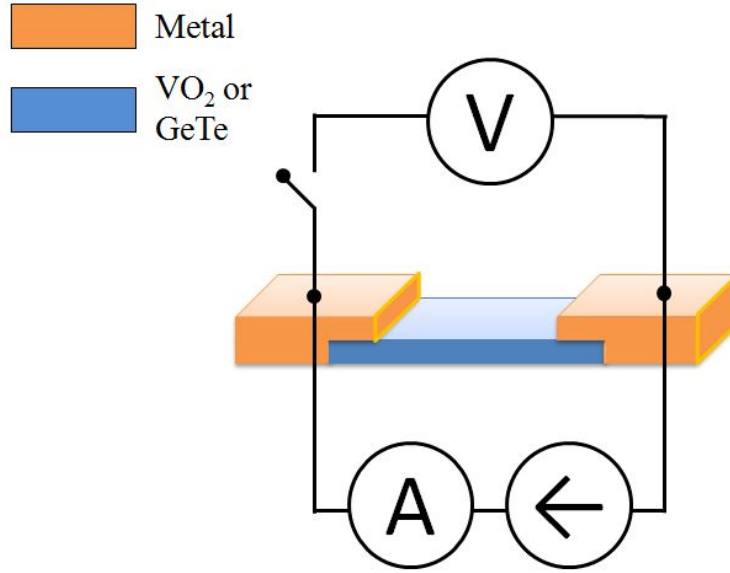


Figure 51. Instrumentation for two-terminal device, including a voltmeter (V), ammeter (A), and power source (\leftarrow). The voltmeter is switched off prior to measuring current. Depending on the resistance of the active layer, the power source is switched between constant voltage (CV) mode and constant current (CC) mode.

Table 6. Parallel resistance R_p for various resistances of voltmeter R_m and device resistance R_d . For less than ten percent error between R_d and R_p , R_d must be less than 1 M Ω .

R_m	R_d	$R_p = R_m R_d$
10 M Ω	1 G Ω	9.90 M Ω
10 M Ω	100 M Ω	9.09 M Ω
10 M Ω	10 M Ω	5 M Ω
10 M Ω	1 M Ω	909.1 k Ω
10 M Ω	100 k Ω	99.0 k Ω
10 M Ω	10 k Ω	9.99 k Ω
10 M Ω	1 k Ω	999.9 Ω
10 M Ω	100 Ω	100 Ω

Additionally, the small resistances of the device when in a conductive phase must be taken into account. Because the materials' resistivities drop by several orders of magnitude, too much of a voltage drop across the device could cause electrical or thermal

breakdown. In this case, a series resistance is used to help support the voltage drop. This setup is routinely used in memory applications to reduce a large voltage drop across a single memory cell [95].

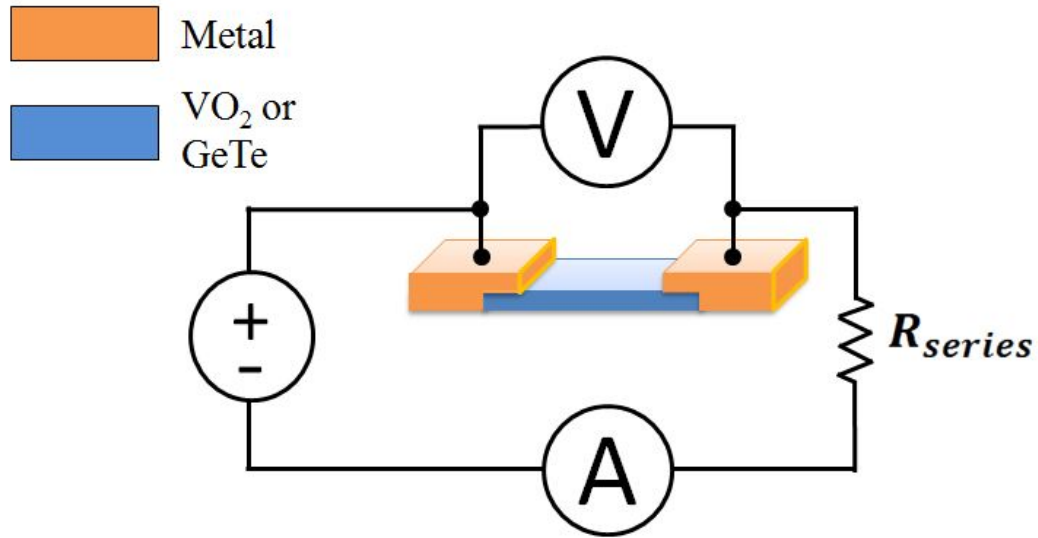


Figure 52. Implementation of a series resistor to reduce the voltage drop across the device under test.

A voltmeter in this case is not necessary, as the quantity $V_{series} = IR_{series}$ can be subtracted from the applied voltage. However, because most voltage sources only display one or two decimals, using the voltmeter provides more precise data. Using a voltmeter here has a negligible effect on the parallel resistance. The series resistance should be on par with the device under test when in its most conductive state (i.e., 1 – 10 k Ω).

Three-terminal devices are tested as well. These are not transistors; they are more akin to two stacked resistors. The additional resistor which lies across the active layer provides additional heating. Figure 53 depicts the measurement setup for a three-

terminal device. The idea is that the voltage across the device is stepped in small increments (e.g., 0.5 V) which is effectively sweeping the voltage, and the voltage for the additional heater is stepped in larger increments (e.g., 5 V). Therefore a family of I-V curves can be generated which test the effect of localized Joule heating.

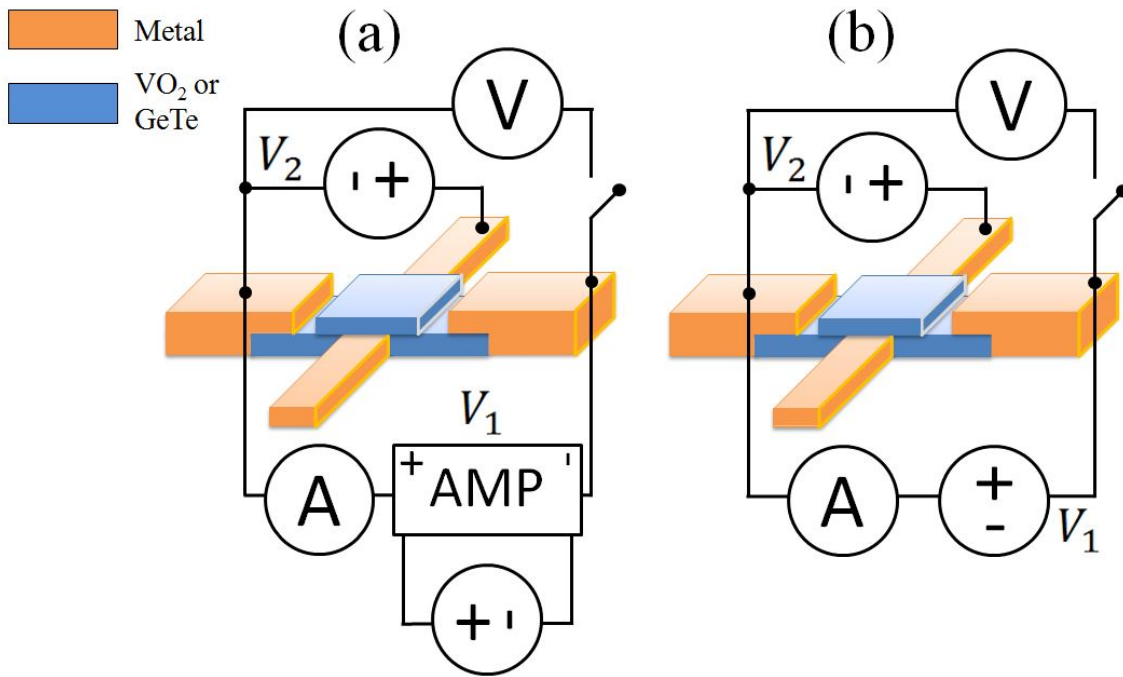


Figure 53. Instrumentation for measuring I-V curves on a three-terminal device. (a) Setup includes an amplifier and (b) Setup for when V_1 is large enough and an amplifier is unnecessary. The voltmeter (V) is open-circuited before measuring current.

Simple resistors and resistors with top/bottom heaters have the same dimensions with the exception of the extra heater. Figure 53(a) shows the instrumentation with an amplifier. There is no advantage to using an amplifier other than to reach high voltages which are otherwise unobtainable with power sources. When using the Agilent N5751A DC power source, however, the simpler configuration in Figure 53(b) can be used

because it is capable of 300 V, 2.5 A, and 750 W. This range is not exceeded when testing.

Capacitors shown in Figure 49(f) are tested by measuring the capacitance between the electrodes. They were designed in order to determine if the capacitance of the metal/PCM/metal system would change as GeTe changed phases. Recall that capacitance C is equal to

$$C = \frac{\epsilon_r \epsilon_0 A}{d} \quad (49)$$

where ϵ_r is the relative permittivity, ϵ_0 is the permittivity of free space, A is the overlapping area of the electrodes, and d is the distance between the electrodes [145]. Because the dimensions are constant, the change in capacitance would come exclusively from the change in the relative permittivity of GeTe between phases. Capacitance is measured vs. temperature.

RF switches are tested by measuring the S parameters with PNAs. The RF switch of Figure 49(d) comprises the RF network. Because this network is bi-directional, $S_{11} = S_{22}$, and because port 1 is considered the input port, the S_{12} term is neglected. The results contain data on S_{11} and S_{21} , to represent the reflection and transmission losses, respectively. In the case of VO_2 active layer, applied power is required to maintain its ON state; for GeTe, no power is required to maintain its state, only to switch between phases. For passive networks like RF switches, 0 dB corresponds to full signal transmission. The relationship between magnitude and decibels is listed in equations 38-41. The Agilent E5070B is used for 300 kHz – 3 GHz and the Agilent E8362C is used for 10 MHz – 20 GHz.

3.5. Materials Characterization

Testing of VO₂ and GeTe when deposited uniformly on a sample is referred to as materials characterization. Several characterization methods were used. The details of each were discussed in Chapter 2.

Figure 54 shows the entire electromagnetic spectrum with the exception of gamma rays (beyond x-rays) and frequencies between DC and the shorter portion of Long Waves (DC to 1 kHz). X-rays and gamma rays can be harmful due to their intense energies and are not usually involved in the characterization of materials. The longer wavelengths (DC to MHz) are typically used to test and operate electronic circuits. Most of the devices presented here were tested with DC power and heat, with the exception of RF switches. The majority of the characterization methods lie in the optical portion of the spectrum. The relationships between energy, frequency, wavelength, and wavenumber are listed in equations 42 – 45.

The major portions of the electromagnetic spectrum not covered with a characterization method are the far infrared (FIR), and extremely high frequencies (EHF) within the microwave spectrum, both of which are adjacent to THz. FIR was accessed by using Fourier transform infrared (FTIR) spectroscopy, but an FTIR system that covers the FIR spectrum is not readily available. For EHF, S parameters may be measured with PNAs—as with the rest of microwave and RF—but a system that covers that range was not accessible either.

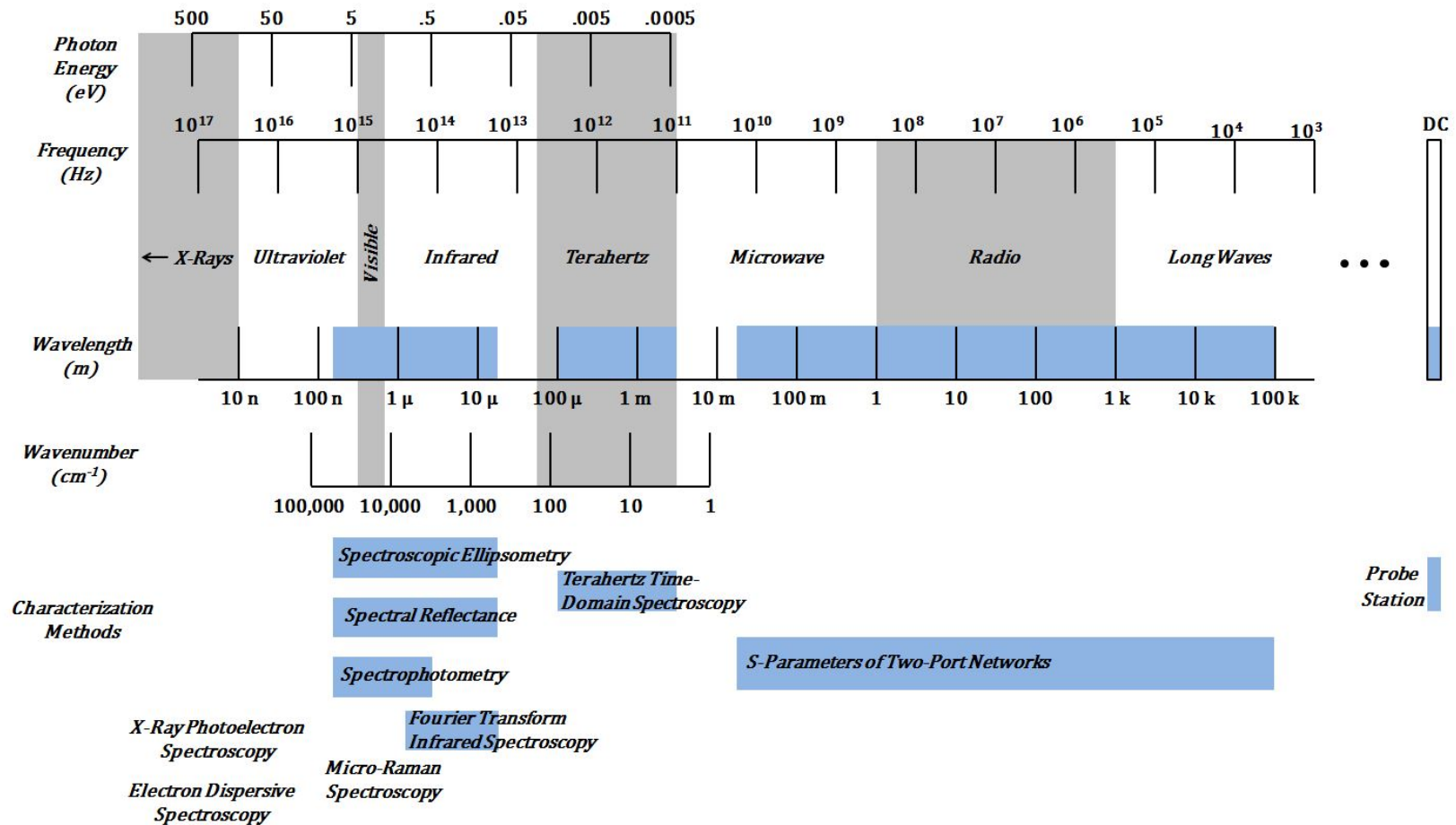


Figure 54. Electromagnetic Spectrum. Blue regions indicate portions of the spectrum used in this research for characterization of materials. The characterization methods are listed at the bottom of the figure. Those methods which do not correspond to a specific portion of the spectrum (XPS, EDS, and Micro-Raman) are listed at the very bottom, roughly correlated to their characteristic energies.

Table 7 lists the materials characterization methods used, which are dependent on the deposition process. For instance, the deposition of VO₂ is complex so materials characterization methods were used to determine the resultant stoichiometry. In the case of GeTe, the deposition is much simpler: A GeTe target is used without reactive gases and substrate heating, so measuring the stoichiometry is not critical to its use. The only methods not listed in this table are the probe station for testing devices and RF S parameters for RF switches.

Table 7. Materials characterization systems used

Method	System	VO ₂	GeTe
Probe Station	Micromanipulator	x	x
EDS	Hitachi SU-70 SEM	x	
XPS	Physical Electronics 5702	x	
Micro-Raman	Horiba LabRam HR 800	x	
Spectroscopic Ellipsometry	Horiba UVISSEL 2		x
Spectral Reflectance	Filmetrics F20-UV		x
Spectrophotometry	Cary 5000		x
FTIR	Bomem MB-157		x
THz-TDS	TeraView TPS Spectra 3000		x

The probe station is primarily used to test devices, but it can also be used to estimate sheet resistance and to determine T_{MIT} for VO₂ and T_c for GeTe. Because the measured resistance drops by several orders of magnitude across the phase transition, the transition temperature can be measured by placing the probe tips at equidistant spacing for all measurements.

Fairly little is known about chalcogenide materials in the THz regime. This research studies the broadband absorption of GeTe in the THz wavelengths while heated. Because GeTe is nonvolatile, *ex-situ* measurements (before and after) of transmission are possible; however, to determine the rate at which it turns opaque to THz wavelengths, *in-situ* measurements are preferred. Transmission and absorption are measured throughout the phase change. The TeraView TPS Spectra 3000 has a sapphire-doped titanium pulsed laser with a spectral range of 0.06 THz to 4 THz. Additionally, there are inherently some losses, chief among them being reflections between the boundaries of the substrate (etalon effects), which reduce the resolution and spectral bandwidth.

This research uses the Cary 5000 spectrophotometer and Bomem 157 Fourier transform infrared (FTIR) spectrometer. The spectral range of the Cary 5000 is 200 nm to 3 μm and the Bomem's is 3.8 cm^{-1} to $7,900\text{ cm}^{-1}$ or 2.59 mm to 1.27 μm , respectively.

Spectroscopic Ellipsometry (SE) measures the reflection coefficients and phase difference of incident and reflected light across a broad (spectroscopic) spectrum. Intense computations are required to convert the measured I_s and I_c data to model material thickness, bandgap energy, index of refraction, and extinction coefficient. Even more computation can be applied in the Classical model to estimate carrier density and carrier mobility as a quasi-replacement for Hall Effect measurements [146]. Additionally, the output data (thickness, refractive index, extinction coefficient, bandgap, etc.) can be mapped across an entire wafer to characterize the deposition system. Each model has an associated goodness of fit, χ^2 . Vastly different results may be obtained using slightly different models, so a fairly accurate estimate of the output variables must be known prior to testing. In this research, GeTe was analyzed *ex-situ* using SE. In its

amorphous and crystalline phases, Tauc-Lorentz and Classical models were used, respectively.

3.6. Considerations when using a Probe Station

When using the Micromanipulator probe station, accurate measurements of resistance vs. temperature can be recorded fairly easily. With that being said, there are many ways to obtain errant data. The following procedures were used based on lessons learned during this research. All of these points apply specifically to using a probe station, but some can apply to any measurement.

1. Only touch the samples with gloved hands. Oils are easily transmitted from the skin and are difficult to remove.
2. Some probes are packaged in cases with adhesive. This adhesive may be difficult to remove and be a barrier to ohmic contact between the probes and probe holders. Use the probes not packaged in adhesive, if possible.
3. Before making measurements, always perform a check using a calibration standard. Checking the resistance of a wafer coated with an aluminum film is a good procedure before collecting data.
4. Probe tips oxidize at high temperatures. When making high temperature measurements, touch the probes to the sample only long enough to make a measurement, and then elevate the probes off the surface of the sample. This is a concern for temperatures exceeding 100°C for periods longer than several minutes.

5. Temperature measurements are time intensive. Letting the system stabilize at the desired temperature can be a long process. Plan ahead and limit the data points to a minimum number required. Use large step sizes when possible and reduce the step size when there may be a rapid response to the applied heat.
6. Temperature equipment is difficult, if not impossible, to calibrate to absolute accuracy. There is inherently some small error in temperature measurements. Confidence should be placed in equipment that is new. Always measure temperature with multiple instruments when possible.
7. Always question the validity of every measurement. With the correct procedures, it should be possible to prove the validity of the measured data.

3.7. Sputtering Experiments

As mentioned previously, the deposition of stoichiometric vanadium dioxide is somewhat complex. As this had never been successfully accomplished at AFIT, a thorough experiment had to be accomplished to determine the exact sputtering parameters. The research accomplished determined parameters as a baseline, and from there, the parameters were varied. It is important to note that a quantity reported in an experiment from one researcher may be different than another due to different equipment, calibration, and experimental conditions. Therefore varying parameters within a small window is necessary to hone in on what is successful with the equipment in the cleanroom at AFIT.

The parameters are listed in Table 8 according to run/experiment number. In order to keep the parameters within a tolerable limit, the following were held constant:

Vanadium target, DC power, 10 μ Torr chamber pressure, 10 mTorr (1.33 Pa) gas pressure, and use of oxygen gas (reactive sputtering). Substrate temperature, oxygen partial pressure, and thickness were varied, as indicated in the table. Either DC or RF power could be used for the vanadium target since it is conductive, but DC was chosen because more researchers had had success with DC sputtering. The trade-off with using DC sputtering is that its deposition rate is slower at any given power.

Table 8. VO₂ sputtering experiments

Run	Temp (°C)	O ₂ (%)	O ₂ /Ar (sccm)	Thickness (nm)	Notes
1	450	7.8	2.0/23.6	200	Vary thickness at 450°C and 7.8% O ₂
2	450	7.8	2.0/23.6	300	Vary thickness at 450°C and 7.8% O ₂
3	450	7.8	2.0/23.6	400	Vary thickness at 450°C and 7.8% O ₂
4	550	7.8	2.0/23.6	200	Higher temperature; vary thickness
5	550	7.8	2.0/23.6	300	Higher temperature; vary thickness
6	550	7.8	2.0/23.6	400	Higher temperature; vary thickness
7	450	8.8	2.0/20.7	200	Higher oxygen partial pressure
8	450	8.8	2.0/20.7	400	Higher oxygen partial pressure
9	450	7.8	2.0/23.6	200	Investigate temp; chamber reached 117°C
10	450	6.0	2.0/31.3	200	Lower oxygen; rule out O ₂ dependence
11	450	7.8	2.0/23.6	200	Substrate temp between 288 and 302°C
12	450	7.8	2.0/23.6	200	Substrate temp between 302 and 343°C
13	550	7.8	2.0/23.6	200	6" wafer platform; substrate temp greater than 510°C

In addition to these varied parameters, multiple substrates were used. For each run, substrates of crystal silicon (c-Si), silicon nitride (Si₃N₄) on c-Si, and silicon dioxide

(SiO₂) on c-Si were used to investigate if one type of substrate was better than the others. Quality in this case would pertain to the amount of modulation of resistance between insulating and metallic phases, lower transition temperature, and less hysteresis. The c-Si substrates are 500 μm thick, lightly doped n or p type, and single-sided-polished (SSP); Si₃N₄ films are stoichiometric films on the same silicon wafers, deposited by PECVD, and are 100 nm thick; and silicon dioxide SiO₂ films are thermally oxidized (dry) at 1,000°C, 1 atm, and are approximately 300 nm thick. These substrates were labeled on the backs of the samples as *a*, *b*, and *c*, respectively, with a diamond scribe. Many researchers have achieved the best results with sapphire substrates due to its high electrical resistivity; however, sapphire wasn't used in these experiments because it is expensive. If a stoichiometric thin film were deposited, then sapphire would be used at the conclusion of the experiment to compare to the other substrates.

3.8. Testing Methodology

This section lists the completed measurements. The results in the next chapter are organized in the same structure as this section. As mentioned previously, care was taken to correctly determine the deposition parameters for stoichiometric VO₂. The testing on VO₂ is primarily materials characterization for this purpose. In the case of nonvolatile GeTe, the testing is either completed *in-situ* with respect to temperature or *ex-situ* in the amorphous and crystalline phases but not throughout the phase transition.

a. VO₂

1. Resistance vs. temperature and determination of T_{MIT} on uniformly coated samples, based on varied sputtering parameters

2. EDS
 3. XPS
 4. Micro-Raman
- b. GeTe
1. Resistance vs. temperature for simple resistors and determination of T_c (*in-situ*)
 2. Phase transitioning by applying power pulses to simple resistors (*in-situ*)
 3. I-V curves for simple resistors and top/bottom resistors (*in-situ*)
 4. Capacitance vs. temperature for capacitors (*in-situ*)
 5. S parameters for RF switches in amorphous and crystalline phases (*ex-situ*)
 6. Determination of T_c for varied thicknesses for uniformly coated samples (*in-situ*)
 7. THz transmittance and absorbance vs. temperature (*in-situ*)
 8. SE in amorphous and crystalline phases (*ex-situ*)
 9. Spectral reflectance in amorphous and crystalline phases (*ex-situ*)
 10. Spectrophotometry and FTIR in amorphous and crystalline phases (*ex-situ*)

3.9. Summary

In this chapter, the design, fabrication, and testing of devices were presented. Additionally, the methodology of materials characterization methods was discussed. Finally, the specific measurements were listed, for which the data will be presented in Chapter 4.

4. Results

4.1. Introduction

This chapter presents data acquired in the experiments discussed in the previous chapter. The data are analyzed in Chapter 5.

The deposition of stoichiometric VO_2 and GeTe is critical to the experimentation in this thesis. Research of vanadium oxide thin films began with a study of deposition methods, in particular reactive sputtering, which were discussed previously in detail. Sputtering was chosen as the best method of depositing VO_2 and GeTe in AFIT's cleanroom due to the availability of equipment, DC and RF methods, V and GeTe targets (both 99.999% pure), and oxygen and argon gases (reactive sputtering). In order to precisely determine the correct parameters for VO_2 deposition, sputtering experiments were conducted, which are presented in the next section. There were several materials characterization tests performed on VO_x thin films in order to provide feedback on the deposition. Because a stoichiometric $\text{Ge}_{0.5}\text{Te}_{0.5}$ target and argon is used when sputtering, deposition of GeTe is considerably simpler than for VO_2 . The SEM capture in Figure 55 shows the fabricated devices and their scale.

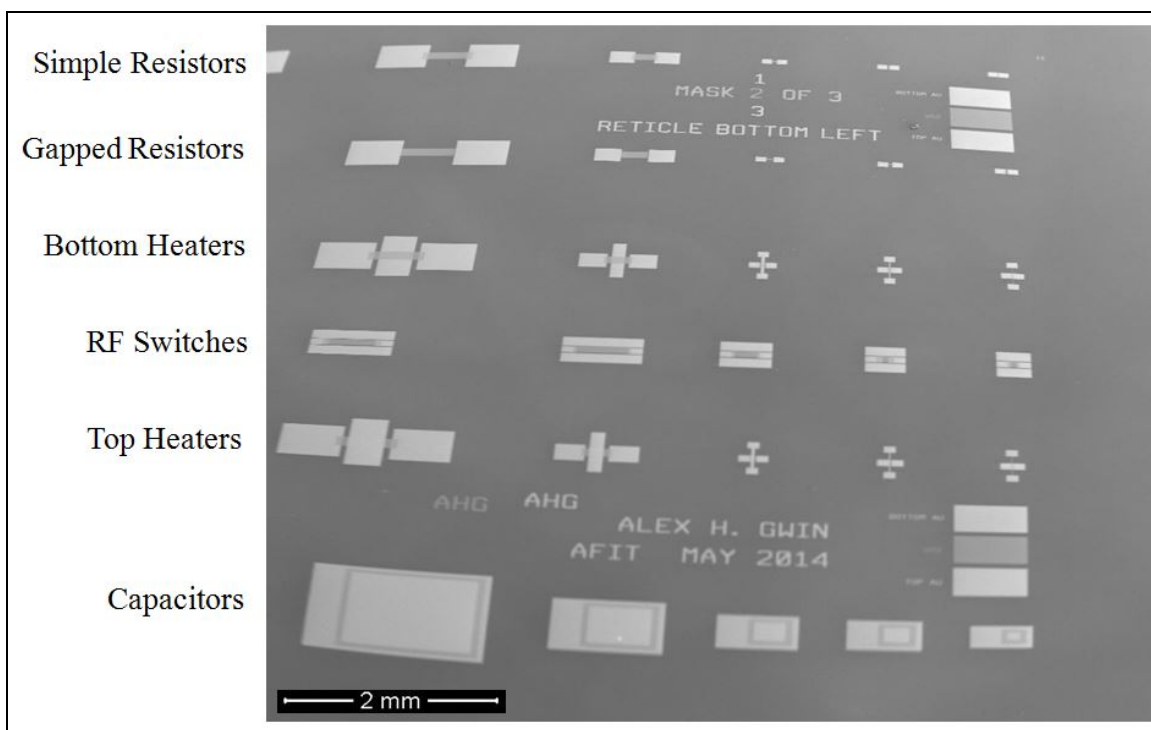


Figure 55. Wide-angle SEM capture of fabricated devices; each category of devices is listed on the left-hand side of the figure.

4.2. Vanadium Oxide

4.2.1. Resistance Measurements

The basic approach of measuring the change of resistance in VO_2 thin films is displayed in Figure 50 and Figure 52. The first and simpler approach is to measure the resistance with an ohmmeter as the sample is heated underneath by a heating stage. The second approach is to measure voltage and current with a series resistance. The voltage/current method was used when the heater on the probe station was undergoing maintenance at the beginning of the research. When using this method, the resistance of the thin film is then calculated based on the measured values. Series resistances are necessary when applying large voltages across thin films to help support the voltage load.

In addition to increasing voltage, experiments were also completed with elevated temperatures. The samples were heated conductively with a hot plate to approximately 45°C (accuracy of approximately 10°C). As discussed in chapter 2 in the experiment by Mun et al., MIT can be achieved with lower voltages by heating VO₂ to some temperature below its T_{MIT}.

The resistance data as a function of applied voltage is presented in Figure 56. Most samples showed little to no increase in electrical conductivity, with the exception of sample 1c.

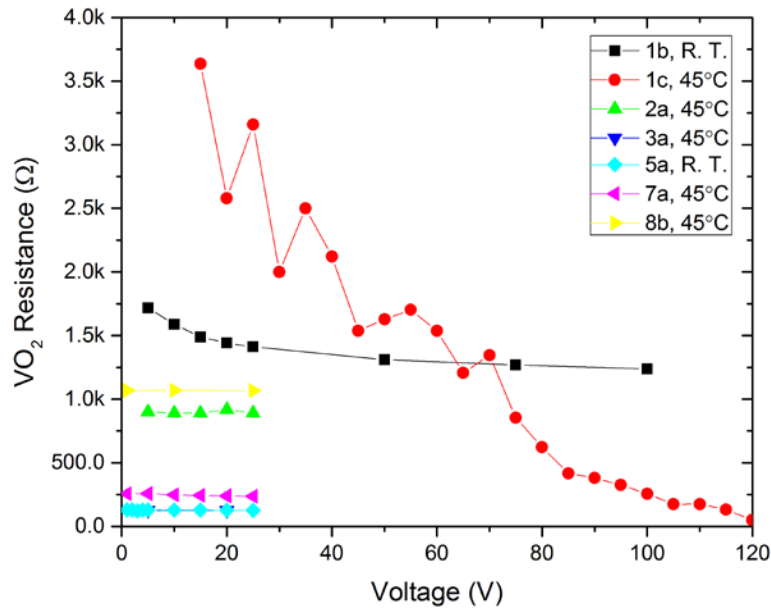


Figure 56. Change in resistance for several VO₂ thin films. The current through the VO₂ thin film and voltage across it are measured, and resistance is calculated from these values. The probe spacing is held constant within each trial.

Based on the results of sample 1c, devices were made with the parameters of run 1. However, all devices were metallic, and any application of voltage only increased the resistance rather than decrease it.

In run 13, vanadium oxide was deposited at substrate temperatures in excess of 510°C on the three types of substrates. These were tested on the Micromanipulator probe station using an ohmmeter. At a probe tip spacing of 15 μm , all three samples had resistances of approximately 120 Ω regardless of temperature. Temperature was tested at R. T., 50°C, 75°C, and 100°C.

4.2.2. EDS

Partially due to the lack of results from resistance measurements and also for the sake of thoroughness, in-depth materials characterization for the thin films was launched in the form of EDS, XPS, and Micro-Raman. These studies were conducted in parallel to the resistance measurements to save time. All three methods tested the same three samples, in case one or more methods were unsuccessful in determining the VO_x stoichiometry. These samples are 5a, 11a, and 12a. Silicon (“a”) was chosen as the substrate for all three to reduce any unnecessary data from the nitrogen or oxygen in the dielectrics. Based on the results from materials characterization, the sputtering parameters would then be adjusted to compensate for errant parameters.

Samples 5a, 11a, and 12a were chosen because they were deposited using the same oxygen partial pressures but different substrate temperatures. The potential problem of the substrate not being hot enough was identified in run 9, and was suspected of being the main reason for the poor resistance measurements. Therefore, EDS, XPS, and Micro-Raman were used to not only identify the O:V ratio but also to identify the stoichiometry difference due to substrate temperature.

EDS was accomplished first, in order to determine the O:V ratio in the sputtered thin films. Ideally, this ratio would be 2.0 in stoichiometric VO_2 . The analysis was completed with a Hitachi SU-70 SEM with EDAX software. The source voltage was 5.290 keV.

Below are two plots from the SEM/EDS system for sample 5a. Figure 58 presents a closer view of the V $L\alpha$ and O $K\alpha$ peaks at approximately 0.5 eV. As can be seen from the second figure, there is a blending of peaks from the V $L\alpha$, V $L\beta$, and O $K\alpha$ peaks. This analysis will be discussed in more detail in the next chapter. The EDS experiments were stopped after the first sample due to these blending of peak intensities.

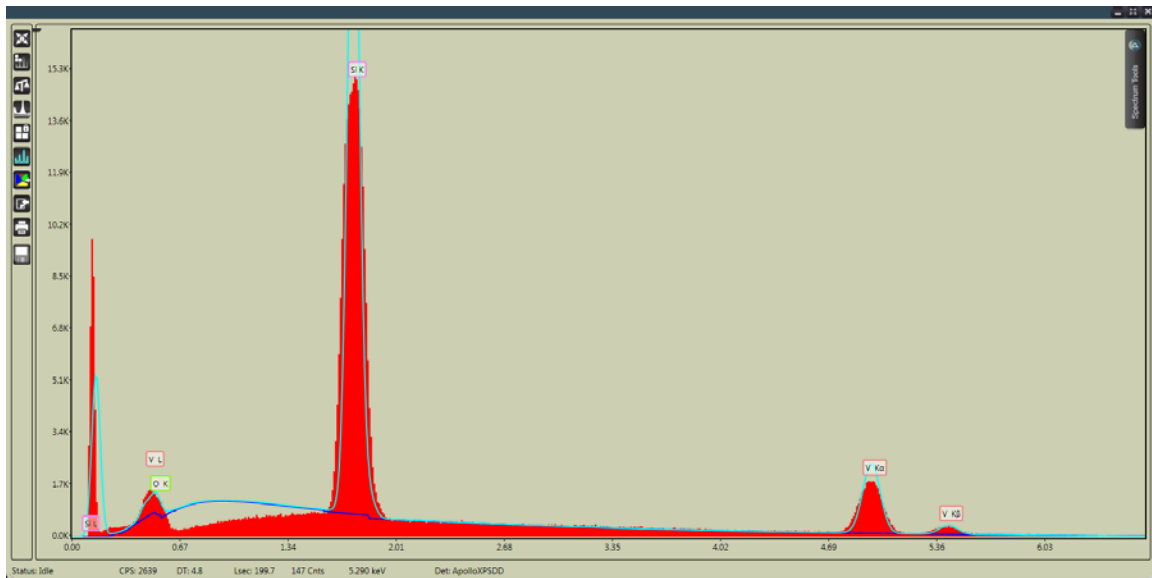


Figure 57. EDS measurement of sample 5a from 0 to approximately 7 eV.

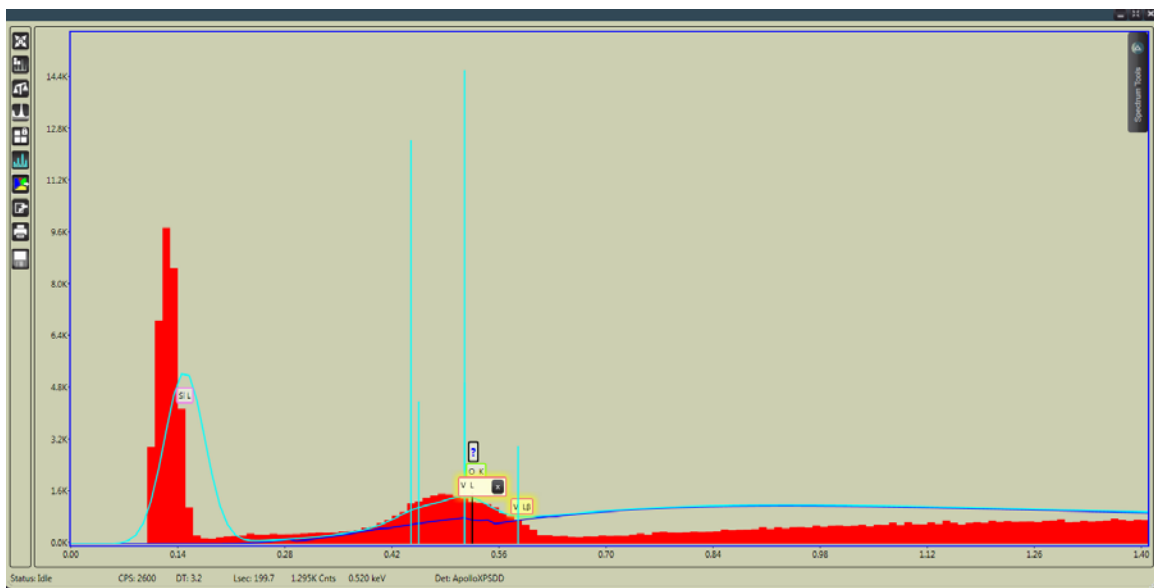


Figure 58. EDS measurement of sample 5a; closer view of the 0 to 1.4 eV range.

4.2.3. XPS

The next method used was XPS. The spectrometer was pumped to an ultra-high vacuum (UHV) of $1 - 2 \times 10^{-9}$ Torr. A monochromatic Al K α x-ray source (1,486.6 eV) was operated at 75 W (15 kV and 5 mA). The hemispherical analyzer was oriented 45° to the sample's normal. Data was collected from -5 to 1,200 eV in steps of 0.8 eV with a dwell time of 20 ms. V 2p and C 1s regions were fitted with a Gaussian-Lorentzian function with a 30% Lorentz contribution.

The following three XPS plots correspond to the detected photoelectrons plotted vs. binding energy. Corresponding angular momenta and VO_x phases are listed above the peaks. The XPS plots are focused on the vanadium and oxygen peaks between 510 and 535 eV. Sample 5a has two oxygen 1s components. In this sample, the carbon-oxygen contribution is more significant than the other two samples. Therefore approximately half of the oxygen in the sample is bonded in organic compounds rather than vanadium

oxide. For samples 11a and 12a, components of both V_2O_5 and V_2O_3 are present in the sample as well as vanadium. The stoichiometry is closer to V_2O_3 than V_2O_5 . In sample 12a, there is the presence of what may be a suboxide, which is V_xO_y with a y:x ratio of less than 3:2. Suboxides typically have lower binding energies than the stoichiometric compounds because of their lower oxidation state [147].

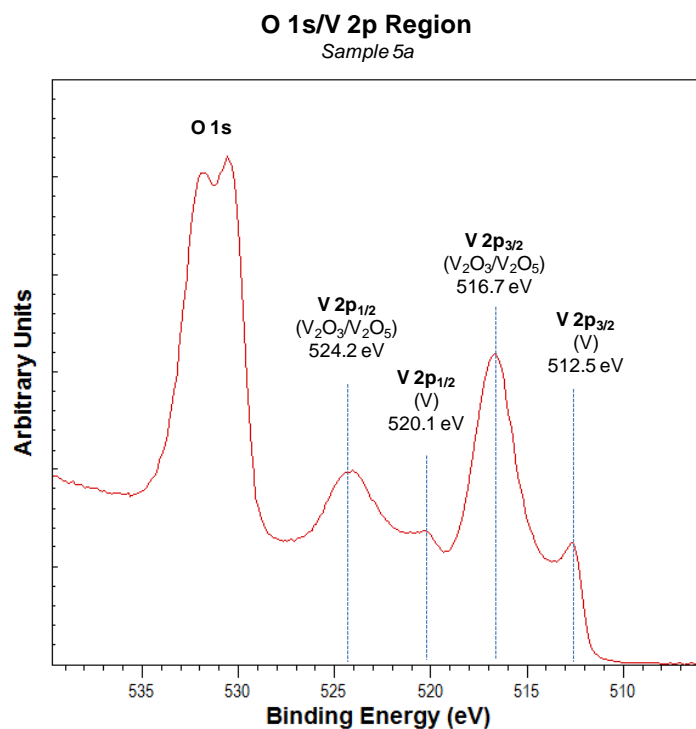


Figure 59. XPS plot of sample 5a.

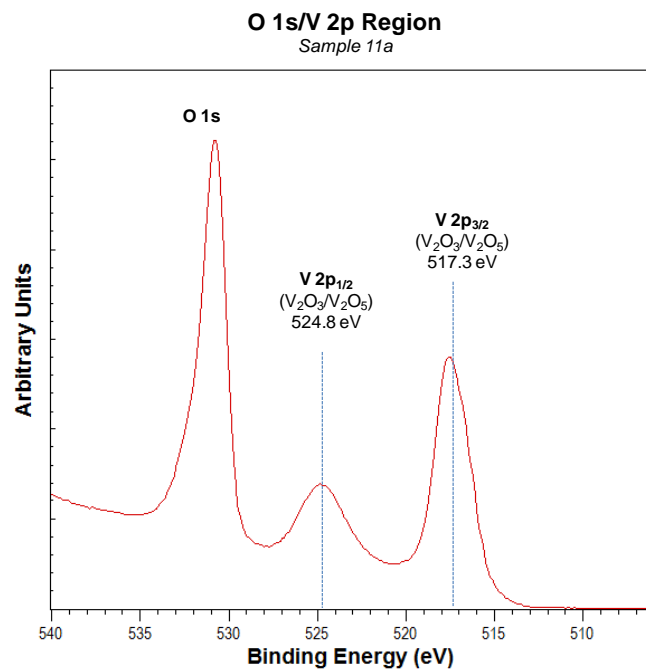


Figure 60. XPS plot of sample 11a.

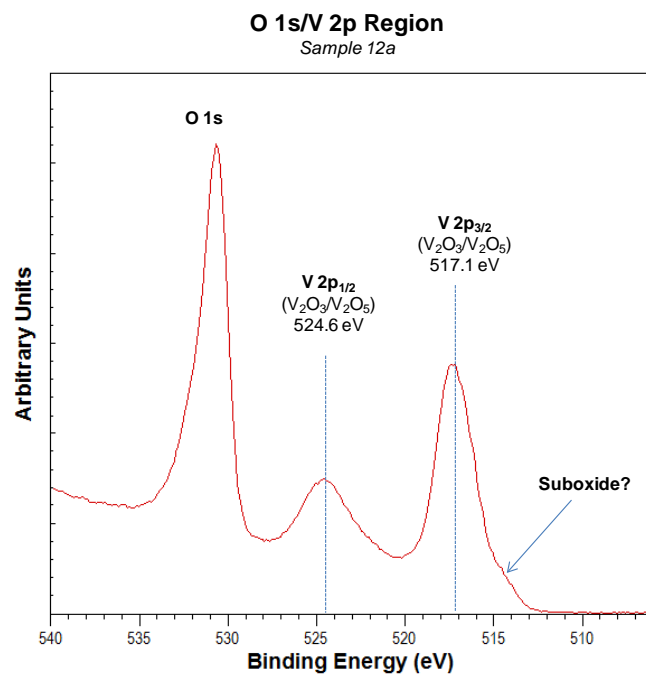


Figure 61. XPS plot of sample 12a; suboxide is V_xO_y with y:x ratio of less than 3:2.

4.2.4. Micro-Raman

Micro-Raman spectroscopy tests were completed on three samples with He-Ne optical sources of 532 nm and 633 nm with spot sizes of approximately 1 μm in diameter. The resolution is approximately 1 cm^{-1} based on 600 grooves per mm and a 300- μm confocal hole. The detector was a thermoelectric-cooled charge coupled device (CCD) with $1,024 \times 526$ pixels. The results from the 633-nm laser gave results which had better defined peak intensities than the 532-nm source. For comparison, several 532-nm results are displayed below in Figure 62.

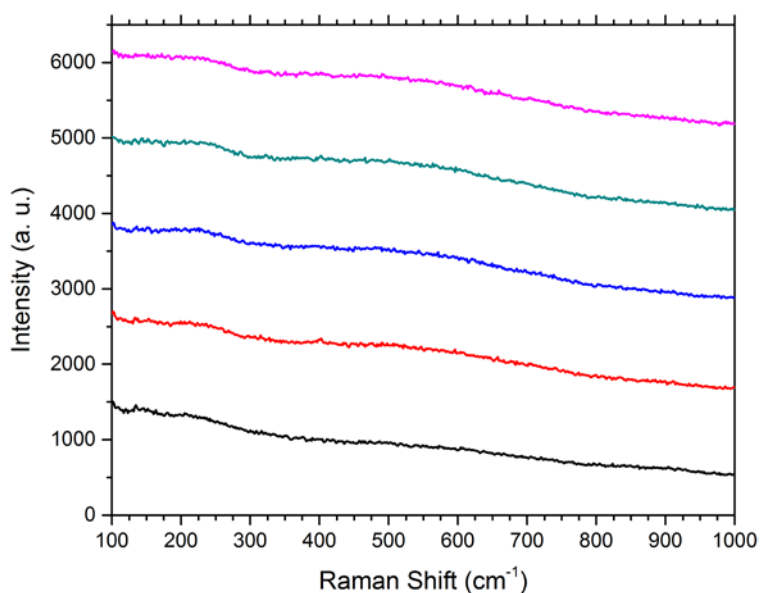


Figure 62. Several Raman spectra of sample 1 excited by a 532-nm laser.

The peak intensities are not very well defined. On the other hand, the 633-nm laser produced excellent results, as shown in the following three plots. By comparing the wavenumber of each peak with those of vanadium oxides in the literature, the phase of

vanadium oxide for each sample should be able to be estimated. As a point of reference, the Raman shift of c-Si is approximately 520 cm^{-1} [148].

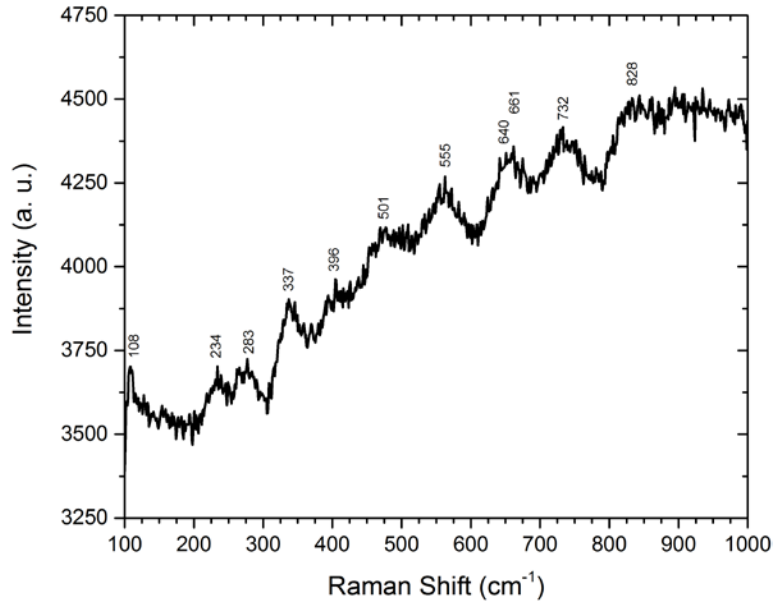


Figure 63. Raman spectra of sample 5a excited by a 633-nm laser.

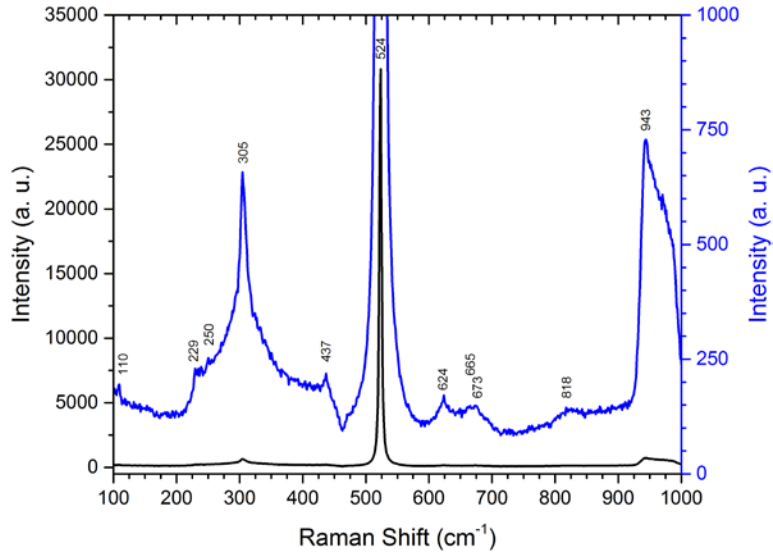


Figure 64. Raman spectra of sample 11a (633-nm laser). The blue and black spectra are the same data set with different magnifications. Because the silicon peak (524 cm^{-1}) is so strong in the black spectra, the other peak intensities are very small by comparison. The intensity range from 0 to 1,000 is magnified for the blue spectra. This aids in identifying the peaks.

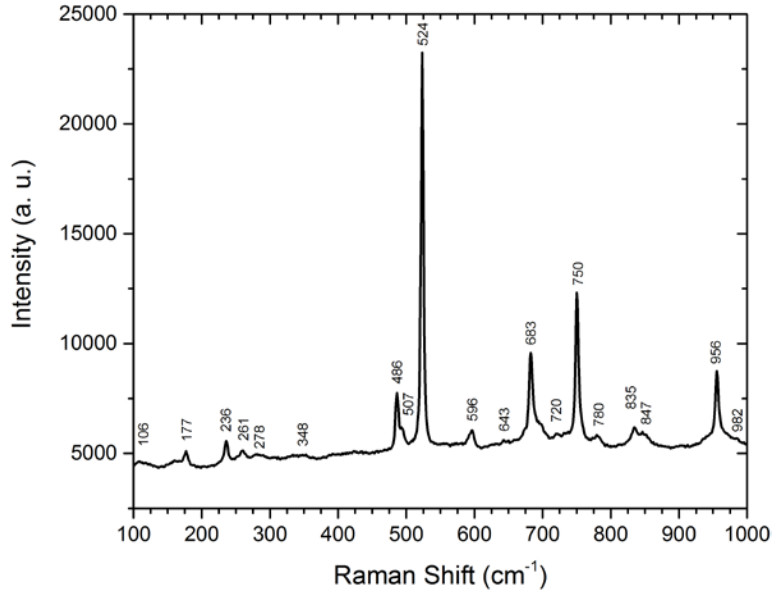


Figure 65. Raman spectra of sample 12a (633-nm laser).

4.3. Germanium Telluride

4.3.1. Resistance Measurements

Resistance measurements were collected on the simple resistors. Within each substrate, all resistors behaved similarly, with the exception of the resistance values. For instance, the resistance of the largest resistor is greater than the smallest, but they crystallize at the same temperature and have the same rate of resistance decrease. The smallest resistors were difficult to align, and some substrates did not have these devices aligned. The third smallest resistors typically had room temperature (R. T.) resistances on the order of $G\Omega$ or too high to be measured by the multimeters. Therefore the second smallest resistors were chosen as the main device used to experiment with resistance vs. temperature among the various substrates.

Figure 66 shows the resistance vs. temperature data for GeTe devices on four different substrates. C-plane (0001) sapphire (Al_2O_3) was used in GeTe deposition in addition to the other three substrates.

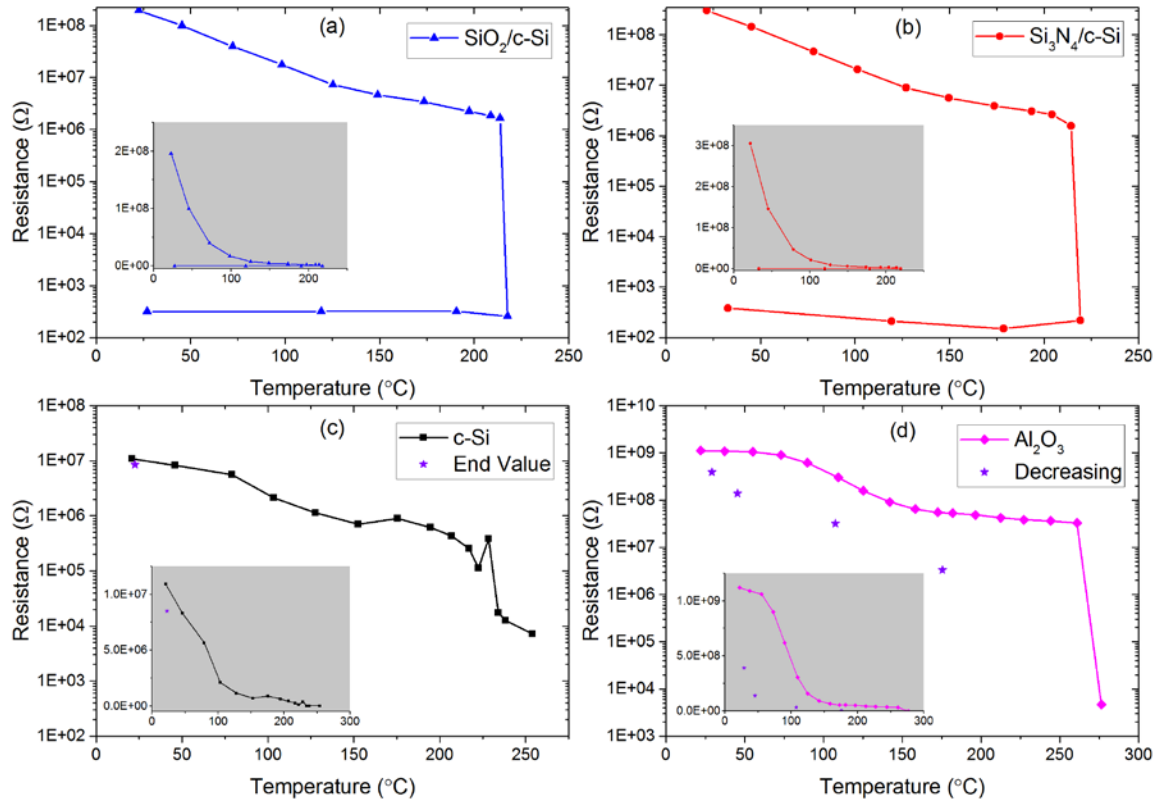


Figure 66. Log plots of resistance vs. temperature with linearly scaled inset plots: (a) GeTe on $\text{SiO}_2/\text{c-Si}$ substrate, (b) GeTe on $\text{Si}_3\text{N}_4/\text{c-Si}$ substrate, (c) GeTe on c-Si substrate, and (d) GeTe on (0001) Al_2O_3 substrate. The top plots show a nonvolatile change in resistance indicative of permanent crystallization, while the bottom plots show a volatile transition.

4.3.2. Application of Voltage Pulses

As mentioned previously, voltage pulsing the phase transition in chalcogenides is somewhat simpler from amorphous to crystalline than from crystalline to amorphous. This is primarily because the material does not need to be heat quenched above its

melting temperature. Therefore in this experiment, the as-deposited amorphous films incorporated into the devices were left in the amorphous state. If voltage pulsing were successfully completed from amorphous to crystalline, at that point attempts would be made to reverse the phase change with reset pulses.

Set (crystallization) pulsing was attempted with a waveform generator on simple resistors and top/bottom heater resistors of all sizes. The waveform output was fed into an oscilloscope in order to verify the generator's settings. The maximum output voltage amplitude is 10 V, and the minimum pulse width is 5 ns. Typically, set pulses are 1 – 2 V, 80 ns in duration, and 5 ns rise/fall times. The experiments on the devices were conducted with the following varied parameters: Amplitudes of 0.5 – 10 V, pulse widths of 5 ns – 10 μ s, and rise and fall times of 5 – 20 ns. The waveform was triggered manually. Success of the experiment was determined by a significant (greater than one order of magnitude) change in resistance. The resistance of the device was measured before and after each pulse with a multimeter. The attempts to crystallize the resistors were unsuccessful, most likely due to an insufficient amount of Joule heating.

4.3.3. I-V Curves

I-V curves were generated on simple resistors and top/bottom heaters. For the simple resistors, no negative differential resistance was detected for sizes 3 – 7. In these devices, the I-V curves were linear. For the two smallest simple resistors, I-V curves showed negative differential resistance. Figure 67 shows the I-V curves generated on the second smallest resistor, with the exception of the sapphire plot (lower right). On the

sapphire substrate, the devices have such high resistance that no measurable current flows in any dimensions except the smallest one.

In these experiments, the resistance of the resistor is initially very high on the order of hundreds of M Ω . The power source starts in constant voltage (CV) mode. As the voltage is incremented, the current increases exponentially as seen by the straight line in log plot of Figure 67(a). As the resistance decreases to the point that it is near the threshold voltage (indicated by V_t), the resistor has reduced its resistance to the point that

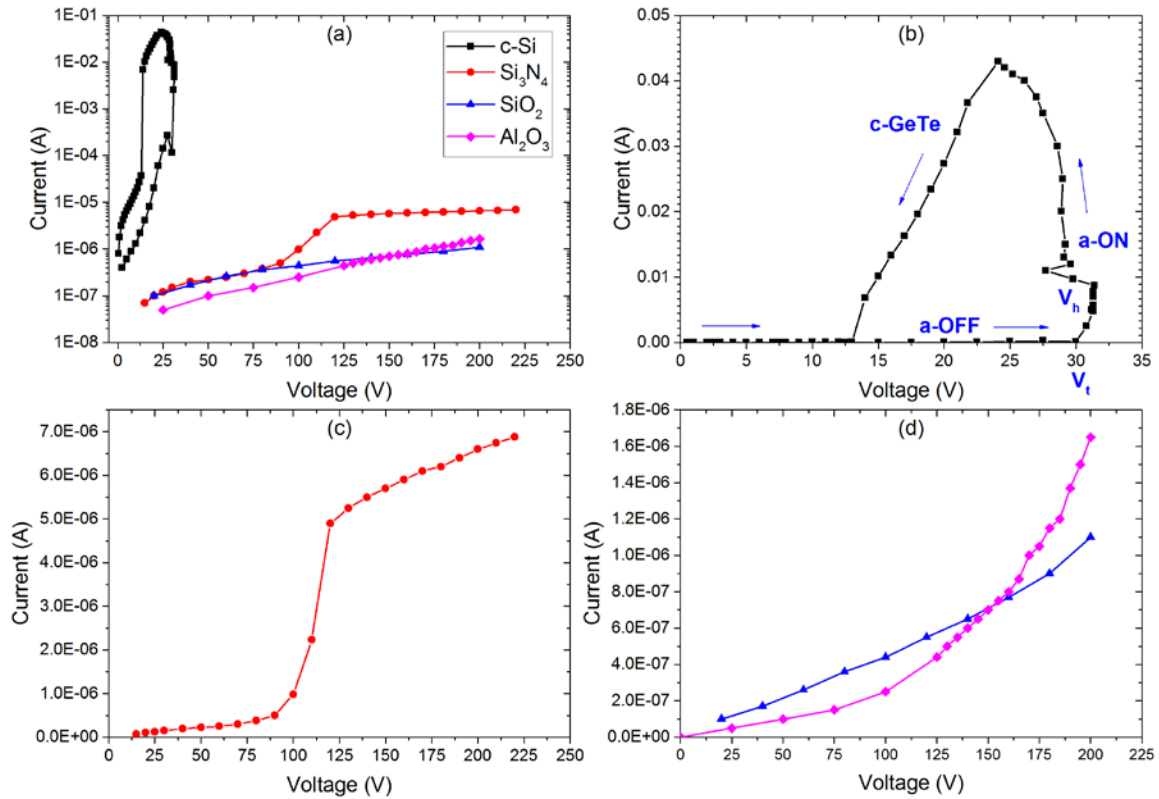


Figure 67. Measured I-V curves for amorphous GeTe thin films in simple resistors (second smallest) on various substrates: (a) Log plot of all four I-V curves for comparison, (b) Memory curve of GeTe on c-Si substrate showing amorphous ON and crystallization, (c) GeTe on Si_3N_4 /c-Si substrate, and (d) SiO_2 /c-Si and Al_2O_3 plots which do not reach an amorphous ON state. The PCM cell on Al_2O_3 is shown in Figure 1(b) whereas all others are 1(a); no current could be measured on Al_2O_3 in the larger cell structure 1(a).

the power source is switched to constant current (CC) mode. The current must be carefully controlled, or the resistor will melt due to current runaway. As soon as the source switches to CC mode, the current can be increased in very small increments. The high current density between the contact pads causes heating in the resistor due to Joule heating, which in turn causes crystallization. Once a sufficient current has been reached to crystallize the resistor, the power can then be reduced. As it is reduced, the resulting I-V curve is linear due to the ohmic nature of the resistor.

Figure 68 shows the same experiment for the smallest simple resistor. The interelectrode distance for these devices is 6 μm with an overlap of 2 μm between the GeTe and the electrodes on either side. Because the resistor on sapphire was presented in Figure 67, it is not shown again. The curves' symbols and colors are the same for each substrate in these two figures. Each resistor melted at the last data point of each experiment.

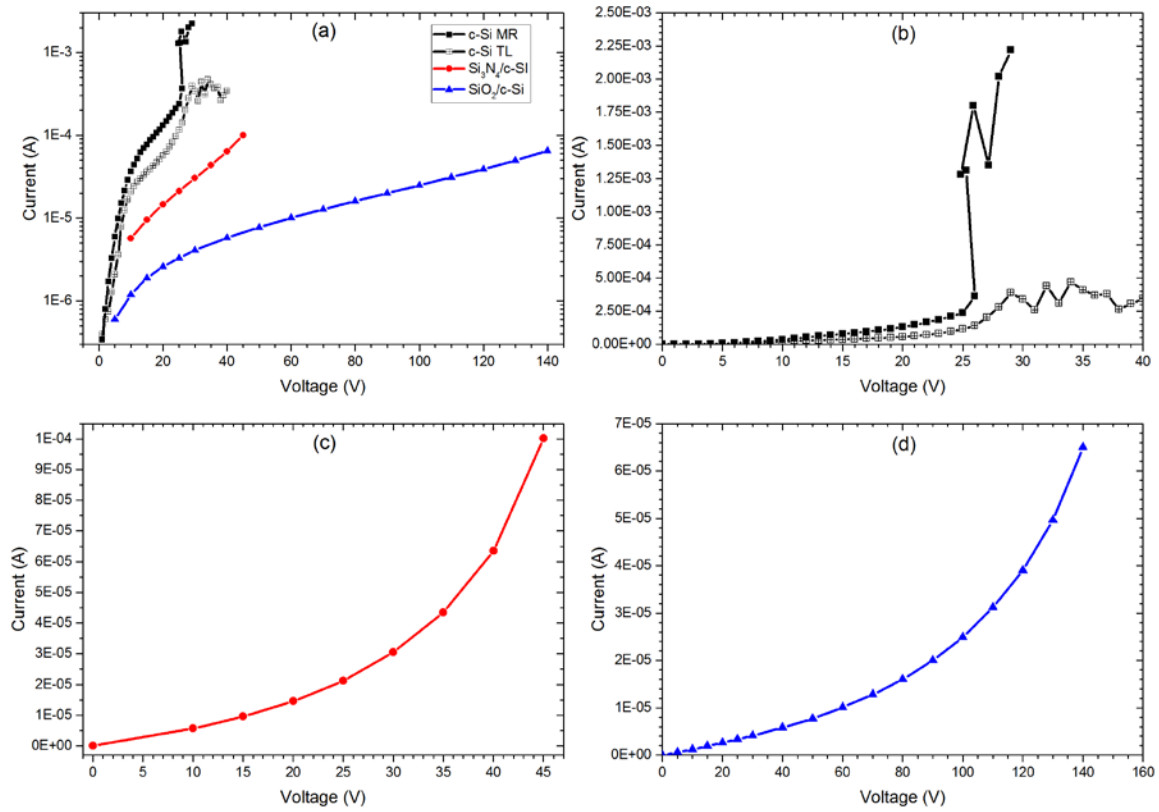


Figure 68. Measured I-V curves for amorphous GeTe thin films in simple resistors (smallest) on various substrates: (a) Log plot of all four I-V curves for comparison, (b) Two curves of GeTe on c-Si substrate from two different devices in the middle right (MR) and top left (TL) reticles, (c) GeTe on $\text{Si}_3\text{N}_4/\text{c-Si}$ substrate, and (d) $\text{SiO}_2/\text{c-Si}$ plot. The PCM cell on sapphire is shown in Figure 67.

Based on the successful results of Figure 67(b), three more trials were completed on the same resistor in order to experiment with what would happen to the I-V curves if several more cycles were completed after the crystallization of the first trial. At the end of each trial, the current and voltage are reduced to zero, and the next trial is begun. On the fourth trial (blue), the current was increased past the crystallization point in order to gain information about the maximum current achievable for this design. The resistor melts at the top of the blue curve. The melted resistor is shown in Figure 70.

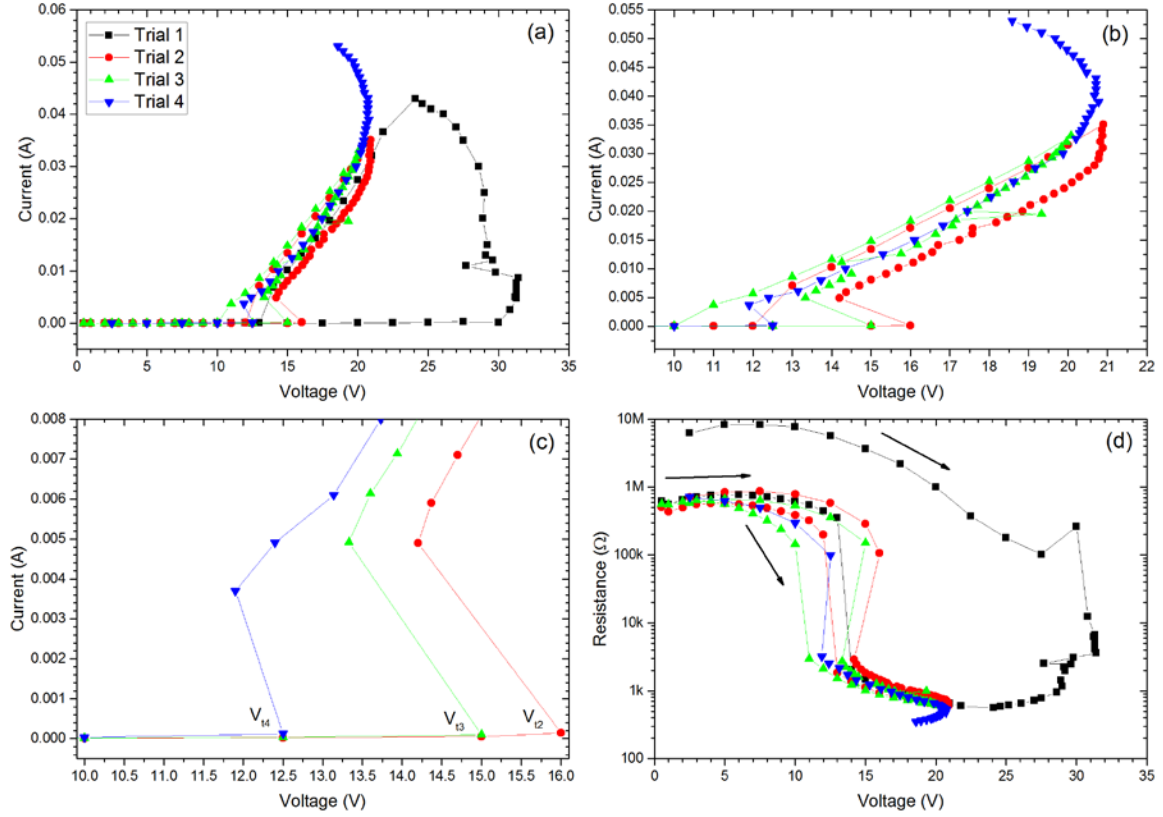


Figure 69. I-V curves of the simple resistor of Figure 67(b) of four subsequent trials, all of which show a voltage snap-back at their threshold voltage: (a) All four trials for comparison where Trial 1 is the same as Figure 67(b), (b) Trials 2, 3, and 4, (c) Closer view of the threshold voltages for trials 2-4, (d) Resistance of the cells vs. applied voltage, where the curves cycle to the right and downward.

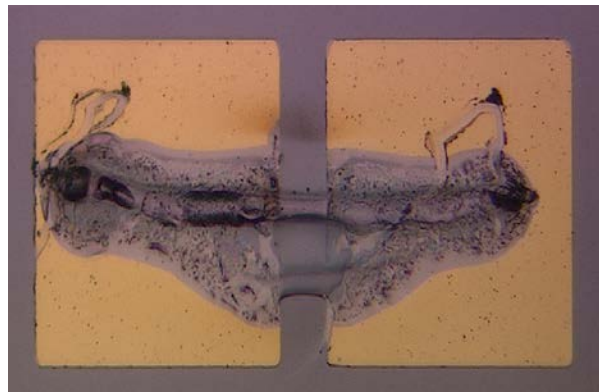


Figure 70. Resistor with melted GeTe and probes removed; 50 \times magnification.

Finally, I-V curves were generated for the cells with additional heaters bisecting the interelectrode gap (top/bottom heaters). These two categories of devices behaved identically; that is, the location of the additional heater either above or below the GeTe strip did not cause any changes to the I-V curves. These devices were prone to melting from the additional current injection, but some interesting results were obtained. The nomenclature “d” and “g” are used for “drain” and “gate” although this is a misnomer because these devices are not transistors. In this experiment, V_d is stepped in 5-V increments at each V_g . The so-called gate voltage, V_g , applied between the middle heater and the right contact pad in Figure 53, was stepped from 0 to 25 V in 5-V increments. The curves in Figure 71 were generated at one V_d for each V_g . For instance, $V_d = 10$ V was collected for $V_g = 0$, then $V_g = -5$ V, then $V_g = -10$ V, and so on. This ensured the maximum amount of data collection for all V_g values before melting occurred. Note that the black and red curves have 9 points, the green curve has 8 points, the blue curve has 7 points, the cyan curve has 6 points, and the magenta curve has 5 points. Also, the amount of current generated for higher V_g with fewer points is commensurate with lower V_g with several more points. This device melted when collecting the next highest point on the black curve. Based on the pattern detected up to that point, the measured current would be approximately 95 μ A at $V_d = 45$ V.

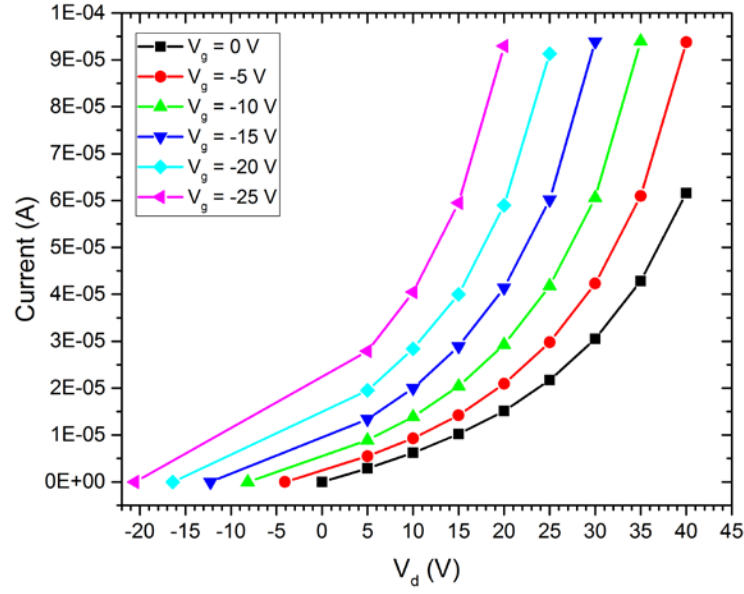


Figure 71. I-V curves of the top heater (smallest) on $\text{Si}_3\text{N}_4/\text{c-Si}$ substrate; V_d is the applied voltage as in the previous figures (“drain” voltage), and V_g is the stepped voltage (“gate” voltage) from the top heater to the “drain” voltage pad. Reference Figure 53 for the experimental setup.

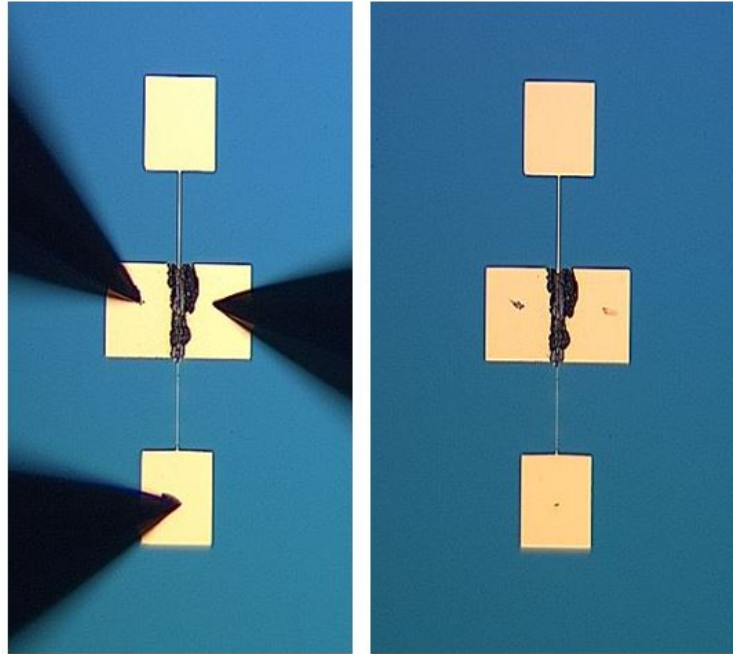


Figure 72. Resistor tested in Figure 71, showing placement of probes and melted GeTe; 10 \times magnification.

4.3.4. Capacitance Measurements

Capacitance was measured with an HP 4192A LF impedance analyzer. Because wires greatly affect the measured capacitance, care was taken to minimize cable lengths and any movement of the cables. Calibration was performed on capacitors of known value before taking measurements. The probes were configured as shown in Figure 73. The measurements were unable to provide any stable values. The capacitance would also vary by several orders of magnitude between measurements.

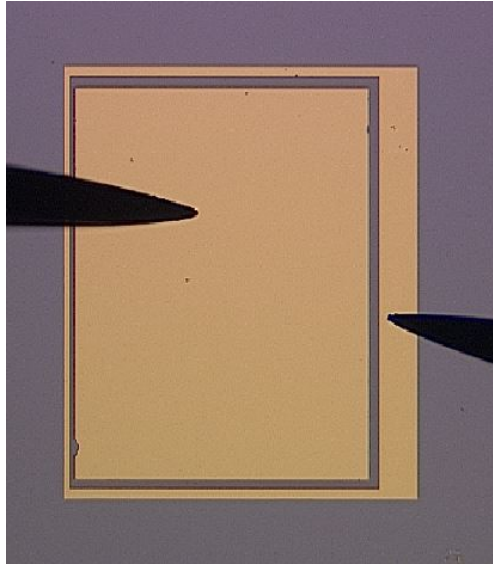


Figure 73. Placement of probes for a capacitance measurement

4.3.5. S Parameters

Testing of GeTe in the microwave and RF spectra was completed by collecting S parameters, specifically S_{11} and S_{21} , in both phases. The GeTe strip is deposited in the signal line between two contact pads. Because the resistivity changes by approximately six orders of magnitude between phases, the S parameters are expected to change based solely on this change in resistivity.

S parameters were collected over the range of 300 kHz to 3 GHz using an Agilent E5070B PNA and from 10 MHz to 20 GHz using an Agilent E8362C PNA. Calibration was completed using the CS-5 calibration kit for both PNAs. A through test of $50\ \Omega$ was completed at the end of each calibration procedure. In this test, the Agilent E5070B had 10-15 dB difference between S_{11} and S_{21} whereas the Agilent E8362C had 20-25 dB difference. The E5070B is an older system but still operates well.

One reticle of each type of substrate was heated on a hot plate past the crystallization temperature of GeTe. On two reticles of each substrate (crystalline and amorphous), the resistances of the signal lines of the switches were measured. These resistances are labeled ON and OFF for crystalline and amorphous in Table 9, respectively. There are seven RF switches in each reticle which vary in size, with RF1 being the smallest switch. As seen here, the OFF resistances for all switches on the sapphire reticles were too large to be measured by the multimeter. Additionally, the ON resistances were extremely high. For this reason, data was not collected for the switches on sapphire. Data is presented below for the other three substrates.

The S parameters are presented vs. frequency in the following figures. Due to size constraints, the captions are kept to a minimum for each figure. Within each figure, (a) corresponds to RF1, (b) to RF2..., and (g) to RF7. The y-axis is dB and the x-axis is frequency in Hz. The y-axes' scales are held constant for all of the plots for easy comparison between the S parameters. For each substrate type, the range of 300 kHz – 3 MHz is presented first and then 10 MHz – 20 GHz.

Table 9. Resistance values for RF switches, organized by substrate type

	Al ₂ O ₃		c-Si		Si ₃ N ₄ /c-Si		SiO ₂ /c-Si	
	ON	OFF	ON	OFF	ON	OFF	ON	OFF
RF1	4.6E+06	OVLD	75	3.5E+06	98	6.2E+07	86	6.5E+07
RF2	5.0E+06	OVLD	57	4.5E+06	124	6.3E+07	88	6.6E+07
RF3	3.7E+06	OVLD	180	4.0E+06	206	2.46E+08	195	2.55E+08
RF4	5.0E+06	OVLD	373	3.7E+06	280	5.50E+08	449	5.76E+08
RF5	2.7E+03	OVLD	320	3.4E+06	295	5.00E+08	334	5.14E+08
RF6	9.7E+02	OVLD	695	3.8E+06	522	1.1E+09	901	1.15E+09
RF7	8.3E+02	OVLD	780	3.0E+06	456	1E+09	749	1.01E+09

When analyzing the plots, compare the pair of amorphous values to the pair of crystalline values. For instance, a high S_{11} (reflected signal) and low S_{21} (transmitted signal) would be expected for the amorphous phase of a switch because more signal is reflected than transmitted. Because these are passive devices and the S parameters are defined as losses, the maximum value is 0 dB. Between the amorphous and crystalline phases, a good RF switch will have a change in the placement of S_{11} and S_{21} . For instance, S_{11} should be higher in the amorphous phase than in the crystalline phase.

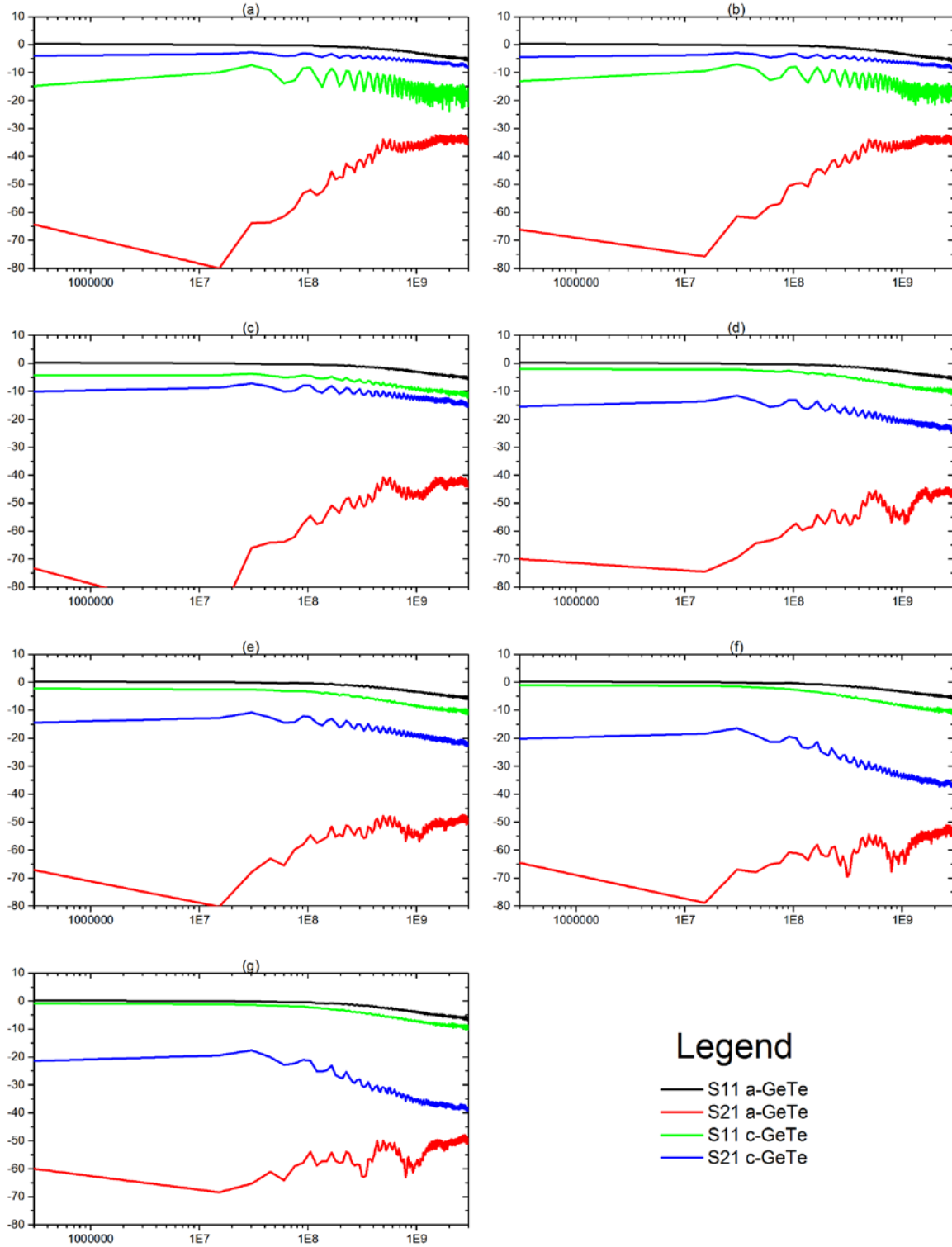


Figure 74. S parameters of RF switches on c-Si substrate, 300kHz to 3 GHz; (a) RF1, (b) RF2, (c) RF3, (d) RF4, (e) RF5, (f) RF6, (g) RF7.

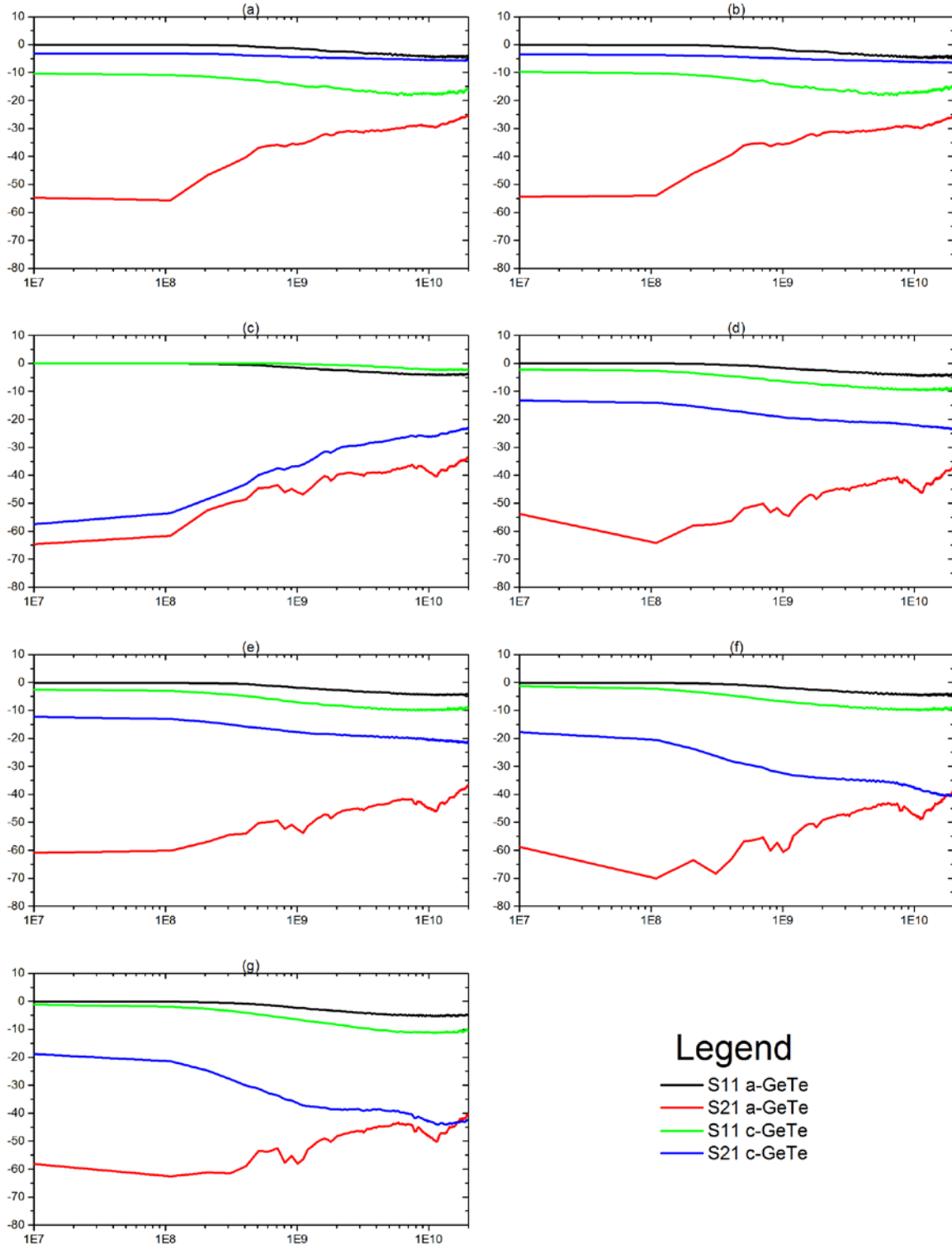


Figure 75. S parameters of RF switches on c-Si substrate, 10 MHz to 20 GHz; (a) RF1, (b) RF2, (c) RF3, (d) RF4, (e) RF5, (f) RF6, (g) RF7.

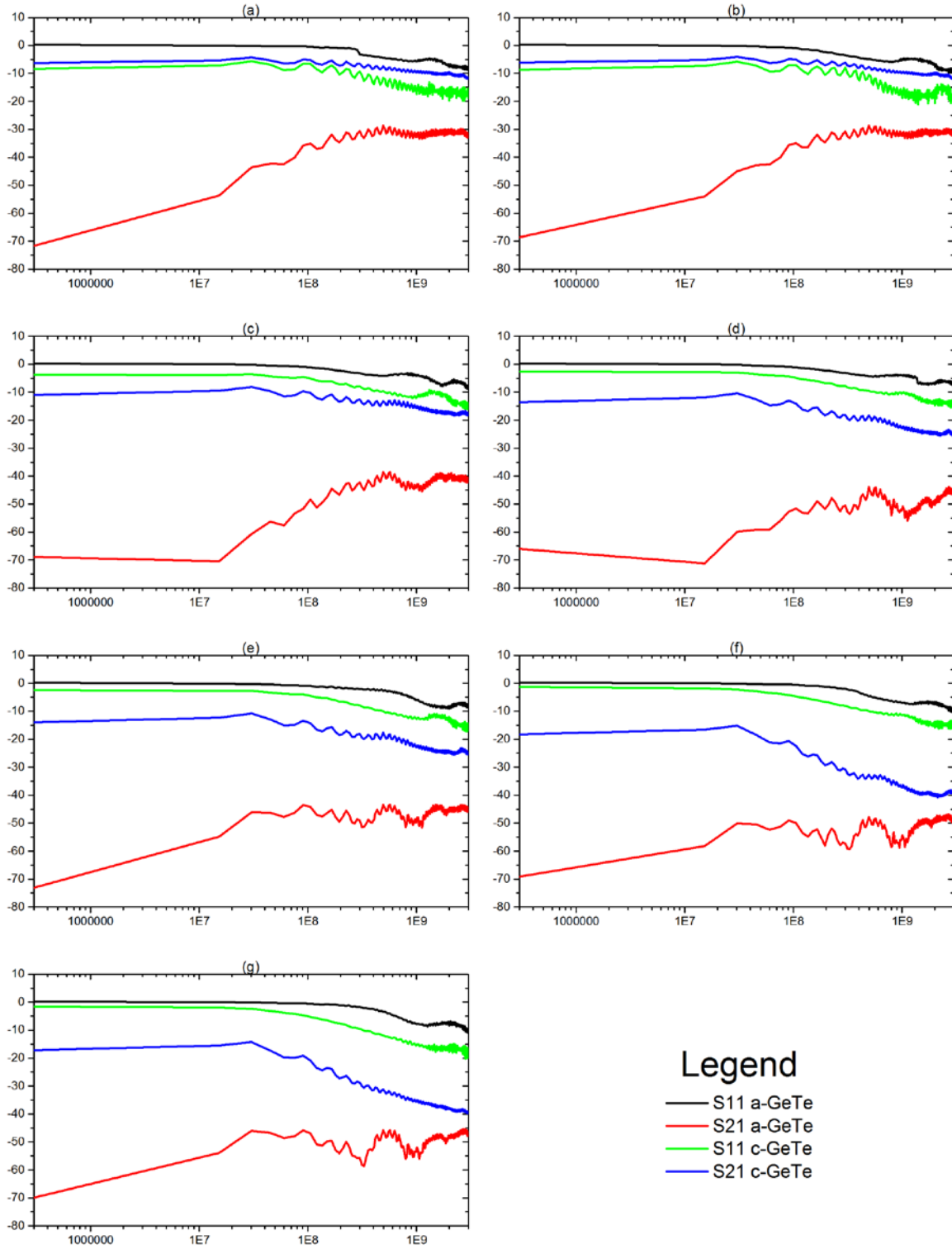


Figure 76. S parameters of RF switches on $\text{Si}_3\text{N}_4/\text{c-Si}$ substrate, 300 kHz to 3 GHz; (a) RF1, (b) RF2, (c) RF3, (d) RF4, (e) RF5, (f) RF6, (g) RF7.

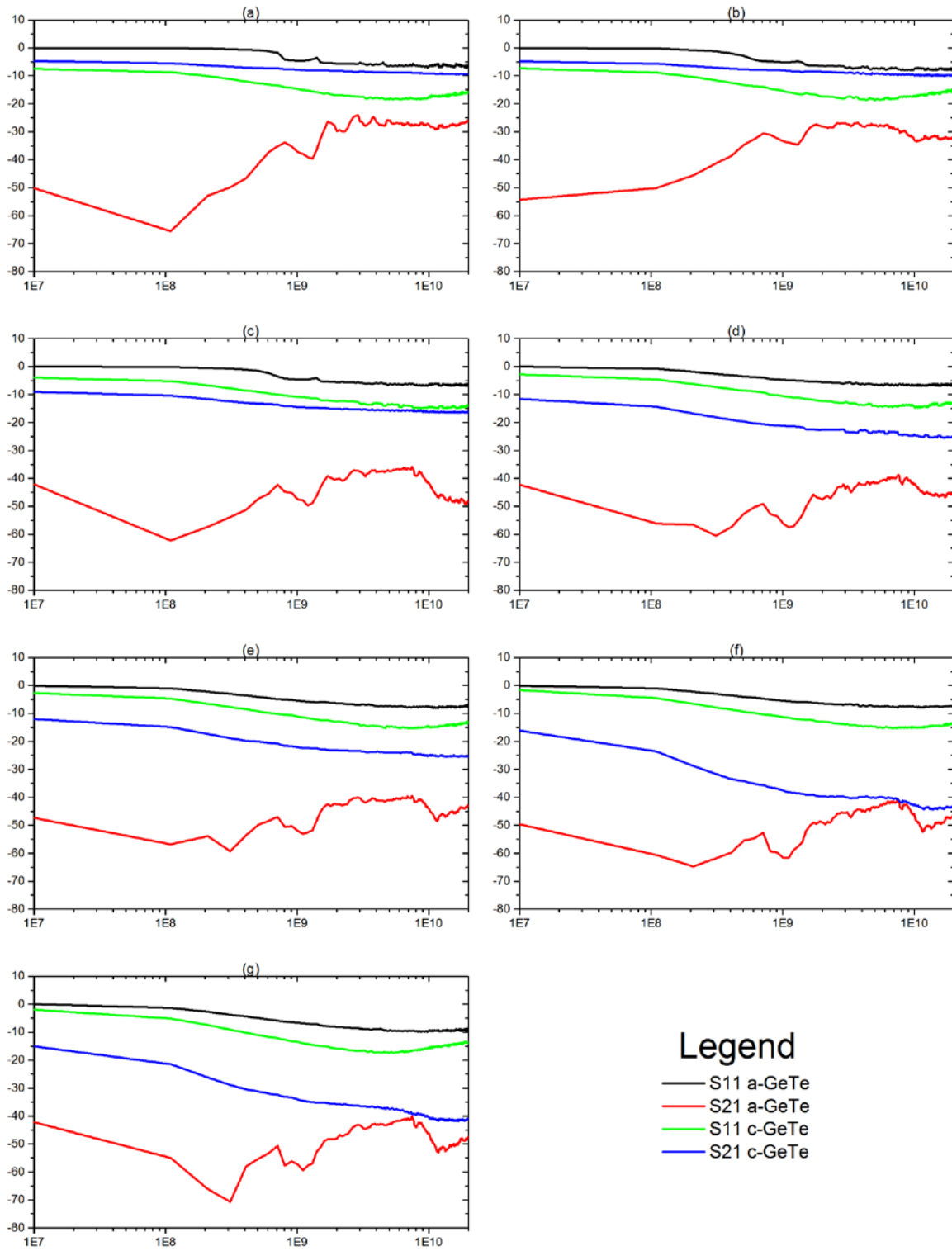


Figure 77. S parameters of RF switches on $\text{Si}_3\text{N}_4/\text{c-Si}$ substrate, 10 MHz to 20 GHz; (a) RF1, (b) RF2, (c) RF3, (d) RF4, (e) RF5, (f) RF6, (g) RF7.

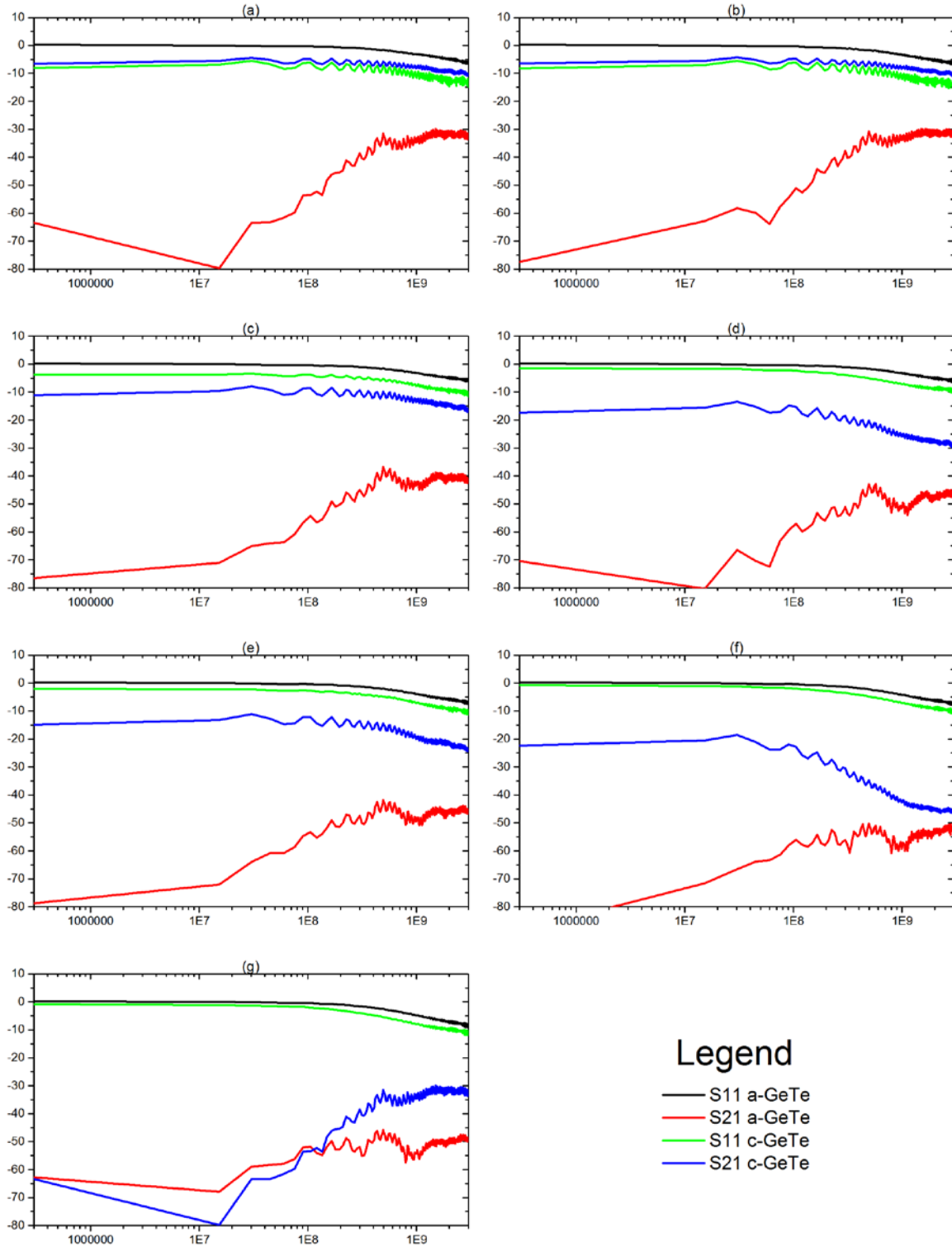


Figure 78. S parameters of RF switches on SiO₂/c-Si substrate, 300 kHz to 3 GHz; (a) RF1, (b) RF2, (c) RF3, (d) RF4, (e) RF5, (f) RF6, (g) RF7.

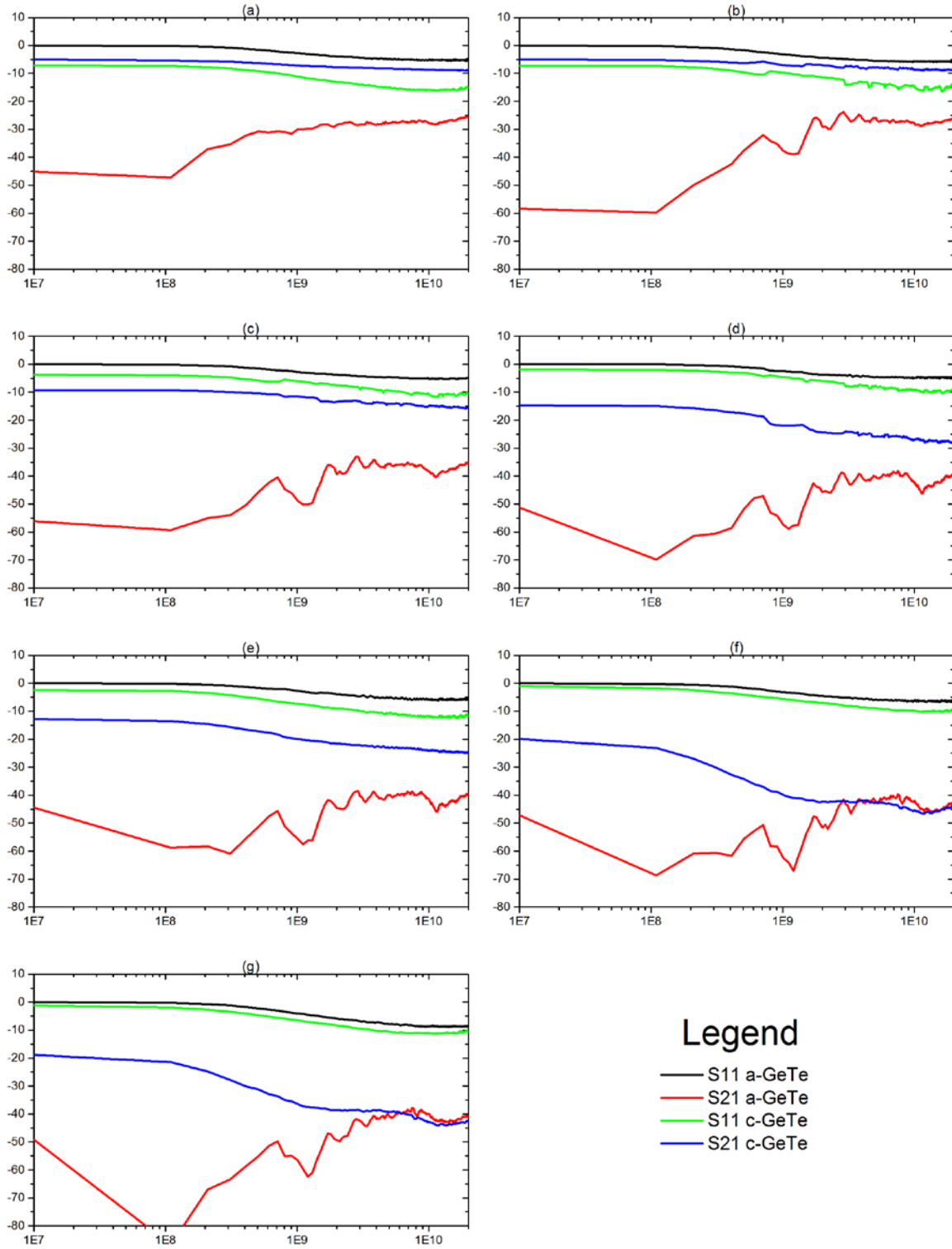


Figure 79. S parameters of RF switches on $\text{SiO}_2/\text{c-Si}$ substrate, 10 MHz to 20 GHz; (a) RF1, (b) RF2, (c) RF3, (d) RF4, (e) RF5, (f) RF6, (g) RF7.

As discussed in Chapter 2, the performance of RF switches can also be measured in terms of insertion loss and isolation. These figures of merit were calculated from the S parameters and are shown below. They are organized in the same manner as the S parameter plots. Because they are measures of power delivered to loads in the ON and OFF states, their calculations were divided by 2. The S parameters were calculated according to the definition of the decibel, 20 times the base-10 logarithm of the magnitude (see equation 40). Power logarithms, on the other hand, are calculated as 10 times the base-10 logarithm. This is due to the squared term of the voltage (or current) which is multiplied by 10. That is, $10 \log_{10} V^2 = 20 \log_{10} V$, which satisfies the equation for the decibel. Therefore, the equations for insertion loss, IL, becomes

$$IL = -\frac{1}{2} S_{21,ON} \quad (50)$$

And the equation for isolation, I, is

$$I = \frac{1}{2} (|S_{21,OFF}| - |S_{21,ON}|) = \frac{1}{2} (S_{21,ON} - S_{21,OFF}) \quad (51)$$

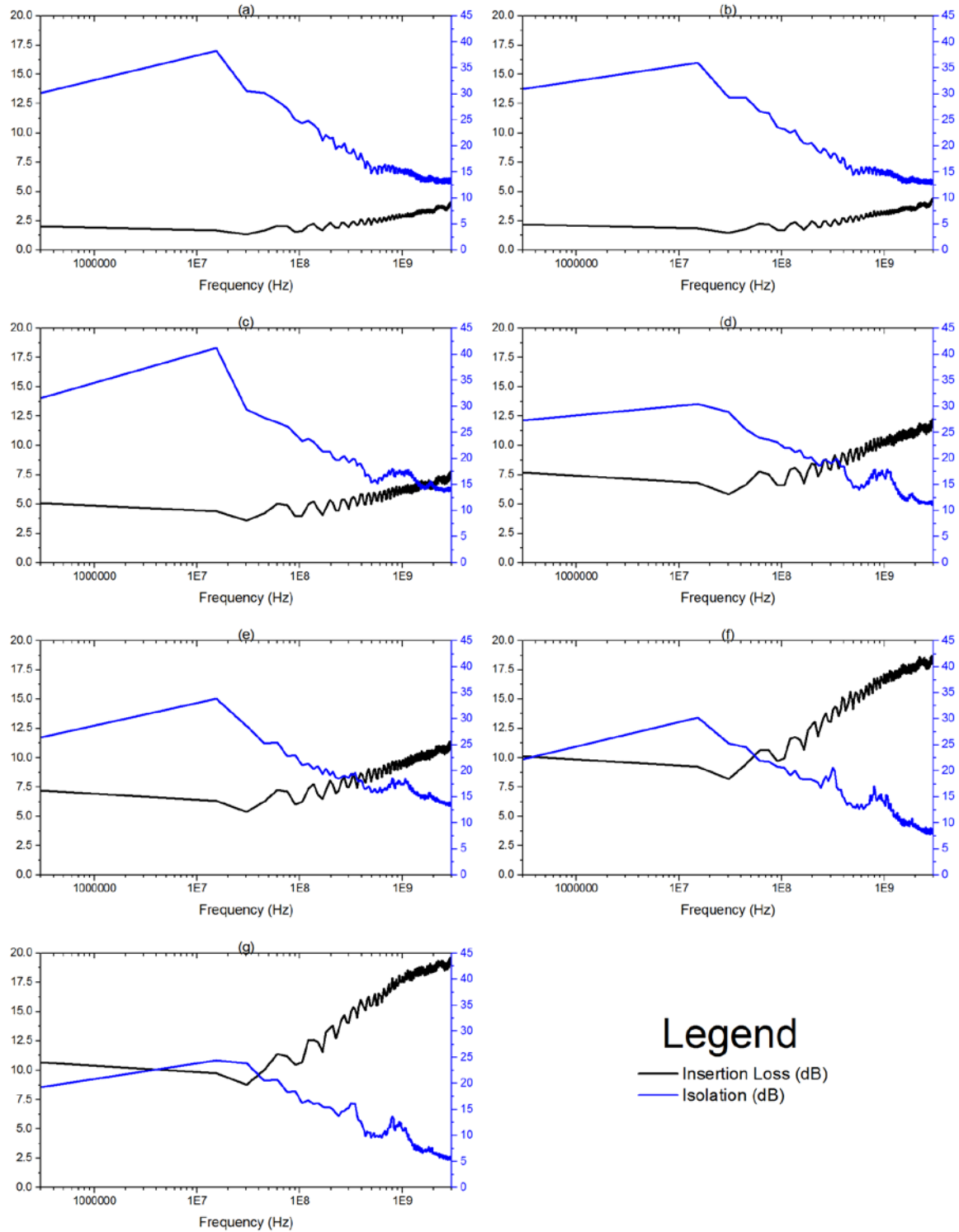


Figure 80. Insertion loss and Isolation of RF switches on c-Si substrate, 300kHz to 3 GHz; (a) RF1, (b) RF2, (c) RF3, (d) RF4, (e) RF5, (f) RF6, (g) RF7.

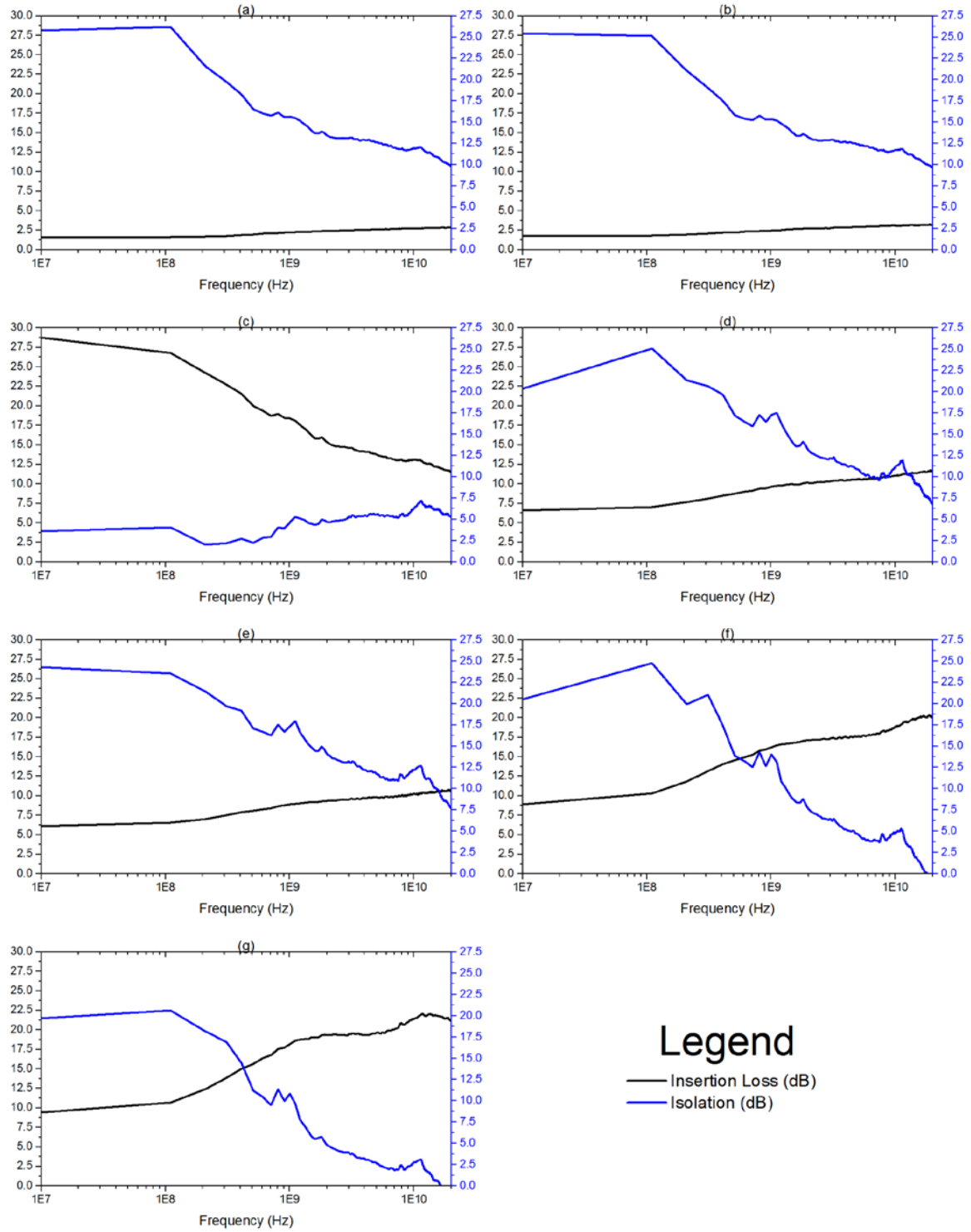


Figure 81. Insertion loss and Isolation of RF switches on c-Si substrate, 10 MHz to 20 GHz; (a) RF1, (b) RF2, (c) RF3, (d) RF4, (e) RF5, (f) RF6, (g) RF7.

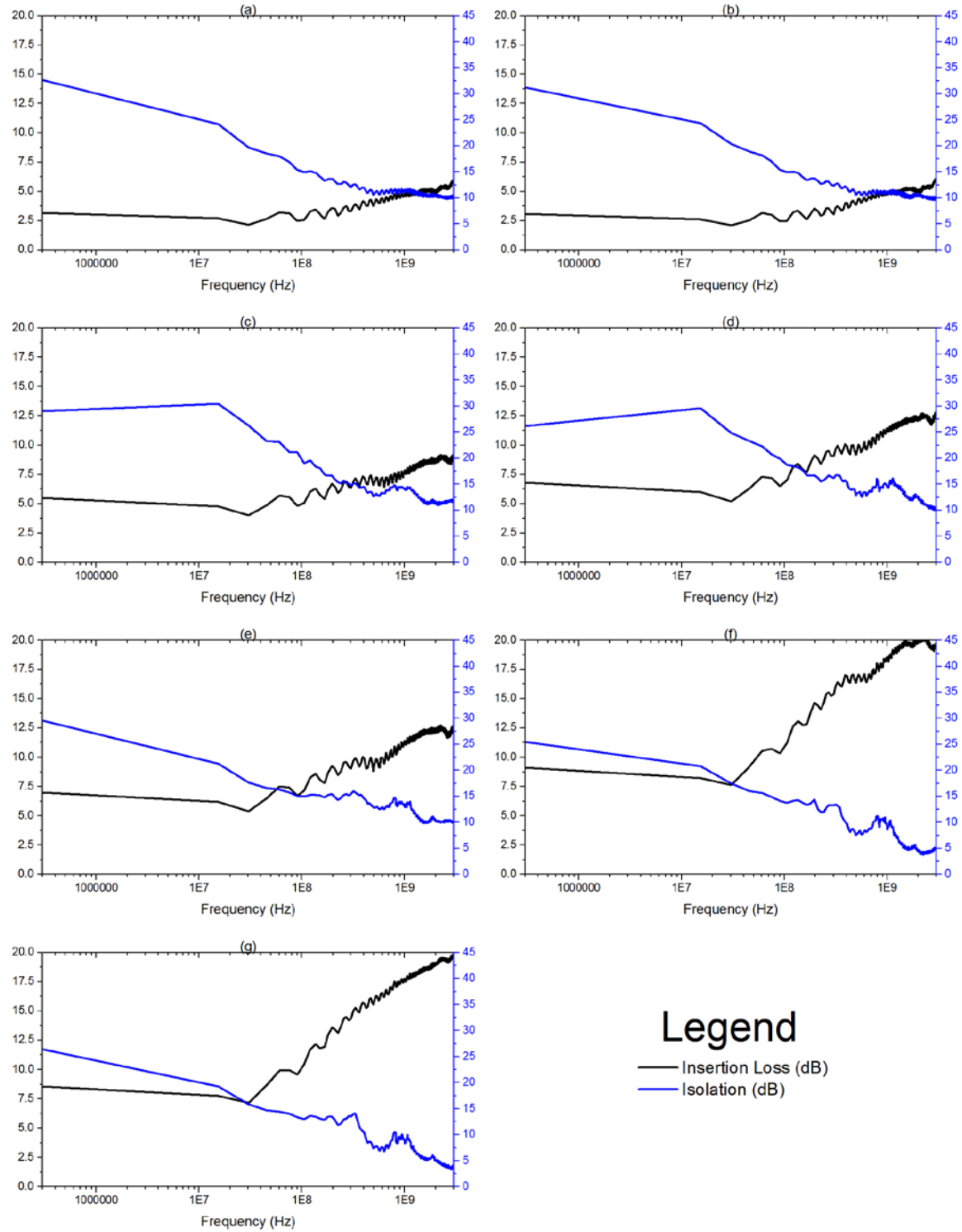


Figure 82. Insertion loss and Isolation of RF switches on $\text{Si}_3\text{N}_4/\text{c-Si}$ substrate, 300kHz to 3 GHz; (a) RF1, (b) RF2, (c) RF3, (d) RF4, (e) RF5, (f) RF6, (g) RF7.

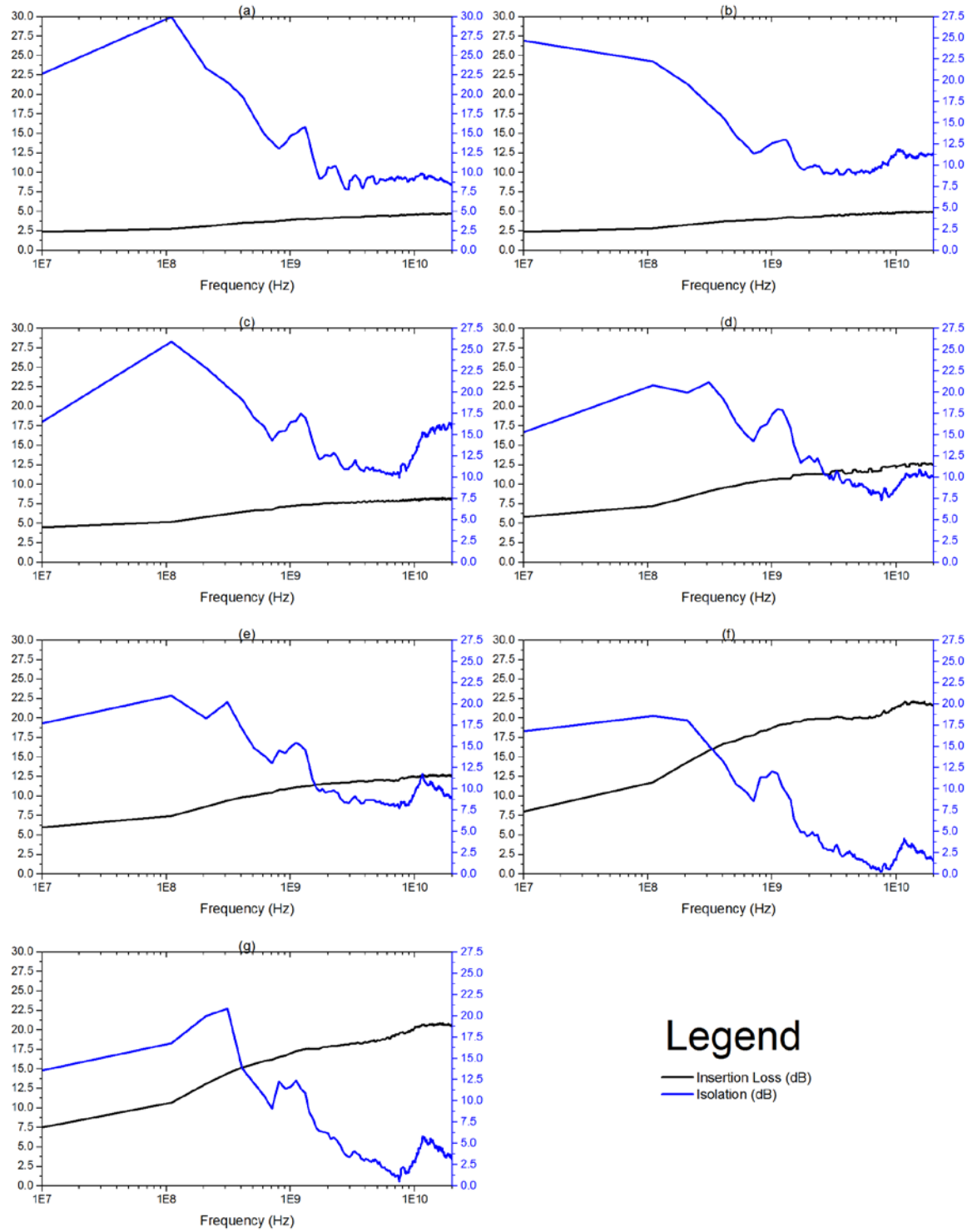


Figure 83. Insertion loss and Isolation of RF switches on $\text{Si}_3\text{N}_4/\text{c-Si}$ substrate, 10MHz to 20 GHz; (a) RF1, (b) RF2, (c) RF3, (d) RF4, (e) RF5, (f) RF6, (g) RF7.

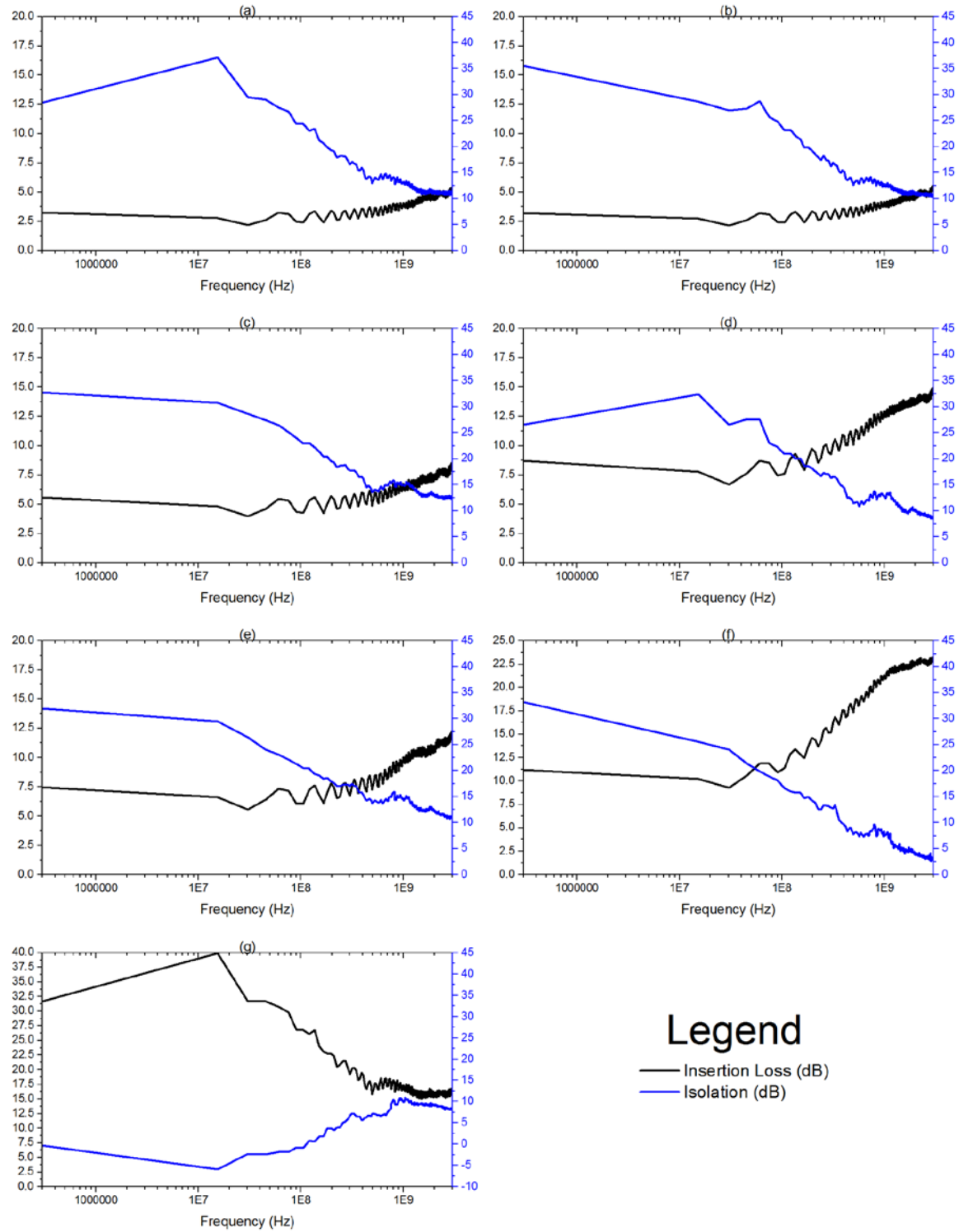


Figure 84. Insertion loss and Isolation of RF switches on $\text{SiO}_2/\text{c-Si}$ substrate, 300kHz to 3 GHz; (a) RF1, (b) RF2, (c) RF3, (d) RF4, (e) RF5, (f) RF6, (g) RF7.

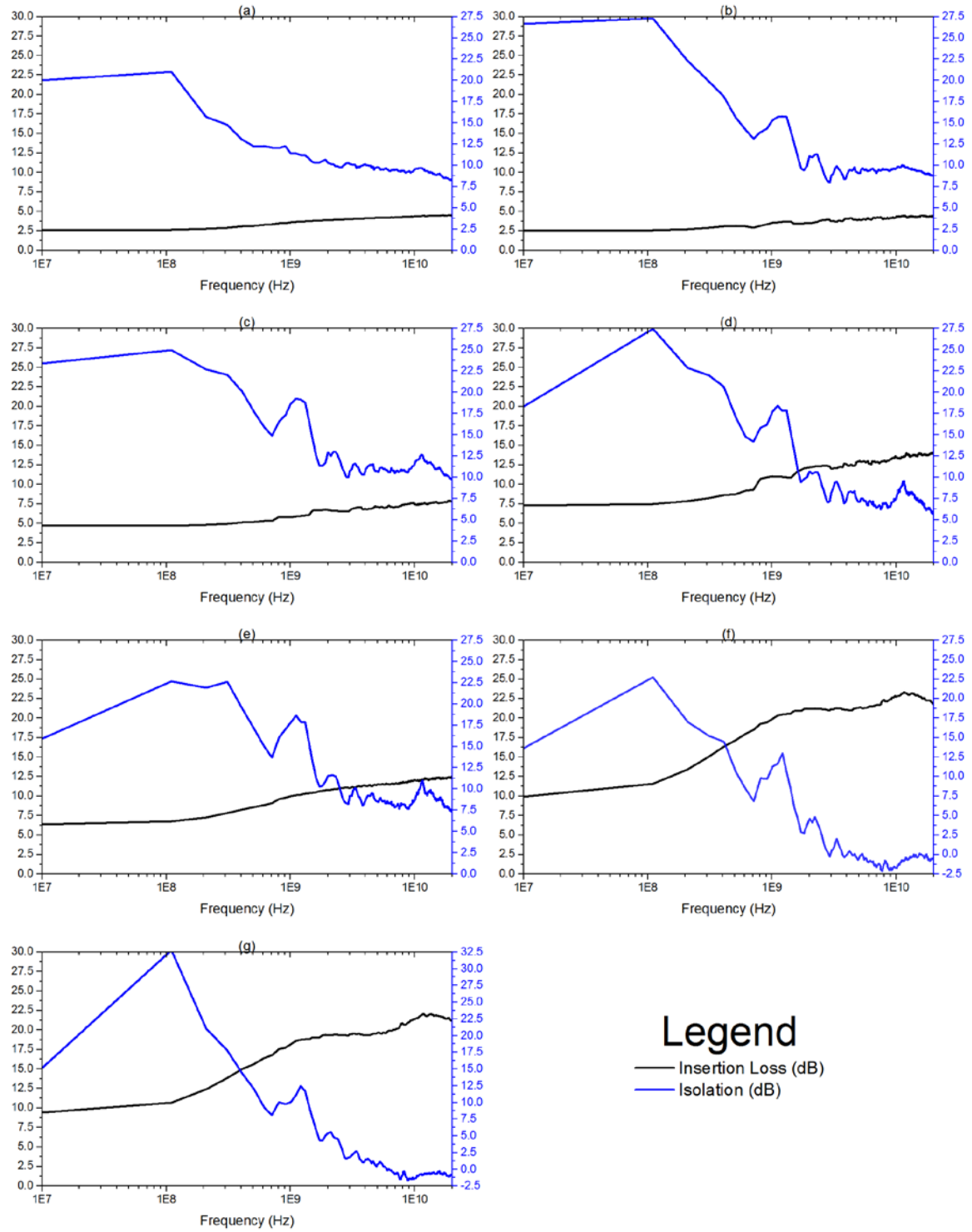


Figure 85. Insertion loss and Isolation of RF switches on SiO₂/c-Si substrate, 10 MHz to 20 GHz; (a) RF1, (b) RF2, (c) RF3, (d) RF4, (e) RF5, (f) RF6, (g) RF7.

4.3.6. Determination of T_c for various thicknesses

An experiment was conducted to determine any changes in the crystallization temperature of GeTe with decreasing film thickness. At the crystallization temperature, T_c , the amorphous film reaches a stable crystalline orientation. This is measured by a large decrease in electrical resistivity on the order of four orders of magnitude. In order to discount any effects of dielectrics or metals, GeTe was sputtered uniformly on c-Si. Prior to testing, the instrumentation is checked on a silicon wafer coated with evaporated aluminum. Under 10 \times optical zoom, the probe tips are placed approximately 10 μm apart and resistance is recorded at room temperature with a digital multimeter. This resistance measurement incorporates all wires, resistance of the probes, contact resistances, and the resistance of the aluminum wafer between the probe tips. The standard is to not exceed 10 Ω ; desired resistance is 5 Ω or less. If the resistance exceeds 10 Ω , the wires, connections, and probes are checked, and if needed, replaced.

In this measurement scheme, there are no defined contact pads for probe placement. Rather, the probes are placed approximately 10 μm apart, and resistance is measured at each temperature. The measured resistance is based on an approximation of the underlying dimensions of the thin film, but more importantly, a significant drop in resistance is detected. Because the resistivity of GeTe drops by six orders of magnitude at its crystallization temperature, this drop can easily be detected with this method. This saves time and resources of fabricating microelectronics when it is unnecessary.

The maximum allowed temperature setting on the Micromanipulator controller is 405°C (761°F). At these high temperatures, the temperature differential between the controller's display and the actual temperature is less than at lower temperatures. At a

setting of 405°C, the maximum measured temperature was 401.6°C. Temperature was measured using an Agilent U1602B digital oscilloscope with a thermocouple attachment. The thermocouple wire between the meter and the sample was fastened to the vertical upright of the table to prevent melting of the wire. When heating under normal conditions, a piece of wax paper was placed between the wire and the ceramic plate. However, wax begins to burn at approximately 310°C, so this could not be used for insulation.

The following table correlates the sputtering parameters with the measured crystallization temperature, T_c . Note that because T_c occurs suddenly, it is difficult to measure as temperature is increasing. In order to narrow T_c to within a few degrees, several samples were measured for each thickness. In the first sample of each set, T_c was determined within 50°C. On subsequent samples, the temperature steps were smaller and within this 50°C interval.

Table 10. Correlation of GeTe crystallization temperature, T_c , and sputtering parameters

Sputtering		T_c Interval	
Power (W)	Time (min)	Lower (°C)	Upper (°C)
300	2	191.9	201.2
100	2	205.1	207.1
100	1	287.3	291.1
100	0.5	260.9	266.4
50	0.5	400.4	Unk
50	0.25	401.6	Unk

4.3.7. Terahertz Transmittance and Absorbance

A terahertz experiment was conducted with stoichiometric GeTe on sapphire. GeTe was RF sputtered at 300 W for 2 minutes with Ar at a flow rate of 20.1 sccm at 10 mTorr pressure. The substrate was not heated, and the resultant thin films were amorphous. The sapphire is c-plane (0001), single-sided-polished, 432- μm -thick, two-inch-diameter wafer, with the GeTe film on the polished side. After deposition, the GeTe/sapphire wafer was diced into a 3×3 grid pattern with each sample being approximately 1.7^2 cm^2 . In order to measure the reference under the exact same conditions as the samples, another blank sapphire wafer was diced in the same dimensions as the first wafer. The references were taken from the same location as the GeTe/sapphire samples (i.e., top left with reference to the wafer's flat). The samples were placed in a small heating chamber which is incorporated into the terahertz system. The samples are sandwiched between two metallic washers which are placed into a small cylindrical volume, through which the terahertz signal passes. The terahertz system is a terahertz time-domain spectroscopy (THz-TDS) system with a mode-locked Ti:sapphire laser. The laser emits NIR light, gated to pulses with widths on the order of tens of femtoseconds. The laser pulse excites a semiconductor antenna which radiates terahertz pulses. The maximum spectral resolution is 0.25 cm^{-1} with a range of 0.06 – 4 THz [149, 150].

The reference is taken at room temperature with the same vacuum pressure as the sample. 5.25 cm^{-1} resolution is used, which is reduced from optimal values due to etalon effects in the thin substrate. Temperature is stepped in increments of 50°C to 200°C , at which point the step size is 10°C to 250°C . A ramp rate of $2.5^\circ\text{C}/\text{min}$ was used, which is

sufficiently slow, in order to ensure the sample's temperature coincides with the controller's set temperature. Probing of the sample's temperature is impossible with anything except for the system's incorporated thermocouple during the experiment. A scanning frequency of 30 Hz is used for 18,000 data points (10-minute duration) at each temperature setting.

The following figures show the time-domain signal, transmittance, and absorbance of the GeTe/sapphire sample as it is heated. The frequency range of 10 – 110 cm^{-1} (300 GHz – 3.3 THz) is used for all plots. The *Relaxed* measurement is of the fully crystalline GeTe film on sapphire at R. T., measured 24 hours after the 250°C data point.

Data smoothing was completed after the measurements were taken for the transmittance data, primarily for frequencies above 60 cm^{-1} . High order (5th to 10th order) polynomials were fit to the data, and a best fit was determined qualitatively based on how

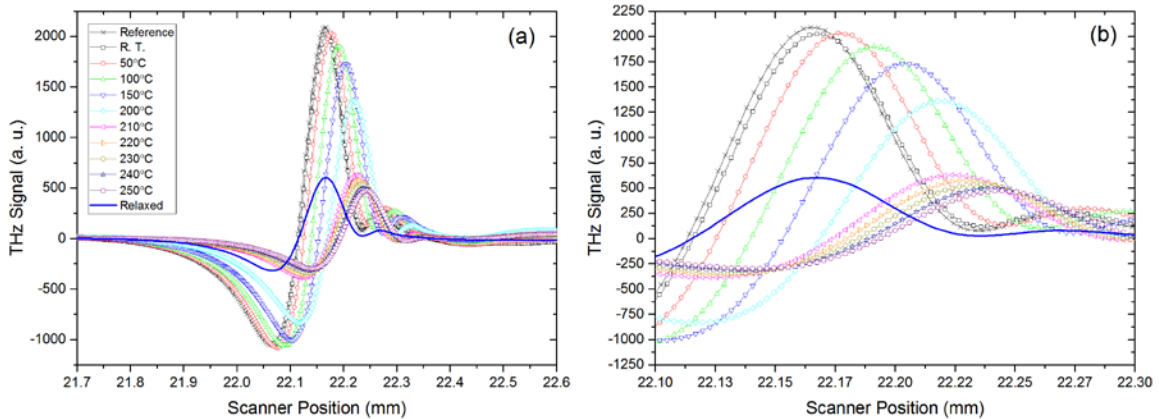


Figure 86. Terahertz time-domain signal showing the peak intensities and scanner position. The decrease in peak intensity corresponds to increased absorbance. A shift of scanner position to the right corresponds to a thicker sample.

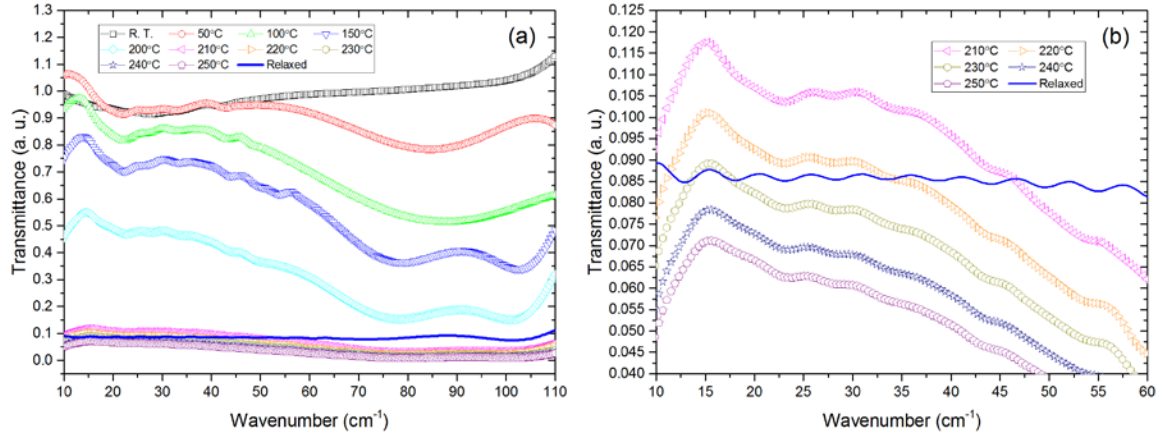


Figure 87. (a) Terahertz transmittance as the sample is heated from R. T. to 250°C, (b) Closer view of 10 – 60 cm⁻¹ and the relative transmittance of the Relaxed sample to the other waveforms.

well the polynomial averaged the oscillations in the higher frequencies. The higher frequency portion of the polynomial was merged with the lower frequency portion of the raw data using Matlab software. The smoothed absorbance data was then calculated based on the smoothed transmittance data, according to equations 32 and 33.

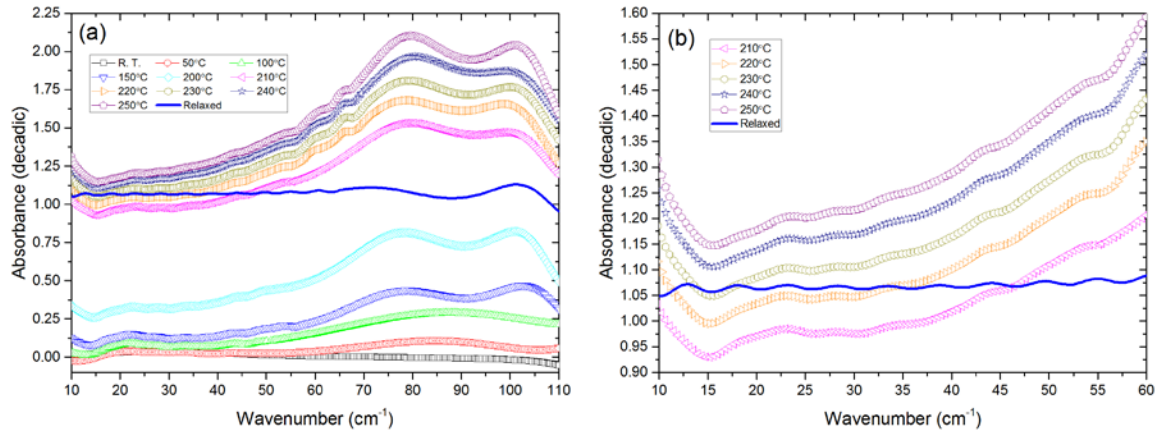


Figure 88. (a) Terahertz absorbance as the sample is heated from R. T. to 250°C, (b) Closer view of 10 – 60 cm⁻¹ and the relative absorbance of the Relaxed sample to the other waveforms.

The transmittance modulations of GeTe/sapphire, GeTe only at 250°C, and GeTe only at room temperature (R. T.) are shown in Figure 89. These are extracted based on the equation for transmittance modulation (equation 34). The modulation of the GeTe/sapphire system at 250°C is calculated by

$$M_{250} = \frac{T_{S,R.T.} - T_{G,250}}{T_{S,R.T.}} \quad (52)$$

where $T_{S,R.T.}$ is the transmittance of the bare sapphire wafer at R. T. and $T_{G,250}$ is the transmittance of the GeTe/sapphire system at 250°C. The modulation of only the GeTe thin film at 250°C is calculated by

$$M_{G,250} = \frac{T_{S,250} - T_{G,250}}{T_{S,250}} \quad (53)$$

where $T_{S,250}$ is the transmittance of only the bare sapphire wafer at 250°C. $T_{S,250}$ was measured in a separate experiment by heating the sapphire wafer at the same rate. Finally, the modulation of the GeTe in its relaxed state is calculated by

$$M_{G,relaxed} = \frac{T_{S,R.T.} - T_{G,relaxed}}{T_{S,R.T.}} \quad (54)$$

where $T_{G,Relaxed}$ is the transmittance of the GeTe/sapphire system in its relaxed (crystalline) state at R. T. It is this final expression which would apply to the modulation of GeTe thin films due to voltage pulsing. The voltage pulsing would raise the temperature of the thin film for tens of nanoseconds then quickly cool it. Therefore, on the order of seconds to minutes, the thin film is at ambient temperature in both phases.

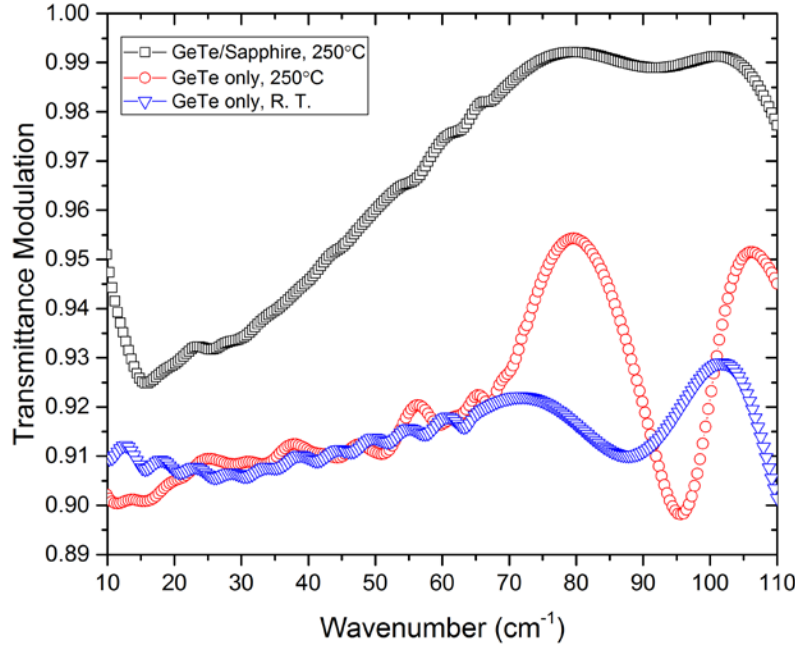


Figure 89. GeTe terahertz transmittance modulation; state-of-the-art systems have modulation depths of 50%, and VO₂ on sapphire (heated) has a modulation depth of approximately 80%.

4.3.8. Spectroscopic Ellipsometry

Ellipsometry is a powerful tool used to analyze thin films. Many parameters can be measured, such as n , k , E_g , ε_r , ε_i , and film thickness. The disadvantage of using it, however, is that all of the outputs are dependent on modeling of the material's dispersion, and any slight change in the model can yield very different output values. GeTe is not a common material, so dispersion files were created for the amorphous and crystalline phases. Because Tauc-Lorentz is very good at modeling amorphous semiconductors, it was used for the amorphous phase. The Classical model was used for the crystalline phase due to its ordered structure and metallic conductivity.

A Horiba UVISEL 2 was used over the range 1.5 – 6.5 eV (827 nm – 191 nm, respectively). The system has the capability of using the full range of 0.59 – 6.5 eV (2.102 μm – 191 nm) but there was a temporary malfunction in the software which

caused a discontinuity in the data at 1.4 eV. This is unfortunate because this region is considered the “fingerprint” region for chalcogenides since samples vary the most from one to the other within this range.

Samples with SSP substrates were used in order to reduce reflections off the back side of the samples. Also, c-Si was used for the substrate because the dispersions for it are well known and change very little. All samples were analyzed with a 70° angle of incidence and a spectral range of 1.50 - 6.50 eV at intervals of 0.05 eV. Samples were analyzed *ex-situ* before and after heating (amorphous and crystalline phases, respectively). Goodness-of-fit χ^2 values were less than 1 (very good fit) and non-diagonal values were approximately zero. As stated previously, the Tauc-Lorentz model was used for a-GeTe, and the Classical model was used for c-GeTe.

In addition to the measured curves in Figure 90, the results show an optical bandgap of 0.72 eV in the amorphous phase and a thickness of approximately 200 nm.

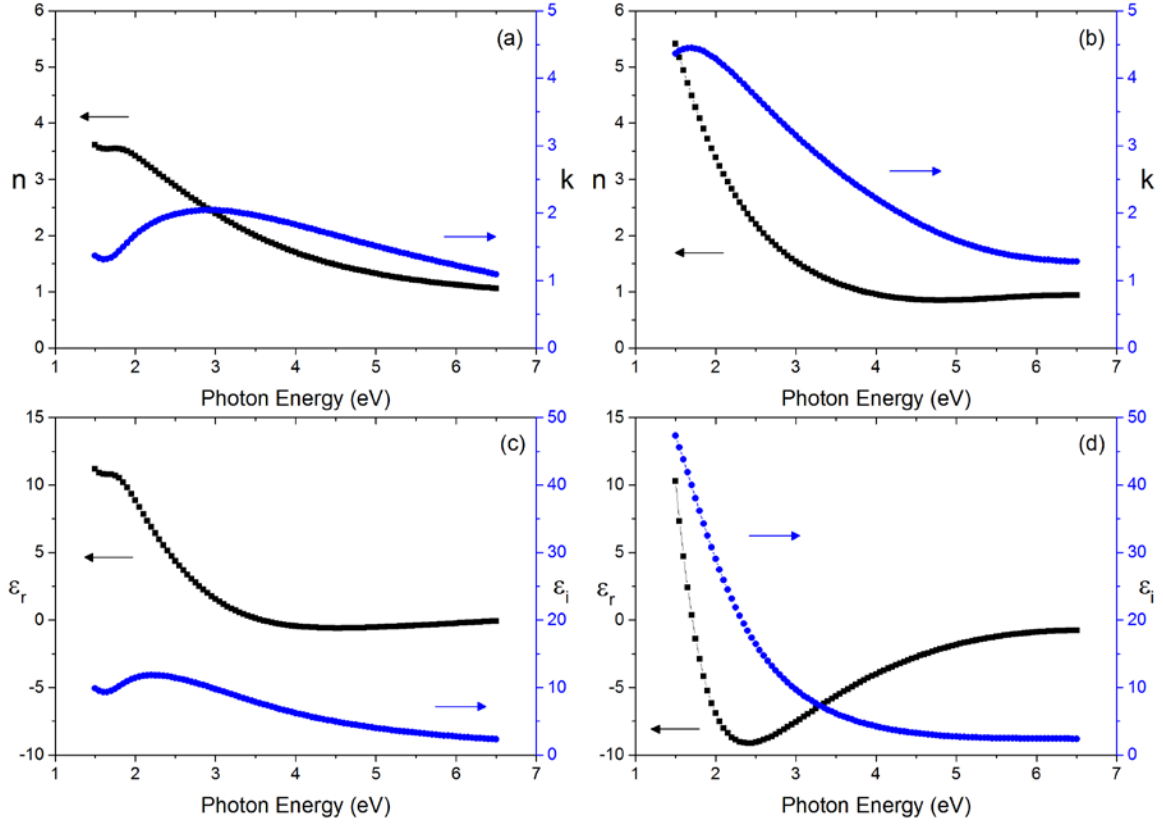


Figure 90. SE models of amorphous and crystalline GeTe from 1.5 eV to 6.5 eV. (a) – (b) Index of refraction, n , and extinction coefficient, k ; (c) – (d) Real and imaginary components of the complex dielectric function, ϵ_r and ϵ_i , respectively. Plots on the left are of an amorphous sample, and plots on the right are of a crystalline sample heated by conduction beyond its crystallization temperature. Both samples were prepared by RF sputtering on single-sided-polished c-Si in the same processing batch. There was no discernible difference between the measured data and ellipsometry models (measured data not plotted).

Based on the measured extinction coefficient values, the absorption coefficient α was generated based on the relationship in equations 29 and 30. Figure 91(a) is the absorption coefficient in both phases plotted vs. photon energy, and (b) is vs. wavelength. The second plot helps to compare the absorption coefficient to other materials because it is conventionally plotted vs. wavelength.

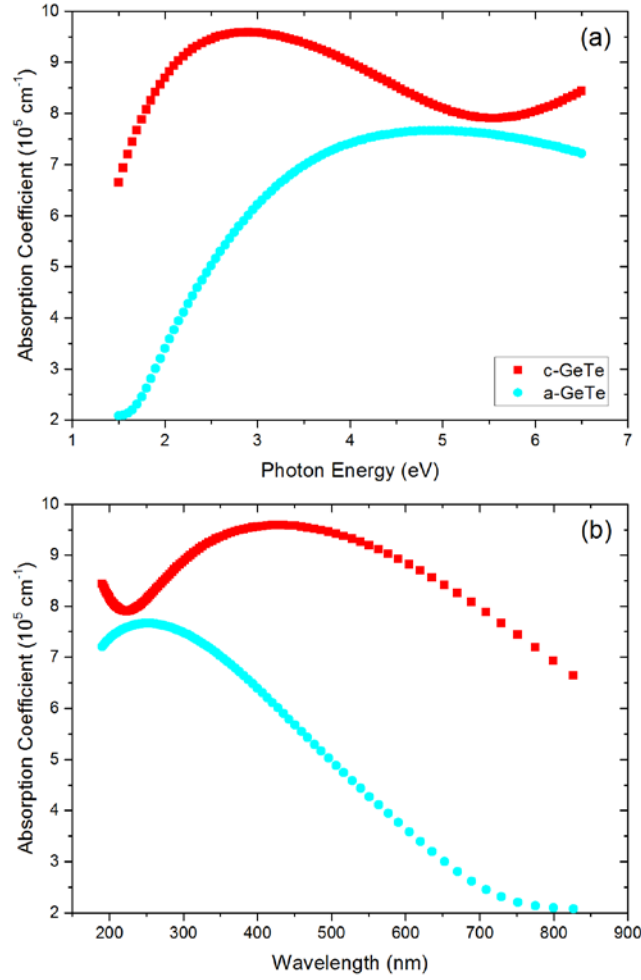


Figure 91. Measured absorption coefficient, α , of GeTe in crystalline and amorphous phases: (a) 1.5 eV – 6.5 eV and (b) 191 nm – 827 nm.

4.3.9. Spectral Reflectance

Because chalcogenides are typically used in optical memory where the modulation in reflection between phases is used, experiments of spectral reflectance were completed. This was done with the Filmetrics F20-UV thin film analyzer in the reflection mode. The UV-Vis-NIR spectrum of 200 nm – 1.1 μm is measured in this system. The software modeling was ignored, and the raw data were recorded. The same

GeTe thin film (300 W, 2 min) was analyzed on four types of substrates. Additionally, data were collected on the thinner films discussed in section 4.3.6.

Figure 92 displays the reflectance data for the 300 W/2 min film. Each curve in part (a) is a sample measurement for all substrates, where the upper envelope of curves is crystalline GeTe and the lower envelope is amorphous. Part (b) shows the average reflection data for the crystalline and amorphous phases of each substrate type, where each color curve is indicated in the legend. This legend applies to parts (b) – (f). The next four plots are the reflectance of both phases for c-Si (black), Si₃N₄/c-Si (green), Al₂O₃ (red), and SiO₂/c-Si (blue).

In Figure 93, the contrast for each substrate type is shown. The contrast is calculated as the reflection of the average amorphous phase subtracted from the average crystalline phase at each wavelength. (The averaged curves of Figure 92(b) are used.) A negative contrast occurs when the reflection of the amorphous phase is greater than the crystalline phase. The same color scheme is used as in Figure 92. Finally, the data for the thinner films are presented in Figure 94. With reference to Table 10, these “thinner” films are considered Sets 2 – 6, where the deposition at 300 W and 2 min is Set 1. Sets 5 and 6 are presented in Figure 95. These were not crystallized so the data is for amorphous GeTe only.

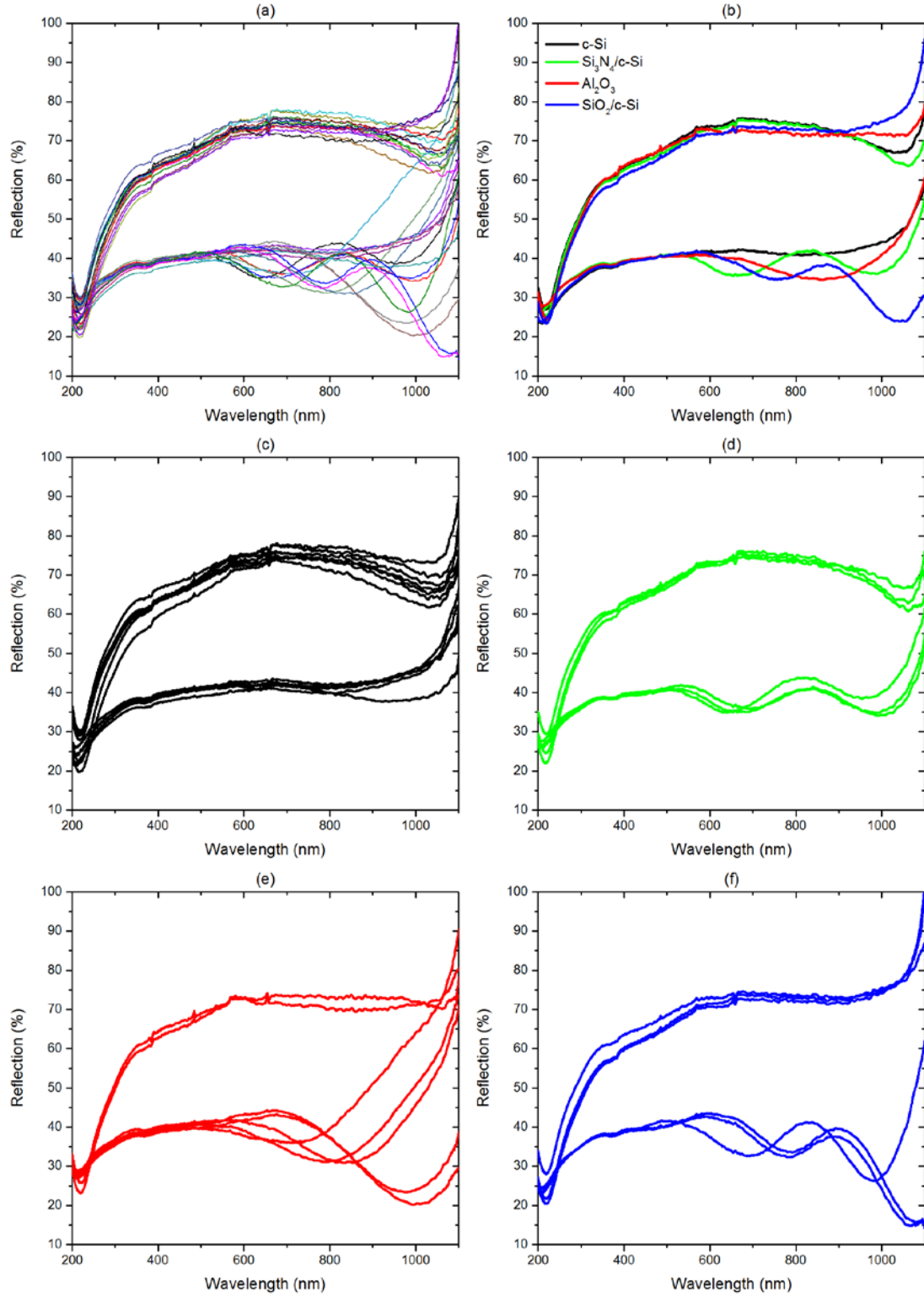


Figure 92. Spectral reflectance of GeTe on various substrates, where each curve corresponds to a sample. Within each plot, the upper set of curves are crystalline and the lower set are amorphous. (a) All sample measurements, (b) Averages within each type of substrate, (c) c-Si, (d) $\text{Si}_3\text{N}_4/\text{c-Si}$, (e) Al_2O_3 , (f) $\text{SiO}_2/\text{c-Si}$.

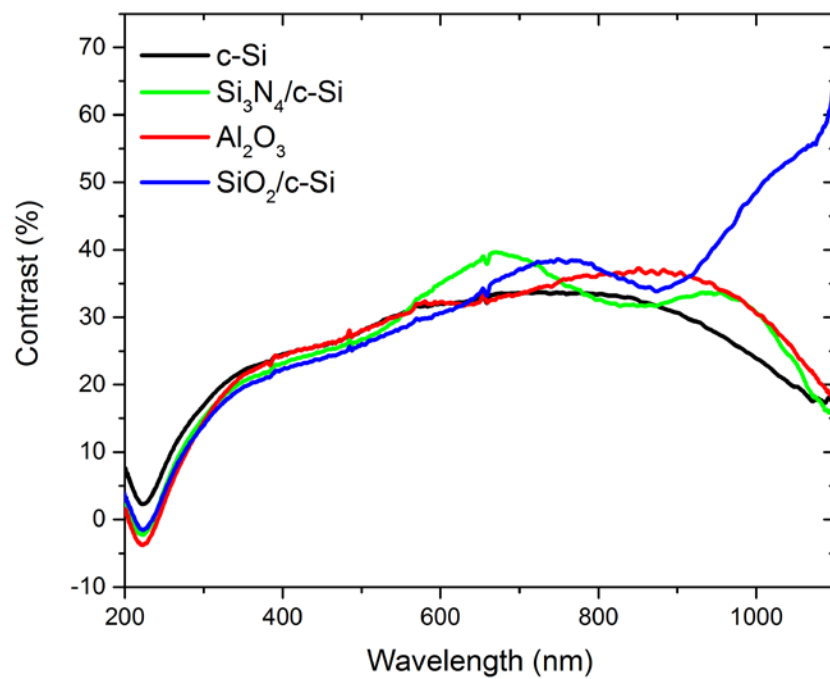


Figure 93. Contrast in spectral reflectance for GeTe by each substrate type. The average of the crystalline and amorphous data are subtracted to determine the contrast, in percent reflection.

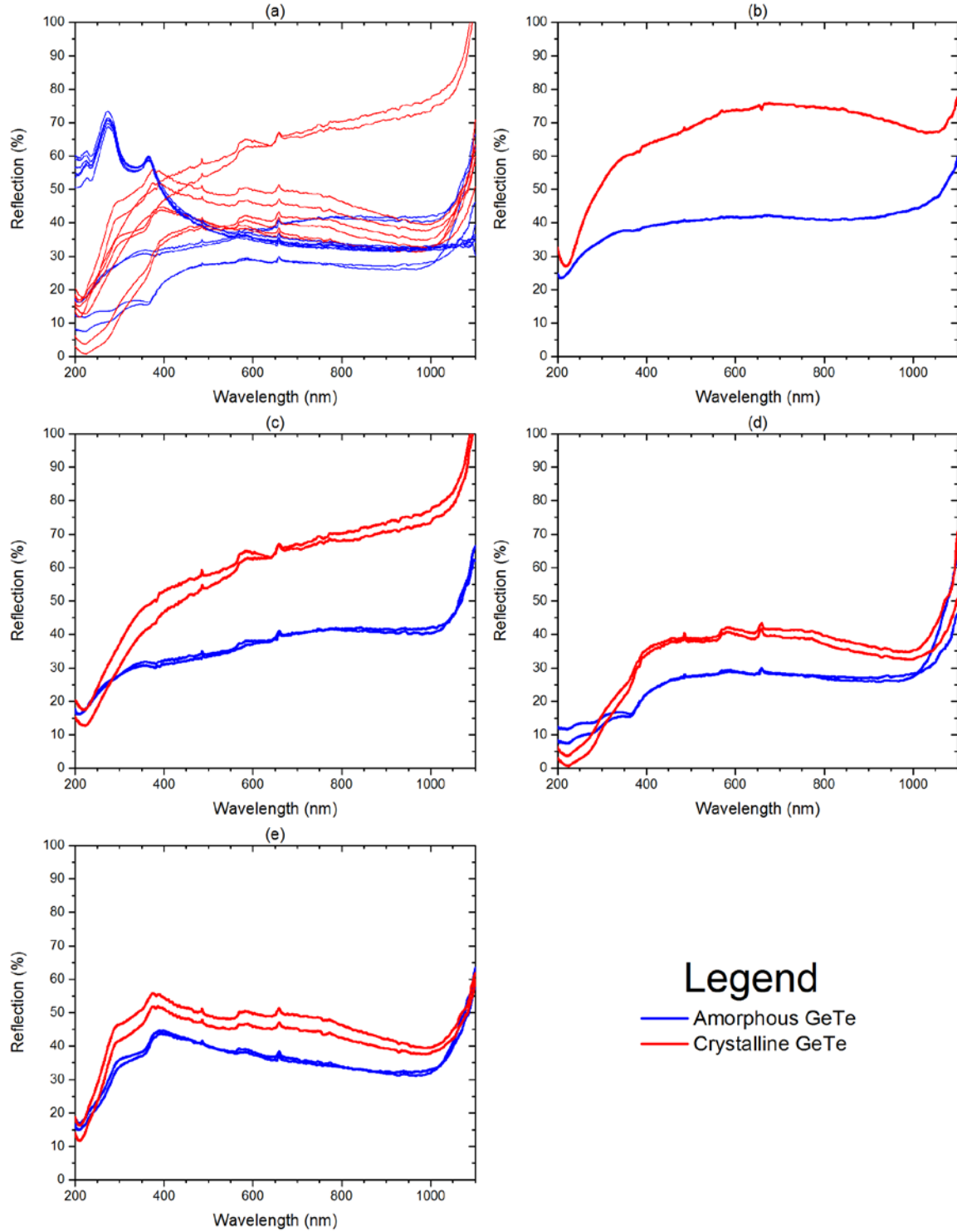


Figure 94. Spectral reflectance of (a) Sets 2 – 5 on c-Si, (b) The average reflection of both phases of Set 1, (c) Measurements of Set 2, (d) Measurements of Set 3, (e) Measurements of Set 4. Sets 5 and 6 were not crystallized and are not shown in this figure.

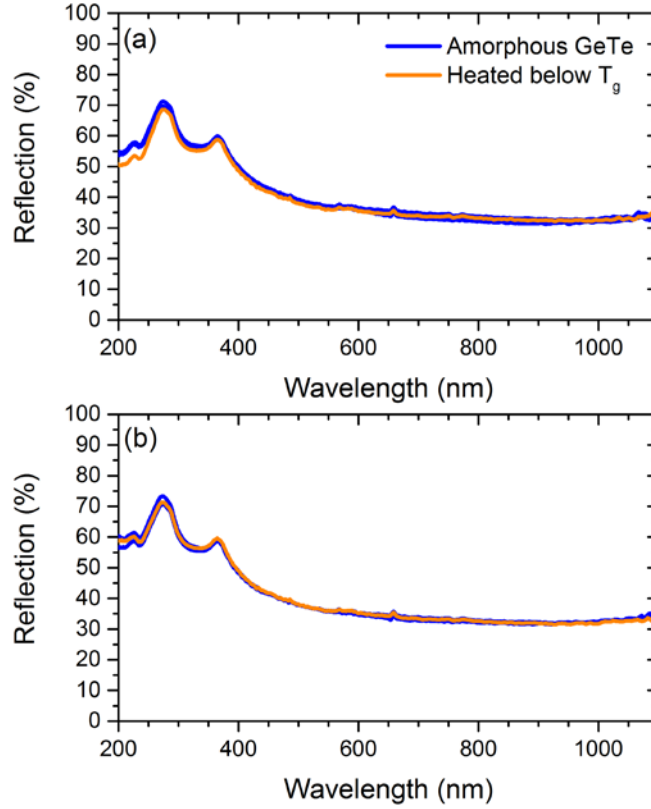


Figure 95. Spectral reflectance of (a) Set 5 and (b) Set 6.

4.3.10. Spectrophotometry and FTIR

Two optical systems were used to measure optical transmission across the UV, Vis, NIR, and MIR wavelengths. The Cary 5000 is a spectrophotometer with several optical sources which has an optical range of 200 nm (UV) to 3 μm (NIR). The Bomem FTIR covers the NIR and MIR from 1.33 μm to approximately 50 μm . The range from 20 μm – 50 μm is unusable, however, due to noise in the signal. In these experiments, the light transmitted through the sample is compared to the source's output and expressed as a percentage from 0 to 100%.

The data shown in Figure 96 is a GeTe thin film (300 W, 2 min) on double-sided-polished (DSP) intrinsic c-Si. Intrinsic silicon was used because of the fewer dopants

which scatter light. Typically in these experiments, the transmitted light is very sensitive to the polishing (SSP or DSP), where DSP has much more transmittance. Three measurements were taken: The substrate with no thin film (reference), amorphous GeTe on the substrate, and crystalline GeTe on the substrate. Because the Bomem FTIR has a gain factor, the gain was adjusted after taking measurements by scaling the data to match the overlap of the Cary 5000 from 1.33 μm to 2.5 μm .

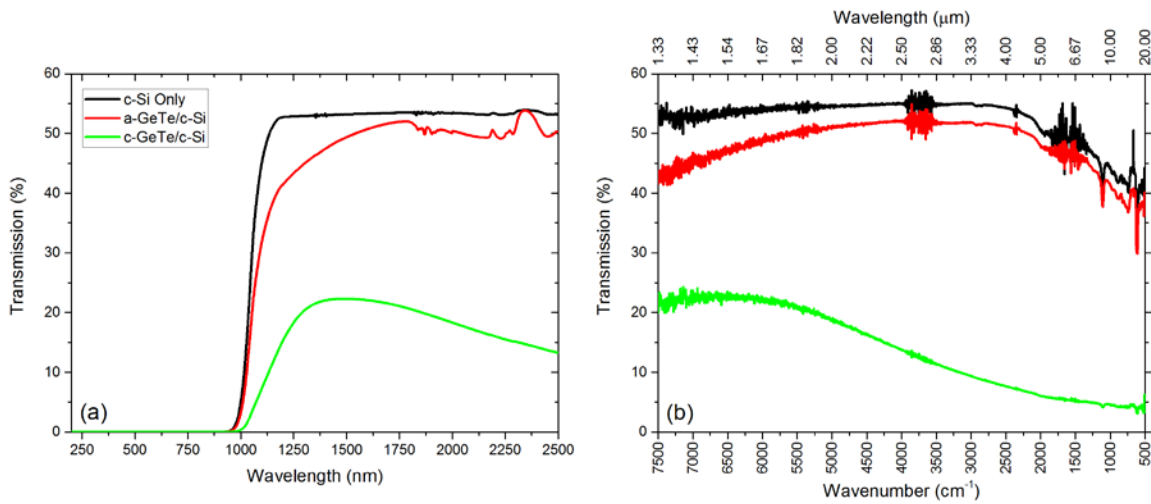


Figure 96. Optical transmission of GeTe on double-sided-polished (DSP) c-Si; (a) Spectrophotometry, (b) FTIR. FTIR is plotted vs. wavenumber, so the upper x-axis is converted to wavelength in microns. There is some overlap between the two plots, from 1.33 to 2.5 μm .

Another experiment was conducted to gain more information about the transmittance of GeTe in the UV region. For this experiment, a sapphire substrate was used which has a relatively broad bandpass region (well above silicon). Unfortunately, DSP sapphire was unavailable, so a SSP substrate was used instead. Figure 97 shows the GeTe transmittance data on the Cary 5000 from 200 nm to 3 μm . Two crystalline samples were measured in order to get more data points on the behavior of GeTe on sapphire due to the interesting fracturing of filaments observed earlier. The two c-GeTe

samples were heated to the same temperature in approximately the same amount of time. The transmission through the SSP substrate is relatively low, so the ratio of the transmission in the thin films to the substrate is shown in part (c).

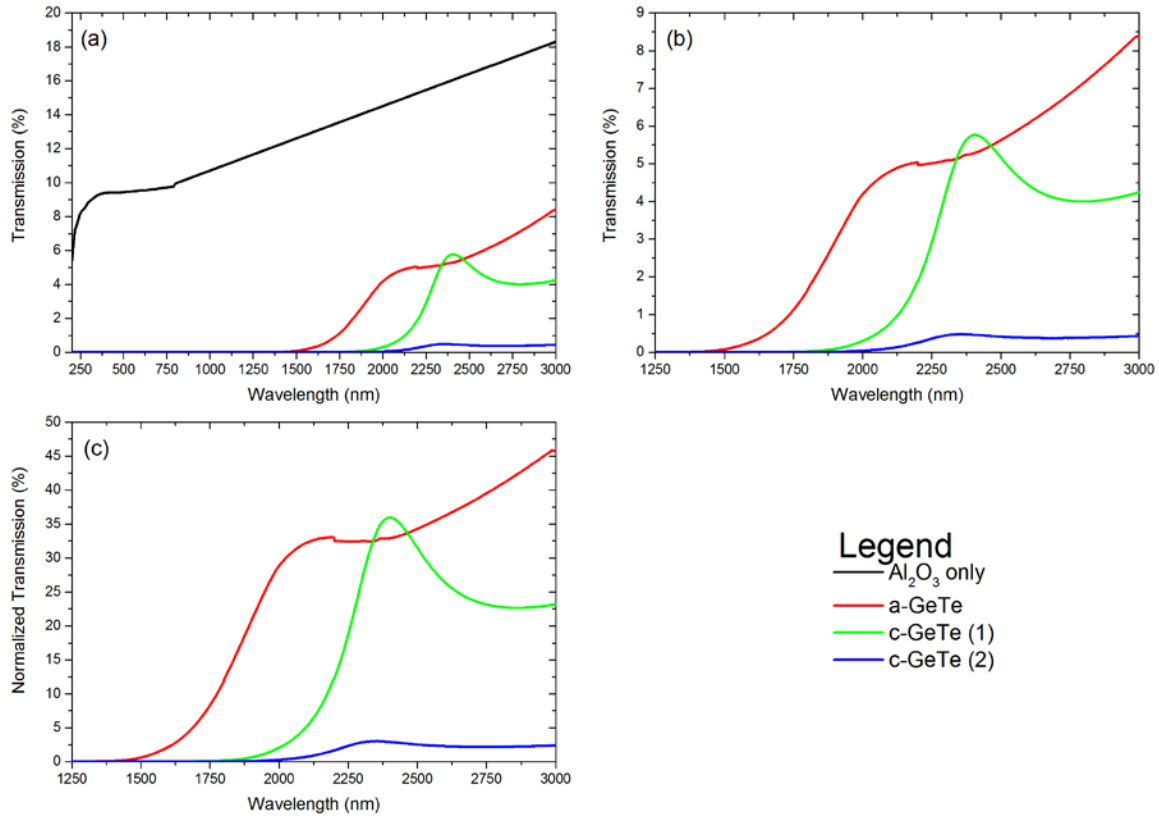


Figure 97. Optical transmission by spectrophotometry of GeTe on sapphire; (a) showing amorphous and crystalline data relative to the sapphire data, (b) closer view of GeTe transmission, (c) GeTe thin film transmission relative to the sapphire transmission at each wavelength. The small jumps apparent in the sapphire and a-GeTe data are due to the mechanical switching of optical sources.

4.4. Summary

In this chapter, data were presented on numerous experiments conducted with VO_2 and GeTe. For VO_2 , materials characterization methods EDS, XPS, and Micro-Raman were completed to determine the stoichiometry of three samples. For GeTe, data

were presented on fabricated devices, namely, resistance vs. temperature, I-V curves, capacitance vs. temperature, and S parameters in the microwave and RF regimes. Additionally, the crystallization temperature was determined for several thicknesses of GeTe independent of dielectric or metal layers adjacent to the material. Finally, GeTe was characterized by terahertz irradiation, spectroscopic ellipsometry, spectral reflectance, and optical transmission on several types of substrates.

5. Analysis

5.1. Introduction

This chapter analyzes the data collected in the experiments presented in the previous chapter. The physics of the observed phenomena are explained, and when appropriate, hypotheses are made which provide a best explanation of the processes which are occurring.

5.2. Vanadium Oxide

5.2.1. Sputtering Experiments

Vanadium oxide was sputtered with several parameters varied over the course of 13 total experiments. As mentioned in the previous chapter, between runs 8 and 9, the proper heating of the substrate was called into question. In order to test the substrate temperature, temperature dots and paint were placed on samples on the substrate. Temperature dots are typically used in the transportation of goods such as food in order to prove a temperature was not exceeded during transportation [151]. The temperature sensitive chemicals turn color when the specified temperature is exceeded. The temperature limit of these dots is 310°C, and for a higher range paint was used. The upper limit of the paint is 510°C. A six-inch-diameter silicon wafer was used in run 13, and temperatures in excess of 510°C were reached.

5.2.2. Resistance Measurements

Run 1c was the most successful resistance measurement. Based on those results, devices incorporating those sputtering parameters were made. However, the VO₂ in the

devices was metallic. Additionally, when sample 1c was retested, the same results were not able to be reproduced. At the end of the research, when the substrate temperature had been reconciled and the temperature was higher than 510°C, the material was again metallic.

5.2.3. EDS

As can be seen by the silicon peak in Figure 57, the energy of the source was great enough to penetrate through the VO_x film. Therefore the results are indicative of the inner bulk material and not only the surface, which could have an oxygen-rich composition [152]. This is a moot point though, because EDS cannot be used for elemental analysis of vanadium oxide materials. This is seen in Figure 58 by the blending of the V L peak and the O K peak. As indicated in Table 4, the K α energy of oxygen is 525 eV, and the L α energy of vanadium is 511 eV. It is unclear what percentage of the peak intensity is attributable to oxygen. In the extreme case of all of it being attributed to oxygen, the material would most closely resemble vanadium monoxide, VO. However, this is clearly not the case. Because of a portion of this peak belongs to vanadium, it seems (qualitatively speaking) that the material is vanadium rich. Clearly, this approach is fairly unscientific, which is why the testing was halted after the first sample and XPS and Micro-Raman were used.

5.2.4. XPS

Because sample 5a has two oxygen 1s components and the presence of carbon is larger in this sample, it can be concluded that approximately half of the oxygen is present

in oxygen-carbon bonding. For samples 11a and 12a, the stoichiometry seems closer to V_2O_3 than V_2O_5 . In sample 12a, the presence of a small amount of suboxide may be indicative of V_xO_y closer to V_6O_{13} , V_5O_9 , or VO . The overall ratios of oxygen to vanadium for samples 5a, 11a, and 12a are 1.9, 1.8, and 1.9, respectively. There is a correlation between increased temperature and vanadium-oxygen bonding. Heating the substrate encourages oxidation of the vanadium ions by increasing the mobility of the atoms on the surface of the wafer.

5.2.5. Micro-Raman

Raman spectroscopy was completed for the same samples as the XPS study. By comparing the Raman shifts of the measured spectra with published values, some information can be gained about the oxidation states of the vanadium. Table 11 lists published data on the measured Raman shifts of several forms of vanadium oxide. V_2O_3 , VO_2 , V_6O_{13} , and V_2O_5 are presented in the table (O:V ratios of 1.5, 2, 2.17, and 2.5, respectively). Because many other forms of vanadium oxide are not easily synthesized, there are not many published findings on the Raman spectra of the other oxidation states.

Sample 5a has the Raman spectra of mixed V_2O_5 and V_2O_3 with several small peaks characteristic of VO_2 . It should be noted that no silicon peak is present for this sample, so the observed spectra are for the surface. Because the samples were stored in a dry box, it is safe to assume that the film and surface are of the same composition and the samples are free from contamination. The spectra are rather noisy with less well defined peaks than the other two samples. This is most likely due to a lower quality of

crystallinity than the other two samples, due to a lower substrate temperature during deposition.

Sample 11a has a very strong 305 cm^{-1} peak which is characteristic of all the vanadium oxides presented in the table. There are other V_2O_3 peaks as well as five VO_2 peaks. The 110 and 943 cm^{-1} peaks are unidentified.

Sample 12a also has many mixed V_2O_3 and V_2O_5 states along with four VO_2 peaks. In this sample, there are four strong peaks which are unidentified. These could belong to other vanadium oxide compositions.

Note that both V_2O_3 and V_2O_5 are metallic at room temperature. V_2O_5 is a metal without a phase transition and is the most stable oxidation phase of VO_x . V_2O_3 does have a transition but it occurs at 165 K (-108°C).

Table 11. Raman spectra of various vanadium oxides; listed values are Raman shifts in units of cm^{-1}

VO_2 [153]	VO_2 [63]	VO_2 [154]	VO_2 [152]	VO_2 [155]	VO_2 [155]	VO_2 [155]	V_2O_5 [156]	V_2O_5 [152]	V_6O_{13} [156]	V_2O_3 [157]	V_2O_3 [158]
195	143	194	142	144	149	149	103	202	132	235	205
222	192	225	191	194	200	199	145	232	203	250	240
264	224	258	223	226	226	225	195	266	266	280	300
304	260	265	262	260	259	259	282	305	303	325	500
338	309	308	310	311	313	265	303	382	416	340	580
392	341	339	392	337	340	313	403	455	504	450	
439	389	392	443	389	392	339	483	504		505	
496	499	395	500	438	436	392	529	580		525	
622	612	444	613	493	501	395	700	640		575	
825		453		595	594	444	992			610	
		489		615	620	453					
		503		627		489					
		585				503					
		618				595					
		650				618					
		825				670					
						830					

5.3. Germanium Telluride

5.3.1. Resistance Measurements

While a nonvolatile transition is typical for GeTe, only a nonvolatile transition was observed with the substrates coated with dielectric layers. The bottom plots, c-Si and Al₂O₃, do exhibit a large decrease in resistance; however, the transition in these particular samples is volatile because the resistance returns to its original value once the PCM cell is cooled. Additionally, the starting resistance of the PCM cell on sapphire is greater than the other substrates, which has been observed with all the devices fabricated. All resistors undergo six orders of magnitude change in resistance except for c-Si, which has only three orders of magnitude change.

While this observation of volatile phase transitions in GeTe is remarkable, the volatility is not directly attributable to any change in stoichiometry of the thin films or volatility of the GeTe material. The process of GeTe on c-Si is due to heating of the substrates during fabrication. The heat transfer via conduction through one material, q_1 , and through two materials, q_2 , are expressed as

$$q_1 = \frac{T_H - T_{L1}}{\left(\frac{d}{kA} \right)} \quad (55)$$

$$q_2 = \frac{T_H - T_{L2}}{\left(\frac{d_1}{k_1 A_1} + \frac{R_i}{A_i} + \frac{d_2}{k_2 A_2} \right)} \quad (56)$$

where T_H is the high temperature, T_L is the low temperature, d is the thickness of the material, k is the thermal conductivity of the material, A is the cross-sectional area through which the heat is conducted, and R_i is the interfacial thermal resistance between

the two materials [159]. By dividing by the area, the denominator terms of d/k_l for the l^{th} layer become thermal resistances R_l in units of m^2KW^{-1} . (Note that $\Delta^\circ\text{C} = \Delta \text{K}$.) In the case of the dielectrics, R_{tot} is the sum of the two layers' resistances and the interfacial resistance; for c-Si and Al_2O_3 , it is simply d/k . G_{tot} , located in the final column of Table 12, is defined here as thermal conductance which is the reciprocal of the total thermal resistance. Thermal conductivities for SiO_2 [160], Si_3N_4 [161], c-Si [21], and Al_2O_3 [162] are 1.4, 0.03, 141.2, and 35, respectively, as indicated in Table 12.

As seen in Table 12, heat is conducted through c-Si more than the other three substrates. This is reinforced by the resistance of GeTe on c-Si being an order of magnitude lower at room temperature. From these observations, some important conclusions can be drawn regarding the crystallization process via conduction of GeTe. The phase transition of GeTe is growth dependent, meaning crystallites form primarily from the interfaces of the thin film. In Figure 66(a-b, d), a typical crystallization occurs because there is a high quality of growth from the GeTe/substrate interface upward into the thin film. The heat source in this experiment is below the substrate and as heat travels vertically through the substrate, dielectric layer, and GeTe, new crystallites are formed. In Figure 66(c), areas of crystallites exist at low temperatures. As the heat travels upward through the pockets of crystallites, the decrease in resistance is somewhat sporadic. This is evidence for the growth of crystallites forming poor interfaces with the existing crystalline pockets. The grain boundaries between the new and existing crystalline areas are poorly formed and highly resistive. When the upward spike occurs at approximately 225°C , there are no remaining amorphous areas along the existing crystalline layer. At the supplied critical thermal energy $E = kT$ ($T \approx 225^\circ\text{C}$), the polycrystalline grains fuse

temporarily to promote electrical conduction between the contact pads. As the temperature is reduced, the polycrystalline grains delaminate and the resistance of the cell increases. When sputtering a-GeTe on c-Si witness samples, and without heating on a hot plate, the transition has been seen to occur normally as seen in Figure 66(a-b).

Table 12. Heat conduction parameters (blank values are N/A).

Material	d [m]	k [Wm ⁻¹ K ⁻¹]	R _i [m ² KW ⁻¹]	R _{tot} [m ² KW ⁻¹]	G _{tot} [Wmm ⁻² K ⁻¹]
SiO ₂	3.00E-07	1.4		2.14E-07	
Si ₃ N ₄	1.00E-07	0.03		3.33E-06	
c-Si	5.00E-04	141.2		3.54E-06	0.28
Al ₂ O ₃	4.32E-04	35		1.23E-05	0.08
SiO ₂ /c-Si			1.78E-06	5.54E-06	0.18
Si ₃ N ₄ /c-Si			2.25E-06	9.12E-06	0.11

The process in sapphire (Figure 66(d)) appears to occur normally until the temperature is reduced, at which point the thin film's resistance increases to almost its original value; however, it is clear that it crystallizes completely. This may be due to the disparity in coefficients of linear thermal expansion. These coefficients (units of 10⁻⁶/°C) for SiO₂ [21], Si₃N₄ [21], c-Si [21], Al₂O₃ [163], and GeTe [164] are 0.5, 2.8, 2.5, 5.3, and 0.56, respectively. Therefore the order of magnitude difference in thermal expansion between sapphire and GeTe may cause fracturing of the conductive crystallites within the thin film and between the two contact pads as it is cooled. Additionally, there appears to be more stress in this system than for GeTe on the other three substrates. Sapphire has a hexagonal lattice; there is likely some stress due to lattice mismatching between GeTe and sapphire.

5.3.2. Application of Voltage Pulses

Despite best efforts to cause crystallization by voltage pulsing, this was not successful. The reason is clear based on the results from DC I-V experiments. The threshold voltage is well in excess of the waveform generator's maximum output voltage. For the second smallest cells on c-Si substrate, the threshold voltage is approximately 30 V, and the maximum the generator can supply is 10 V. Attempts to amplify the waveform were unsuccessful in either DC or AC modes. For a waveform, amplifying in AC mode is typical; however, due to the short pulse durations and fast rise/fall times, the amplifier was not able to amplify the signal. Diagnosis was performed using an oscilloscope, which verified that amplification was unsuccessful. By decreasing the interelectrode distance in the design, the threshold voltage would decrease and crystallization would be easily obtainable. For a design with an adjacent metal layer, the amorphization would be possible because metal quickly draws heat from the GeTe film.

5.3.3. I-V Curves

Figure 67 shows the I-V data for GeTe cells on four different substrates. In Figure 67(b), the typical I-V characteristic curve for PCRAM is observed. Conductivity is seen to increase exponentially until it reaches a threshold voltage, V_t , between 30 V and 30.8 V. An inward snap of the I-V curve is apparent, whereby the voltage in the cell is reduced and the current increases (large increase in conductivity). The subsequent voltage is called the holding voltage, V_h [69]. Once it is reached, the current increases with very little change in V_h ; however, some negative differential resistance (NDR) is seen in this region as well. The high levels of current provide enough Joule heating to

crystallize the GeTe thin film. Once the power is reduced, the conductivity is ohmic due to the crystallization.

These observations match those of Ielmini and Zhang based on their analytical model of subthreshold switching in chalcogenides, which was discussed previously. As u_a increases in their model, resistance increases, subthreshold slope of current decreases, and threshold voltage increases [93].

Based on this relationship between u_a and conductivity, the results in Figure 66 can be explained. In the horizontal design tested, u_a is actually three orders of magnitude larger (30 μm) than the vertically integrated design used in the model (30 nm). In the c-Si case, the effective u_a is decreased due to partial crystallization of the bottom portion of the GeTe film. It can be assumed that there are pockets of crystalline areas because the heat transferred during fabrication was not great enough to create a solid crystalline film. In the case of the others in Figure 66(c-d), u_a is too large to generate substantial current. The starting resistance is an order of magnitude larger than c-Si, the subthreshold slope is shallow, and the threshold voltage is not reached; however, NDR is visible in all three cells.

The presence of these non-idealities does not mean that amorphous chalcogenides cannot be used for threshold switching. If u_a were shorter ($\sim 1 \mu\text{m}$), typical memory curves like Figure 66(b) would be expected with a smaller threshold voltage ($F = V_A/u_a$). The horizontal design is simpler than the vertical design because it requires fewer lithography steps and fewer requirements are placed on the electrode materials [95]. By using electron-beam lithography for 1- μm -long or shorter cells for the horizontal

structure in the future, programming power can be reduced. Additionally, dielectric substrates reduce the power losses due to their low thermal conductivities.

Based on the results shown in Figure 68 for the smallest resistors, all of the resistors show an exponential increase in current consistent with the subthreshold model. Again for the dielectric substrates, the interelectrode distance is too large to facilitate threshold switching. These devices fail as a result of electric field breakdown. For the c-Si substrate devices in part (b), there is a much larger increase in current of approximately four orders of magnitude. Threshold switching does occur, as seen with the sudden increase in current. However, for these devices, the contact resistance dominates the current-voltage curve due to the large cross-sectional area. The interelectrode distance is 6 μm and the height of the GeTe strip is the height of the contact pad, which is 100 μm . For the second smallest resistor for which memory I-V curves were obtained, the interelectrode distance is 30 μm with a height of 10 μm , so the contact resistance was negligible. Oscillations occur for the smallest resistors at a current that depends on the initial crystallinity of the material and the contact resistance.

Some interesting I-V curves result as a function of increasing degrees of crystallinity in Figure 69. As seen in part (d), the resistance decreases by approximately 4 orders of magnitude over the course of Trial 1, and the ending resistance of Trial 1 is only one order of magnitude lower than its starting resistance. For the subsequent trials, there is less of a modulation of resistance, which indicates that the majority of the cell is crystallized during the first trial—but not all of it. What is also interesting is the reduction in threshold voltage as indicated in part (c). The threshold voltages for the four trials are 30 V, 16 V, 15 V, and 12.5 V, respectively. Because the amount of the cell that

is crystalline is increasing after each trial, the effective interelectrode distance decreases as well, just as was explained for the fabrication-dependent mechanism. Within each trial, the current through the crystalline filaments acts to heat and crystallize the surrounding amorphous material; more is crystallized after each trial. Also present in each curve is the characteristic voltage snap-back. This threshold switching is easily seen on the resistance curves as a drop of approximately two orders of magnitude. The bend in the lower portion of these resistance curves is due to the reduction of voltage at the peak of the memory switching region. Although there is very little modulation in the resistance between Trials 2 and 4, a significant contribution of 3.5 V is made to the threshold voltage.

The localized heating results of the top/bottom heaters are fairly straightforward. The black curve in Figure 71 is a typical I-V curve for which the threshold voltage is not reached. In the other curves, an upward shift in current is observed for a given voltage across the length of the GeTe (V_d). The step in current increases as V_g increases. Additionally, a negative voltage is observed for $V_d = 0$ with less magnitude than the applied V_g . These results are fairly intuitive when considering the flow of current due to the voltage drops across the GeTe cell. Due to the applied voltage V_d , current flows from the left to the right (positive terminal to the negative terminal) because electrons are moving toward the positively biased terminal from right to left. The applied heater voltage V_g is biased negatively with respect to the right contact pad. That is, the negative terminal of V_g is on the middle heater and the positive terminal is on the right contact pad. For this applied voltage, the current flows from the heater and current is injected from the heater's metal layer through a portion of the GeTe strip and to the opposite

terminal at the “drain”. The injected current contributes to the overall current in a fairly predictable manner based on V_g .

5.3.4. Capacitance Measurements

The capacitance measurements of GeTe as the dielectric layer in a capacitor were unstable and inconsistent. This is most likely due to a poor design of leaving areas of the bottom metal layer exposed. Ideally, the dielectric layer would completely overlap both of the electrodes in order to produce a stronger electric field across the dielectric layer. This was not possible with horizontally designed capacitors, however, because the bottom probe pad must be contacted by a probe tip. A possible implementation in the future would be to have GeTe completely overlap the bottom metal layer and to run a small metal connection between a small probe pad and the bottom electrode.

5.3.5. S Parameters

The S parameters were presented in the previous chapter based on substrate type and device size. For all of the RF switches in the amorphous phase, S_{11} (reflection coefficient) is approximately zero across the entire frequency range, and S_{21} (insertion loss) is very high in magnitude and varies between -30 and -80 dB. Therefore, the switches have a high quality OFF state due to the high resistance in the $M\Omega$ range. For the switches in the crystalline phase, there are some devices which perform better than others. For all of the substrates and all the frequency ranges, only the first two switches performed well. In the ON state, these two switches had S_{11} lower than S_{21} ; that is, there are fewer reflection losses than insertion losses. For the next five switches, they behave

as if they are OFF with fewer losses than the amorphous phase. This is due to the increasing resistance of the signal line caused by the longer lengths of GeTe. Therefore, these switches perform very well but could be even better by reducing the size of the GeTe strip in the signal line. This would decrease the resistance of the crystalline phase so that an impedance matched $50\ \Omega$ could be achieved.

For the two smallest RF switches identified for their superior S parameters, insertion losses are very small. On c-Si, losses are between 1.25 and 2.5 dB over the entire frequency range. On the dielectric substrates, these same switches' losses are slightly greater, between 2.5 and 5.0 dB. The five larger switches have losses which are far too large (approximately 5 to 25 dB) to be practical in any switching applications. For these switches, the losses are too great and not enough power is delivered to the load. Isolation (blue curves and axes) is also the largest for the two smallest switches, which is very encouraging due to the highly attenuating nature while in the OFF state. Highest isolations of 20 – 30 dB are indicative of strong OFF performance. These isolation values do decrease as the frequency increases, which is typical of RF switches in general. Note that while there is some ringing in the upper frequencies of the 300 kHz to 3 GHz range, this is due to poor calibration of the PNA, and those oscillations can be neglected due to the overlap with the 10 MHz – 20 GHz measurements. Shim et al. [138] fabricated a phase change RF switch and had insertion losses of approximately 0.6 dB and isolation of approximately 20 dB. In terms of isolation, these switches perform comparably, but insertion losses are too great. However, by down-scaling the length of the signal line by approximately two-thirds, insertion losses of less than 1 dB should be readily obtainable.

5.3.6. Determination of T_c for various thicknesses

The first range of 191.9 – 201.2°C was obtained for 300 W and 2 min of sputtering, which is the same thickness as the resistance vs. temperature data collected on various substrates in section 5.3.1. The crystallization temperature shown in Figure 66 on the dielectric layers is approximately 215°C; therefore, the introduction of the dielectric does increase the crystallization temperature by approximately 15°C. The second set (100 W, 2 min) sees an increase in T_c of approximately 5°C. The largest increase is set 3 which has a T_c of approximately 290°C. This seems uncharacteristic of the rate of increase of sets 1, 2, and 4, especially since set 4's T_c is approximately 263°C. It is possible the third set had a thicker layer of native oxide than the others which contributed to the increased temperature. For the last two sets, the crystallization temperature was not achieved because it was higher than the capability of the probe station. These experiments prove that crystallization temperature does change based solely on the thickness of the material.

The physical reason for this increase is most likely due to a surface screening of the material, as seen with VO_2 . The native oxide on c-Si acts as a crystallization inhibitor, and a very thin (~1 nm) interfacial screening layer exists within the bottom portion of GeTe. Past this critical thickness, the growth-dominated crystallization occurs. As the thickness of GeTe is decreased, this interfacial layer occupies a larger percentage of the thin film's volume, and its effects play a larger role.

This effect is especially important for PCRAM, where in vertically integrated PCRAM cells, threshold voltage can be decreased by depositing a thinner layer of the PCM since it is electric field-dependent. However, because the crystallization

temperature is higher, a higher voltage will be required to supply enough current to crystallize the layer. On the other hand, materials with higher crystallization temperatures are more thermally stable, and data retention will be ensured at higher temperatures. There is clearly a tradeoff between lower threshold voltages and higher crystallization temperatures.

5.3.7. Terahertz Transmittance and Absorbance

Terahertz irradiation was tested on GeTe films of approximately 200 nm thick. The time-domain signal of the thin film/substrate samples with respect to the relaxed measurement yield some important information. (Recall that the relaxed measurement tested the transmittance of fully crystalline GeTe on sapphire at room temperature.) Based on the peak intensity of the relaxed sample and 200°C and 210°C, the crystallization temperature of this system is approximately 209°C. This is a few degrees greater than observed on the c-Si substrate. Additionally, based on the scanner position (x-axis), the thin film and substrate become appreciable thicker as they are heated. This is expected due to thermal expansion. As noted previously in the thermal characterization, the linear thermal coefficient of expansion of GeTe is approximately 10% of sapphire. The scanner position of the reference is 22.16 mm, and the final position at 250°C is approximately 22.24 mm, for a total expansion of 0.08 mm or 80 μm . The sapphire substrate is 432 μm thick at room temperature. Because the GeTe film is only 0.2 μm thick, the contribution of expansion from GeTe is negligible and sapphire experiences 15.6% growth along the c-axis.

Based on Figure 87, the transmittance decreases with increasing temperature, with its largest increment at its crystallization temperature. It is important to note that there is a transmittance peak at approximately 15 cm^{-1} (450 GHz). There are more noticeable perturbances in the broadband transmittance at lower temperatures, whereas past its crystallization temperature the transmittance is generally flat. The curves with temperature below the crystallization temperature can be considered different insulators with varying degrees of density in their lattice. Past the crystallization temperature, the material can be considered a metal with a relatively dense structure. Terahertz is known to poorly transmit through metal layers, which is utilized in metamaterials in the form of SRRs. Past the crystallization temperature, there is a small decrease in transmittance partly due to an increase in carrier density as a function of temperature. Most of the decrease past T_c is most likely due to thermally-induced lattice vibrations. Based on the value of the relaxed sample relative to the crystalline curves between 10 and 60 cm^{-1} , the relaxed sample traverses the data of 210°C , 220°C , and 230°C . Above 60 cm^{-1} , the relaxed sample has a transmittance between 200°C and 210°C .

The absorbance is the inverse log of the transmittance, so where there are transmittance peaks there are absorbance valleys and vice versa. The absorbance is generally greater in the region of $70 - 100\text{ cm}^{-1}$, where a plateau region appears at temperatures greater than or equal to 150°C .

From Figure 89, the modulation can be inspected based on the contributions of the sapphire substrate and the GeTe thin film. By using equations 52 – 54, the GeTe modulation is isolated from that of the sapphire substrate. As seen by the black curve, there is a transmittance peak at 15 cm^{-1} due to sapphire. The absorbance of GeTe and

sapphire increases from 15 to 70 cm^{-1} . At this point, the density contribution of the carriers at high temperature significantly increase the absorbance at two absorbance peaks of 80 cm^{-1} and 105 cm^{-1} which was noted previously in the absorbance spectra. The contribution of the sapphire tends to flatten these two peaks into a relatively flat plateau of high absorbance. Of utmost importance is the modulation of GeTe only at R.T. which does not fall below 90% modulation across the entire spectrum. At its highest level, its modulation is 93%. These results are remarkable considering that the modulation of VO_2 on sapphire while heated is 80% at its highest point. When used on sapphire and heated to 250°C, the modulation depth is approximately 99.5% between 75 and 105 cm^{-1} .

5.3.8. Spectroscopic Ellipsometry

The extinction coefficient increases from amorphous to crystalline phases at every wavelength measured, and the index of refraction increases for energies less than approximately 2.5 eV. The contrast for optical phase change media is quantified as $\Delta\tilde{N} = \Delta n + i\Delta k$ where the amorphous n and k values are subtracted from the crystalline values. This is typically done at 405 nm, which is the Blu-ray wavelength. In this case for GeTe, $\Delta n + i\Delta k = -0.858 + i1.056$ at 407 nm (3.05 eV). This is approximately 80% of the Blu-ray PCM, $\text{Ge}_8\text{Sb}_2\text{Te}_{11}$ [78]. The contrast decreases for shorter wavelengths, which demonstrates the challenge for engineering optical media for Blu-ray and the fourth generation of optical memory. Additionally, the ϵ_i peak is broad in the amorphous phase, as expected, which corresponds to a smearing of electronic states. The increase of extinction coefficient from amorphous phase to crystalline phase is indicative of

increased absorption, primarily in the infrared wavelengths. These data correspond to the optical transmission experiments where the broadband absorption increases from amorphous to crystalline phases. Additionally, the *in-situ* rate of increase in absorption seems to proportionately follow the rate of decrease in resistivity—a monotonic relationship with the largest change occurring at the crystallization temperature.

5.3.9. Spectral Reflectance

Spectral reflectance measurements are worthwhile because they directly measure the reflection that is typical in optical memory applications. In the place of writing bits with a laser, the material was crystallized by conduction. The crystalline and amorphous curves form an envelope of contrast between approximately 200 nm and 1100 nm. At the endpoints, the contrast is approximately zero or even negative. For a negative contrast, the reflection of the crystalline phase is lower than the amorphous phase. These shorter wavelength (below about 400 nm) are UV wavelengths; Blu-ray uses 407-nm laser diodes. As seen on the c-Si curves, the contrast at 407 nm is approximately 25%. This is without any optical engineering of dielectric layers to increase the contrast. For the dielectric layers in parts (d) and (f) in Figure 92, oscillations are apparent in the amorphous reflection. These oscillations correspond to the thickness of the underlying dielectric. Because the reflection in this region of GeTe is relatively constant, the oscillations of the dielectric are easily seen. Therefore, for the Si_3N_4 layer, the thickness can easily be approximated as 120 nm since the peaks occur at integral multiples of the thickness of the dielectric. For the SiO_2 layer, it seems that there are samples which have

thicknesses which vary quite a bit. As seen in Figure 98, samples 2 and 3 have an SiO₂ thickness that is different than sample 1.

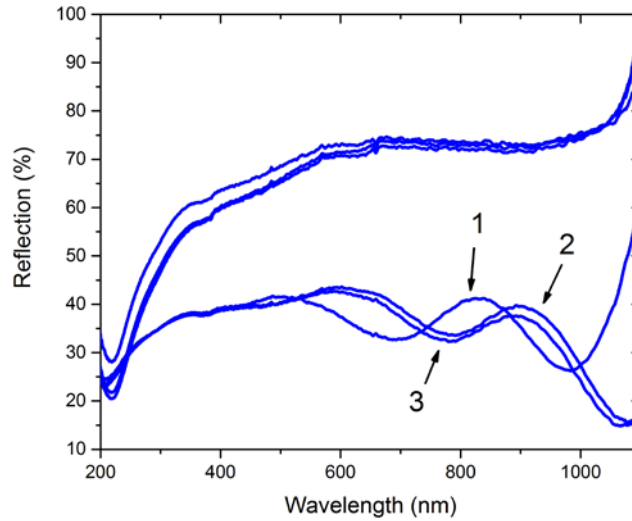


Figure 98. Measured spectral reflectance of GeTe on SiO₂/c-Si substrate.

The thicknesses of samples 2 and 3 are approximately 300 nm, and the thickness of sample 1 is approximately 250 nm. For the sapphire samples, the structural relaxation of GeTe in the amorphous phase is apparent. The underlying sapphire layer is the same thickness as is the GeTe thickness for these samples. The amorphous samples were not heated in any way, even during fabrication. Therefore the variance is due to defect annihilation based on varying degrees of relaxation. Based on these results, it seems that the structural relaxation may be more apparent on sapphire than the other substrates. This is most likely an effect of the induced strain between the sapphire substrate and GeTe thin film. Additionally, based on the GeTe/dielectric data, it is apparent how engineering of dielectric layers can increase contrast for a particular wavelength: By controlling the thickness of the dielectric, the lowest point (valley) of an oscillation in the

amorphous phase can be chosen to coincide with the wavelength of choice (i.e., approximately 680 nm for line 1 in Figure 98). For instance, based on the contrast plot (crystalline minus amorphous) in Figure 93, the contrast for the SiO₂/c-Si substrate is nearly 70% at 1,100 nm. In that measurement, there was only one dielectric layer; contrast can be increased even more by using two layers. The thickness of the GeTe layer also matters, as seen with the thinner samples.

The spectral reflectance of the thinner samples is shown in Figure 94, with part (b) as a reproduction of the average c-Si data in Figure 92(b). As the samples become thinner, the contrast seems to decrease. Also apparent are small peaks in reflection at wavelengths 650 nm, 575 nm, and 475 nm. These are seen in the thicker samples as well but are more visible in the thinner samples. In part (e), a peak is observed at approximately 350 nm in both crystalline and amorphous phases. This peak is more intense in the two thinnest sets of samples, shown in Figure 95. The peaks at 300 nm and 250 nm are due to the underlying native oxide, which have been seen on other samples. These two sets were not crystallized. Unfortunately the thickness of these samples cannot be accurately measured. Because the reflection in the amorphous phase is so high, it is reasonable to assume that based on the pattern for the other samples, that the contrast is very small or perhaps nonexistent.

5.3.10. Spectrophotometry and FTIR

The plots in Figure 96 of GeTe on c-Si show that for wavelengths greater than 1,100 nm the transmission of light through the GeTe/c-Si sample is within a few percentage points of c-Si only. When crystallized, however, the light transmission is

decreased by more than half. This absorbance of light increases toward the FIR. Because data cannot be collected above silicon's bandgap, another substrate was used to attempt to get that information.

The GeTe/sapphire data in Figure 97 show more attenuation than expected. In the amorphous phase before the transmission rolls off, between 30 and 50% of light is transmitted. What is most interesting about this experiment is the increase in transmittance of the first crystalline sample above that of the amorphous sample at 2,400 nm. The second crystalline sample (< 5% transmission) is closer to what would be expected based on the experiment on c-Si. As seen in the spectral reflectance experiment, a-GeTe is sensitive to structural relaxation especially when deposited on sapphire. Additionally, when in the crystalline phase, the conductive (crystalline) filaments tend to fracture as the substrate is cooled after GeTe is crystallized. Based on these two observations, it would be possible to have a c-GeTe film which transmits more light than a-GeTe. (The likelihood that there is an error in the measurement system is negligible, based on the repeatability of measurements on the system.) The most likely explanation for this phenomenon is that the amorphous film has undergone structural relaxation and also the crystalline film has many fractured crystallites.

5.4. Summary

5.4.1. Vanadium Oxide

Based on the lack of success of the resistance measurements and the results of the XPS and Raman experiments, the best hypothesis to explain the results is that there is not enough oxygen present in the VO_x system. XPS showed that higher temperatures

generally encouraged V-O bonding, but still no phase transition was present for samples deposited with the same parameters above 510°C.

It is possible that less oxygen is entering the sputtering chamber than indicated on the flow meter. A calibration of the equipment would verify the correct flow and mixture of O when reactive sputtering.

To support this hypothesis, as a next attempt, the best recommendation would be to sputter three times with the parameters of run 13, with oxygen pressures of 8.5%, 9.0%, and 9.5%. Testing with an ohmmeter on the probe station as temperature is increased would help to see if increasing the oxygen content would help increase the resistance at room temperature. Additionally, RF sputtering with a V_2O_5 metallic target at approximately 1.25% O_2 could reach stoichiometric films more easily due to a starting stoichiometry of O:V of 2.5.

5.4.2. Germanium Telluride

Many experiments were conducted involving GeTe. Most of them were successful and much has been learned about the material and its applications. Unsuccessful experiments were voltage pulsing and capacitance measurements; the rest were successful. Resistance vs. temperature data was collected for GeTe in devices on four types of substrates, DC I-V curves were generated for three device geometries and the underlying physics were explained, S parameters were collected for seven geometries of RF electrical switches on three substrates across two frequency ranges, and insertion loss and isolation were quantified for these RF switches. Additionally, the crystallization temperature was determined for four thicknesses of GeTe, and terahertz time-domain

spectroscopy experiments were conducted to determine that GeTe is a very good broadband transmittance modulator. Finally, GeTe was characterized using spectroscopic ellipsometry, spectral reflectance was gathered in both phases, on four types of substrates, and for varying thicknesses, and optical transmission data were gathered for GeTe in both phases on two types of substrates, from UV to MIR.

6. Conclusions

6.1. Conclusions of Research

Many aspects of two important materials, vanadium dioxide (VO_2) and germanium telluride (GeTe), were researched. In-depth analyses were provided for the physical mechanisms of the phase transitions for both materials. The major difference between the transitions is the volatility, which is caused by the type of structural change that occurs. Based on this difference and their physical orientations, the materials have very unique electrical and optical properties, which can be used for many different applications.

The complex deposition of VO_2 was researched, and experiments were conducted to test the relationship between sputtering parameters and MIT behavior. Several materials characterization methods were used for feedback on the deposition process. When reactive sputtering using a vanadium target, oxygen is lost to carbon bonding and to stoichiometries other than VO_2 . However, as the substrate temperature is increased, the quantity of vanadium-oxygen bonding increases. While the exact parameters for stoichiometric VO_2 were not discovered, much progress was made.

Microelectronic devices were designed and fabricated in the AFIT cleanroom. These devices incorporated GeTe as the active layer. Interesting results were measured as a function of device type and dimensions and substrate type. GeTe was used for the application of phase change random access memory (PCRAM). While the threshold voltage of the devices is rather large, the material looks promising for this application for interelectrode distances on the order of $1\text{ }\mu\text{m}$. This research reinforces that GeTe is better

suited to electronic memory than optical memory (due to lack of contrast and slower laser-induced crystallization speeds). Additionally, using GeTe in electronic RF switches, where ON and OFF states are determined by crystalline and amorphous phases, respectively, looks very promising.

Lastly, many materials characterization methods were used to explore GeTe and its numerous applications to many fields. In addition to DC I-V and resistance experiments and Microwave and RF S-parameters, the following were completed: Determination of the crystallization temperature based on the film's thickness, terahertz time-domain spectroscopy, spectroscopic ellipsometry, spectral reflectance in the UV-Vis-NIR, spectrophotometry in the UV-Vis-NIR, and FTIR in the NIR-MIR ranges. The modulation of terahertz transmittance is as high as 99.5% for GeTe/sapphire at 250°C and 93% for only GeTe at room temperature (compared to 80% of VO₂ and 50% for state-of-the-art modulators). The optical contrast between phases was determined by spectroscopic ellipsometry to be $\Delta n + i\Delta k = -0.858 + i1.056$ at 407 nm (3.05 eV). Additionally, the optical transmission and reflection have a measured contrast of up to 70% between crystalline and amorphous phases.

6.2. Contributions

The following are significant discoveries and actions which will benefit AFIT's microelectronics engineering department as well as the community of physicists and engineers studying phase change materials.

- Research and defining of the important sputtering parameters for the deposition of stoichiometric VO₂.

- The demonstration of the excellent RF switching properties of GeTe in the microwave and RF regimes; for the smallest switches, insertion losses were approximately 2 dB and isolation was greater than 30 dB.
- The defining of the critical physical dimensions for the best RF electronic switches using GeTe.
- The demonstration of GeTe as a suitable material for PCRAM applications, including regions of subthreshold/amorphous OFF, voltage snap-back, amorphous ON, memory switching, and crystallization due to Joule heating.
- The discovery of the fracturing of conductive filaments/crystallites in GeTe on sapphire substrates due to differences in thermal expansion between the thin film and sapphire substrate.
- The demonstration of six orders of magnitude decrease in resistance for GeTe when heated to its crystallization temperature from room temperature.
- The discovery and demonstration of the growth-dominated crystallization of GeTe.
- The demonstration of the importance of the relationship between interelectrode distance and threshold switching in chalcogenides for PCRAM applications.
- The demonstration of GeTe as having 80% of the optical contrast of $\text{Ge}_8\text{Sb}_2\text{Te}_{11}$ for 405-nm-light applications such as Blu-ray.
- The creation of a simple thin film/substrate system which has 70% contrast between ON (crystalline) and OFF (amorphous) phases at 1,100 nm.

- The discovery of the unique and directly applicable properties of GeTe as a nonvolatile, tunable absorber in the terahertz regime with unprecedented modulation depths.
- The demonstration of 99.5% terahertz transmittance modulation for a GeTe/sapphire system.
- The demonstration of increasing crystallization temperature for increasingly thinner GeTe films, to temperatures in excess of 400°C.
- The demonstration of infrared transmission filtering of over 30% between amorphous and crystalline phases.
- The discovery of the enhanced effects of structural relaxation of GeTe in its amorphous phase when on sapphire substrates.
- The creation of a unique GeTe microelectronics cell which demonstrates the effects of localized Joule heating .

6.3. Recommendations for Future Research

The following are recommendations for future research based on knowledge gained during this thesis work.

- Further experimentation with deposition of VO₂. Recommendations are RF sputtering of a V₂O₅ target, 1.25% O₂, with substrate heating, and V target, 10% O₂, with substrate heating. It has been observed that some oxygen will be lost to carbon bonding and stoichiometries other than VO₂.
- Completion of an etch study of stoichiometric VO₂; as a baseline, use the etch study documented by Gurvitch et al. [53] discussed in section 3.3.

- Creation of GeTe cells which have an interelectrode distance of less than 1 μm . Perhaps the best design is a vertically-oriented one since the interelectrode distance is the thickness of the sputtered GeTe. The drawback of this design, however, is the multiple fabrication steps, including PECVD of a dielectric layer and RIE.
- Demonstration of voltage pulsing of GeTe for crystallization and amorphization, using the above cell structure.
- Demonstration of voltage pulsing RF electronic switches. The above cell structures can be easily modified to include 3 RF-type terminals on either electrode. As a baseline, the length of the GeTe strip should be approximately 75 μm , given the constraints of the height of ground/signal/ground heights and 200-nm-thick GeTe film. From this baseline, construct some devices slightly smaller and slightly larger with varying amounts of overlaps between the metal contacts and GeTe. Optimum performance is achieved with a total signal line resistance of 50 Ω .
- In the above RF cell structure when using localized heating with voltage pulses, all four S parameters should be measured. Because the heating is not uniform, the losses associated with each device port may not be equal.
- Creation of a metamaterial-like terahertz device which allows the voltage pulsing of the GeTe thin film. The device should also permit the transmittance of the terahertz light through the GeTe thin film. An underlying metal layer will block the terahertz signal, so engineering an SRR-type design is optimal.

Appendix A. Process Follower for GeTe on 3" Silicon Wafers

Initials	Process Step	Notes	Date/ Time
	General Comments <input type="checkbox"/> Page 1: Bottom layer of Au (Mask 1) <input type="checkbox"/> Page 2: Middle layer of GeTe (Non-inverted Mask 2) <input type="checkbox"/> Page 3: Top layer of Au (Mask 3)	<u>Start Date</u> <u>Start Time</u>	
	Cleaning of Wafer (Acid Hood) <input type="checkbox"/> Note: If wafer is SiO ₂ /Si or Si ₃ N ₄ /Si, clean the wafer instead of using BOE. Refer to the first step of page 2. <input type="checkbox"/> Submerge in BOE for approx. 2 min while agitating the wafer <input type="checkbox"/> Rinse in DI water for approx. 30 sec <input type="checkbox"/> Dry with nitrogen on Texwipes <input type="checkbox"/> Bake on hot plate for 2 min at 110°C		
	Cleaning of Mask 1 (Solvent Hood) <input type="checkbox"/> Rinse with acetone for 30 sec <input type="checkbox"/> Rinse with methanol for 30 sec <input type="checkbox"/> Rinse with de-ionized water for 30 sec <input type="checkbox"/> Dry with nitrogen on Texwipes		
	1818 Photoresist (Solvent Hood) <input type="checkbox"/> Flood wafer with 1818 photoresist using dropper <input type="checkbox"/> Spin wafer for 30 sec at 4,000 rpm; Ramp at 200 rpm/sec <input type="checkbox"/> Bake wafer on hot plate for 75 sec at 110°C		
	Alignment & Exposure (MJB-3 Mask Aligner) <input type="checkbox"/> Align mask and wafer in x, y, and theta directions <input type="checkbox"/> Expose for 7 sec		
	Developing of Photoresist (Base Hood) <input type="checkbox"/> Place wafer in Petri dish and flood wafer with 351 Developer <input type="checkbox"/> Agitate Petri dish for 45 sec <input type="checkbox"/> Rinse wafer with DI water for approx. 30 sec <input type="checkbox"/> Dry with nitrogen on Texwipes		
	Inspection of Lithographic Process (Optical Microscope) <input type="checkbox"/> How is the alignment? Focus on the smallest features. <input type="checkbox"/> Are the features clean and open with sharp definition? <input type="checkbox"/> If necessary, strip photoresist using acetone or re-develop		
	Pre-metallization Cleaning (Plasma Asher) <input type="checkbox"/> Place wafer in O ₂ plasma asher for 2 min at 75 W (default setting)		
	Contact technician when samples are ready for metallization Evaporation: Ti (100 Å) adhesion layer, Au (1,000 Å) on top of Ti		
	Metal Lift-off <input type="checkbox"/> Adhere Scotch tape to wafer and pull metal from surface		
	Ultrasonic <input type="checkbox"/> Place the wafer in a Petri dish and place the dish in ultrasonic bath <input type="checkbox"/> Using a beaker, fill the bath with water until the Petri dish floats <input type="checkbox"/> Submerge the wafer in the Petri dish with acetone <input type="checkbox"/> Ultrasonic for approximately 8 min; continue longer if needed <input type="checkbox"/> Rinse/spin with acetone, methanol, and DI water at 500 rpm (30 sec for each solvent, as in cleaning process on next page). Dry with nitrogen. <input type="checkbox"/> Inspect quality of lift-off using optical microscope; repeat as necessary <input type="checkbox"/> Bake at 110°C for 2 min		

Initials	Process Step	Notes	Date/ Time
	Cleaning of Wafer (Solvent Hood) <input type="checkbox"/> Note: One layer of Au is currently on the wafer <input type="checkbox"/> Rinse in acetone for 30 sec at 500 rpm <input type="checkbox"/> Rinse in methanol for 30 sec at 500 rpm <input type="checkbox"/> Rinse in DI water for 30 sec at 500 rpm <input type="checkbox"/> Dry with nitrogen on spinner at 500 rpm and on Texwipes <input type="checkbox"/> Bake on hot plate for 2 min at 110°C		
	Cleaning of Mask 2 (Non-inverted Mask; Solvent Hood) <input type="checkbox"/> Rinse with acetone for 30 sec <input type="checkbox"/> Rinse with methanol for 30 sec <input type="checkbox"/> Rinse with DI water for 30 sec <input type="checkbox"/> Dry with nitrogen on Texwipes		
	1818 Photoresist (Solvent Hood) <input type="checkbox"/> Flood wafer with 1818 photoresist using dropper <input type="checkbox"/> Spin wafer for 30 sec at 4,000 rpm; Ramp at 200 rpm/sec <input type="checkbox"/> Bake wafer on hot plate for 75 sec at 110°C		
	Alignment & Exposure (MJB-3 Mask Aligner) <input type="checkbox"/> Align mask and wafer in x, y, and theta directions <input type="checkbox"/> Expose for 7 sec		
	Developing of Photoresist (Base Hood) <input type="checkbox"/> Place wafer in Petri dish and flood wafer with 351 Developer <input type="checkbox"/> Agitate Petri dish for 45 sec <input type="checkbox"/> Rinse wafer with DI water for approx. 30 sec <input type="checkbox"/> Dry with nitrogen on Texwipes		
	Inspection of Lithographic Process (Optical Microscope) <input type="checkbox"/> How is the alignment? Focus on the smallest features. <input type="checkbox"/> Are the features clean and open with sharp definition? <input type="checkbox"/> If necessary, strip photoresist using acetone or re-develop		
	Sputtering of GeTe (Sputtering Machine; Dr. Coutu) <input type="checkbox"/> Insert wafer with witness sample (used to measure thickness) <input type="checkbox"/> RF ash with substrate bias at 100 W for 45 sec <input type="checkbox"/> RF sputter from GeTe target at 10 mTorr, 20.1 sccm Ar, and no heating <input type="checkbox"/> Sputter at a specific power and time. Nominal values: 300 W and 2 min; these settings yield about a 185 nm-thick film.		
	Metal Lift-off <input type="checkbox"/> Adhere Scotch tape to wafer and pull metal from surface		
	Ultrasonic <input type="checkbox"/> Place the wafer in a Petri dish and place the dish in ultrasonic bath <input type="checkbox"/> Using a beaker, fill the bath with water until the Petri dish floats <input type="checkbox"/> Submerge the wafer in the Petri dish with acetone <input type="checkbox"/> Ultrasonic for approximately 8 min; continue longer if needed <input type="checkbox"/> Rinse/spin with acetone, methanol, and DI water at 500 rpm (30 sec for each solvent, as in cleaning process on next page). Dry with nitrogen. <input type="checkbox"/> Inspect quality of lift-off using optical microscope; repeat as necessary <input type="checkbox"/> Bake at 110°C for 2 min		

Initials	Process Step	Notes	Date/Time
	Cleaning of Wafer (Solvent Hood) <ul style="list-style-type: none"> □ Note: Layers of Au and GeTe are currently on the wafer □ Rinse in acetone for 30 sec at 500 rpm □ Rinse in methanol for 30 sec at 500 rpm □ Rinse in DI water for 30 sec at 500 rpm □ Dry with nitrogen on spinner at 500 rpm and on Texwipes □ Bake on hot plate for 2 min at 110°C 		
	Cleaning of Mask 3 (Solvent Hood) <ul style="list-style-type: none"> □ Rinse with acetone for 30 sec □ Rinse with methanol for 30 sec □ Rinse with DI water for 30 sec □ Dry with nitrogen on Texwipes 		
	1818 Photoresist (Solvent Hood) <ul style="list-style-type: none"> □ Flood wafer with 1818 photoresist using dropper □ Spin wafer for 30 sec at 4,000 rpm; Ramp at 200 rpm/sec □ Bake wafer on hot plate for 75 sec at 110°C 		
	Alignment & Exposure (MJB-3 Mask Aligner) <ul style="list-style-type: none"> □ Align mask and wafer in x, y, and theta directions □ Expose for 7 sec 		
	Developing of Photoresist (Base Hood) <ul style="list-style-type: none"> □ Place wafer in Petri dish and flood wafer with 351 Developer □ Agitate Petri dish for 45 sec □ Rinse wafer with DI water for approx. 30 sec □ Dry with nitrogen on Texwipes 		
	Inspection of Lithographic Process (Optical Microscope) <ul style="list-style-type: none"> □ How is the alignment? Focus on the smallest features. □ Are the features clean and open with sharp definition? □ If necessary, strip photoresist using acetone or re-develop 		
	Pre-metallization Cleaning (Plasma Asher) <ul style="list-style-type: none"> □ Place wafer in O2 Plasma Asher for 2 min at 75W (default setting) 		
	Contact technician when samples are ready for metallization Evaporation: Ti (100 Å) adhesion layer, Au (1,000 Å) on top of Ti		
	Metal Lift-off <ul style="list-style-type: none"> □ Adhere Scotch tape to wafer and pull metal from surface 		
	Ultrasonic <ul style="list-style-type: none"> □ Place the wafer in a Petri dish and place the dish in ultrasonic bath □ Using a beaker, fill the bath with water until the Petri dish floats □ Submerge the wafer in the Petri dish with acetone □ Ultrasonic for approximately 8 min; continue longer if needed □ Rinse/spin with acetone, methanol, and DI water at 500 rpm (30 sec for each solvent, as in cleaning process on next page). Dry with nitrogen. □ Inspect quality of lift-off using optical microscope; repeat as necessary □ Bake at 110°C for 2 min 		
	Dicing <ul style="list-style-type: none"> □ Note: If devices will be heated while testing, they must be diced prior to testing. Dicing is also a good standard procedure to prevent accidental cleaving of the wafer while handling it. □ Coat entire wafer with 1818 photoresist and bake at 110°C for 75 sec □ Dice in tic-tac-toe format □ Remove each diced reticle from adhesive backing with tweezers. Spin each reticle individually at 500 rpm to remove photoresist and clean it. 	<u>Finish Date</u> <u>Finish Time</u>	

Appendix B. Process Follower for GeTe on 2” Sapphire Wafers

Initials	Process Step	Notes	Date/ Time
	General Comments <input type="checkbox"/> Page 1: Bottom layer of Au (Mask 1) <input type="checkbox"/> Page 2: Middle layer of GeTe (Non-inverted Mask 2) <input type="checkbox"/> Page 3: Top layer of Au (Mask 3)	<u>Start Date</u> <u>Start Time</u>	
	Cleaning of Wafer (Solvent Hood) <input type="checkbox"/> Rinse in acetone for 30 sec at 500 rpm <input type="checkbox"/> Rinse in methanol for 30 sec at 500 rpm <input type="checkbox"/> Rinse in DI water for 30 sec at 500 rpm <input type="checkbox"/> Dry with nitrogen on spinner at 500 rpm and on Texwipes <input type="checkbox"/> Bake on hot plate for 2 min at 110°C		
	Cleaning of Mask 1 (Solvent Hood) <input type="checkbox"/> Rinse with acetone for 30 sec <input type="checkbox"/> Rinse with methanol for 30 sec <input type="checkbox"/> Rinse with de-ionized (DI) water for 30 sec <input type="checkbox"/> Dry with nitrogen on Texwipes		
	1818 Photoresist (Solvent Hood) <input type="checkbox"/> Flood wafer with 1818 photoresist using dropper <input type="checkbox"/> Spin wafer for 30 sec at 3,000 rpm; Ramp at 200 rpm/sec <input type="checkbox"/> Bake wafer on hot plate for 75 sec at 110°C		
	Alignment & Exposure (MJB-3 Mask Aligner) <input type="checkbox"/> Align mask and wafer in x, y, and theta directions <input type="checkbox"/> Expose for 7 sec		
	Developing of Photoresist (Base Hood) <input type="checkbox"/> Place wafer in Petri dish and flood wafer with 351 Developer <input type="checkbox"/> Agitate Petri dish for 45 sec <input type="checkbox"/> Rinse wafer with DI water for approx. 30 sec <input type="checkbox"/> Dry with nitrogen on Texwipes		
	Inspection of Lithographic Process (Optical Microscope) <input type="checkbox"/> How is the alignment? Focus on the smallest features. <input type="checkbox"/> Are the features clean and open with sharp definition? <input type="checkbox"/> If necessary, strip photoresist using acetone or re-develop		
	Pre-metallization Cleaning (Plasma Asher) <input type="checkbox"/> Place wafer in O2 plasma asher for 2 min at 75 W (default setting)		
	Contact technician when samples are ready for metallization Evaporation: Ti (100 Å) adhesion layer, Au (1,000 Å) on top of Ti		
	Metal Lift-off <input type="checkbox"/> Adhere Scotch tape to wafer and pull metal from surface		
	Ultrasonic <input type="checkbox"/> Place the wafer in a Petri dish and place the dish in ultrasonic bath <input type="checkbox"/> Using a beaker, fill the bath with water until the Petri dish floats <input type="checkbox"/> Submerge the wafer in the Petri dish with acetone <input type="checkbox"/> Ultrasonic for approximately 8 min; continue longer if needed <input type="checkbox"/> Rinse/spin with acetone, methanol, and DI water at 500 rpm (30 sec for each solvent, as in cleaning process on next page). Dry with nitrogen. <input type="checkbox"/> Inspect quality of lift-off using optical microscope; repeat as necessary <input type="checkbox"/> Bake at 110°C for 2 min		

Initials	Process Step	Notes	Date/ Time
	Cleaning of Wafer (Solvent Hood) <input type="checkbox"/> Note: One layer of Au is currently on the wafer <input type="checkbox"/> Rinse in acetone for 30 sec at 500 rpm <input type="checkbox"/> Rinse in methanol for 30 sec at 500 rpm <input type="checkbox"/> Rinse in DI water for 30 sec at 500 rpm <input type="checkbox"/> Dry with nitrogen on spinner at 500 rpm and on Texwipes <input type="checkbox"/> Bake on hot plate for 2 min at 110°C		
	Cleaning of Mask 2 (Non-inverted Mask; Solvent Hood) <input type="checkbox"/> Rinse with acetone for 30 sec <input type="checkbox"/> Rinse with methanol for 30 sec <input type="checkbox"/> Rinse with DI water for 30 sec <input type="checkbox"/> Dry with nitrogen on Texwipes		
	1818 Photoresist (Solvent Hood) <input type="checkbox"/> Flood wafer with 1818 photoresist using dropper <input type="checkbox"/> Spin wafer for 30 sec at 3,000 rpm; Ramp at 200 rpm/sec <input type="checkbox"/> Bake wafer on hot plate for 75 sec at 110°C		
	Alignment & Exposure (MJB-3 Mask Aligner) <input type="checkbox"/> Align mask and wafer in x, y, and theta directions <input type="checkbox"/> Expose for 7 sec		
	Developing of Photoresist (Base Hood) <input type="checkbox"/> Place wafer in Petri dish and flood wafer with 351 Developer <input type="checkbox"/> Agitate Petri dish for 45 sec <input type="checkbox"/> Rinse wafer with DI water for approx. 30 sec <input type="checkbox"/> Dry with nitrogen on Texwipes		
	Inspection of Lithographic Process (Optical Microscope) <input type="checkbox"/> How is the alignment? Focus on the smallest features. <input type="checkbox"/> Are the features clean and open with sharp definition? <input type="checkbox"/> If necessary, strip photoresist using acetone or re-develop		
	Sputtering of GeTe (Sputtering Machine; Dr. Coutu) <input type="checkbox"/> Insert wafer with witness sample (used to measure thickness) <input type="checkbox"/> RF ash with substrate bias at 100 W for 45 sec <input type="checkbox"/> RF sputter from GeTe target at 10 mTorr, 20.1 sccm Ar, and no heating <input type="checkbox"/> Sputter at a specific power and time. Nominal values: 300 W and 2 min; these settings yield about a 185 nm-thick film.		
	Metal Lift-off <input type="checkbox"/> Adhere Scotch tape to wafer and pull metal from surface		
	Ultrasonic <input type="checkbox"/> Place the wafer in a Petri dish and place the dish in ultrasonic bath <input type="checkbox"/> Using a beaker, fill the bath with water until the Petri dish floats <input type="checkbox"/> Submerge the wafer in the Petri dish with acetone <input type="checkbox"/> Ultrasonic for approximately 8 min; continue longer if needed <input type="checkbox"/> Rinse/spin with acetone, methanol, and DI water at 500 rpm (30 sec for each solvent, as in cleaning process on next page). Dry with nitrogen. <input type="checkbox"/> Inspect quality of lift-off using optical microscope; repeat as necessary <input type="checkbox"/> Bake at 110°C for 2 min		

Initials	Process Step	Notes	Date/Time
	Cleaning of Wafer (Solvent Hood) <ul style="list-style-type: none"> □ Note: Layers of Au and GeTe are currently on the wafer □ Rinse in acetone for 30 sec at 500 rpm □ Rinse in methanol for 30 sec at 500 rpm □ Rinse in DI water for 30 sec at 500 rpm □ Dry with nitrogen on spinner at 500 rpm and on Texwipes □ Bake on hot plate for 2 min at 110°C 		
	Cleaning of Mask 3 (Solvent Hood) <ul style="list-style-type: none"> □ Rinse with acetone for 30 sec □ Rinse with methanol for 30 sec □ Rinse with DI water for 30 sec □ Dry with nitrogen on Texwipes 		
	1818 Photoresist (Solvent Hood) <ul style="list-style-type: none"> □ Flood wafer with 1818 photoresist using dropper □ Spin wafer for 30 sec at 3,000 rpm; Ramp at 200 rpm/sec □ Bake wafer on hot plate for 75 sec at 110°C 		
	Alignment & Exposure (MJB-3 Mask Aligner) <ul style="list-style-type: none"> □ Align mask and wafer in x, y, and theta directions □ Expose for 7 sec 		
	Developing of Photoresist (Base Hood) <ul style="list-style-type: none"> □ Place wafer in Petri dish and flood wafer with 351 Developer □ Agitate Petri dish for 45 sec □ Rinse wafer with DI water for approx. 30 sec □ Dry with nitrogen on Texwipes 		
	Inspection of Lithographic Process (Optical Microscope) <ul style="list-style-type: none"> □ How is the alignment? Focus on the smallest features. □ Are the features clean and open with sharp definition? □ If necessary, strip photoresist using acetone or re-develop 		
	Pre-metallization Cleaning (Plasma Asher) <ul style="list-style-type: none"> □ Place wafer in O2 Plasma Asher for 2 min at 75W (default setting) 		
	Contact technician when samples are ready for metallization Evaporation: Ti (100 Å) adhesion layer, Au (1,000 Å) on top of Ti		
	Metal Lift-off <ul style="list-style-type: none"> □ Adhere Scotch tape to wafer and pull metal from surface 		
	Ultrasonic <ul style="list-style-type: none"> □ Place the wafer in a Petri dish and place the dish in ultrasonic bath □ Using a beaker, fill the bath with water until the Petri dish floats □ Submerge the wafer in the Petri dish with acetone □ Ultrasonic for approximately 8 min; continue longer if needed □ Rinse/spin with acetone, methanol, and DI water at 500 rpm (30 sec for each solvent, as in cleaning process on next page). Dry with nitrogen. □ Inspect quality of lift-off using optical microscope; repeat as necessary □ Bake at 110°C for 2 min 		
	Cleaning of Mask 2 (Non-inverted Mask; Solvent Hood) <ul style="list-style-type: none"> □ Rinse with acetone for 30 sec □ Rinse with methanol for 30 sec □ Rinse with DI water for 30 sec □ Dry with nitrogen 	<u>Finish Date</u> <u>Finish Time</u>	

Bibliography

- [1] J. P. McKelvey, Solid State Physics, Malabar, FL: Krieger Publishing Co., 2003.
- [2] W. B. Jensen, "The Place of Zinc, Cadmium, and Mercury in the Periodic Table," *J. Chem. Educ.*, vol. 80, no. 8, pp. 952-961, 2003.
- [3] M. Nic, J. Jirat, B. Kosata and A. Jenkins, "IUPAC Gold Book," 2014. [Online]. Available: <http://goldbook.iupac.org>. [Accessed 1 June 2014].
- [4] A. Helmenstine, "Science Notes," [Online]. Available: <http://sciencenotes.org>. [Accessed 1 January 2015].
- [5] P. A. Cox, Transition Metal Oxides: An introduction to their electronic structure and properties, New York: Oxford University Press, 2010.
- [6] S. M. Sze and K. K. Ng, Physics of Semiconductor Devices, 3rd ed., Hoboken, NJ: John Wiley & Sons, 2007.
- [7] F. J. Morin, "Oxides of the 3d Transition Metals," *Semiconductors*, 1958.
- [8] F. J. Morin, "Oxides which show a Metal-to-Insulator Transition at the Neel Temperature," *Phys. Rev. Lett.*, vol. 3, no. 1, 1959.
- [9] N. F. Mott, "Metal-Insulator Transition," *Rev. Modern Phys.*, vol. 40, no. 4, 1968.
- [10] F. Gebhard, The Mott Metal-Insulator Transition, New York, NY: Springer, 1997.
- [11] Z. Yang, C. Ko and S. Ramanathan, "Oxide Electronics Utilizing Ultrafast Metal-Insulator Transitions," *Annu. Rev. Mater. Res.*, 2011.
- [12] M. Imada, A. Fujimori and Y. Tokura, "Metal-insulator transitions," *Rev. Modern Phys.*, vol. 70, no. 4, pp. 1039-1263, 1998.
- [13] M. Dayah, "Dynamic Periodic Table," Ptable, 1 October 1997. [Online]. Available:

<http://www.ptable.com>. [Accessed 1 June 2014].

- [14] A. L. Pergament, G. B. Stefanovich and A. A. Velichko, "Oxide Electronics and Vanadium Dioxide Perspective: A Review," *IEEE J. Sel. Topics Nano Electron. Comput.*, 2013.
- [15] D. Ruzmetov, D. Heiman, B. B. Claflin, V. Narayanamurti and S. Ramanathan, "Hall carrier density and magnetoresistance measurements in thin-film vanadium dioxide across the metal-insulator transition," *Phys. Rev. B*, 2009.
- [16] J. Nag and R. F. Haglund Jr., "Synthesis of vanadium dioxide thin films and nanoparticles," *J. Phys. Condens. Matt.*, vol. 20, 2008.
- [17] S. Hormoz and S. Ramanathan, "Limits on vanadium oxide Mott metal-insulator transition field-effect transistors," *Solid-State Electronics*, 2010.
- [18] J. G. Simmons, "Poole-Frenkel Effect and Schottky Effect in Metal-Insulator-Metal Systems," *Phys. Rev.*, vol. 155, no. 3, pp. 657-660, 1967.
- [19] B. S. Mun, J. Yoon, S.-K. Mo, K. Chen, N. Tamura, C. Dejoie, M. Kunz, C. Park, K. Moon and H. Ju, "Role of joule heating effect and bulk-surface phases in voltage-driven metal-insulator transition in VO₂ crystal," *J. Appl. Phys.*, 2013.
- [20] A. Zimmers, L. Aigouy, M. Mortier, A. Sharoni, S. Wang, K. G. West, J. G. Ramirez and I. K. Schuller, "Role of Thermal Heating on the Voltage Insulator-Metal Transition in VO₂," *Phys. Rev. Lett.*, vol. 110, 2013.
- [21] R. S. Muller, T. I. Kamins and M. Chan, *Device Electronics for Integrated Circuits*, 3rd ed., New York, NY: John Wiley & Sons, 2003.
- [22] D. M. Newns, J. A. Misewich, C. C. Tsuei, A. Gupta, B. A. Scott and A. Schrott, "Mott transition field effect transistor," *Appl. Phys. Lett.*, vol. 73, no. 6, 1998.
- [23] Y. Zhou and S. Ramanathan, "Correlated Electron Materials and Field Effect Transistors for Logic: A Review," *Critical Reviews in Solid State and Materials Sciences*, vol. 38, no. 4, pp. 286-317, August 2013.
- [24] B. S. Mun, K. Chen, Y. Leem, C. Dejoie, N. Tamura, M. Kunz, Z. Liu, M. E. Grass, C. Park, J. Yoon, Y. Y. Lee and H. Ju, "Observation of insulating-

insulating monoclinic structural transition in macro-sized VO₂ single crystals," *Phys. Status Solidi*, vol. 5, no. 3, pp. 107-109, 2011.

- [25] N. J. Podraza, B. D. Gauntt, M. A. Motyka, E. C. Dickey and M. W. Horn, "Electrical and optical properties of sputtered amorphous vanadium oxide thin films," *J. Appl. Phys.*, vol. 111, 2012.
- [26] S. J. Yun, J. W. Lim, B.-G. Chae, B. J. Kim and H.-T. Kim, "Characteristics of vanadium dioxide thin films deposited by RF-magnetron sputter deposition technique using V-metal target," *Phys. Rev. B*, 2007.
- [27] K. Okimura and N. Kubo, "Growth of VO₂ films with metal-insulator transition on silicon substrates in inductively coupled plasma-assisted sputtering," *Thin Solid Films*, vol. 515, pp. 4992-4995, 2007.
- [28] G. Stefanovich, A. Pergament and D. Stefanovich, "Electrical switching and Mott transition in VO₂," *J. Phys. Cond. Matt.*, vol. 12, pp. 8837-8845, 2000.
- [29] T. Maruyama and Y. Ikuta, "Vanadium dioxide thin films prepared by chemical vapour deposition from vanadium(III) acetylacetonate," *J. Mater. Sci.*, vol. 28, pp. 5073-5078, 1993.
- [30] M. B. Sahana, G. N. Subbanna and S. A. Shivashankar, "Phase transformation and semiconductor-metal transition in thin films of VO₂ deposited by low-pressure metalorganic chemical vapor deposition," *J. Appl. Phys.*, vol. 92, no. 11, pp. 6495-6504, 2002.
- [31] Y. L. Wang, X. K. Chen, M. C. Li, R. Wang, G. Wu, J. P. Yang, W. H. Han, S. Z. Cao and L. C. Zhao, "Phase composition and valence of pulsed laser deposited vanadium oxide thin films at different oxygen pressures," *Surface & Coatings Tech.*, vol. 201, pp. 5344-5347, 2007.
- [32] K. G. West, J. Lu, L. He, D. Kirkwood, W. Chen, T. P. Adl, M. S. Osofsky, S. B. Qadri, R. Hull and S. A. Wolf, "Ferromagnetism in Rutile Structure Cr Doped VO₂ Thin Films Prepared by Reactive-Bias Target Ion Beam Deposition," *J. Superconductivity and Novel Magnetism*, vol. 21, pp. 87-92, 2007.
- [33] E. E. Chain, "The influence of deposition temperature on the structure and optical properties of vanadium oxide films," *J. Vac. Sci. Technol. A*, vol. 4, no. 3, pp.

432-435, June 1986.

- [34] E. D. McClanahan and N. Laegreid, "Thin Films by Controlled Deposition of Sputtered Material," in *Sputtering by Particle Bombardment III: Characteristics of Sputtered Particles, Technical Applications*, R. Berhrisch and K. Wittmaack, Eds., Berlin, Springer-Verlag, 1991, pp. 339-377.
- [35] S. A. Campbell, *Fabrication Engineering at the Micro- and Nanoscale*, 4th ed., New York, NY: Oxford University Press, 2013.
- [36] J. A. Thornton, "Influence of apparatus geometry and deposition conditions on the structure and topology of thick sputtered coatings," *J. Vac. Sci. Technol.*, vol. 11, no. 4, pp. 666-670, August 1974.
- [37] D. Ruzmetov, S. D. Senanayake, V. Narayanamurti and S. Ramanathan, "Correlation between metal-insulator transition characteristics and electronic structure changes in vanadium oxide thin films," *Phys. Rev. B*, vol. 77, 2008.
- [38] D. Ruzmetov, K. T. Zawilski, V. Narayanamurti and S. Ramanathan, "Structure-functional property relationships in rf-sputtered vanadium oxide thin films," *J. Appl. Phys.*, vol. 102, 2007.
- [39] J. B. Kana Kana, J. M. Ndjaka, B. D. Ngom, A. Y. Fasasi, O. Nemraoui, R. Nemutudi, D. Knoesen and M. Maaza, "High substrate temperature induced anomalous phase transition temperature shift in sputtered VO₂ thin films," *Opt. Mat.*, vol. 32, pp. 739-742, 2010.
- [40] M. Marezio, B. McWhan, J. P. Remeika and P. D. Dernier, "Structural Aspects of the Metal-Insulator Transitions in Cr-Doped VO₂," *Phys. Rev. B*, vol. 5, no. 7, pp. 2541-2551, 1972.
- [41] D. Brassard, S. Fourmaux, M. Jean-Jacques, J. C. Kieffer and M. A. El Khakani, "Grain size effect on the semiconductor-metal phase transition characteristics of magnetron-sputtered VO₂ thin films," *Appl. Phys. Lett.*, vol. 87, 2005.
- [42] Z. Yang and S. Ramanathan, "Direct measurement of compositional complexity-induced electronic inhomogeneity in VO₂ thin films grown on gate dielectrics," *Appl. Phys. Lett.*, 2011.

- [43] G. Fu, A. Polity, N. Volbers and B. K. Meyer, "Annealing effects on VO₂ thin films deposited by reactive sputtering," *Thin Solid Films*, vol. 515, pp. 2519-2522, 2006.
- [44] W. Burkhardt, T. Christmann, S. Franke, W. Kriegseis, D. Meister, B. K. Meyer, W. Niessner, D. Schalch and A. Scharmann, "Tungsten and fluorine co-doping of VO₂ films," *Thin Solid Films*, vol. 402, pp. 226-231, 2002.
- [45] R. C. Jaeger, Introduction to Microelectronic Fabrication (Volume V), Reading, MA: Addison Wesley Longman, 1993.
- [46] D. Ruzmetov, G. Gopalakrishnan, J. Den, V. Narayanamurti and S. Ramanathan, "Electrical Triggering of Metal-Insulator Transition in Nanoscale Vanadium Oxide Junctions," *J. Appl. Phys.*, vol. 106, 2009.
- [47] D. Ruzmetov, G. Gopalakrishnan, C. Ko, V. Narayanamurti and S. Ramanathan, "Three-terminal field effect devices utilizing thin film vanadium oxide as the channel layer," *J. Appl. Phys.*, vol. 107, 2010.
- [48] D. Ruzmetov, K. T. Zawilski, S. D. Senanayake, V. Narayanamurti and S. Ramanathan, "Infrared reflectance and photoemission spectroscopy studies across the phase transition boundary in thin film vanadium dioxide," *J. Phys.: Cond. Matt.*, vol. 20, 2008.
- [49] C. Ko and S. Ramanathan, "Stability of electrical switching properties in vanadium dioxide thin films under multiple thermal cycles across the phase transition boundary," *J. Appl. Phys.*, 2008.
- [50] C. Ko and S. Ramanathan, "Dispersive capacitance and conductance across the phase transition boundary in metal-vanadium oxide-silicon devices," *J. Appl. Phys.*, vol. 106, 2009.
- [51] Z. Yang, C. Ko, V. Balakrishnan, G. Gopalakrishnan and S. Ramanathan, "Dielectric and carrier transport properties of vanadium dioxide thin films across the plane transition utilizing gated capacitor devices," *Phys. Rev. B*, vol. 82, 2010.
- [52] K. J. Kuhn, U. Avci, A. Cappellani, M. D. Giles, M. Haverty, S. Kim, R. Kotlyar, S. Manipatruni, D. Nikonov, C. Pawashe, M. Radosavljevic, R. Rios, S. Shankar, R. Vedula, R. Chau and I. Young, "The Ultimate CMOS Device and

Beyond," in *IEEE*, 2012.

- [53] M. Gurvitch, S. Luryi, A. Polyakov, A. Shabalov, M. Dudley, G. Wang, S. Ge and V. Yakovlev, "VO₂ films with strong semiconductor to metal phase transition prepared by the precursor oxidation process," *J. Appl. Phys.*, vol. 102, 2007.
- [54] Y. Guo and J. Robertson, "Analysis of metal insulator transitions in VO₂ and V₂O₃ for RRAMs," *Microelec. Engr.*, vol. 109, pp. 278-281, 2013.
- [55] J.-G. Ramirez, R. Schmidt, A. Sharoni, M. E. Gomez, I. K. Schuller and E. J. Patiño, "Ultra-thin filaments revealed by the dielectric response across the metal-insulator transition in VO₂," *Appl. Phys. Lett.*, vol. 102, 2013.
- [56] L. Pellegrino, N. Manca, T. Kanki, H. Tanaka, M. Biasotti, E. Bellingeri, A. S. Siri and D. Marre, "Multistate Memory Devices Based on Free-standing VO₂/TiO₂ Microstructures Driven by Joule Heating," *Adv. Mater.*, vol. 24, pp. 2929-2934, 2012.
- [57] R. Cabrera, E. Merced and N. Sepulveda, "Performance of Electro-Thermally Driven VO₂-Based MEMS Actuators," *IEEE J. MEMS*, 2013.
- [58] J. Givernaud, C. Champeaux, A. Catherinot, A. Pothier, A. Blondy and A. Crunteanu, "Tunable band stop filters based on metal-insulator transition in vanadium dioxide thin films," in *IEEE*, 2008.
- [59] D. Bouyge, A. Crunteanu, J.-C. Orlianges, D. Passerieux, C. Champeaux, A. Catherinot, A. Velez, J. Bonache, F. Martin and P. Blondy, "Reconfigurable Bandpass Filter Based on Split Ring Resonators and Vanadium Dioxide (VO₂) Microwave Switches," in *IEEE*, 2009.
- [60] C. Chen, Y. Zhu, Y. Zhao, J. H. Lee, H. Wang, A. Bernussi, M. Holtz and Z. Fan, "VO₂ multidomain heteroepitaxial growth and terahertz transmission modulation," *Appl. Phys. Lett.*, vol. 97, 2010.
- [61] H. Tao, N. I. Landy, C. M. Bingham, X. Zhang, R. D. Averitt and W. J. Padilla, "A metamaterial absorber for the terahertz regime: Design, fabrication and characterization," *Optics Express*, vol. 16, no. 10, May 2008.

- [62] M.-H. Lee and M.-G. Kim, "RTA and stoichiometry effect on the thermochromism of VO₂ thin films," *Thin Solid Films*, vol. 286, pp. 219-222, 1996.
- [63] T. D. Manning, I. P. Parkin, M. E. Pemble, D. Sheel and D. Vernardou, "Intelligent Window Coatings: Atmospheric Pressure Chemical Vapor Deposition of Tungsten-Doped Vanadium Dioxide," *Chem. Mater.*, vol. 16, pp. 744-749, 2004.
- [64] T. Christmann, B. Felde, W. Niessner, D. Schalch and A. Scharmann, "Thermochromic VO₂ thin films studied by photoelectron spectroscopy," *Thin Solid Films*, vol. 287, pp. 134-138, 1996.
- [65] M.-H. Lee and J.-S. Cho, "Better thermochromic glazing of windows with anti-reflection coating," *Thin Solid Films*, vol. 365, no. 1, pp. 5-6, April 2000.
- [66] M. A. Kats, R. Blanchard, S. Zhang, P. Genevet, C. Ko, S. Ramanathan and F. Capasso, "Vanadium Dioxide as a Natural Disordered Metamaterial: Perfect Thermal Emission and Large Broadband Negative Differential Thermal Emittance," *Phys. Rev. X*, vol. 3, no. 4, October 2013.
- [67] A. T. Waterman, "On the positive ionization from certain hot salts, together with some observations on the electrical properties of molybdenite at high temperatures," *Phil. Mag.*, vol. 33, no. 195, pp. 225-257, 1917.
- [68] C. H. Lam, "History of Phase Change Materials," in *Phase Change Materials: Science and Applications*, S. Raoux and M. Wuttig, Eds., New York, Springer, 2009, pp. 1-14.
- [69] S. R. Ovshinsky, "Reversible Electrical Switching Phenomena in Disordered Structures," *Phys. Rev. Lett.*, vol. 21, no. 20, pp. 1450-1453, November 1968.
- [70] J. Feinleib, J. deNeufville, S. C. Moss and S. R. Ovshinsky, "Rapid Reversible Light-induced Crystallization of Amorphous Semiconductors," *J. Appl. Phys.*, vol. 18, no. 6, 1971.
- [71] A. E. Bell, "Recent developments in optical storage technology," *Nature*, vol. 297, pp. 104-106, May 1982.

- [72] Philips, January 2015. [Online]. Available:
<http://www.research.philips.com/technologies/projects/cd>.
- [73] L. van Pieterse, M. H. R. Lankhorst, M. van Schijndel, A. E. T. Kuiper and J. H. J. Roosen, "Phase-change recording materials with a growth-dominated crystallization mechanism: A materials overview," *J. Appl. Phys.*, vol. 97, no. 8, 2005.
- [74] W. Welnic and M. Wuttig, "Reversible switching in phase-change materials," *Materials Today*, vol. 11, no. 6, pp. 20-27, June 2008.
- [75] M. Çelikbilek, A. E. Ersundu and S. Aydın, "Crystallization Kinetics of Amorphous Materials," in *Advances in Crystallization Processes*, Y. Mastai, Ed., Rijeka, InTech, 2012, pp. 127-162.
- [76] L. van Pieterse, "Experimental Methods for Material Selection in Phase-change Recording," in *Phase Change Materials: Science and Applications*, S. Raoux and M. Wuttig, Eds., New York, Springer, 2009, pp. 81-98.
- [77] F. A. Cotton, G. Wilkinson, C. A. Murillo and M. Bochmann, *Advanced Inorganic Chemistry*, 6th ed., New York: John Wiley & Sons, 1999.
- [78] M. Wuttig and N. Yamada, "Phase-change materials for rewritable data storage," *Nature Materials*, vol. 6, pp. 824-832, November 2007.
- [79] X. S. Miao, T. C. Chong, Y. M. Huang, K. G. Lim, P. K. Tan and L. P. Shi, "Dependence of Optical Constants on Film Thickness of Phase-Change Media," *Jpn. J. Appl. Phys.*, vol. 38, pp. 1638-1641, 1999.
- [80] M. Mitra, Y. Jung, D. S. Gianola and R. Agarwal, "Extremely low drift of resistance and threshold voltage in amorphous phase change nanowire devices," *Appl. Phys. Lett.*, vol. 96, no. 22, 2010.
- [81] L. Shi, "Optical Memory: From 1st to 3rd Generation and its Future," in *Phase Change Materials: Science and Applications*, S. Raoux and M. Wuttig, Eds., New York, Springer, 2009, pp. 251-284.
- [82] N. Yamada, E. Ohno, K. Nishiuchi, N. Akahira and M. Takao, "Rapid-phase transitions of GeTe-Sb₂Te₃ pseudobinary amorphous thin films for an optical

- disk memory," *J. Appl. Phys.*, vol. 69, no. 5, pp. 2849-2856, March 1991.
- [83] N. Yamada, "Development of Materials for Third Generation Optical Storage Media," in *Phase Change Materials: Science and Applications*, S. Raoux and M. Wuttig, Eds., New York, Springer, 2009, pp. 199-226.
- [84] S. K. Bahl and K. L. Chopra, "Amorphous versus Crystalline GeTe Films. III. Electrical Properties and Band Structure," *J. Appl. Phys.*, vol. 41, no. 5, pp. 2196-2212, 1970.
- [85] S. Gidon, O. Lemonnier, B. Rolland, O. Bichet and C. Dressler, "Electrical probe storage using Joule heating in phase change media," *Appl. Phys. Lett.*, vol. 85, no. 26, pp. 6392-6394, December 2004.
- [86] M. Chen, K. A. Rubin and R. W. Barton, "Compound materials for reversible, phase-change optical data storage," *Appl. Phys. Lett.*, vol. 49, no. 9, pp. 502-504, 1986.
- [87] N. Kaiser, "Crystallization of Amorphous Antimony Films," *Thin Solid Films*, vol. 116, no. 1-3, pp. 259-265, June 1984.
- [88] A. H. Edwards, A. C. Pineda, P. A. Schultz, M. G. Martin, A. P. Thompson and H. P. Hjalmarson, "Theory of persistent, p-type, metallic conduction in c-GeTe," *J. Phys. Condens. Matt.*, vol. 17, no. 32, pp. 329-335, August 2005.
- [89] M. Wuttig, D. Lüsebrink, D. Wamwangi, W. Welnic, M. Gilleßen and R. Dronskowski, "The role of vacancies and local distortions in the design of new phase-change materials," *Nature Materials*, vol. 6, pp. 122-128, February 2007.
- [90] A. V. Kolobov and J. Tominaga, "Local structure of crystallized GeTe films," *Appl. Phys. Lett.*, vol. 82, no. 3, pp. 382-384, January 2003.
- [91] T. Chattopadhyay, J. X. Boucherle and H. G. von Schnering, "Neutron diffraction study on the structural phase transition in GeTe," *J. Phys. C: Solid State Phys.*, vol. 20, no. 10, pp. 1431-1440, April 1987.
- [92] E. M. Levin, M. F. Besser and R. Hanus, "Electronic and thermal transport in GeTe: A versatile base for thermoelectric materials," *J. Appl. Phys.*, vol. 114,

no. 8, 2013.

- [93] D. Ielmini and Y. Zhang, "Analytical model for subthreshold conduction and threshold switching in chalcogenide-based memory devices," *J. Appl. Phys.*, vol. 102, no. 5, 2007.
- [94] R. Bez, E. Camerlenghi, A. Modelli and A. Visconti, "Introduction to Flash Memory," *IEEE*, vol. 91, no. 4, pp. 489-502, 2003.
- [95] M. H. R. Lankhorst, B. W. S. M. M. Ketelaars and R. A. M. Wolters, "Low-cost and nanoscale non-volatile memory concept for future silicon chips," *Nature Materials*, vol. 4, pp. 347-352, 2005.
- [96] M. Gill, T. Lowrey and J. Park, "Ovonic Unified Memory - A High-Performance Nonvolatile Memory Technology for Stand-Alone Memory and Embedded Applications," in *IEEE Intl. Solid-State Circuits*, 2002.
- [97] A. Fantini, L. Perniola, M. Armand, J. F. Nodin, V. Sousa, A. Persico, J. Cluzel, C. Jahan, S. Maitrejean, S. Lhostis, A. Roule, C. Dressler, G. Reimbold, B. DeSalvo, P. Mazoyer, D. Bensahel and F. Boulanger, "Comparative assessment of GST and GeTe Materials For Application to Embedded Phase-Change Memory Devices," in *IEEE*, 2009.
- [98] M. Boniardi, A. Redaelli, A. Pirovano, I. Tortorelli, D. Ielmini and F. Pellizzer, "A physics-based model of electrical conduction decrease with time in amorphous Ge₂Sb₂Te₅," *J. Appl. Phys.*, vol. 105, no. 8, 2009.
- [99] A. L. Lacaita and D. Ielmini, "Reliability issues and scaling projections for phase change non volatile memories," in *IEEE IEDM*, Washington D.C., 2007.
- [100] D. Ielmini, S. Lavizzari, D. Sharma and A. L. Lacaita, "Temperature acceleration of structural relaxation in amorphous Ge₂Sb₂Te₅," *Appl. Phys. Lett.*, vol. 92, no. 19, 2008.
- [101] D. Ielmini, S. Lavizzari, D. Sharma and A. L. Lacaita, "Physical interpretation, modeling and impact on phase change memory (PCM) reliability of resistance drift due to chalcogenide structural relaxation," in *IEEE IEDM*, Washington D.C., 2007.

- [102] L. Perniola, V. Sousa, A. Fantini, E. Arbaoui, A. Bastard, M. Armand, A. Fargeix, C. Jahan, J.-F. Nodin, A. Persico, D. Blachier, A. Toffoli, S. Loubriat, E. Gourvest, G. B. Beneventi, H. Feldis, S. Maitrejean, S. Lhostis, A. Roule, O. Cueto, G. Reimbold, L. Poupinet, T. Billon, B. De Salvo, D. Bensahel, P. Mazoyer, R. Annunziata, P. Zuliani and F. Boulanger, "Electrical Behavior of Phase-Change Memory Cells Based on GeTe," *IEEE Elec. Dev. Lett.*, vol. 31, no. 5, May 2010.
- [103] S. Kohara, S. Kimura, H. Tanaka, N. Yasuda, Y. Fukuyama, H. Murayama, J. Kim, M. Takata, K. Kato, Y. Tanaka, T. Usuki, K. Suzuya, H. Tanaka, Y. Moritomo, T. Matsunaga, R. Kojima and N. Yamada, "Structural basis for fast phase change in DVD-RAM - Topological order in the amorphous phase," in *Proc. European Phase Change and Ovonic Symposium*, 2007.
- [104] A. Fantini, V. Sousa, L. Perniola, E. Gourvest, J. C. Bastien, S. Maitrejean, S. Braga, N. Pashkov, A. Bastard, B. Hyot, A. Roule, A. Persico, H. Feldis, C. Jahan, J. F. Nodin, D. Blachier, A. Toffoli, G. Reimbold, F. Fillot, F. Pierre, R. Annunziata, D. Bensahel, P. Mazoyer, C. Vallee, T. Billon, J. Hazart, B. De Salvo and F. Boulanger, "N-doped GeTe as Performance Booster for Embedded Phase-Change Memories," in *IEEE IEDM*, San Francisco, 2010.
- [105] G. B. Beneventi, L. Perniola, V. Sousa, E. Gourvest, S. Maitrejean, J. C. Bastien, A. Bastard, B. Hyot, A. Fargeix, C. Jahan, J. F. Nodin, A. Persico, A. Fantini, D. Blachier, A. Toffoli, S. Loubriat, A. Roule, S. Lhostis, H. Feldis, G. Reimbold, T. Billon, B. De Salvo, L. Larcher, P. Pavan, D. Bensahel, P. Mazoyer, R. Annunziata, P. Zuliani and F. Boulanger, "Carbon-doped GeTe: A promising material for Phase-Change Memories," *Solid-State Elec.*, Vols. 65-66, pp. 197-204, November-December 2011.
- [106] S. Raoux, "Scaling Properties of Phase Change Materials," in *Phase Change Materials: Science and Applications*, S. Raoux and M. Wuttig, Eds., New York, Springer, 2009, pp. 99-124.
- [107] M. H. R. Lankhorst, "Modelling glass transition temperatures of chalcogenide glasses. Applied to phase-change optical recording materials," *J. Non-crystalline Solids*, vol. 297, pp. 210-219, 2002.
- [108] J. Tominaga, "4th Generation Optical Memories Based on Super-resolution Near-field structure (Super-RENS) and Near-field Optics," in *Phase Change Materials: Science and Applications*, S. Raoux and M. Wuttig, Eds., New York,

Springer, 2009, pp. 285-298.

- [109] K. Kurihara, Y. Yamakawa, T. Shima, T. Nakano and J. Tominaga, "Super-RENS ROM Disc with Narrow Track Pitch," in *IEEE Opt. Data Storage Topical Mtg.*, Montreal, 2006.
- [110] T. Driscoll, H.-T. Kim, B.-G. Chae, B.-J. Kim, Y.-W. Lee, N. M. Jokerst, S. Palit, D. R. Smith, M. D. Ventra and D. N. Basov, "Memory Metamaterials," *Science*, vol. 325, no. 5947, pp. 1518-1521, September 2009.
- [111] L. E. Bell, "Cooling, Heating, Generating Power, and Recovering Waste Heat with Thermoelectric Systems," *Science*, vol. 321, pp. 1457-1461, September 2008.
- [112] F. Huang, G.-Y. Xu and P. Zou, "Thermoelectric Properties of InGeTe Fabricated by High Pressure Sintering Method," *J. Elec. Mater.*, November 2014.
- [113] R. Venkatasubramanian, E. Siivola, T. Colpitts and B. O'Quinn, "Thin-film thermoelectric devices with high room-temperature figures of merit," *Nature*, vol. 413, pp. 597-602, October 2001.
- [114] Y. Leng, *Materials Characterization: Introduction to Microscopic and Spectroscopic Methods*, Singapore: John Wiley & Sons (Asia), 2008.
- [115] J. B. Wachtman, *Characterization of Materials*, Stoneham: Butterworth-Heinemann, 1993.
- [116] L. A. Woodward, "General Introduction," in *Raman Spectroscopy: Theory and Practice*, H. A. Szymanski, Ed., New York, Plenum Press, 1967.
- [117] B. E. A. Saleh and M. C. Teich, *Fundamentals of Photonics*, 2nd ed., Hoboken: John Wiley & Sons, 2007.
- [118] H. G. Tompkins, *A User's Guide to Ellipsometry*, San Diego: Academic Press, 1993.
- [119] G. E. Jellison and F. A. Modine, "Parameterization of the optical functions of amorphous materials in the interband region," *Appl. Phys. Lett.*, vol. 69, no. 3, pp. 371-373, 1996.

- [120] M. Gaillet, L. Yan and E. Teboul, "Optical characterization of complete TFT-LCD display devices by phase modulated spectroscopic ellipsometry," *Thin Solid Films*, vol. 516, no. 2-4, pp. 170-174, 2007.
- [121] Filmetrics, "Understanding Film Thickness Measurements: Spectral Reflectance," 1 November 2014. [Online]. Available: <http://www.filmetrics.com/technology>.
- [122] H. Tao, W. J. Padilla, X. Zhang and R. D. Averitt, "Recent Progress in Electromagnetic Metamaterial Devices for Terahertz Applications," *IEEE J. Sel. Top. Quantum Elec.*, vol. 17, no. 1, 2011.
- [123] A. G. Markelz, A. Roitberg and E. J. Heilweil, "Pulsed terahertz spectroscopy of DNA, bovine serum albumin and collagen between 0.1 and 2.0 THz," *Chem. Phys. Lett.*, vol. 320, no. 1-2, pp. 42-48, March 2000.
- [124] S. Nakajima, H. Hoshina, M. Yamashita and C. Otani, "Terahertz imaging diagnostics of cancer tissues with a chemometrics technique," *Appl. Phys. Lett.*, vol. 90, no. 4, 2007.
- [125] C. J. Strachan, T. Rades, D. A. Newnham, K. C. Gordon, M. Pepper and P. F. Taday, "Using terahertz pulsed spectroscopy to study crystallinity of pharmaceutical materials," *Chem. Phys. Lett.*, vol. 390, no. 1-3, pp. 20-24, May 2004.
- [126] M. Mizuno, K. Fukunaga, S. Saito and I. Hosako, "Analysis of calcium carbonate for differentiating between pigments using terahertz spectroscopy," *J. European Optical Society*, vol. 4, September 2009.
- [127] M. Naftaly and R. E. Miles, "Terahertz Time-Domain Spectroscopy for Material Characterization," *IEEE*, vol. 95, no. 8, pp. 1658-1665, 2007.
- [128] J. B. Pendry, D. Schurig and D. R. Smith, "Controlling Electromagnetic Fields," *Science*, vol. 312, pp. 1780-1782, June 2006.
- [129] D. Schurig, J. J. Mock, B. J. Justice, S. A. Cummer, J. B. Pendry, A. F. Starr and D. R. Smith, "Metamaterial Electromagnetic Cloak at Microwave Frequencies," *Science*, vol. 314, pp. 977-980, November 2006.

- [130] L. A. Sweatlock and K. Diest, "Vanadium dioxide based plasmonic modulators," *Optics Express*, vol. 20, no. 8, pp. 8700-8709, 2012.
- [131] T. Driscoll, S. Palit, M. M. Qazilbash, M. Brehm, F. Keilmann, B.-G. Chae, S.-J. Yun, H.-T. Kim, S. Y. Cho, N. M. Jokerst, D. R. Smith and D. N. Basov, "Dynamic tuning of an infrared hybrid-metamaterial resonance using vanadium dioxide," *Appl. Phys. Lett.*, vol. 93, 2008.
- [132] M. A. Kats, D. Sharma, J. Lin, P. Genevet, R. Blanchard, Z. Yang, M. M. Qazlibash, D. N. Basov, S. Ramanathan and F. Capasso, "Ultra-thin absorber employing a tunable phase change material," *Appl. Phys. Lett.*, vol. 101, 2012.
- [133] M. Zalkovskij, C. Z. Bisgaard, A. Novitsky, R. Malureanu, D. Savastru, A. Pepescu, P. U. Jepsen and A. Lavrinenko, "Ultrabroad terahertz spectroscopy of chalcogenide glasses," *Appl. Phys. Lett.*, vol. 100, 2012.
- [134] T. Kleine-Ostmann, P. Dawson, K. Pierz, G. Hein and M. Koch, "Room-temperature operation of an electrically driven terahertz modulator," *Appl. Phys. Lett.*, vol. 84, no. 18, 2004.
- [135] W. L. Chan, H.-T. Chen, A. J. Taylor, I. Brener, M. J. Cich and D. M. Mittleman, "A spatial light modulator for terahertz beams," *Appl. Phys. Lett.*, vol. 94, 2009.
- [136] W. H. Hayt, J. E. Kemmerly and S. M. Durbin, *Engineering Circuit Analysis*, 7th ed., New York, NY: McGraw-Hill, 2007.
- [137] R. J. Trew, "RF Switches," in *RF and Microwave Circuits, Measurements, and Modeling*, M. Golio and J. Golio, Eds., Boca Raton, Taylor & Francis Group, 2008.
- [138] Y. Shim, G. Hummel and M. Rais-Zadeh, "RF Switches using Phase Change Materials," in *IEEE MEMS*, Taipei, 2013.
- [139] A. S. Sedra and K. C. Smith, *Microelectronic Circuits*, 5th ed., New York, NY: Oxford University Press, 2004.
- [140] P. Fay, "Introduction to Microwaves and RF," in *RF and Microwave Circuits, Measurements, and Modeling*, M. Golio and J. Golio, Eds., Boca Raton, Taylor

& Francis Group, 2008.

- [141] G. T. A. Kovacs, *Micromachined Transducers Sourcebook*, New York: McGraw-Hill, 1998.
- [142] G. E. Anner, *Planar Processing Primer*, New York, NY: Van Nostrand Reinhold, 1990.
- [143] "1818 Photoresist MSDS," April 2004. [Online]. Available: kni.caltech.edu/facilities/msds/Shipley_1818_photoresist.pdf.
- [144] S. Wolf and R. F. M. Smith, *Student Reference Manual for Electronic Instrumentation Laboratories*, 2nd ed., Upper Saddle River: Pearson Prentice Hall, 2004.
- [145] N. H. E. Weste and D. M. Harris, *CMOS VLSI Design: A Circuits and Systems Perspective*, 4th ed., Boston, MA: Addison-Wesley, 2011.
- [146] D. C. Look, K. D. Leedy and D. L. Agresta, "Nondestructive quantitative mapping of impurities and point defects in thin films: Ga and VZn in ZnO:Ga.," *Appl. Phys. Lett.*, vol. 104, 2014.
- [147] M. L. Jespersen, Interviewee, *Discussion of XPS of Vanadium Dioxide*. [Interview]. 16 January 2015.
- [148] G. Sarau, A. Bochmann, R. Lewandowska and S. Christiansen, "From Micro- to Macro-Raman Spectroscopy: Solar Silicon for a Case Study," in *Advanced Aspects of Spectroscopy*, M. A. Farrukh, Ed., InTech, 2012, pp. 221-246.
- [149] TeraView, "TPS 3000 Modular Terahertz Instrument: General Information," [Online]. Available: http://www.lot-oriel.com/files/downloads/teraview/eu/TPS_3000_General_information_eu.pdf. [Accessed 1 January 2015].
- [150] TeraView, "TPS Spectra 3000 - THz Pulsed Imaging and Spectroscopy," 2013. [Online]. Available: <http://www.teraview.com/products/terahertz-pulsed-spectra-3000>. [Accessed 1 January 2015].

- [151] Omega, "Non-Reversible Labels," 2015. [Online]. Available: http://www.omega.com/Temperature/pdf/TL-C5_LABELS.pdf. [Accessed 1 January 2015].
- [152] J. C. Parker, "Raman scattering from VO₂ single crystals: A study of the effects of surface oxidation," *Phys. Rev. B*, vol. 42, no. 5, pp. 3164-3166, August 1990.
- [153] H.-T. Kim, B.-G. Chae, D.-H. Youn, G. Kim and K.-Y. Kang, "Raman study of electric-field-induced first-order metal-insulator transition in VO₂-based devices," *Appl. Phys. Lett.*, vol. 86, 2005.
- [154] M. Pan, J. Liu, H. Zhong, S. Wang, Z.-f. Li, X. Chen and W. Lu, "Raman study of the phase transition in VO₂ thin films," *J. Crystal Growth*, vol. 268, pp. 178-183, 2004.
- [155] P. Schilbe, "Raman scattering in VO₂," *Physica B*, Vols. 316-317, pp. 600-602, 2002.
- [156] X. J. Wang, H. D. Li, Y. J. Fei, X. Wang, Y. Y. Xiong, Y. X. Nie and K. A. Feng, "XRD and Raman study of vanadium oxide thin films deposited on fused silica substrates by RF magnetron sputtering," *Appl. Surface Science*, vol. 177, pp. 8-14, 2001.
- [157] X.-B. Chen, J.-H. Shin, H.-T. Kim and Y.-S. Lim, "Raman analyses of co-phasing and hysteresis behaviors in V₂O₃ thin film," *J. Raman Spectrosc.*, vol. 43, pp. 2025-2028, 2012.
- [158] A. Okamoto, Y. Fujita and C. Tatsuyama, "Raman study on the High Temperature Transition in V₂O₃," *J. Phys. Soc. Jpn.*, vol. 52, no. 1, pp. 312-317, 1983.
- [159] Y. A. Çengel, R. H. Turner and J. M. Cimbala, *Fundamentals of Thermal-Fluid Sciences*, 3rd ed., New York: McGraw-Hill, 2008.
- [160] T. Yamane, N. Nagai, S.-i. Katayama and M. Todoki, "Measurement of thermal conductivity of silicon dioxide thin films using a 3 ω method," *J. Appl. Phys.*, vol. 91, no. 12, pp. 9772-9776, 2002.
- [161] A. J. Griffin, F. R. Brotzen and P. J. Loos, "The effective transverse thermal conductivity of amorphous Si₃N₄ thin films," *J. Appl. Phys.*, vol. 76, no. 7, pp.

4007-4011, 1994.

- [162] J. C. Lambropoulos, M. R. Jolly, C. A. Amsden, S. E. Gilman, M. J. Sinicropi, D. Diakomihalis and S. D. Jacobs, "Thermal conductivity of dielectric thin films," *J. Appl. Phys.*, vol. 66, no. 9, pp. 4230-4242, 1989.

- [163] Kyocera. [Online]. Available:
<http://americas.kyocera.com/kicc/pdf/Kyocera%20Sapphire.pdf>.

- [164] H. Wiedemeier and P. A. Siemers, "The Thermal Expansion of GeS and GeTe," *Z. anorg. allg. Chem.*, vol. 481, pp. 299-304, 1977.

REPORT DOCUMENTATION PAGE			Form Approved OMB No. 0704-0188	
<p>The public reporting burden for this collection of information is estimated to average 1 hour per response, including the time for reviewing instructions, searching existing data sources, gathering and maintaining the data needed, and completing and reviewing the collection of information. Send comments regarding this burden estimate or any other aspect of this collection of information, including suggestions for reducing this burden to Department of Defense, Washington Headquarters Services, Directorate for Information Operations and Reports (0704-0188), 1215 Jefferson Davis Highway, Suite 1204, Arlington, VA 22202-4302. Respondents should be aware that notwithstanding any other provision of law, no person shall be subject to any penalty for failing to comply with a collection of information if it does not display a currently valid OMB control number. PLEASE DO NOT RETURN YOUR FORM TO THE ABOVE ADDRESS.</p>				
1. REPORT DATE (DD-MM-YYYY) 26-03-2015		2. REPORT TYPE Master's Thesis		3. DATES COVERED (From — To) Oct 2013 – Mar 2015
4. TITLE AND SUBTITLE Materials Characterization and Microelectronic Implementation of Metal-insulator Transition Materials and Phase Change Materials		5a. CONTRACT NUMBER		
		5b. GRANT NUMBER		
		5c. PROGRAM ELEMENT NUMBER		
6. AUTHOR(S) Gwin, Alexander H., 1st Lt, USAF		5d. PROJECT NUMBER 15G451C		
		5e. TASK NUMBER		
		5f. WORK UNIT NUMBER		
7. PERFORMING ORGANIZATION NAME(S) AND ADDRESS(ES) Air Force Institute of Technology Graduate School of Engineering and Management (AFIT/EN) 2950 Hobson Way Wright-Patterson AFB, OH 45433-7765		8. PERFORMING ORGANIZATION REPORT NUMBER AFIT-ENG-MS-15-M-016		
9. SPONSORING / MONITORING AGENCY NAME(S) AND ADDRESS(ES) Air Force Office of Scientific Research (AFOSR) Attn: Kenneth Goretta 875 N. Randolph St. Suite 325, Room 3112 Arlington AFB, VA 22203 (703) 696-7349, kenneth.goretta@us.af.mil		10. SPONSOR/MONITOR'S ACRONYM(S) AFOSR/RTA		
		11. SPONSOR/MONITOR'S REPORT NUMBER(S)		
12. DISTRIBUTION / AVAILABILITY STATEMENT Distribution Statement A: Approved for Public Release; Distribution Unlimited.				
13. SUPPLEMENTARY NOTES This work is declared a work of the U. S. government and is not subject to copyright protection in the United States.				
14. ABSTRACT Vanadium dioxide (VO ₂) is a metal-insulator transition (MIT) material, and germanium telluride (GeTe) is a phase change material (PCM), both of which undergo several orders of magnitude increase in electrical conductivity from room temperature to their transition temperatures. They are candidates for many important technologies, including ultra-fast electronic memory, optical switches and filters, and active layers in terahertz metamaterials, among others. The physical mechanisms causing the phase transitions in these materials are explained and investigated experimentally. These materials were incorporated into six types of microelectronic devices, which were designed, fabricated, and tested at the Air Force Institute of Technology (AFIT). Additionally, these materials were investigated by materials characterization methods spanning the majority of the electromagnetic spectrum. The results show a most suitable applicability to electronic radio frequency (RF) switches, terahertz (THz) modulators, and phase change random access memory (PCRAM). Simple RF switches had 2 dB insertion losses and 30 dB of isolation, THz transmittance modulation of up to 99.5%, and PCRAM cells with threshold electric fields of approximately 1 V/μm.				
15. SUBJECT TERMS Germanium telluride, phase change random access memory, radio frequency switch, terahertz modulator, vanadium dioxide				
16. SECURITY CLASSIFICATION OF:		17. LIMITATION OF ABSTRACT UU	18. NUMBER OF PAGES 230	19a. NAME OF RESPONSIBLE PERSON Dr. Ronald A. Coutu, Jr., AFIT/ENG
a. REPORT U	b. ABSTRACT U			c. THIS PAGE U